MAGNETISM AND NEUTRON SCATTERING STUDIES OF RARE-EARTH CHROMATE SINGLE CRYSTALS

by

Yinghao ZHU

Doctor of Philosophy in Applied Physics and Materials Engineering

2022

Institute of Applied Physics and Materials Engineering

University of Macau

MAGNETISM AND NEUTRON SCATTERING STUDIES OF RARE-EARTH CHROMATE SINGLE CRYSTALS

by

Yinghao ZHU

SUPERVISOR: Prof. Haifeng Li

Doctor of Philosophy in Applied Physics and Materials Engineering

2022

Institute of Applied Physics and Materials Engineering

University of Macau

Acknowledgements

The present Ph.D. thesis would not have been possible without the guide and help of my supervisor, friends, colleagues, and family. I would like to thank them for their kind help and support over the past 4 years. Here I express my earnest gratitude especially to the following persons:

My foremost thank goes to my supervisor Prof. Dr. Haifeng Li. I still remember that I was almost a layman having seldom experience on experimental physics when I came to the University of Macau. He taught me how to perform experiments: from polycrystalline synthesis, to single crystal growth, in-house characterizations, and neutron scattering experiments, etc. He rise me up so I can see the fantastic world of neutron scattering. His guidance and encouragement make me overcome so many difficulties during my Ph.D. study. I will cherish what I have learnt from him in my whole life.

During this difficult time of COVID-19 epidemic, it is really hard to travel to do neutron scattering experiments. Hence, I benefit quite a lot from the instrument scientists for their help with the neutron scattering experiments:

Dr. Shin-ichiro Yano (SIKA @ ANSTO).

Prof. Dr. Ryoichi Kajimoto and Dr. Kazuki Iida (4SEASONS @ J-PARC).

Prof. Dr. Qingzhen Huang (BT-1 @ NSIT).

Prof. Dr. Lunhua He, Prof. Dr. Jie Chen, Prof. Dr. Sihao Deng, Dr. Yaoda Wu (GPPD @ CSNS).

Dr. Chin-Wei Wang (WOMBAT @ ANSTO).

Moreover, I owe my thanks to Prof. Dr. Ruiqin Zhang for supporting me carrying out the study on first-principles calculations at the City University of Hong Kong. Thanks for Prof. Dr. Dao-Xin Yao and Shangjian Jin from the Sun Yat-sen University for their assistance of theoretical support. Thanks for Prof. Dr. Hui Pan from the University of Macau for his invaluable discussion with me on DFT calculations. And thank Prof. Dr. Lieh-Jeng Chang from National Cheng Kung University for his

Abstract

Rare-earth transition-metal oxides (RETMOs) provide a strongly correlated electronic platform to couple the degrees of freedom including charge, spin, lattice, and orbital. Among various RETMOs compounds, rare-earth orthochromates with a chemical formula of $RECrO_3$ are an interesting family of RETMOs materials. It was suggested that the interactions of $4f$-$3d$ spins play an important role in producing electric polarization below the Néel temperature, and the magnetoelectric effect may exist in the family of orthochromates. Moreover, there also exist various novel magnetic behaviors in the compound.

Firstly, high-quality $RECrO_3$ single crystals were achieved with the laser-diode floating-zone method. With the as-grown single crystals, in-house characterizations were performed to shed light on their properties. A systematic room-temperature X-ray powder diffraction study was carried out on the as-grown single crystals. Structural refinements show that the $RECrO_3$ single crystals belong to orthorhombic crystal system with $Pbnm$ space group. We performed magnetization measurements as functions of temperature and external magnetic fields on as-grown single crystals, providing intrinsic magnetic properties. The t_{2g}-e_g hybridization was also investigated by first-principles calculations.

A neutron powder diffraction study of a single-crystalline $YCrO_3$ compound was carried out at a temperature range from 12 to 1200 K. The high-temperature (321–1200 K) structural information and magnetism indicate a strong magnetic frustration. Meanwhile, the neutron powder diffraction study at low temperatures (12–300 K) revealed its magnetic structure. Anisotropic magnetostriction effect was observed. An inelastic neutron scattering experiment was carried out based on a $YCrO_3$ single crystal. A Linear spin-wave theoretical model considering Heisenberg exchange and Dzyaloshinskii-Moriya interaction was built to study the magnon dispersion. The result indicates a strong spin-orbit coupling in the $YCrO_3$ antiferromagnet.

The structural and magnetic properties of the $GdCrO_3$ single crystal were carried

out. We observed the indications of the canted AFM structure of Cr^{3+} ions at $T_{\text{N-Cr}}$, the spin reorientation of Cr^{3+} moments at T_{SR}, and the formation of a long-range-ordered Gd^{3+} magnetic structure at $T_{\text{N-Gd}}$. The magnetic phase diagrams of $T_{\text{N-Gd}}$ and $T_{\text{N-Cr}}$ are also studied. The $GdCrO_3$ single crystal displays nice potential application on magnetic refrigeration.

Declaration

I declare that the thesis here submitted is original except for the source materials explicitly acknowledged and that this thesis as a whole, or any part of this thesis has not been previously submitted for the same degree or for a different degree.

I also acknowledge that I have read and understood the Rules on Handling Student Academic Dishonesty and the Regulations of the Student Discipline of the University of Macau.

LIST OF TABLES

LIST OF FIGURES

List of abbreviations

AC	alternating current
AFE	antiferroelectric
AFM	antiferromagnetic
BOA	Born-Oppenheimer approximation
BVSs	bond valence states
C_p	specific heat
CVT	chemical vapor transport
CW	Curie-Weiss
DC	direct current
DOSs	density of states
DFT	density functional theory
DM	Dzyaloshinskii-Moriya
EDS	energy-dispersive X-ray spectroscopy
ENS	elastic neutron scattering
FC	field cooling
FE	ferroelectric
FM	ferromagnetic
FZ	floating zone
G-AFM	G-type antiferromagnetic
GGA	general gradient approximation
GKA	Goodenough-Kanamori-Anderson
HF	Hartree-Fock
HK	Hohenberg-Kohn

HP	Holstein-Primakoff
INS	inelastic neutron scattering
KNB	Katsura-Nagaosa-Balatsky
LDA	local density approximation
LSWT	linear spin-wave theory
M	magnetization
MCE	magnetocaloric effect
MIT	metal-insulator transition
NPD	neutron powder diffraction
PM	paramagnetic
PPMS	physical property measurement system
RETMOs	rare-earth transition-metal oxides
RKKY	Ruderman-Kittel-Kasuya-Yosida
rpm	revolutions per minute
SEM	scanning electronic microscopy
SOC	spin-orbit coupling
SR	spin reorientation
T	temperature
T_C	Curie temperature
T_N	Néel temperature
T_{SR}	SR transition temperature
VCT	virtual charge transfer
XRPD	X-ray powder diffraction
ZFC	zero-field cooling
μ_B	Bohr magneton

CHAPTER 1

INTRODUCTION

1.1 General overview

Since the 1920s, the fundament of quantum theory has opened a new window for people to understand the world of atoms. In a periodic system, various quantum effects make things, e.g. electronic state, spontaneous spin polarization, and quasi-particle collective excitations, much different from what they originally are in single atoms [1]. An evident case is spin, which is an intrinsic property of a particle, i.e., completely a quantum phenomenon, having no classical correspondence. The versatile quantum behaviors in solid have led to tremendous attraction to the study of quantum materials [2]. During the past decades, the coupling between degrees of freedom comprising charge, spin, lattice, and orbital has displayed a tour-de-force performance in the area of condensed matter science, e.g. high-temperature conductivity [3], multiferroics [4, 5], quantum Hall effect [6], quantum spin Hall effect [7], and quantum spin liquid [8].

In the post-Moore era, the simple reduction on the scale of devices has met its limitation, composed of high power consumption [9], Fermi pinning [10], quantum tunneling [11], *etc.*, making the development of new-generation nonvolatile storage technology a blue ocean market. Multiferroicity, cultivated from the coexistence of ferroelectricity and magnetism, is of interest to technological applications and fundamental study on the origin of multiple orders. More significantly, magnetism and ferroelectric polarization can be coupled with each other in a magnetoelectric material, making it possible to switch the electric polarization/magnetization by an external applied magnetic/electric field [4]. The novel property then provides people a new route to get around the state-of-art bottleneck of information storage, paving the way for big data, artificial intelligence, blockchain technology, cloud computing, *etc.* The dramatic potential has made multiferroic materials an attractive class in material science. During the past years, multiferroic materials have come under the spotlight for the dis-
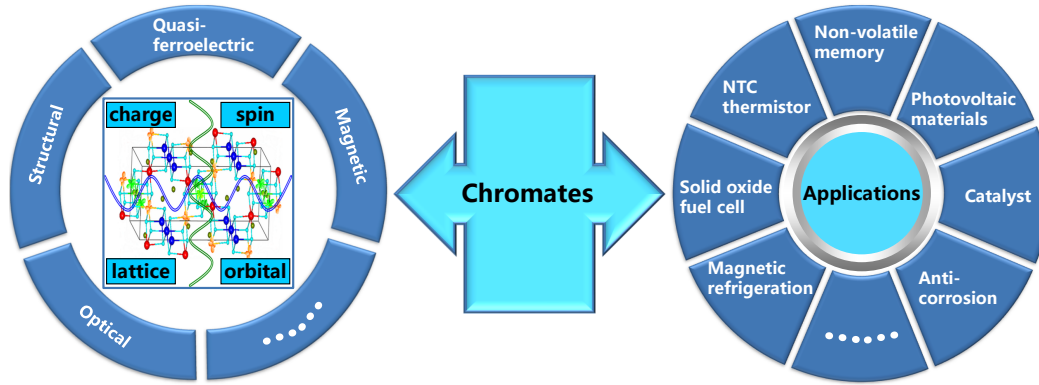
Figure 1.1: The chromates display some interesting properties such as quasi-ferroelectric, structural, magnetic, and optical, resulting from couplings between charge, spin, orbital, and lattice degrees of freedom (left). These make chromates potential as magnetic refrigeration, solid oxide fuel cell, negative-temperature-coefficient (NTC) thermistor, non-volatile memory application, photovoltaic materials, catalyst, and anti-corrosion field (right).

covery of new multiferroic materials, the origin of multiferroicity, device process, etc. Up to the present, multiple multiferroic materials have been proposed to display appreciable potential for applications. One class is single-phase multiferroic materials, e.g. $BiFeO_3$ [12], $TbMnO_3$ [13], $YMnO_3$ [14], $Ca_3Mn_2O_7$ [15]. The other famous class is the multiferroic magnetoelectric composites, like the heterostructure composed of ferri-/ferromagnetic and ferroelectric layers [16]. Recently, it was also reported that there exists metal multiferroicity in some van der Waals 2D magnets [17], while that is another story beyond the scope of the present thesis. For single-phase multiferroic materials, a great deal of interest in the origin of multiferroicity has also been spurred, making multiferroics a hot topic in condensed matter physics.

The set of chromium-based $RECrO_3$ (RE = rare earth) compounds was suggested to be another family of multiferroic materials, usually displaying ferroelectricity, weak ferromagnetism, and a wide application in fields of catalyst, thermistor, solid-oxide fuel cell, non-volatile memory device, $etc.$ [18], as visualized in Fig. 1.1. The pioneering study on $RECrO_3$ compounds was started by Náray-Szabo in 1943, at which $LaCrO_3$ became the earliest reported compound of the $RECrO_3$ family [19]. However, the crystal structure of $LaCrO_3$ was mistakenly characterized to be a cubic structure with Pm-$3m$ space group. In 1950, Jonker and Santen synthesized polycrystalline

samples of $LaCrO_3$ with a standard ceramic technique [20]. Their study mainly focused on the magnetism of transition-metal perovskite oxides, as a comparison with varieties of manganites, $LaCrO_3$ is poorly ferromagnetic. It is worth mentioning that they also tried the single crystal growth by flux method, but did not succeed, unfortunately. Over the same period, the superexchange theory in transition-metal oxides was perfected by Goodenough [21], Kanamori [22], and Anderson [23, 24]. To apply the theory in real compounds, it rose to be a pressing issue to extract the precise crystallographic information of various transition-metal oxides. In the 1950s, it used to be a controversial issue on the actual crystal structure of rare-earth chromate, i.e., whether it is a monoclinic or an orthorhombic structure [25]. One famous case is the yttrium chromate compound $YCrO_3$, which was firstly reported by Looby and Katz in 1954. Their X-ray diffraction study on $YCrO_3$ gave a monoclinic structure with $a = c = 7.61$ Å, $b = 7.54$ Å [26]. In 1956, Geller and Wood have marked the end of the debate by pointing out that $(h+l)$ has been treated as odd by counting the diffraction lines from impurity from Cr_2O_3 in the previous X-ray diffraction on rare-earth chromates [27, 28, 29]. By omitting the undesired lines, they acquired a $GdFeO_3$-type orthorhombic crystal structure with $Pbnm$ space group (No. 62). As for $YCrO_3$, lattice parameters were given with $a = 5.238$ Å, $b = 5.518$ Å, $c = 7.54$ Å [28], which are close to the state-of-art study by neutron diffraction, as illuminated in chapter 6. Afterward, a neutron diffraction study on $LaCrO_3$ by Koehler and Wollan also gave the orthorhombic crystal structure with $a = 5.487$ Å, $b = 5.551$ Å, $c = 7.75$ Å, determining the $Pbnm$ space group of $RECrO_3$ compounds [30]. Based on the X-ray diffraction data on $RECrO_3$ in the present thesis, the $Pbnm$ crystal structure of a $RECrO_3$ compound is plotted in a primitive cell, as exhibited in Fig. 1.2. In 1961, Weinberg and Larssen performed an electron paramagnetic resonance investigation on $LaCrO_3$, in which the Néel temperature is determined to be $T_N \approx 295$ K [31]. In the following decades, rare-earth orthochromates have got tremendous attention for their magnetism, consisting of actual magnetic structures [32], spin-reorientation phase transitions [33], absorption on RE^{3+} exciton [34], $etc.$ The crystal structures, magnetic structures of Cr^{3+} spins, avail-
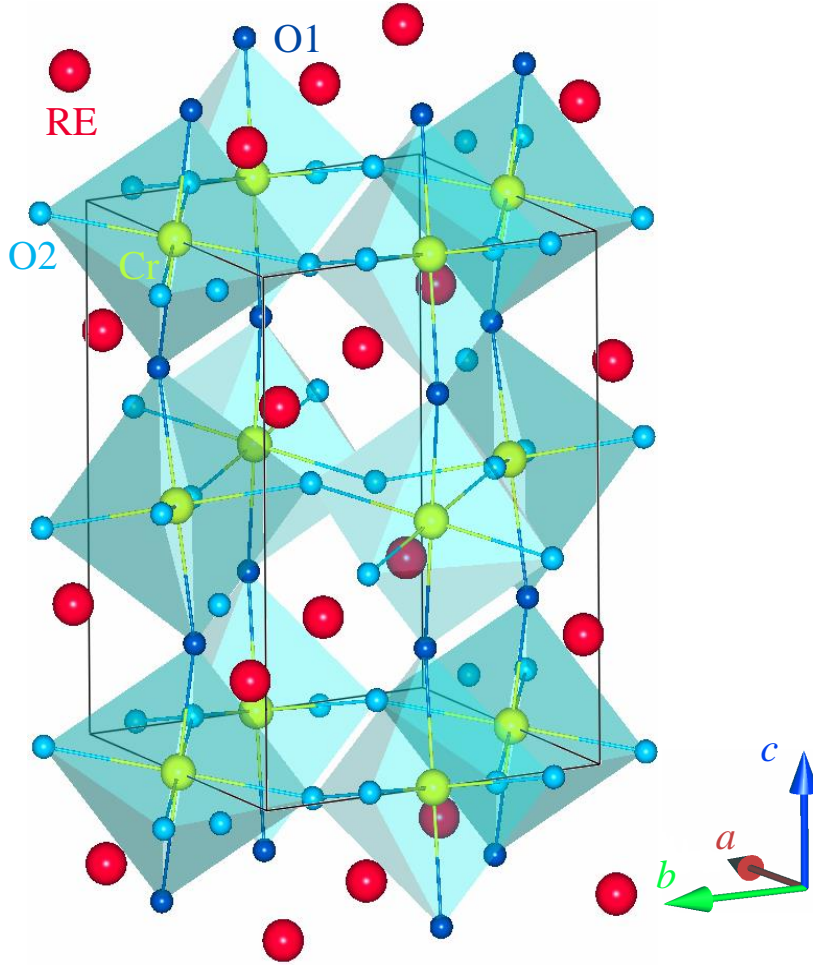
Figure 1.2: Crystal structure of an RECrO$_3$ compound in one primitive cell (solid lines) of $Z = 4$ with $Pbnm$ space group (No. 62). The RE, Cr, O1, and O2 ions are labeled, respectively.

able parameters of ferroelectric polarization as well as conditions of measurement are summarised in Table 1.1.

As the most prominent property of RECrO$_3$ compounds, the study on multiferroicity started from YCrO$_3$. Later, it was also reported that the formation of the Cr^{3+} magnetic orders has an apparent correlation with the ferroelectric property. Thus, to study the underlying relation between magnetism and ferroelectricity in RECrO$_3$ may shed light on the nature of multiferroics [50, 62]. Chromium ions in RECrO$_3$ compounds hold a single-valence state, i.e., Cr^{3+} ($t_{2g}^3 e_g^0$), naturally discarding the e_g orbital ordering and its perturbation on the t_{2g} electrons. This leads to a tightly localized electric environment, an ideal platform for the potential coexistence of ferroelectricity and magnetism. The ferroelectric transition temperature ($T_{FE} \sim 473$ K) of the YCrO$_3$ com-

Table 1.1: Crystal structure, magnetic structure of Cr^{3+} spins, Néel temperatures of Cr^{3+} spins T_N^{Cr}, available Néel temperatures of RE^{3+} spins T_N^{RE}, electric polarizations P, and corresponding electric field E and temperature T_{meas} of measurement of $RECrO_3$ (RE = Y, La–Lu) compounds. The magnetic structures are marked with the notions of Γ_1 (A_x, G_x, C_z), Γ_2 (F_x, C_y, G_z), Γ_4 (G_x, A_y, F_z). The values of electric polarization summarised here were all measured via polycrystalline samples. The data sources are cited accordingly. → denotes a magnetic spin reorientation upon cooling. * represents the marked information is still a controversial issue which has different opinions.

$RECrO_3$ (RE = Y, and La–Lu)								
RE^{3+} =	Y^{3+}	La^{3+}	Ce^{3+}	Pr^{3+}	Nd^{3+}	Pm^{3+}	Sm^{3+}	Eu^{3+}
cryst. struct.	Orthorhombic, $Pbnm$ space group (No. 62)							
magn. struct.	Γ_4 [35, 36]	Γ_4 [37]	G_y [38]	Γ_2 [39]	$\Gamma_4 \to \Gamma_1$ [40]	-	*$\Gamma_4 \to \Gamma_1$ [41]	Γ_4 [42]
T_N^{Cr}	141 K [35]	298 K [43]	260 K [44]	240 K [45]	219 K [40]	-	191 K [41]	181.6 K [46]
T_N^{RE}	N/A	N/A	-	-	-	-	1.3 K [47]	N/A
P	0.25 µC/cm²	-	-	-	435 µC/m²	-	~ 0.7 µC/cm²	-
E	~ 0.03 kV/cm	-	-	-	4 kV/cm	-	1.4 kV/cm	-
T_{meas}	300 K [48]	-	-	-	74 K [49]	-	10–15 K [50]	-
RE^{3+} =	Gd^{3+}	Tb^{3+}	Dy^{3+}	Ho^{3+}	Er^{3+}	Tm^{3+}	Yb^{3+}	Lu^{3+}
cryst. struct.	Orthorhombic, $Pbnm$ space group (No. 62)							
magn. struct.	$\Gamma_4 \to \Gamma_2$ [51]	Γ_2 [39]	Γ_2 [52, 53]	Γ_2 [32]	$\Gamma_4 \to \Gamma_1$ [54]	Γ_2 [55]	Γ_2 [56]	Γ_2 [57]
T_N^{Cr}	169 K [58]	157.9 K [46]	148.5 K [46]	143.2 K [46]	135.4 K [46]	125.9 K [46]	117.9 K [46]	122.3 K [46]
T_N^{RE}	2.3 K [58]	3.05 K [59]	*2.8 K [46]	-	*8 K [46]	-	-	N/A
P	0.7 µC/cm²	0.5 µC/cm²	-	0.32 µC/cm²	~ 70 µC/m²	0.25 µC/cm²	-	100 µC/m²
E	2.25 kV/cm	1.43 kV/cm	-	1.2 kV/cm	174 kV/m	1.43 kV/cm	-	165 kV/m
T_{meas}	15 K [50]	15 K [50]	-	10 K [60]	8 K [61]	15 K [50]	-	8 K [61]

pound is higher than that of the antiferromagnetic (AFM) phase transition of Cr^{3+} ions ($T_N^{Cr} \sim 141.5$ K) [35, 48]. An isosymmetric structural phase transition was observed at ~ 900 K in the neutron powder diffraction study on a pulverized $YCrO_3$ single crystal, where the incompressibility of the lattice constants a, b, and c is anisotropic, and there exist obvious atomic displacement and charge subduction on the Y and O2 sites [63]. Net electric polarization was observed for polycrystalline $LuCrO_3$ and $ErCrO_3$ compounds below T_N^{Cr}, indicating the presence of a possible ferroelectric state, whereas this is clearly absent above T_N^{Cr}. Most importantly, the study demonstrates that the paramagnetic (PM) nature of the RE sites is not necessary to accommodate the ferroelectricity in orthochromates [61]. In addition, for $LuCrO_3$ and $ErCrO_3$ compounds, their respective polarizations reach maximum values of ~ 90 $\mu C/m^2$ ($LuCrO_3$ at E = 165 kV/cm) and ~ 70 $\mu C/m^2$ ($ErCrO_3$ at E = 174 kV/cm). Both polarizations can be reversed and could be explained by either the Cr^{3+} off-centering or the ferroelasticity, or their couplings, and even by Cr^{3+} vacancies [61]. The $SmCrO_3$ compound displays an electric polarization with a maximum of ~ 8 $\mu C/m^2$ at E = 1.43 kV/cm and ~ 15 K [64], which was ascribed to a breaking of the local symmetry via Cr^{3+} off-centering [64]. It was demonstrated that electric dipoles exist in the $DyCrO_3$ compound, which was attributed to the displacement of Cr^{3+} cations [65]. Electric polarization was observed in $TbCrO_3$ and $TmCrO_3$ compounds at E = 1.43 kV/cm below T_N^{Cr} [50], though the existence of the electric dipoles in the $TmCrO_3$ compound is still in debate [66].

In addition to the multiferroic property, the series of rare-earth chromate compounds also display other multiple applications, e.g. solid oxide fuel cells, catalyst, NTC thermistor, photovoltaic application, anti-corrosion, magnetic cooling, and thermal electricity [67]. More specifically, with a high-energy micro-arc alloying depositing method, $DyCrO_3$-based coatings can be used to inhibit the oxidation of 430 stainless steel [68]. After comparing with a series of catalysts, Hou *et al.* have found that the Pd/$GdCrO_3$ composite displays better photocatalytic reduction efficiency of nitrate as well as selectivity to N_2, implying a noteworthy potential for wastewater

treatment [69]. A recent study based on first-principles calculations on $EuCrO_3$ has investigated its thermal electric property comprising electric conductivity and Seeback coefficient, and ZT value. The study demonstrates an appreciable electric conductivity of $EuCrO_3$, which may serve as a candidate material for thermoelectric technology [70]. Moreover, there exist amounts of studies indicating that the $GdCrO_3$ compound displays better performance on magnetic refrigeration, compared with other rare-earth transition-metal oxides [58]. Here I just listed several representatives about the application of rare-earth chromate compounds. The applications of $RECrO_3$ compounds are far more than I have referred to in the thesis, and I believe such a family of $RECrO_3$ will, and should, be developed in diversified areas shortly.

The coupling between the RE^{3+} ($4f^n$) electrons and the Cr^{3+} ($t_{2g}^3 e_g^0$) electrons makes $RECrO_3$ an excellent platform to study various interesting magnetism. In 2010, Zhou et $al.$ performed a series of neutron diffraction studies on $RECrO_3$ and $REFeO_3$, accompanied by characterizations of their Néel T_N temperatures. Their study displayed that the t_{2g}-e_g orbital hybridization is the reason why $RECrO_3$ exhibits a more dramatic change of T_N than that of $REFeO_3$. The Cr^{3+} ($t_{2g}^3 e_g^0$) state could realize a virtual charge transfer of t_{2g}^3-O-e_g^0, leading to a ferromagnetic coupling to the total exchange interaction, i.e., $J = J^\pi - J_{hb}^\sigma$ [43]. While such a mechanism does not exist in ferrites due to the Fe^{3+} ($t_{2g}^3 e_g^2$) state. A new degree of freedom is provided from the t-e hybridization in the platform of chromates, enabling one to manipulate the competition between ferromagnetic coupling and antiferromagnetic coupling. One case is the spinel chromate oxide ACr_2O_4, in which novel quantum states can be cultivated by tuning the ferromagnetic contribution in the antiferromagnetic matrix [71, 72].

A long-standing obstacle to studying chromium-based oxides is the difficulty in growing large-scale single crystals due to the high vapor pressure of Cr_2O_3 at melting points of chromates [73]. The intense volatility of chromium oxides can reduce the heating power, particularly for the four-mirror furnace [74], which makes it not easy to stably grow the single crystals of chromates. Consequently, most existing studies of rare-earth chromates were carried out based on polycrystalline samples. To unravel

the intrinsic nature of a certain compound, it is really demanded to carry out based on single-crystal samples. Previous single crystal growths of rare-earth chromates utilized usually the flux method [51], however, impurities from the flux exist in grown single crystals and strongly affect their macroscopic properties [58, 75]. Moreover, single crystals grown by the flux method are small (millimeters in size) and not suitable for studies that make excessive demands on the sample's quality and mass. In the present thesis, centimeter-scale rare-earth chromates can be grown for the first time, providing a basis of materials for understanding the nature of chromate oxides.

This briefly summarizes the current situation of the study on perovskite rare-earth chromate compounds. It should be noted that, for a clear understanding of the nature of $RECrO_3$, single crystal growth on chromate compounds is a not easy, but, ineluctable route. With high-quality single-crystal samples, single-crystal based in-house characterizations and neutron scattering experiments were carried out accompanied by theoretical modeling, shedding light on the intrinsic nature of the rare-earth chromates compounds.

1.2   Scope of this thesis

The present thesis consists of polycrystalline synthesis, single crystal growth, in-house characterizations, neutron scattering experiments, and theoretical modeling of rare-earth chromate compounds. The purpose of the thesis is to shed light on the nature of physical properties and possible coupling between degrees of freedom in the $RECrO_3$ family.

Chapter 2 introduces the concepts of several phenomena that exist in $RECrO_3$ compounds. Firstly, I illuminate the multiferroics, which are separated into two classes, i.e., type-I mutiferroicity and type-II multiferroicity. The state-of-art mechanisms proposed to be responsible for these two types of multiferroics have been expressed in detail. Moreover, I include the concept of some physical behaviors that I have studied in the thesis, including but not limited to strongly correlated electronic systems, spin-orbit coupling, magnetic exchange interactions (consisting of superexchange, double

exchange, and RKKY exchange), $4f$-$3d$ exchange coupling, magnetostriction effect, and magnetocaloric effect.

To finish the present thesis, a series of experimental techniques have been used. In chapter 3, I refer to the experimental methods from sample synthesis to various characterizations. Firstly, I illustrate the procedure of polycrystalline synthesis, following which are the experimental details of single-crystal-growth techniques, comprising of laser-diode floating-zone technique and chemical vapor transport method. Then, the in-house characterizations that I have used are introduced, accompanied by their basic principles. Finally, I include the theory of the neutron scattering technique, meanwhile, the neutron scattering spectrometers that have been used are also briefly introduced.

The theoretical methods that I have used to explain the experimental data are presented in chapter 4. Firstly, I introduce the origin, development, and current situation of the first-principles calculation method based on density functional theory. The density functional theory is introduced starting from the outset of quantum mechanics to Hartree-Fock equations, to Honhenberg-Kohn theorems and Kohn-Sham equations, and finally to Jacob's ladder of exchange-correlation functions. Further, the principle of the linear spin-wave theory is also deduced in detail, this usually acts as an excellent method for one to understand the results of inelastic neutron scattering.

Chapter 5 is dedicated to the crystal growth engineering, crystal structure, and magnetism of the rare-earth chromates RECrO$_3$. Besides, the t_{2g}-e_g orbital hybridization in RECrO$_3$ is also studied based on density functional theory. The monitor of the evolution of Bragg (0 2 0), (1 1 2), (2 0 0), and (0 2 1) peaks implies a regular basis with rare-earth ionic radius indicative of changes in lattice constants.

Chapter 6 discusses the yttrium oxide compound YCrO$_3$. Based on neutron powder diffraction, high-temperature crystal structure (321–1200 K) and on a pulverised YCrO$_3$ single crystal is studied. The characterization of high-temperature magnetism (300–980 K) is also carried out. Structural refinement of neutron powder diffraction data has been performed to extract lattice parameters and bond-length information. It is shown that YCrO$_3$ exhibits a strong magnetic frustration and a formation of mag-

netic polarons. The Y and O2 ions display evident atomic displacement and charge subduction, which might be related to the dielectric property of the YCrO$_3$ compound. A low-temperature (12–300 K) neutron powder diffraction study was carried out to investigate the crystal structure and magnetic structure. In addition, low-temperature magnetization and specific-heat studies are also included. YCrO$_3$ crystallizes into $Pnma$ space group at the referred temperature range. With lattice parameters (a, b, c, and V) extracted from refinement, an anisotropic magnetostriction effect is observed accompanied by a magnetoelastic effect. The Cr^{3+} spin interactions are probably two-dimensional Ising-like within the reciprocal (1 1 0) scattering plane. An inelastic neutron scattering study is also performed based on a YCrO$_3$ single crystal. There exist evident spin-wave dispersions coming from Cr^{3+} spins. To explain the spin-wave excitation, we built a linear spin-wave model, in which the Dzyaloshinskii–Moriya interaction is indispensably considered.

Chapter 7 deals with the gadolinium oxide compound GdCrO$_3$. X-ray diffraction of a pulverized single crystal indicates GdCrO$_3$ also crystallizes into an orthorhombic crystal structure. The studies on magnetism and the magnetocaloric effect of GdCrO$_3$ are discussed. Under an external magnetic field of 1000 Oe, Cr^{3+} spins form a canted antiferromagnetic structure at $T_{\text{N-Cr}}$ = 169.28(2) K. Upon cooling, a spin reorientation from Γ_4 (G_x, A_y, F_z) to Γ_2 (F_x, C_y, G_z) takes place at T_{SR} = 5.18(2) K due to Gd^{3+}-Cr^{3+} magnetic couplings. This is followed by a long-range antiferromagnetic ordering at $T_{\text{N-Gd}}$ = 2.10(2) K. Moreover, the present as-grown GdCrO$_3$ single crystal exhibits a prominent magnetocaloric effect for potential application in magnetic refrigeration.

Chapter 8 summarizes the important results described in this thesis and discusses the outlook of future studies of the rare-earth chromate compounds.

CHAPTER 2

SCIENTIFIC BACKGROUND: RARE-EARTH TRANSITION-METAL
OXIDES

Rare-earth transition-metal oxides (RETMOs) have gradually become a featured field in condensed matter physics. It provides a strongly correlated electronic platform, in which degrees of freedom including charge, spin, lattice, and orbital could couple between each other pairwise or even more, giving rise to novel physical phenomena and huge potentials in technology [76, 77].

The focus of RETMOs has consisted of but will not be limited to the following academic topics: multiferroics, unconventional superconductivity, magnetic frustration, spin-orbit coupling, magnetostriction effect, magnetocaloric effect, solid fuel cells, *etc.* [3, 4, 78]. Tremendous exploitation of the above novel phenomena may lead to the development of applications on advanced technologies, for example, spintronics, quantum computation, information memory, magnetic sensors, magnetic refrigeration, and new energy resources. For the current situation, understanding the attractive physical properties of RETMOs turns to the prerequisite of its application in industry. And there are still a lot of unsolved problems to be addressed.

In the present chapter, a brief introduction of multiferroic materials will be introduced with elucidating type-I and type-II multiferroics and their mechanism in the first part, followed by several concepts of novel magnetism and coupled freedoms including strongly correlated electronic systems, spin-orbit coupling, superexchange, $4f$-$3d$ exchange interaction, magnetostriction effect, and magnetocaloric effect that are related to this Ph.D. thesis in the second part.

2.1 Multiferroic materials

In the late nineteen century, the concept that magnetism and ferroelectricity may coexist or couple with each other was predicted by Curie on the framework of crystal-

lographic symmetry [79]. In 1926, Debye proposed the possibility that the magneto-electric effect may also exist [80]. The pioneering work of experimental attempt of realizing the coexistence of magnetism and ferroelectricity started in the late 1950s in the Soviet Union, that is ceramic samples of $Pb(Fe_{1/2}Nb_{1/2})O_3$ and $Pb(Fe_{1/2}Ta_{1/2})O_3$ were synthesized with both antiferromagnetic (AFM) and ferroelectric (FE) [81]. The d^0 rule was also proposed, i.e., diamagnetic metal ions with noble gas configurations such as Ti^{4+} and Nb^{5+} are essential for the FE polarization in perovskite oxides. At the same time, the magnetoelectric effect was also realized in the AFM Cr_2O_3 compound by Dzyaloshinskii [82]. Actually, as a specific term, the magnetoelectric effect is more useful than multiferroics; the former can be used for describing the interaction between spin (or magnetic induction $\mu_0 H$) and electric dipole (or electric field E). It is widely believed that the word "multiferroics" was firstly proposed in 1994 by Schmid, who also emphasized the importance to verify the multiferroicity in single-crystal-based samples, rather than only in the ceramic form [83]. At the beginning of this century, two famous systems were reported, triggering an upsurge of studies on multiferroic materials. One is $BiFeO_3$, which remains a large remanent FE polarization with $\sim$ 55 $\mu C/cm^2$ accompanied by a high FE transition temperature with $T_E \sim 1103$ K [12]; the other is $TbMnO_3$ in which strong magnetoelectric coupling exists associated with tunable FE polarization by an external magnetic field [13].

Multiferroic materials are a prominent class of systems, in which multiple long-range orders (typically magnetism and ferroelectricity) could coexist with each other, leading to the prominent extraordinary properties [84]. What makes multiferroics scientifically and technologically fascinating is not only the coexistence of two or more types of orders but also the tunable couplings between them, providing a novel mode for information writing and reading [85]. Multiferroic composites are also a prominent topic, while in the present section I mainly focus on the single-phase multiferroic materials [16]. Multiferroic materials can usually be divided into two types according to the strength of couplings between the magnetism and ferroelectricity. In the following section, detailed elucidation of type-I and type-II multiferroics is given accompanied
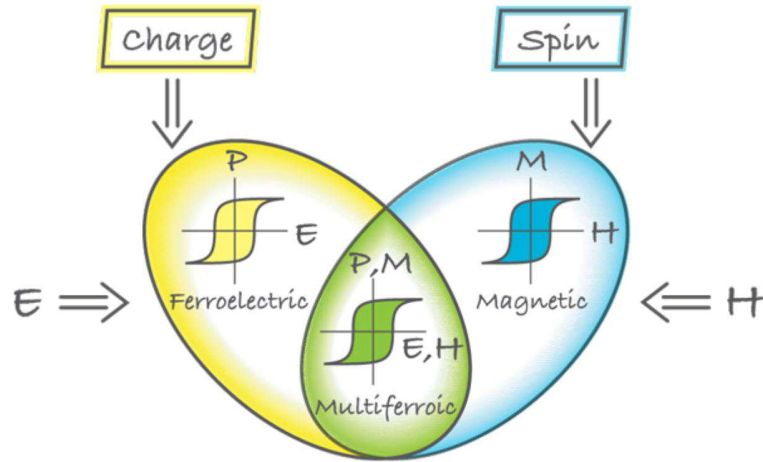
Figure 2.1: Multiferroics combine the properties of ferroelectrics and magnets. In the ideal case, the magnetization of a ferromagnet in a magnetic field displays the usual ferromagnetic hysteresis (blue), ferroelectrics which has a similar response to an electric field (yellow), and multiferroics that are simultaneously ferromagnetic and ferroelectric (green) [4].

by corresponding ferroelectric mechanisms and coupling between the orders.

2.1.1 Type I

The first class, named type-I multiferroic, includes those compounds in which FE polarization and magnetism have different origins and seldom display coupling between each other. In these materials, ferroelectricity usually occurs at much higher temperatures (higher than room temperature) than temperatures of magnetic ordering. Besides, an appreciable value of spontaneous FE polarization P is often rather given with magnitudes of larger than $10~\mu C/cm^2$. The type-I multiferroics contain kinds of well-known TM oxides such as $BiFeO_3$, $YMnO_3$, $YCrO_3$, $LuFe_2O_4$, $TbMn_2O_5$, Ca_3CoMnO_6 etc. A brief overview of several common mechanisms of ferroelectricity in type-I multiferroics is introduced in the following parts.

2.1.1.1 Lone electron pairs

Lone electron pairs mean the outer valence electrons which do not take part in chemical bonds, display anisotropic distribution and result in spatial inequivalence. Usually, appreciable ferroelectricity can be induced by lone electron pairs. As shown in
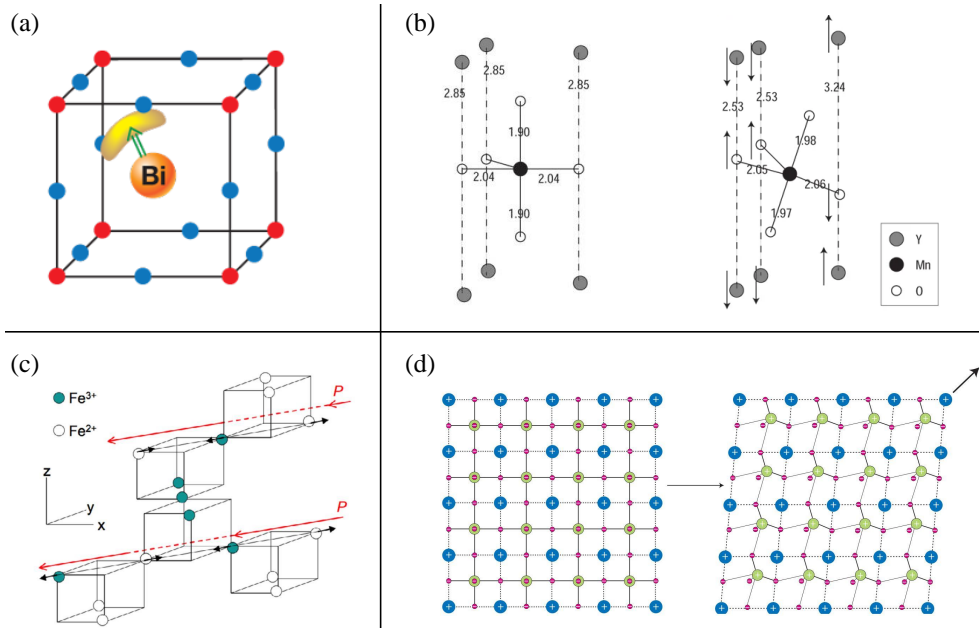
Figure 2.2: The main ferroelectric origin found in Type-I multiferroics. (a) In materials like $BiFeO_3$ and $Pb(Zr_xTi_{1-x})O_3$, the ordering of lone pairs (yellow "lobes") of Bi^{3+} and Pb^{2+} cations (orange), contributes to the polarization (green arrow) [4]. (b) Illustration of a MnO_5 polyhedron with Y layers above and below. The calculated atomic positions of the centrosymmetric (left) and ferroelectric structures (right). The numbers give the bond lengths in Å.The arrows indicate atomic displacements with respect to the centrosymmetric structure [14]. (c) Illustration of ferroelectricity induced by site-centered and bond-centered charge order in magnetite (Fe_3O_4). Emphasized are the Fe chains running in the [110] direction of magnetite—a pyrochlore lattice made by the spinel B sites. In the xy chains there is an alternation of Fe^{2+} and Fe^{3+} ions (open and filled circles). There appears an alternation of short and long Fe–Fe bonds simultaneously; shifts of Fe ions are displayed by short black arrows. The long diagonal red arrows denote the resulting polarization [86]. (d) Ferroelectricity in typical perovskite manganites with d^0 cations, like $BaTiO_3$. Shifts of green Ti ions from the centre of the oxygen octahedra (pink) create ferroelectric polarization (P), which is incompatible with any spontaneous magnetic moment, i.e., d^n cations [87].

Fig. 2.2(a), the two $6s$ electrons do not participate the sp orbital hybridization in the $BiFeO_3$, and they move from Bi^{3+} cations to FeO_6 octahedrons, finally a very large FE polarization displays due to the spatial anisotropy of $6s$ lone electron pairs [4, 12, 88]. Another example is lead zirconate titanate with a chemical formula of $Pb(Zr_xTi_{1-x})O_3$, which is often abbreviated as PZT. The $6s$ lone electron pairs of Pb^{2+} cations improve the FE properties which then realize considerable applications in the field of micro-electromechanical systems (MEMS) and non-volatile memory [89, 90].

2.1.1.2 Geometric mechanism

Unlike FE polarization induced by chemical bonds instability or spatial symmetry breaking via $6s$ lone-pair shifting, the geometric mechanism implies a breaking of the centrosymmetry may result from off-center atomic displacements, and thus a net FE polarization appears [91]. One well-known example is the hexagonal $YMnO_3$ (h-$YMnO_3$), in which the MnO_5 rotational buckling involves appreciable Y-O displacement. As a consequence, Y^{3+} cations display relative displacement from the symmetric site, and the two Y-O bonds vary from ~ 2.85 Å to ~ 2.53 Å and ~ 3.54 Å, as shown in Fig. 2.2(b) [14].

2.1.1.3 Charge order

For ionic crystals, positive and negative centers display at ionic positions due to the behavior of localized electrons, producing an electric dipole moment between each positive and negative charge [86, 92, 93]. One case is the site-centered charge-order (CO) compound, such as NaCl. For this compound, the spatial inversion symmetry is not broken. Hence, the electric dipole moments between $+e$ and $-e$ ions cancel out each other and there remains no net FE polarization. Another case is the bond-centered CO compound, in this case, ionic sites keep equivalent, while positive ions and negative ions have different bond lengths. And the bond-centered CO compound still remains centrosymmetric, leading to no net electric dipole moments, thus, no macroscopic FE polarization either. The interesting case is the combination of site-centered and bond-centered CO systems, which breaks the spatial inversion symmetry, making those electric dipole moments pointing in opposite directions can not cancel out each other, finally, a net FE polarization appears in such a kind of system [86]. Magnetite (Fe_3O_4) is one example, the Fe^{2+} and Fe^{3+} cations display typical site-centered CO accompanied by a modulation of Fe-Fe bond lengths in the xy chains [86, 94]. Therefore, as shown in Fig. 2.2(c), the site- and bond-centered CO chain along [110] direction leads to a net FE polarization.

2.1.1.4 Off-center shifts of cations

For perovskite compounds with empty d orbital at B-site cations, i.e., d^0 cations, charge transfer prefers to exist from the filled oxygen $2p$ orbital to the empty d state, forming strong covalent bonds between the B-site cations and oxygen anions [87]. Usually, a decreasing of symmetry from cubic to tetragonal, orthorhombic then to rhombohedral appears in perovskite compounds, thus enabling a long-range shift of B-site cations from the center of oxygen octahedra to corner oxygen anions, as shown in Fig. 2.2(d) [95]. A well-known example is $BaTiO_3$, in which a low-temperature FE polarization was proposed [96]. While, a Ti $3d$-O $2p$ orbital hybridization is needed in this case, leading to the notorious d^0 rule for FE polarization [97]. Besides, there also exist studies reporting on antiferroelectric (AFE) properties in compounds with hexagonal Barium titanate (h-$BaTiO_3$) structure ($P6_3/mmc$ space group), such as Ba_2FeSbO_6, $Ba_3Fe_2TeO_9$, and $Ba_3Fe_2WO_9$. In these compounds with an h-$BaTiO_3$ structure, elastic neutron scattering proved a rattling of Ba^{2+} cations in the BaO_8 polyhedra which was then proposed to be responsible for the AFE and dielectric behavior [98, 99]. Overall, three main structural degrees were summarized to be important in ferroic distortions: (1) shifts of cations, (2) oxygen polyhedral distortion in A-site or B-site sublattice, (3) oxygen octahedral tilting [100].

2.1.2 Type II

Type-II multiferroic is an interesting class in which FE polarizations are induced by certain special types of magnetism including spiral magnetic order and collinear magnetic order, usually a magnetoelectric coupling effect between the ferroelectricity and magnetism is accompanied. A prominent example is TbMnO3, which displays tunable FE order by an external magnetic field as shown in the temperature versus magnetic field phase diagram in Fig. 2.3(b) [13]. It is a very interesting behavior of the magnetoelectric coupling, which enables spin-driven FE polarizations, exhibiting huge potential to combine two existing memory technologies, ferroelectric random access memories (FeRAMs) and magnetic random access memories (MRAMs). This may
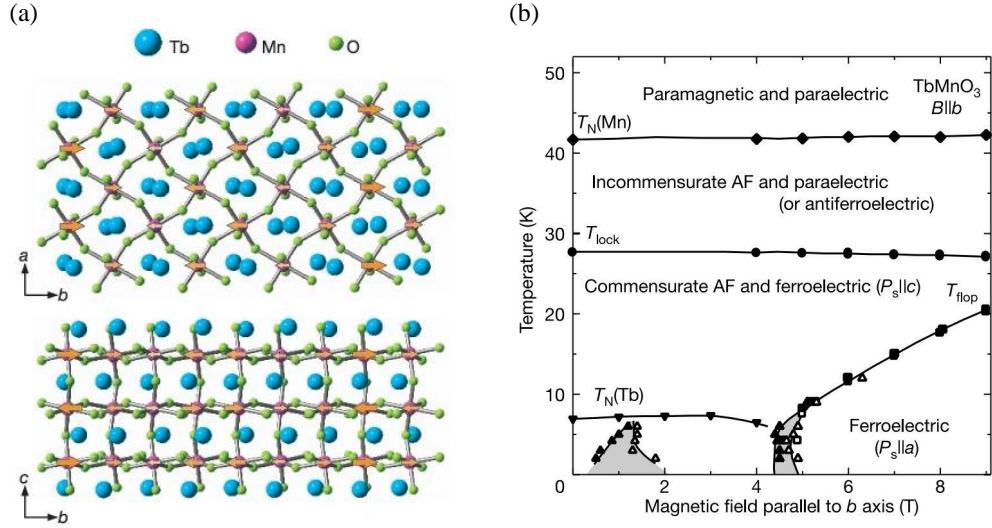
Figure 2.3: (a) Rough sketches of crystal structure at room temperature. (b) Temperature versus magnetic field phase diagram for $TbMnO_3$ for magnetic field applied along the b axis. Open and filled symbols represent the data points in the cooling (or magnetic-field increasing) and warming (or magnetic-field decreasing) runs, respectively. $T_N(Mn)$ (determined from the dielectric anomaly in ϵ_a) and $T_N(Tb)$ (determined from the anomaly in the $M-T$ curve) indicate the antiferromagnetic ordering temperature of the Mn^{3+} and Tb^{3+} moments, respectively. T_{lock} and T_{flop}, which were determined from the dielectric anomaly, denote the temperatures of incommensurate–commensurate (or lock-in) transition and electric polarization flop, respectively. Triangles indicate the points where the magnetization curves show steep steps. The shaded areas show magnetic field hysteresis regions [13].

further lead to a novel memory technology combining fast low-power electrical writing and non-destructive magnetic reading [101]. In a review written by Dong *et al.*, two main origins were proposed to produce the magnetoelectric coupling: One is the spin-orbit coupling which consists of Dzyaloshinskii-Moriya (DM) interaction and spin-dependent metal-ligand hybridization; the other is spin-lattice coupling which leads to a symmetric exchange striction [102]. In the following part, I will introduce the physical nature of two well-known mechanisms of magnetoelectric coupling, i.e., DM interaction and symmetric exchange striction.

2.1.2.1 Inverse Dzyaloshinskii-Moriya interaction

The most popular origin of magnetoelectric coupling should be the inverse DM interaction, which is also called the spin current model [103, 104]. At the very beginning, Dzyaloshinskii explained the observed weak ferromagnetism behavior in Cr_2O_3 on

17
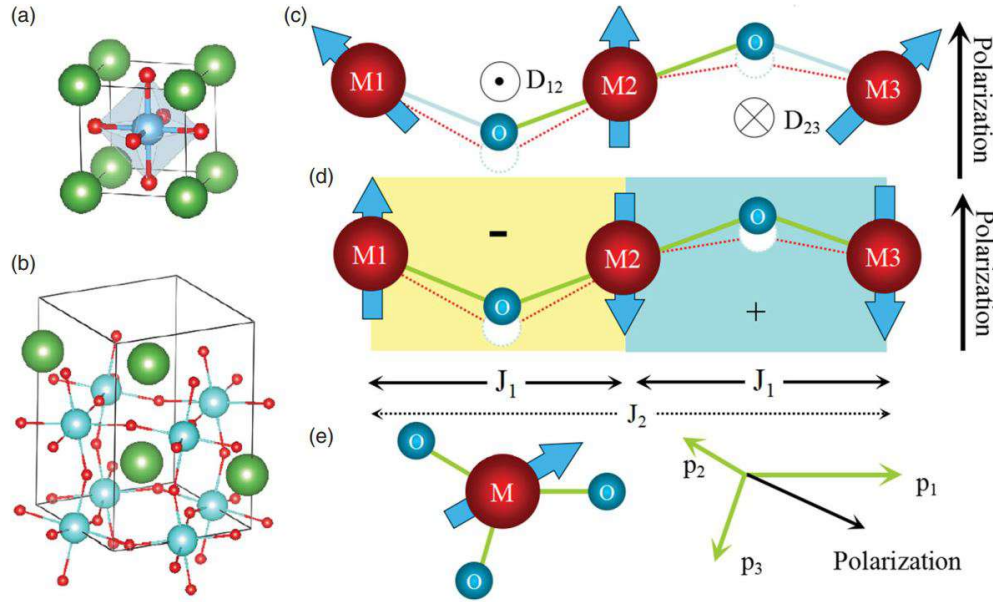
Figure 2.4: (a) and (b) Crystal structure of an ABO_3 perovskite. Green: A; Cyan: B. (a) an ideal cubic perovskite. All the nearest-neighbor B–O–B bonds are straight. (b) An orthorhombic perovskite lattice with the $GdFeO_3$-type distortion. All the nearest-neighbor B–O–B bonds are bent. (c) A breaking of the rotation symmetry regarding the M_i–M_j axis (M denotes metal ion) due to the bond bending. The asymmetric DM interaction is allowed, with the $\mathbf{D}_{ij}$ vector perpendicular to the M_i–M_j axis and oxygen displacement vector, for example, pointing in/out the paper plane, as sketched. A noncollinear spin pattern with a fixed helicity will uniformly modulate the $\mathbf{D}_{ij}$ vector to lower the energy, generating aligned ferroelectric dipoles. (d) A schematic of the exchange striction-induced ferroelectric polarization. The ionic displacements caused by the ↑↓ and ↓↓ spin pairs are not compensated, giving rise to a net dipole moment. The exchange frustration, namely antiferromagnetic J_2, favors the spin orders as shown in (c) or (d). (e) A metal ion is surrounded in an anion cage, breaking the inversion symmetry (left), and the metal–ligand hybridization can give rise to the three spin-dependent dipoles for the three bonds, allowing a net polarization [102].

the framework of thermodynamics [105]. Later, in 1960, Moriya demonstrated how the asymmetric exchange interaction could be derived from the spin-orbit coupling in the framework of the second-quantization-based perturbation theory [106]. In 1992, it was re-interpreted by Shekhtman *et al.* [107]. The origin of spin-orbit coupling is elucidated in section 2.2. It was widely accepted that the DM interaction gives rise to various novel physical phenomena beyond the magnetoelectric coupling effect, for example, the magnetic skyrmion, frustration effect, *etc.*

Since the whole thesis focuses on rare-earth chromate compounds which crystallize into an ABO_3 orthorhombic perovskite structure, the coupling mechanism between

magnetism and ferroelectricity in an ABO_3 perovskite oxide is illustrated in this part. In an ABO_3-type perovskite oxide with a cubic structure, the B–O–B bonds are completely straight with a bond angle of 180°, as shown in 2.4(a). The rotation symmetry is well kept for each B-B axis in such a system. Nevertheless, the tilting of oxygen octahedra can be usually resulted because of the mismatching between A and B cations, reducing the structural symmetry from cubic to tetragonal or orthorhombic or even lower. In this case, a bending of the B-O-B bond angle appears accompanied by the breaking of B-B-axis rotation symmetry, as shown in Fig. 2.4(b). Then the DM interaction could be induced due to the relativistic effect from magnetic cations at B-site, i.e., spin-orbit coupling, whose origin is illustrated thereinafter. The Hamiltonian of the DM interaction can be expressed as [106]

$$H_{\mathrm{DM}} = \mathbf{D}_{ij} \cdot (\mathbf{S}_i \times \mathbf{S}_j), \tag{2.1}$$

in which $\mathbf{D}_{ij}$ represents the parameter of the asymmetric exchange interaction. Usually, the DM interaction points perpendicular to the plane of the B-O-B bending angle. In the framework of first-order approximation proposed by Sergienko and Dagotto, the magnitude of $\mathbf{D}_{ij}$ should be proportional to the value of $\mathbf{d}_{\mathrm{O}}$, i.e., the displacement of the oxygen anions from the equilibrium point [104]

$$\mathbf{D}_{ij} = \xi \mathbf{e}_{ij} \times \mathbf{d}_{\mathrm{O}}, \tag{2.2}$$

where ξ denotes the coefficient, $\mathbf{e}_{ij}$ denotes the unit vector between two neighboring spins $\mathbf{S}_i$ and $\mathbf{S}_j$ with orienting from i-site to j-site. The detailed deduction of the asymmetric exchange interaction $\mathbf{D}_{ij}$ based on second quantization can be found in Ref. [106]. In this model of the DM interaction, one may obtain: (1) in a perovskite oxide with cubic structure, the DM interaction could be derived with $\mathbf{D}_{ij} = 0$; (2) in a distorted structure with reduced symmetry, such as the orthorhombic $YCrO_3$ system with the distortion of oxygen octahedra, reversed the direction of $\mathbf{D}_{ij}$ between neighboring B-O-B bonds could be derived based on the condition of rigid oxygen

octahedra, i.e., all bond angle ∠O-B-O = 180°. The asymmetric exchange interaction in a spin Hamiltonian can be expressed as Eq. (2.1), based on which a noncollinear alignment and canted spins can be deduced. To understand the competition between Heisenberg exchange interaction and DM interaction, the spin Hamiltonian of a 1D B-O-B-O-B chain can be written as

$$H = \sum [J_{ij}\mathbf{S}_i \cdot \mathbf{S}_j + \mathbf{D}_{ij} \cdot (\mathbf{S}_i \times \mathbf{S}_j)], \tag{2.3}$$

where J_{ij} represents the parameter of the Heisenberg exchange. If J_{ij} and $\mathbf{D}_{i,i+1}$ are identical between each neighboring site, one can derive a spiral spin order with a neighbouring spin angle of $\arctan(|D|/J)$ when $J < 0$, or π - $\arctan(|D|/J)$ when $J > 0$ [102].

Usually, a uniform bias of D can be produced in a spiral spin order due to the inverse effect of the DM interaction, thus a corresponding uniform bias of oxygen shift can be induced. The mechanism of the process can be described in following Hamiltonian [102]

$$H = (\xi\mathbf{e}_{ij} \times \mathbf{d}_O) \cdot (\mathbf{S}_i \times \mathbf{S}_j) + (\kappa/2)\mathbf{d}_O^2, \tag{2.4}$$

where the first term denotes the DM interaction, and the second term denotes the elastic energy with κ representing the stiffness. After minimizing the total energy with $H = 0$, the displacement of oxygen anion can be obtained with $\mathbf{d}_O = -(\xi/\kappa)\mathbf{e}_{ij} \times (\mathbf{S}_i \times \mathbf{S}_j)$. In a system with a helical magnetic structure and a constant helicity, $\mathbf{S}_i \times \mathbf{S}_j$ usually points to a mono orientation, thus resulting in a uniform direction of atomic displacements, as shown in 2.4(c). That is how the FE polarization is introduced. The above model was firstly proposed by Sergienko and Dagotto and was used for explaining the magnetoelectric effect in TbMnO$_3$ [104]. Actually, there indeed exists a cycloid spiral magnetic order within the bc plane of TbMnO$_3$ accompanied by a spiral wave vector along the crystallographic b axis below 28 K. And in TbMnO$_3$, it was observed that the FE polarization points along the crystallographic c axis which is

identical to the prediction of $\sim \mathbf{e}_{ij} \times (\mathbf{S}_i \times \mathbf{S}_j)$ [108, 109, 110]. This model can also be used to illustrate external magnetic field-driven polarization flop behavior, i.e., the flip of FE polarization from the crystallographic b axis to the crystallographic a axis as well as the flop of cycloid plane from the bc plane to the ab plane [109, 111].

In addition to the above model of atomic displacement, the spin-orbit coupling itself (without necessitating an asymmetric exchange interaction) can lead to distortion of the electron cloud around the ionic core for a noncollinear spin pair, thus enabling a charge dipole, i.e., the spin current model. Under the framework of quantum perturbation theory, Katsura, Nagaosa, and Balatsky studied the Hubbard model with spin-orbit coupling, and this was also known as the KNB theory, which demonstrates that the induced charge dipole is proportional to [103]

$$\mathbf{P} \sim \mathbf{e}_{ij} \times (\mathbf{S}_i \times \mathbf{S}_j), \tag{2.5}$$

which is the main result of the spin current model on magnetoelectric coupling without considering atomic displacements. This model may act as a counterpart of the model of atomic displacement proposed by Sergienko and Dagotto. For more detail on the theory, one could find in following references [102, 112, 113]. With the spin current model, a clear final prediction can be vividly understood and agrees well with the Sergienko–Dagotto model which starts from the asymmetric exchange interaction. One may find these two mechanisms are cognate although two different freedoms were used with ionic shifts for Sergienko–Dagotto model, and electronic bias for the spin current model. And they are all included in the overall FE polarization. The predominance of atomic displacements was demonstrated by calculation based on density functional theory (DFT) [114, 115, 116] and experiments as well [117]. The Sergienko–Dagotto model indeed agrees well with the viewpoint of helicity and acts as a very good model to depict the FE polarization driven by magnetic fields in multiferroics under spiral magnetic order.
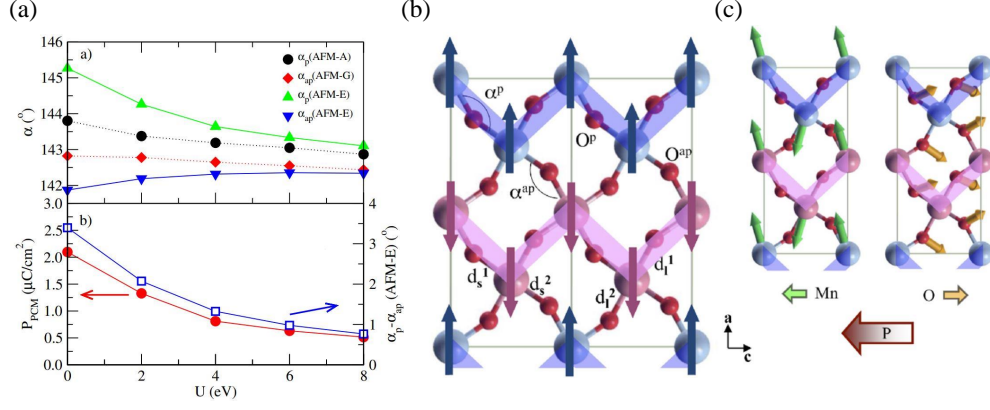
Figure 2.5: (a) (up) Mn-O-Mn angles (in degrees), α_p and α_{ap}, vs U. (Down) P_{PCM} and α_p - α_{ap} vs U in AFM-E. (b) In-plane arrangement of Mn and O atoms. Arrows denote the direction of spins and AFM-coupled zigzag spin chains are highlighted by shaded areas. (c) Arrows show the directions of the ionic displacements for Mn (left) and O (right) in AFM-E. The thick arrows at the bottom show the direction of the resulting displacements of Mn and O sublattices and **P**. [119].

2.1.2.2 Exchange striction

In the above part, the physics was illustrated about how the multiferroics and magnetoelectric coupling can be induced by spin-orbit coupling. Besides, the spin-lattice coupling is another important origin that couples magnetism and ferroelectricity. Since the spin-orbit coupling is usually weak for $3d$ transition-metal ions, to explain the magnetoelectric coupling in HoMnO$_3$, Sergienko, Şen, and Dagotto proposed that the ferroelectricity can be also introduced by the symmetric exchange striction [118].

HoMnO$_3$ compound is a nice example to illustrate how the FE polarization could be produced via the exchange striction. By an optimized method of chemical synthesis, Muñoz et al. obtained orthorhombic perovskite HoMnO$_3$ with $Pbnm$ space group (No. 62) which belongs to a type-II multiferroic, differing from the normally crystallized hexagonal structure [120]. Upon cooling, Mn^{3+} spins of the orthorhombic HoMnO$_3$ undergoes a sinusoidal modulated magnetic structure at ~ 41 K, accompanied by a wave vector **k** = (k_x, 0, 0). Then Mn^{3+} spins stabilize at an E-type AFM order with zigzag chains in the ab plane at ~ 26 K, as shown in Fig. 2.5(b) [121].

According to the well-known Goodenough-Kanamori-Anderson (GKA) rule, we understand that the superexchange J between two nearest-neighboring transition-metal

cations depends on their bond length d and bond angle θ [21, 22]. For instance, in rare-earth orthorferrites (REFeO$_3$), the empirical depiction of the superexchange J has gone through an evolution from $J \sim \cos\theta$ to $J \sim \cos^2\theta$, and further to $J \sim \cos^4(\omega/2)/d^7$ where $\omega = 180° - \theta$ [122, 43]. This relationship between superexchange interaction and bond parameters implies the existence of an inverse modulation effect from J on the lattice. In addition, the superexchange interaction also depends on the scale of the on-site Coulomb interaction with the form of $J \sim b^2/U$, indicating a variation of the Hubbard U is also able to vary the bond angle, as exhibited in Fig. 2.5(a). This is just an empirical formula on the superexchange interaction, whose detailed deduction was discussed thereinafter. To the best of my knowledge, the lattice has a higher energy scale than that of magnetic exchange, resulting in almost constant d and θ. Neverthe-less, d and θ are supposed to be tuned by the Heisenberg exchange $J\mathbf{S}_i{\cdot}\mathbf{S}_j$ when the formation energy of the lattice is close to the energy scale of J. This is the so-called ex-change striction [102, 123]. The exchange striction effect is able to cause a collective effect of atomic displacements and oxygen octahedral rotation without necessitating the canted spins. As predicted within a classical Heisenberg model of Mn^{3+} spins ($S = 2$), bending Mn-O-Mn bond angle associated with a net polarization along the crystal-lographic a axis can result from the $J\mathbf{S}_i{\cdot}\mathbf{S}_j$-type magnetostriction in the orthorhombic perovskite REMnO$_3$ [124, 125]. With regard to the issue of FE polarization orienta-tion, one needs to understand that it is only the production of two neighboring spins of $\mathbf{S}_i{\cdot}\mathbf{S}_j$ that fosters the exchange striction mechanism for FE polarization whose di-rection is not spin-dependent actually but depends on the intrinsic crystallographic symmetry. The group theory analysis by Arima et $al.$ revealed that the FE polarization flop accompanied by the magnetic field along the b axis (H_b) is correlated with the modulation vector of q_{Mn} and q_{Tb} in TbMnO$_3$. At 5 K, three discernible peaks of (0, 4 + 2q_{Tb} - 2q_{Mn}, 1) at k = 4.284, (0, 4 + 2q_{Tb}, 1) at k = 4.424, and (0, 4 + 2q_{Mn}, 1) at k = 4.569 under zero field change to (0, 4 + q_{Tb}, 1) at k = 4.333, (0, 4 + 2q_{Tb} - 2q_{Mn}, 1) at k = 4.39, and a broader peak of (0, 4 + 2q_{Mn}, 1) [126].

Moreover, from the viewpoint of theoretical calculation, it was reported that the

spin-lattice coupling may not act as a compulsory condition to drive the FE polarization in orthorhombic perovskite $HoMnO_3$, as a substitute, the distortion of electronic cloud may also to large extent contribute to the macroscopic ferroelectricity. For instance, the DFT calculation by Picozzi $et\ al.$ has shown that there appears a larger ratio of the orbital polarization apart from the ferroelectricity by polar-type atomic displacements [119].

Overall, the exchange-striction driven FE polarization in orthorhombic perovskite manganites $REMnO_3$ has attracted amounts of verifications, such as the reported ferroelectricity in $YMnO_3$, $GdMnO_3$, $DyMnO_3$, $HoMnO_3$, etc [127, 128, 129]. It may have a wider validity in proper materials beyond the orthorhombic perovskite manganites. The exchange striction induced FE polarization does not only exist through the superexchange pathway of TM^{3+}-O^{2-}-TM^{3+} where TM^{3+} is transition-metal cations but also plays a significant role between rare-earth cations and transition-metal cations. Via a single-crystal sample of $DyFeO_3$ in which each Dy^{3+} layer is sandwiched by two adjacent Fe^{3+} layers, Tokunaga $et\ al.$ found the spin-driven ferroelectricity is comparable to previously studied orthomanganites. With a precise manipulation of the external magnetic field, they determined that the exchange striction between neighboring Dy^{3+} and Fe^{3+} layers might be a possible mechanism, leading to the magnetoelectric coupling multiferroics [130]. Moreover, based on a single-crystal sample, a FE polarization along the crystallographic c axis was observed in orthorhombic perovskite $HoMnO_3$, and this is quite unlike the previous prediction on FE direction in a spin model of Mn^{3+} cations. The evident divergence between the theoretical prediction and experiments may imply the coupling between $4f$ and $3d$ electrons, which plays a significant role in determining the direction of FE polarization [131, 132]. And it is a prerequisite to growing the single-crystal sample if one is going to report on the intrinsic ferroelectricity of a certain rare-earth transition-metal oxide compound.

2.2 Coupled freedoms and novel magnetism in RETMOs

Rare-earth transition-metal oxide (RETMO) compounds are a tremendous class of materials. Charge, spin, lattice, and/or orbital could be active at the same time in RETMO compounds. Above degrees of freedom and their possible couplings enable varieties of novel phenomena and potential consequences for applications. Among the tremendous features of RETMOs, revealing the strongly correlated electronic behavior has been a long-standing puzzle. In the present section, firstly, I introduce the origin of strongly correlated electronic systems, following which are several types of couplings and novel phenomena addressed in the present thesis, such as spin-orbit coupling, the mechanism of magnetic exchange interactions, $4f$-$3d$ exchange coupling, magnetostriction effect, and magnetocaloric effect.

2.2.1 Strongly correlated electronic systems

It is the strongly correlated electronic behavior that enables RETMOs to be a prominent family in condensed matter science [77, 78, 133]. The coupled degrees of freedom in RETMOs make them an interesting playground that enables various nontrivial phenomena, for instance, metal-insulator transition [134], unconventional superconductivity [135, 136], colossal magnetoresistance, $etc.$ [137]. To discuss the origin of strongly correlated electronic systems, one can never bypass the issue of metal-insulator transition and the formation of the Mott insulator.

Before the wide studies on strongly correlated electronic systems, the band structure of solids was usually calculated on the framework of free electron gas (also called Fermi gas) model and Bloch model. Electrons are then treated as non-interacting Fermions without including the correlation between electrons except for the Pauli exclusion. Thus, one can determine the conducting or insulating behavior according to whether the Fermi level lies in the band gap or goes across a conduction band. In this way, several RETMO compounds (such as NiO) with incompletely filled d- or f-electron shells should be metal [138]. Nevertheless, the truth is most RETMO compounds are insulators with band gaps instead of metals whose conduction band

25
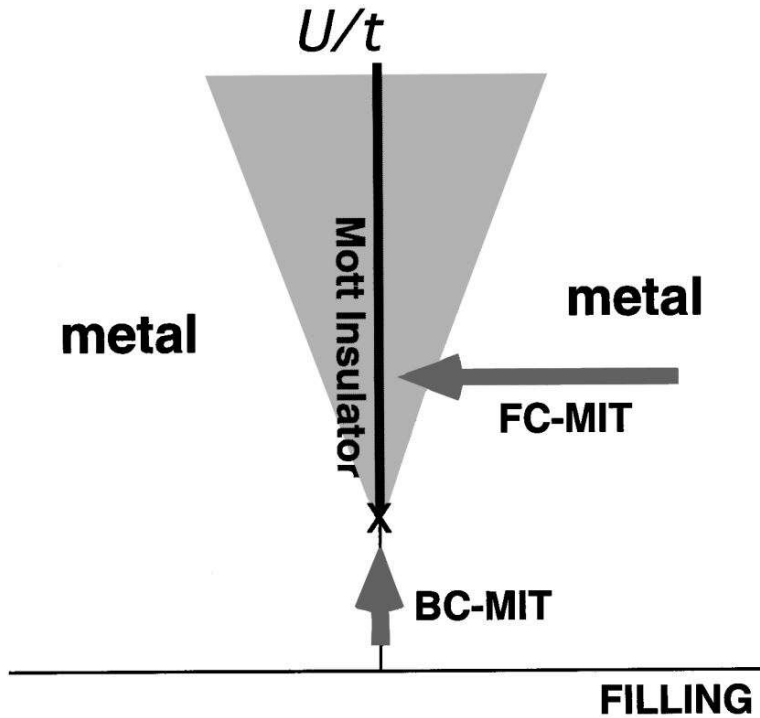
Figure 2.6: Metal-insulator phase diagram based on the Hubbard model in the plane of U/t and filling n. The shaded area is in principle metallic but under the strong influence of the metal-insulator transition, in which carriers are easily localized by extrinsic forces such as randomness and electron-lattice coupling. Two routes for the MIT (metal-insulator transition) are shown: the FC-MIT (filling-control MIT) and the BC-MIT (bandwidth-control MIT) [140].

is across the Fermi level. The key issue to address the puzzle is the strong Coulomb repulsion potential between electrons, as clarified by Mott and Peierls in 1937 [139]

It is quite possible that the electrostatic interaction between the electrons prevents them from moving at all. At low temperatures, the majority of the electrons are in their proper places in the ions. The minority which has happened to cross the potential barrier finds therefore all the other atoms occupied. And to get through the lattice, they have to spend a long time in ions already occupied by other electrons. This needs a considerable addition of energy and so is extremely improbable at low temperatures [139].

Unlike a delocalized electronic system, where electrons can be considered as staying in a "sea" of the averaged motion of other electrons, i.e., a simple one-electron theory like the local-density approximation of density-functional theory or the Hartree–Fock theory [141]. Here, the Coulomb repulsion potential should be introduced and can no

longer be ignored. That is why this class of materials is known as strongly corre-lated electronic systems. To describe the formation of insulating behavior, Mott has proposed a lattice model in which each site can be occupied by two electrons, one is spin-up and the other is spin-down. While, the on-site Coulomb repulsion U may split the band into two, making the lower band filled by one electron and leaving the up-per band empty. Hence, the Fermi level lies in the gap, enabling the system to be an insulator. This is the prototype of the well-known Mott insulator [142].

To unravel the physics of Mott insulator, under the framework of second quantiza-tion, Hubbard has proposed a simple one-band model considering the on-site Coulomb interaction and electron hopping integral. This model was also called as Hubbard model, whose Hamiltonian can be expressed as [143]

$$\hat{H} = -t \sum_{\langle i,j \rangle} (\hat{c}^{\dagger}_{i,\sigma} \hat{c}_{j,\sigma} + \hat{c}_{i,\sigma} \hat{c}^{\dagger}_{j,\sigma}) + U \sum_{i} n_{i\uparrow} n_{i\uparrow}, \qquad (2.6)$$

where the Hamiltonian can be separated into two terms. The first term reads the kinetic energy of the system with t denoting the hopping integral. The second term describes the on-site Coulomb interaction U to express the repulsion potential between electrons. The creation and annihilation of a single-band electron at site i with spin σ is marked by $c^{\dagger}_{i\sigma}$ and $c_{i\sigma}$. And the particle number operators are introduced with $n_{i\uparrow} = c^{\dagger}_{i\uparrow} c_{i\uparrow}$ and $n_{i\downarrow} = c^{\dagger}_{i\downarrow} c_{i\downarrow}$.

By introducing the second term of the on-site Coulomb repulsion, the Hubbard model shows people a strongly correlated electronic system with a controllable elec-tronic band structure. This also triggers the idea that an insulator could become a metal just by tuning the parameters, i.e., the metal-insulator transition (MIT) [144]. One could obtain a metal/insulator system by manipulating the competition between hopping integral t and on-site Coulomb repulsion U, like the variant ratio of U/t, or the band filling (charge doping). Thus, the MIT could be further divided into filling-control MIT and band-control MIT according to the driven force near the quantum crit-ical point of an MIT, as shown in Fig. 2.6 of the metal-insulator phase diagram [140].

RETMO compounds are a prominent class of strongly correlated electronic sys-
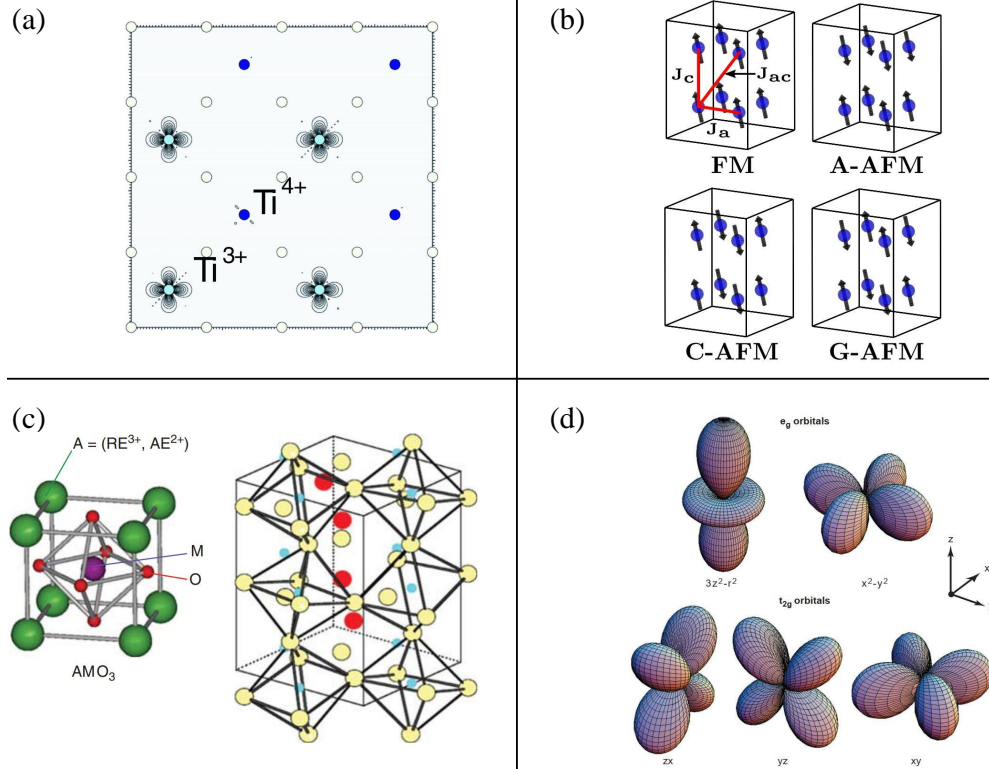
Figure 2.7: (a) 45 checkerboard charge density distribution of the occupied $3d$ states in the charge-ordered TiO_2 layer in the FM (1,1) multilayer. Orbital ordering due to d_{xy} orbital occupation is apparent. The positions of O, Ti^{3+}, and Ti^{4+} ions are marked by white, light blue (gray), and dark blue (black) circles, respectively [145]. (b) With the $2 \times 2 \times 2$ repetition of the elemental five-atom cell of super-tetragonal $BiFeO_3$, the four magnetic configurations (FM, A-AFM, C-AFM, G-AFM) of the Fe sublattice are displayed [146]. (c) A possible structural transition from cubic to orthorhombic structure of AMO_3 perovskite compound with trivalent (3^+) rare-earth (RE) ions or divalent (2^+) alkaline-earth (AE) ions at the perovskite A site and the transition-metal element on the perovskite B site. (d) Five d orbitals [77]. In a crystal field of cubic structure, the fivefold degeneracy is lifted to two e_g orbitals [(x^2-y^2) and ($3z^2 - r^2$)] and three t_{2g} orbitals [(xy), (yz), and (zx)] [76].

tems, in addition to the controllable competition on-site Coulomb repulsion U, it also provides a promising playground at which novel quantum states could be realized by tuning multiple degrees of freedom such as charge, spin, lattice, and orbital. Several usual macroscopic behaviors of above four degrees of freedom are displayed in Fig. 2.7, such as the charge density distribution of the occupied $3d$ states in the charge-ordered TiO_2 layer in the FM (1,1) multilayer as shown in Fig. 2.7(a) [145], four typical magnetic states as shown in Fig. 2.7(b) [146], the structural phase transition with reducing symmetry as shown in Fig. 2.7(c) [77], and the orbital states with five-fold degeneracy of d-shell ($d_{3z^2-r^2}$, $d_{x^2-y^2}$, d_{xy}, d_{yz}, and d_{xz}) as shown in Fig. 2.7(d) [76].

Furthermore, possible couplings can also work between freedoms of charge, spin, lattice, and orbital. One of the famous examples is the spin-orbit coupling, which gives rise to amounts of novel quantum states, the detailed description of spin-orbit coupling is elucidated in the next subsection. Another well-known example is the spin-lattice coupling, which produces a response from lattice distortion on magnetic order, like the magnetostriction effect. Recently, there also exist studies reporting on a possible coupling among charge, spin, and lattice degrees of freedom in $LuFe_2O_4$, and the spin-charge ordered phases could be manipulated via external pressure [147]. With the development of experimental technology (like neutron scattering with high resolution/high flux, and ultra-low temperature condition), there displays an increasing amount of studies on the behavior of $4f$ electronic systems, in which stronger on-site Coulomb repulsions may exist between $4f$ electrons, enabling more novel quantum states to be observed.

2.2.2 Spin-orbit coupling

The spin-orbit coupling (SOC) is a usually used but effective method to tune multiple degrees of freedom in various strongly correlated electronic systems. To the best of my knowledge, physicists have found diversified promising phenomena among which the SOC plays a significant role such as the Kitaev quantum spin liquid [8, 148, 149], magnetic skyrmion [150, 151], topological magnon [152, 153], the nematicity in iron-based superconductors, etc. [154, 155]. In the present subsection, the SOC is going to be derived from relativistic quantum mechanics with the Dirac theory [156].

Since the electron moves through a system of charged nuclei, which makes an electrostatic field of $\mathbf{E} = -\nabla\phi$. With the spherically symmetric nuclear potential, i.e., the central field approximation, which usually gives a good description of hydrogen and hydrogen-like ions, the electrostatic field can be then expressed as

$$\mathbf{E} = -\nabla\phi = -\frac{\mathbf{r}}{r}\frac{d\phi}{dr},\tag{2.7}$$

where ϕ is the electric potential of the electron in the spherically symmetric potential.

We know the electron moves to undertake the magnetic field **B** from nuclei, according to the relativistic electrodynamics, **B** could be given as

$$\mathbf{B} = \gamma\left(\mathbf{B}' - \frac{1}{c}\beta \times \mathbf{E}\right) - \frac{\gamma^2}{\gamma + 1}\beta(\beta \cdot \mathbf{B}'), \tag{2.8}$$

in which $\beta = \mathbf{v}/c$, $\mathbf{B}'$, and $\mathbf{E}'$ are the fields in the rest frame of the nucleus with $\mathbf{B}' = 0$, while **B** and **E** are for the rest frame of the electron. Since the frame is not inertial, with $v \ll c$ and a Lorentz factor of $\beta \approx 1$ under the non-relativistic condition, we then have

$$\mathbf{B} = -\frac{1}{c^2}\mathbf{v} \times \mathbf{E}, \tag{2.9}$$

substituting Eq. 2.7 to the above formula, and treating the velocity with the momentum of an electron with $\mathbf{p} = m_e\mathbf{v}$, the vector product of the **B** field could then be written as

$$\mathbf{B} = -\frac{1}{m_ec^2}\left(\frac{1}{r}\frac{d\phi}{dr}\right)\mathbf{r} \times \mathbf{p}, \tag{2.10}$$

in the above formula, using the classical angular momentum of $\mathbf{L} = \mathbf{r} \times \mathbf{p}$, we then have the final expression of the **B** field

$$\mathbf{B} = -\frac{1}{m_ec^2}\left(\frac{1}{r}\frac{d\phi}{dr}\right)\mathbf{L}, \tag{2.11}$$

in which the **B** field is parallel to the angular momentum **L** and perpendicular to the velocity of the electron.

Furthermore, the spin angular momentum of the electron can be written as

$$\mu_s = -g_s\mu_B\frac{\mathbf{S}}{\hbar} = \gamma\mathbf{S} = -\frac{e}{m_e}\mathbf{S}, \tag{2.12}$$

where $g_s \approx 2$ denotes the g-factor of the electron spin, $\mu_B = e\hbar/2m_e$ denotes the Bohr magneton, and **S** denotes the spin angular momentum. With the above elementary constants, the gyromagnetic ratio could then be obtained with $\gamma = -g_se/2m_e$. Here one

may need to notice that the spin magnetic moment μ_s is antiparallel to the spin angular momentum **S**.

The energy splitting term of a magnetic moment in an external magnetic field could be usually given with

$$H = -\mu \cdot \mathbf{B}, \tag{2.13}$$

The SOC contains two terms, the first one is the perturbation term of the interaction between the electronic spin magnetic moment and the **B** field of the nucleus when they are in the co-moving frame of the electron. The second one is the Thomas precession correction term. Substituting Eq. (2.11) into the above equation, and treating the magnetic moment with $\mu = \mu_s$, one can obtain

$$H_L = -\mu_s \cdot \mathbf{B} = -\frac{e}{m_e^2 c^2}\left(\frac{1}{r}\frac{d\phi}{dr}\right)\mathbf{L} \cdot \mathbf{S}, \tag{2.14}$$

Since the static coordination of the electron is a non-inertial frame, the second term of the Thomas precession correction needs to be considered, i.e., the Thomas half is supposed to be included in Eq. 2.14. Finally the Hamiltonian of the electron of the SOC interaction in an external electrostatic potential could be written as

$$H_{\text{SOC}} = H_L + H_T = \frac{1}{2}H_L = -\frac{e}{2m_e^2 c^2}\left(\frac{1}{r}\frac{d\phi}{dr}\right)\mathbf{L} \cdot \mathbf{S}, \tag{2.15}$$

with the sample expression of $4\pi\varepsilon_0\phi(r) = Z^*e/r$, the perturbation term of the SOC interaction could be re-written as

$$H_{\text{SOC}} = \frac{1}{8\pi\varepsilon_0 m_e^2 c^2}\frac{Z^*e^2}{r^3}\mathbf{L} \cdot \mathbf{S} = \lambda\mathbf{L} \cdot \mathbf{S}, \tag{2.16}$$

where Z^* is the effective ionic charge, and λ is the SOC scaling factor which decreases rapidly with increasing distance r.

With the above perturbation term of the SOC Hamiltonian, the energy shift could be evaluated in detail. Since the L_z and S_z are not conserved quantities, one needs a basis

31
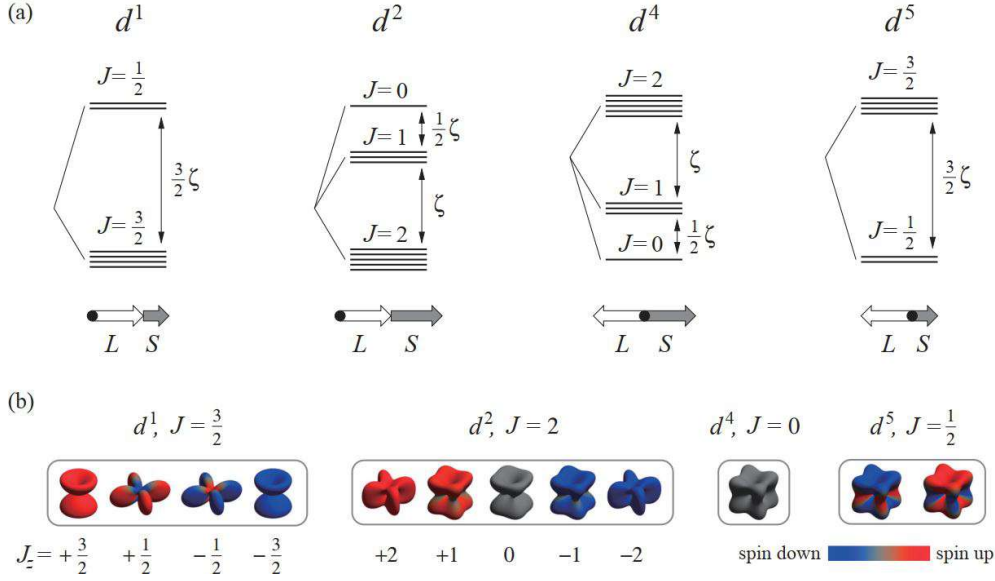
Figure 2.8: (a) Low-energy levels of d^1, d^2, d^4, and d^5 ions in cubic crystal field. The degeneracy of the levels is shown by the number of close lines. For less than half-filled t_{2g} shell, the SOC aligns the effective orbital angular momentum L and spin S to form larger total angular momentum: $J = 3/2$ quartet in d^1 case and $J = 2$ quintuplet in d^2 case, respectively. In the case of more than half-filled t_{2g} shell, L and S are antialigned, leading to $J = 0$ singlet ground state for the d^4 configuration while the d^5 one hosts pseudospin $J = 1/2$. (b) Orbital shapes corresponding to the ground-state J-levels. Only the angular distribution of the electron density is considered. It is represented by a surface plot where the distance to the origin is proportional to the integral density in the corresponding direction. The color of the surface indicates normalized spin polarization $(\rho_\uparrow - \rho_\downarrow)/(\rho_\downarrow + \rho_\uparrow)$ taking values in the range $[-1, +1]$. It is shown for electrons in the case of d^1 and d^2 states and for the holes in the t_{2g}^6 configuration in the case of d^4 and d^5 states [157].

that could diagonalize both H_0 (the zero-order Hamiltonian) and H_{SOC}. Firstly, the total angular momentum operator $\mathbf{J}$ can be defined with $\mathbf{J} = \mathbf{L} + \mathbf{S}$, one then has the dot product with itself of $\mathbf{J}^2 = \mathbf{L}^2 + \mathbf{S}^2 + 2\mathbf{L} \cdot \mathbf{S}$, according to which the dot product between the orbital angular momentum operator and the spin angular momentum operator could be given with

$$\mathbf{L} \cdot \mathbf{S} = \frac{1}{2}(\mathbf{J}^2 - \mathbf{L}^2 - \mathbf{S}^2). \tag{2.17}$$

It can be easily found that the four operators H_0, $\mathbf{J}^2$, $\mathbf{L}^2$, and $\mathbf{S}^2$ all commute with each other and with H_{SOC}, implying the co-eigenfunction $|n, j, l, s\rangle$ of the operators can be treated as zero-order eigenfunction, with which the first-order perturbation of the en-

ergy shift $E_n^{(1)}$ can also be calculated. Here n is the principal quantum number, j is the total angular momentum quantum number, l is the orbital angular momentum quantum number, and s is the spin angular momentum quantum number. The expectation of $\mathbf{L} \cdot \mathbf{S}$ can be expressed as

$$\langle n, j, l, s | \mathbf{L} \cdot \mathbf{S} | n, j, l, s \rangle = \frac{\hbar^2}{2} [j(j+1) - l(l+1) - s(s+1)], \qquad (2.18)$$

with which one may understand the fine structure of the energy term generated from the H_{SOC}

$$E_{nl} = E_{nl}^{(0)} + \lambda_{nl} \frac{\hbar^2}{2} [j(j+1) - l(l+1) - s(s+1)], \qquad (2.19)$$

where the SOC constant λ_{nl} is given with

$$\lambda_{nl} = \frac{Z^* e^2}{8\pi\varepsilon_0 m_e^2 c^2} \langle n, j, l, s | r^{-3} | n, j, l, s \rangle = \frac{1}{4\pi\varepsilon_0 m_e^2 c^2 a_0^3} \frac{Z^{*4} e^2}{n^3 l(l+1)(2l+1)}, \quad (2.20)$$

where $a_0 = 4\pi\varepsilon_0 \hbar^2 / m_e e^2$ is the Bohr radius.

Moreover, taking the d orbital as an example, it could be vividly displayed how the spin-orbital entanglement works [157]. Its SOC interaction reads the form of $H = \pm \lambda \mathbf{L} \cdot \mathbf{S}$, whose negative (positive) sign corresponds to a less (more) than half-filled shell of t_{2g} state in d^1, d^2 (d^4, d^5) configurations. And λ refers to the SOC strength with $\lambda = \zeta/2S$. As shown in Fig. 2.8(a), due to the above changing sign, the spin-orbit levels can be mutually inverted. And the orbital shape of the ground-state electronic densities is illustrated in Fig. 2.8(b) as well.

2.2.3 Magnetic exchange interactions

The origin of magnetism used to be a long-standing puzzle before the development of quantum theory. In 1907, Weiss proposed that in addition to any externally applied field H, in a ferromagnet there exists an internal "molecular field" which should be proportional to its magnetization. But no convincing theoretical explanation can be

found until 1928, Heisenberg proposed the exchange interaction model, and people began to understand the molecular field is actually the mean-field approximation of exchange interactions between electrons. One needs to know that the Heisenberg exchange model assumes the electronic contribution of magnetism is localized surrounding an atom, and it gives a very good description of the magnetism on magnetic oxides and rare-earth ($4f$ family) alloys. While for metals and alloys consisting of transition-metal ($3d$) elements, like Fe, Co, Ni, *etc.* whose d electrons are itinerant between the d orbital of each atom, the localized electron model is not appropriate here. To overcome this issue, Bloch and Stoner *et al.* have proposed a model which treats the electrons of a ferromagnet as a narrow band, i.e., the well-known Stoner picture on magnetism. These two existed models go to two extremes of electronic behavior, and many recent studies imply that the current theory of magnetism has encountered a bottleneck in some real materials, meaning an overall model connecting both of them may need to be explored. Since the magnetism of RETMO compounds can be well explained by local electron model, in the present part, I mainly focus on the local electron model.

In the present subsection, firstly I take the H_2 molecule as an example to illustrate how the direct exchange interaction was developed. Then, three types of indirect exchange interactions are illustrated, including double exchange, superexchange, and Ruderman–Kittel–Kasuya–Yosida (RKKY) exchnage.

2.2.3.1 Direct exchange

In the present part, the direct exchange interaction is deduced by following the Heitler–London method. By omitting the spin-spin and spin-orbit interactions, the Hamiltonian of a two-electron system of H_2-molecule can be expressed as an unperturbed term H_0 and a perturbed term H_1 [156, 158]

$$H = H_0 + H_1, \tag{2.21}$$

$$H_0 = -\frac{\hbar^2}{2m}(\nabla_1^2 + \nabla_2^2) - \frac{e^2}{4\pi\varepsilon_0}\left(\frac{1}{r_{1a}} + \frac{1}{r_{2b}}\right), \tag{2.22}$$
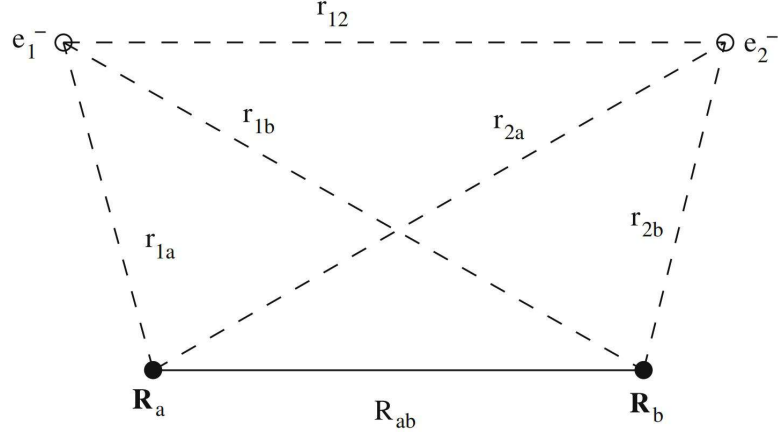
Figure 2.9: A schematic description of the distances in the H_2 molecule [156].

$$H = \frac{e^2}{4\pi\varepsilon_0}\left(\frac{1}{R_{ab}} + \frac{1}{r_{12}} - \frac{1}{r_{1b}} - \frac{1}{r_{2a}}\right). \tag{2.23}$$

By treating the mass and the distance of two nuclei to be infinite with $m_a = m_a = \infty$, and letting the two hydrogen atoms be independent, two uncoupled hydrogen atoms can then be obtained. Their exact solutions could be given with

$$\left(-\frac{\hbar^2}{2m} - \frac{e^2}{4\pi\varepsilon_0 r_{1a}}\right)|\phi_a^{(1)}\rangle = E_a|\phi_a^{(1)}\rangle, \tag{2.24}$$

$$\left(-\frac{\hbar^2}{2m} - \frac{e^2}{4\pi\varepsilon_0 r_{2b}}\right)|\phi_b^{(2)}\rangle = E_b|\phi_b^{(2)}\rangle. \tag{2.25}$$

Since electrons are identical particles, both $|\phi_a^{(1)}\rangle|\phi_b^{(2)}\rangle$ and $|\phi_b^{(2)}\rangle|\phi_a^{(1)}\rangle$ are eigenstates of Eq. 2.22, the ground-state wavefunction is supposed to be the linear combination of them. Then the non-interacted two-electron system gives the form

$$|q\rangle^{(\pm)} = \frac{1}{\sqrt{2}}(|\phi_a^{(1)}\rangle|\phi_b^{(2)}\rangle \pm |\phi_a^{(2)}\rangle|\phi_b^{(1)}\rangle) = \frac{1}{\sqrt{2}}(|q_1\rangle \pm |q_2\rangle), \tag{2.26}$$

where $1/\sqrt{2}$ is the normalization constant, which should be $\sqrt{1/2(1\pm L^2)}$, and L denotes the orbital overlap integral of $L = \langle\phi_a^{(1,2)}|\phi_b^{(1,2)}\rangle$. Here we assume that they are orthogonal to each other, i.e., $L = 0$. With further considering the spin eigenstates and

the asymmetric condition, the eigenfunction can be given by

$$|\psi_A\rangle = |q\rangle^{(+)}|0;0\rangle; \; |\psi_S\rangle = |q\rangle^{(-)}|1;m_S\rangle. \tag{2.27}$$

Using the *variation ansatz*, the ground-state energy of the total Hamiltonian H can be expressed as

$$E_\pm = E_0 + \frac{V \pm X}{1 \pm L}, \tag{2.28}$$

where E_0 is the summation of some constant values including the eigenvalues of two uncoupled electrons and the energy between two protons. V, X, and L are several special integrals.

Overlap integral:

$$L = \langle \phi_a^{(1,2)} | \phi_b^{(1,2)} \rangle, \tag{2.29}$$

Coulomb integral:

$$V \equiv \langle q_1 | H | q_1 \rangle = \langle q_2 | H | q_2 \rangle, \tag{2.30}$$

Exchange integral:

$$X \equiv \langle q_1 | H | q_2 \rangle = \langle q_2 | H | q_1 \rangle. \tag{2.31}$$

Hence, the Hamiltonian can be replaced by an effective Hamiltonian of exchange interactions between each spin:

$$H_{\text{eff}} = constant - J_{12}\mathbf{S}_1 \cdot \mathbf{S}_2, \tag{2.32}$$

$$J_{12} = \frac{1}{\hbar^2}(E_+ - E_-) = -\frac{1}{\hbar^2}\frac{VL^2 - X}{1 - L^4}, \tag{2.33}$$

Figure 2.10: The double exchange interaction. The electron hops with spin memory from one localized ion core to the next [158].

where $L \ll 1$ and $X < 0$, leading to an exchange interaction with $J_{12} < 0$, which means the singlet state has the lowest energy. Moreover, the effective Hamiltonian exchange interactions of the H_2-molecule system can be generalized to multi-electron atoms, giving rise to the Heisenberg exchange model

$$H = -\sum_{ij} J_{ij}\mathbf{S}_i\cdot\mathbf{S}_j, \tag{2.34}$$

2.2.3.2 Double exchange

A double exchange interaction usually occurs between transition-metal $3d$ cations in which d-type localized electrons and delocalized electrons coexist, making an FM alignment between adjacent spins to minimize the total energy of the spin system. As an indirect exchange that the coupling between two adjacent cations acts via a mediate anion, one may find the double-exchange is similar to the superexchange interaction which is elucidated in the following text. Nonetheless, the different points are [158]: (1) For a superexchange interaction, the electron is localized in the orbital, while for the double exchange, the electron is delocalized. (2) The superexchange often occurs between cations with the same valence state, the double exchange favors two cations with distinctive valence states, like the $La_{1-x}Sr_xMnO_3$, which has Mn^{3+} and Mn^{4+} valence states simultaneously. (3) Electron hopping in the superexchange usually happens in parallel spin alignment and is forbidden in antiparallel alignment. While in the double exchange, electron hopping happens only between spins with FM alignment,

the detail is discussed below.

The FM nature of the double exchange interaction can also be understood via the transfer integral. After expanding into a powerful formula, the double-exchange Hamiltonian can be expressed as [156]

$$H_{\text{DE}} = -t \sum_{n=0}^{\infty} J_n(S)(\mathbf{S}_1 \cdot \mathbf{S}_2)^n, \qquad (2.35)$$

where t is the transfer integral which varies as $\cos(\theta/2)$, θ is the canting angle between two adjacent spins of $\mathbf{S}_1$ and $\mathbf{S}_2$. It is easy to find that the transfer integral t will be zero in the case of AFM configuration between two adjacent spins because an antiparallel alignment may lead to $\theta = \pi$.

One famous class of materials in which the double exchange exists is the alkali metal doped lanthanum manganite [159]. In this class, manganese cations allow different charge states with both Mn^{3+} and Mn^{4+}, where d^3 electrons occupy a narrow $t_{2g}^{\uparrow}$ band, leaving the 4th d electron at a wider $e_g^{\uparrow}$ band. The strong on-site Hund's rule splits an exchange of about $J_{ex} \sim 2$ eV, leading to a large energy barrier between the occupied $t_{2g}^{\uparrow}$ band and the unoccupied $t_{2g}^{\downarrow}$ band Thus, the electron at the $e_g^{\uparrow}$ band could hop between two d^3 configurations with parallel spins easily.

2.2.3.3 Superexchange

The superexchange interaction is another type of exchange interaction in the framework of the localized electron model. It is so named due to its large ionic distances in which diamagnetic ions are usually occupied. The superexchange theory has given great success in explaining the magnetic ordering of transition-metal ionic moments and rare-earth ionic moments in RETMO compounds [160], rare-earth transition-metal halide compounds etc. [161, 162]. Among the above systems, there is little direct exchange resulting from d-d orbital overlap, while a virtual charge transfer (VCT) occurs by orbital overlap in a pathway of TM-X-TM where TM denotes transition-metal cations and X denotes non-magnetic anions.

In 1934, the superexchange was firstly introduced by Kramers who tried to ex-
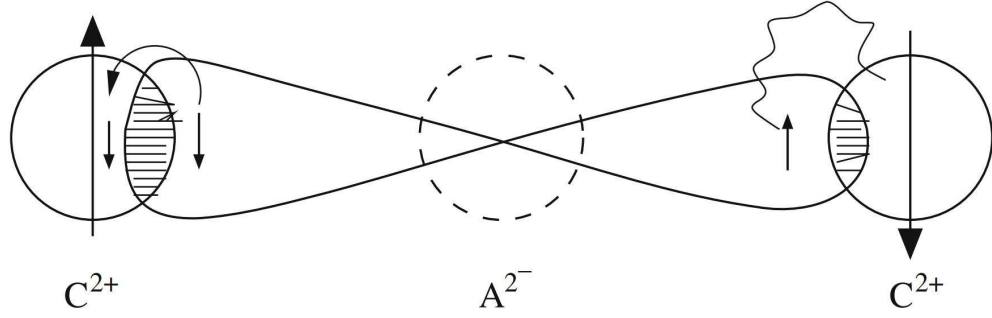
Figure 2.11: Alternative cluster model according to Kanamori and Goodenough to explain the superexchange mechanism [21, 22].

plain exchange interactions in paramagnetic salts, while no specific mechanism was discussed [163]. In 1950, Anderson optimized Kramer's proposal and applied it in explaining the antiferromagnetism of manganese oxide MnO [23]. However, the optimized theory consists of a third order of the perturbation theory, leading to poorly convergent calculation. To solve the problem, Anderson proposed a new theory of the superexchange interaction in 1959, he started with molecular orbitals consisting of localized d orbitals and p orbitals [24]. The AFM exchange that the electron transferring from one $3d$ orbital of a magnetic cation to another adjacent magnetic cation can be expressed with the second-order perturbation by [164]

$$ J \sim \frac{4b^2}{U} \mathbf{S}_1 \cdot \mathbf{S}_2, \tag{2.36} $$

where b represents the electron hopping integral, and U represents the on-site Coulomb interaction. With this Hubbard Hamiltonian, one may understand if electrons behave in metal under the limitation of $U \ll b$, or localized surrounding lattice points. Also, a series of semi-empirical rules were developed by Goodenough in 1955 [21], followed by a subsequently rigorous mathematical deduction formulated by Kanamori in 1959 [22]. This also agrees well with the superexchange theory by Anderson. The main conclusions of the superexchange interaction are summarized in terms of the so-called GKA rule, which can be simplified as [158, 165]

(1) When two adjacent cations have lobes of singly occupied $3d$ orbitals, pointing towards each other and resulting in large orbital overlap and hopping integrals, then the

exchange will be strong and coupling antiferromagnetically. This is the normal case in TM-O-TM bonds with 120°.

(2) If the overlap integrals are zero by the symmetry between singly occupied $3d$ orbitals of two adjacent cations, the exchange is then FM coupled and relatively weak. This suits the case in TM-O-TM bond with $\sim 90°$.

(3) When two cations have orbital overlap between singly occupied $3d$ orbitals and unoccupied or doubly occupied orbitals of the same type, the exchange is also weakly FM coupled.

In real materials, the superexchange interaction is usually AFM coupled in normal cases and seldom results in FM coupling, since there is a very tiny possibility of the orbital overlap integrals being zero. Ferrites and manganese oxide are two typical classes for illustrating how the superexchange works. They both behave in a singly occupied $3d$ orbital with Fe^{3+} ($t_{2g}^3 e_g^2$) and Mn^{2+} ($t_{2g}^3 e_g^2$) states. With the oxygen $2p$ orbital as an intermediate, the virtual electron transfer can occur between adjacent TM cations accompanied by the generation of a $3d^6 2p^5$ excited state, and the superexchange interaction gives the form of $J \sim b^2/U$. Usually, transition-metal oxides give energy scales of $b \sim 0.1$ eV and $U \sim 3$–5 eV, and the exchange interaction J varies with the bond angle and bond length d of a superexchange pathway TM-O-TM [158]. In the study on rare-earth orthoferrite series compounds, Zhou and Goodenough summarised an empirical formula of the superexchange interaction with $J \sim \cos^4(\omega/2)/d^7$ where ω = 180° − θ, here θ denotes the bond angle of TM-O-TM, and d denotes the TM-O bond length [122].

Zhou et $al.$ have introduced the t_{2g}-e_g orbital hybridization in the case of rare-earth orthochromates whose chemical formula is $RECrO_3$, in which only the t_{2g} orbitals are half filled, leaving empty e_g orbitals [43]. For the Cr^{3+} $t_{2g}^2 e_g^0$ state, the t_{2g}^3-t_{2g}^3 transfer produces a dominant AFM coupling J^π. Whereas the intersite t_{2g}-e_g orbitals may lead to an orthogonal hybridization in the case of the TM-O-TM pathway with a 180° superexchange angle, a virtual charge transfer of t_{2g}^3-O-e_g^0 then appears, resulting in an FM coupling J_{hb}^σ according to the superexchange rules. The total superexchange
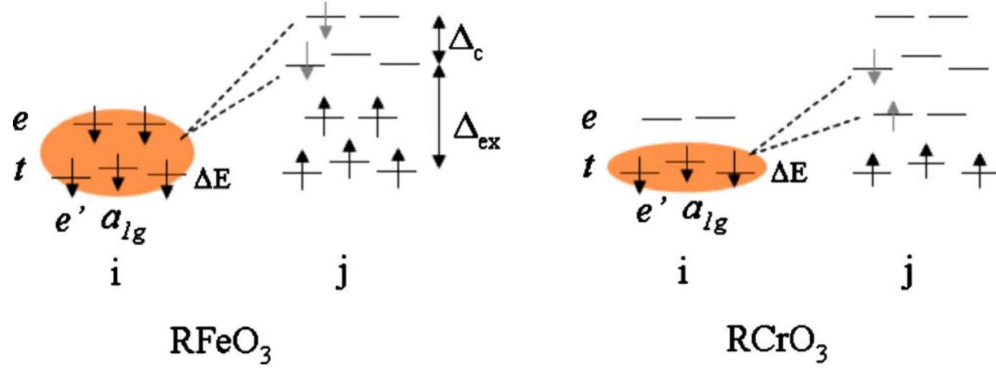
Figure 2.12: Schematic diagram of the hybridization effect on the virtual charge transfer for the superexchange interaction in perovskites of $RECrO_3$ and $REFeO_3$. The VCT occurs for all occupied spin states; only those for the representative magnetic couplings are shown in the figure. Δ_c stands for the crystal-field splitting, Δ_{ex} is the exchange splitting, $\Delta_E = E_{a1g} - E_e$ [43].

interaction in a $RECrO_3$ system can then be expressed as [43]

$$ J = J_0[(b^\pi)^2 - \eta(b_{\text{hb}}^\sigma)^2]; \eta = \frac{U + \Delta_{ex}}{U + \Delta_c} \left(\frac{V_{pd\sigma}}{V_{pd\pi}} \right)^2, \qquad (2.37) $$

where $V_{pd\sigma}$ and $V_{pd\pi}$ are corresponding overlap integrals, Δ_{ex} and Δ_c denote the exchange splitting and crystal-field splitting, respectively. The effect from t_{2g}-e_g orbital hybridization on $RECrO_3$ is very different from the case of rare-earth orthoferrites $REFeO_3$. Fig. 2.12 displays how the virtual charge transfer works in $RECrO_3$ and $REFeO_3$ compounds. In the case of $REFeO_3$ systems, both the t_{2g}^3-O-t_{2g}^3 and e_g^2-O-e_g^2 superexchange interactions are coupled antiferromagnetically, implying no new FM-coupling contribution can be introduced to the overall superexchange interaction. And the electron hopping through the pathway of the FM coupling is forbidden [43].

One may need to understand that although transition-metal oxides such as manganites and ferrites are often used to illustrate the physics of superexchange interaction in most textbooks, the superexchange interaction also exists through the pathways of RE-O-TM and RE-O-RE, among which the former one contributes significantly to the $4f$-$3d$ exchange coupling. The mechanism of $4f$-$3d$ exchange coupling is introduced in the next subsection.

41
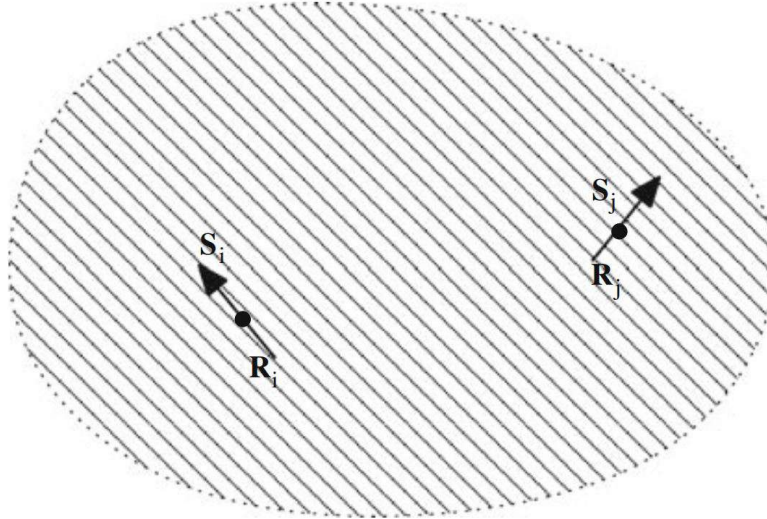
Figure 2.13: Two localized spins $\mathbf{S}_i$ and $\mathbf{S}_j$ at the lattice sites $\mathbf{R}_i$ and $\mathbf{R}_j$ within a "sea" of conduction electrons [156].

2.2.3.4 RKKY exchange

RKKY is the short name of four scientists of Ruderman, Kittel, Kasuya, and Yosida who proposed the theoretical model of the RKKY interaction, which describes a magnetic coupling between the localized electrons on d- or f-shells via the $5d/6s$ conduction electrons [166, 167, 168].

The theoretical model of the RKKY interaction uses a second-order perturbation theory to describe an indirect exchange coupling whereby the nuclear spin of one atom interacts with a conduction electron through the hyperfine interaction, and this conduction electron then interacts with another nuclear spin, thus creating correlation energy between the two nuclear spins. The on-site interaction between a localized $4f$ core spin $\mathbf{S}$ and a conduction electron spin $\mathbf{s}$ is expressed by -$J_{sf}\mathbf{S} \cdot \mathbf{s}$, usually, J_{sf} has a scale of ~ 0.2 eV.

The RKKY interaction helps people understand the oscillation of giant magnetoresistance materials. It shows that a single magnetic impurity could produce a nonuniform, oscillating spin polarization in the conduction band which decreases as r^{-3}. The spin polarization may induce a long-range oscillatory coupling between core spins. As

for free electrons, the polarization is proportional to the RKKY function [158]

$$F(\xi) = (sin\xi - \xi cos\xi)/\xi^4, \tag{2.38}$$

where $\xi = 2k_F r$, and k_F denotes the Fermi wavevector. The effective coupling between two localized spins can be expressed as

$$J_{\text{eff}} \approx \frac{9\pi J_{sf}^2 \nu^2 F(\xi)}{64\epsilon_F}, \tag{2.39}$$

where ν denotes the number of conduction electrons in each atom, ϵ_F denotes the Fermi energy. Oscillatory behavior of the exchange coupling was found in FE multilayers separated by nonmagnetic spacer layers. Such as in the sandwiched layers of $Ni_{80}Co_{20}$/Ru/$Ni_{80}Co_{20}$, the oscillation of the exchange coupling between FM and AFM as a function of the distance between the layers can be well described by RKKY far-field function [169].

2.2.4 $4f$-$3d$ exchange coupling

In RETMO compounds, the $4f$-$3d$ exchange interaction usually works through the RE-O-TM superexchange pathway, in which a virtual charge transfer $4f$-O^{2-}-$3d$ may occur with obeying similar rules of electron hopping as in the TM-O-TM superexchange interaction. It is the exchange coupling between $4f$ and $3d$ electrons that makes the RETMO compounds a promising class accompanied by rich novel physical phenomena such as spin reorientation (SR) of the magnetization [51, 170], exchange bias effect [171], and magnetoelectric multiferroics, which is elucidated in the above text. Compared with the exchange interaction of TM-O-TM, it is almost an untapped outlet in magnetism for the RE-O-TM superexchange and the $4f$-$3d$ exchange coupling, the nature of which still remains to be an unsolved puzzle and worth a further in-depth study. In the present subsection, the challenges when facing the questions of $4f$-$3d$ exchange coupling is introduced, as well as two possible routes which might be worth trying. The study on $4f$-$3d$ exchange coupling is a frontier question, and I have to
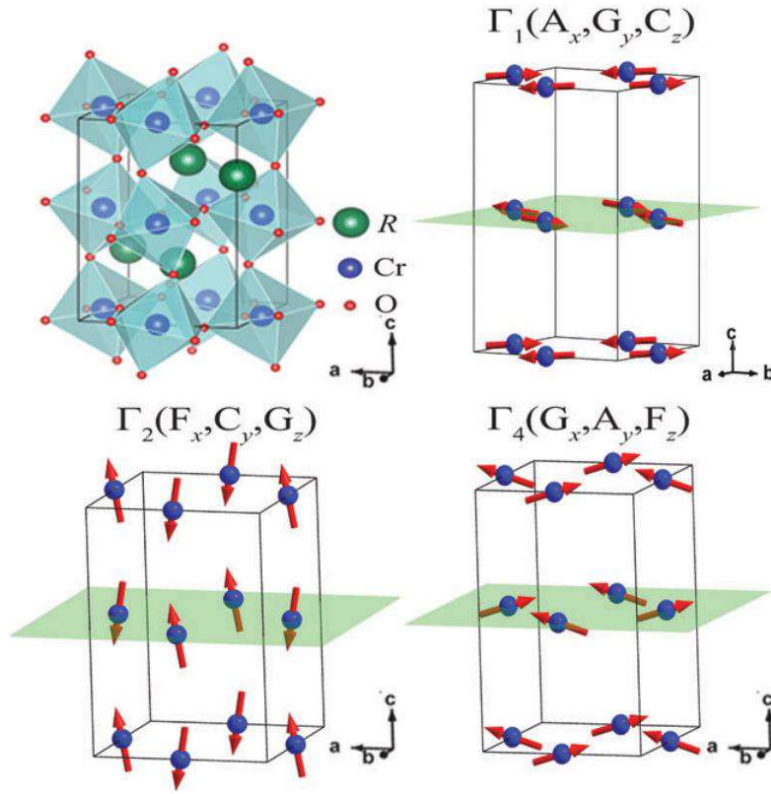
Figure 2.14: Schematic view of the crystal structure and several typical spin configurations of the Cr^{3+} sublattice in $RECrO_3$ systems [172].

admit my knowledge is merely a drop in the bucket.

Usually, we use the Heisenberg exchange Hamiltonian $-J_{ij}\mathbf{S}_i \cdot \mathbf{S}_j$ for describing the TM-O-TM superexchange interaction in insulating oxides. Since the orbital angular momentum $\mathbf{L}$ is quenched for a $3d$ system, the spin angular momentum quantum number $\mathbf{S}$ is then a good quantum number, and the Heisenberg exchange will act as a nice model. However, in the case of the $4f$ system, the orbital angular momentum $\mathbf{L}$ is unquenched, enabling a strong spin-orbit entanglement, thus the Heisenberg exchange with the form of $-J_{ij}\mathbf{S}_i \cdot \mathbf{S}_j$ is invalid. In this way, the spin angular momentum and the orbital angular momentum are not observable quantities anymore, precluding the study on the $4f$-$3d$ coupling.

In addition to the above issue, another difficulty is that the $4f$-$3d$ exchange interaction usually appears accompanied by the $3d$-$3d$ exchange interaction in RETMO perovskites. Compared with the $4f$-$3d$ exchange, the $3d$-$3d$ exchange is quite strong, signals coming from the $4f$-$3d$ exchange are often concealed by signals of the $3d$-$3d$

exchange, making it hard to distinguish the one from the other [58].

To detect the direct exchange coupling between spins of $4f$ electrons and $3d$ electrons, one may need to choose a variety of rare-earth cations with quenched L, i.e., the spin angular momentum is not entangled with the orbital angular momentum. Gd^{3+} ion is a perfect platform that satisfies the above issues. For a Gd^{3+} $(4f^7)$ state with a half-filled $4f$ shell, it has $S = 7/2$, $L = 0$, and $J = 7/2$, implying that a natural quenched orbital angular momentum exists in the Gd^{3+} ion. Hence, gadolinium-based RETMO compounds can serve as a nice system for modeling the exchange interaction between the pure spins of $4f$ and $3d$ electrons. One example is the gadolinium-based orthochromate $GdCrO_3$, in which the $4f$-$3d$ exchange coupling works through the Gd^{3+}-O^{2-}-Cr^{3+} superexchange pathway. Moreover, novel magnetism including exchange bias effect, SR transition of the Cr^{3+} sublattice, and short-range order of the Gd^{3+} sublattice was reported in $GdCrO_3$ where there exist exchange interactions between $4f$ and $3d$ spins [58, 173]. $GdCrO_3$ displays an SR transition from Γ_4 (G_x, A_y, F_z) to Γ_2 (F_x, C_y, G_z) upon cooling [51], the graphic description of allowable magnetic structures Γ_1, Γ_2, and Γ_4 of the Cr^{3+} sublattice are exhibited in Fig. 2.14 [172]. While, one notorious drawback is the intense neutron absorption of gadolinium elements, impeding the neutron scattering study on it. Therefore, a hot neutron beam will be indispensable to carry out a neutron scattering study on the $4f$-$3d$ exchange coupling in a gadolinium-based transition-metal oxide.

To make the $4f$-$3d$ exchange coupling clear, one may need to decrease or cancel the $3d$-$3d$ exchange interaction. In this aspect, Luo *et al.* proposed a new class of anion-vacancy alkali-earth transition-metal perovskites with the chemical formulas of Ba_2YFeO_5 and $Ba_2YFe_2O_{7.5}$, in which the Fe–O–Fe linkages are absent [174, 175]. Starting from the above idea, Kundu *et al.* synthesized a series of materials by changing the yttrium ion with various lanthanum ions, i.e., Ba_2LnFeO_5 and $Ba_3LnFe_2O_{7.5}$ (Ln = Sm, Eu, Gd, Dy, Ho, Er, Yb) [176, 177]. Similar to Ba_2YFeO_5, the strong superexchange interaction TM-O-TM is canceled in this class of materials, and two competing exchanges of R^{3+}-O^{2-}-Fe^{3+} and R^{3+}-O^{2-}-Fe^{3+} play the dominant role. It

is worth mentioning in RECrO$_4$ the $4f$-$3d$ exchange coupling also predominates the global magnetism [178].

2.2.5 Magnetostriction effect

The magnetostriction effect was firstly found in iron by Joule in 1842 [179]. It describes a property of magnetic materials (mostly FM materials) that cause them to change their shape accompanied by the process of magnetization (spontaneously/by external magnetic fields). The magnetostriction effect can be further divided into linear magnetostriction effect and volumetric magnetostriction effect. In general, the magnetostriction effect also includes piezomagnetism, in which one can induce a spontaneous magnetization by applying physical stress [180]. It is an intrinsic nature of magnetic materials for the magnetostriction effect, which has displayed wide potential on technological applications such as various sensors, wave filters, ultrasonic generators, receivers, *etc.* [181, 182]. From the aspect of statistical physics, the magnetostriction effect is the result of a thermodynamic evolution. In the present subsection, details of how the magnetostriction effect is evoked to minimize the total free energy are illustrated.

Considering the deformation induced by the magnetostriction effect in an FM material, the free energy of an FM crystal per unit volume can be then divided into three parts: [183, 184]

(1) Pure magnetocrystalline anisotropic energy F_K^0 without any deformation:

$$F_K^0 = K_0 + K_1(\alpha_1^2\alpha_2^2 + \alpha_2^2\alpha_3^2 + \alpha_3^2\alpha_1^2) + K_2\alpha_1^2\alpha_2^2\alpha_3^2, \qquad (2.40)$$

where (α_1, α_2, α_3) is the directional cosine of the magnetization to three coordinates.

(2) Pure elastic part energy: [185]

$$F_e = \frac{1}{2}c_{11}(e_{xx}^2 + e_{yy}^2 + e_{zz}^2) + \frac{1}{2}c_{44}(e_{xy}^2 + e_{yz}^2 + e_{zx}^2) + c_{12}(e_{xx}e_{yy} + e_{yy}e_{zz} + e_{zz}e_{xx}) \qquad (2.41)$$

where $e_{xx}, e_{yy}, e_{zz}, e_{xy}, e_{yz}$, and e_{zx} are six components of the deformation tensor. The

former three are length strains, the latter three are shear strains. Besides, c_{11}, c_{44}, and c_{12} are second-order elastic modules.

(3) Magnetoelastic part energy:

$$F_K = F_K^0 + \sum_{i \geq j} \left(\frac{\partial F_K}{\partial e_{ij}} \right) e_{ij} + ..., \qquad (2.42)$$

where e_{ij} $(i, j, = x, y, z)$ is the deformation that can be applied to get the expansion of the magnetocrystalline anisotropic energy F_K, with only considering the linear term then one can get Eq. 2.42. The interacting coefficients between magnetization and deformation B_1 and B_2 can be given by

$$\frac{\partial F_K}{\partial e_{xx}} = B_1 \alpha_1^2; \frac{\partial F_K}{\partial e_{xy}} = B_2 \alpha_1 \alpha_2; \qquad (2.43)$$
$$\frac{\partial F_K}{\partial e_{yy}} = B_1 \alpha_2^2; \frac{\partial F_K}{\partial e_{yz}} = B_2 \alpha_2 \alpha_3;$$
$$\frac{\partial F_K}{\partial e_{zz}} = B_1 \alpha_3^2; \frac{\partial F_K}{\partial e_{zx}} = B_2 \alpha_3 \alpha_1;$$

where the coefficients $\partial F_K / \partial e_{ij}$ are related to the direction cosine of the magnetization $(\alpha_1, \alpha_2, \alpha_3)$, resulting in anisotropic magnetoelastic energy.

While merging the above three parts of F_K^0, F_e, and F_K, the total free energy of an FM material can be expressed as [184]

$$F = K_1 (\alpha_1^2 \alpha_2^2 + \alpha_2^2 \alpha_3^2 + \alpha_3^2 \alpha_1^2) + B_1 (\alpha_1^2 e_{xx}^2 + \alpha_2^2 e_{yy}^2 + \alpha_3^2 e_{zz}^2) \qquad (2.44)$$
$$+ B_2 (\alpha_1 \alpha_2 e_{xy} + \alpha_2 \alpha_3 e_{yz} + \alpha_3 \alpha_1 e_{zx}) + \frac{1}{2} c_{11} (e_{xx}^2 + e_{yy}^2 + e_{zz}^2)$$
$$+ \frac{1}{2} c_{44} (e_{xy}^2 + e_{yz}^2 + e_{zx}^2) + c_{12} (e_{xx} e_{yy} + e_{yy} e_{zz} + e_{zz} e_{xx}) + ...$$

where the constants and high-order terms are neglected. At a stable state, the minimization of the free energy can be given by

$$\frac{\partial F_K}{\partial e_{xx}} = \frac{\partial F_K}{\partial e_{yy}} = \frac{\partial F_K}{\partial e_{zz}} = 0; \qquad (2.45)$$
$$\frac{\partial F_K}{\partial e_{xy}} = \frac{\partial F_K}{\partial e_{yz}} = \frac{\partial F_K}{\partial e_{zx}} = 0,$$

the solution to the above equations are

$$e_i = \frac{B_1[c_{12} - a_i^2(c_{11} + 2c_{12})]}{(c_{11} - c_{12})(c_{11} + 2c_{12})}; e_{ij} = -\frac{B_2\alpha_i\alpha_j}{c_{44}}. \tag{2.46}$$

Substitute Eq. (2.44) and Eq. (2.46) into Eq. (2.45), one then has the final total free energy of FM materials

$$F = (K + \Delta K)(\alpha_1^2\alpha_2^2 + \alpha_2^2\alpha_3^2 + \alpha_3^2\alpha_1^2), \tag{2.47}$$

where ΔK denotes the magnetoelastic coupling constant, which consists of the additional energy coming from B_1, B_2, c_{11}, c_{12}, and c_{44}. Hence, considering only the linear terms of the deformation tensor e_{ij}, the form of magnetocrystalline anisotropic energy does not change. What changes is the anisotropic constant.

2.2.6 Manetocaloric effect

The magnetocaloric effect (MCE) is a magneto-thermodynamic phenomenon in which a temperature change of a suitable material is caused by exposing the material to a changing magnetic field. In 1881, MCE was firstly observed by Warburg, followed by Weiss and Piccard in 1917 [186]. The most interesting application of MCE is that it can be utilized to realize a low temperature, i.e., a magnetic refrigerator. In the present subsection, I introduce how a magnetic refrigerator works, followed by some specific parameters to evaluate an MCE material. Later, several kinds of materials that are appropriate for magnetic refrigeration are included.

A magnetic refrigerator works through a refrigeration cycle that bears a close resemblance to the well-known Carnot refrigeration cycle, while the driven force of the temperature is a magnetic field rather than pressure [187]. As shown in Fig. 2.15, the process of magnetic refrigeration can be divided into four main stages:

(1) Adiabatic magnetization:

In this stage, the MCE material stays adiabatic. With increasing magnetic field ($+\mu_0 H$), ordering spins occur in the MCE material, accompanied by decreasing mag-
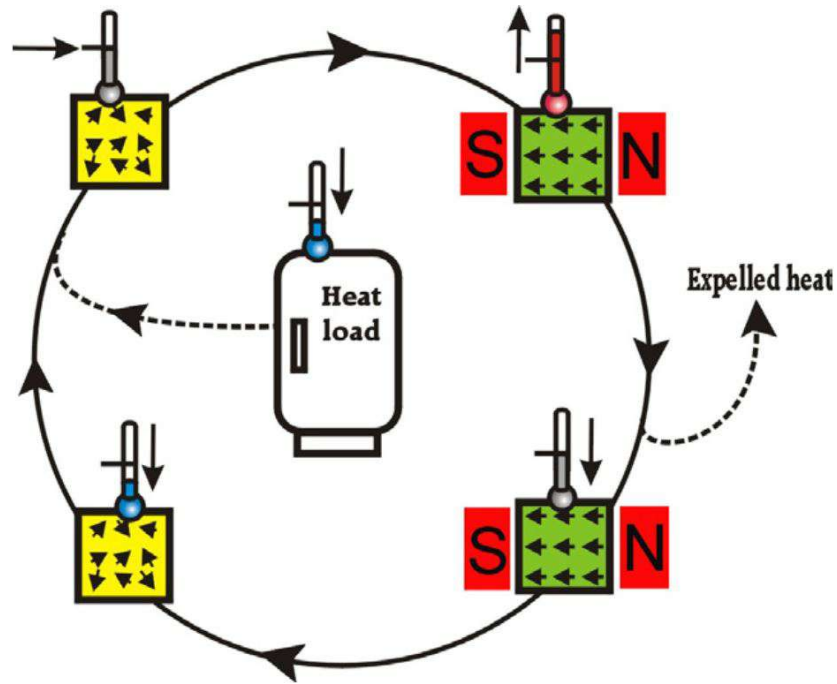
Figure 2.15: Schematic representation of a magnetic-refrigeration cycle that transports heat from the heat load to the ambient. Left and right depict material in low and high magnetic fields, respectively [187].

netic entropy and specific heat. While, the overall energy of the system remains constant, implying constant total energy according to the thermodynamic laws. Hence, the MCE material is heated with an adiabatic change in temperature $+\Delta T_{\text{ad}}$.

(2) Isomagnetic enthalpic transfer:

In this stage, the extra heat in the adiabatic magnetization process can be expelled $(-Q)$ by a refrigerant, like freon or liquid helium. Meanwhile, the magnetic field is held constantly to prevent the MCE materials from reabsorbing any heat. Once the MCE material is cool enough, it will be separated with the refrigerant.

(3) Adiabatic demagnetization:

The MCE material is transferred to another adiabatic condition, the total entropy of which keeps being a constant. While, in this process, the external magnetic field is withdrawn, resulting in an alteration from order to the disorder of the MCE material. Thermal entropy becomes magnetic entropy, and the MCE material then cools.

(4) Adiabatic magnetization:

The magnetic field is still not applied to the MCE material, which is then placed

in thermal contact with the environment and is prepared to be refrigerated. Since the MCE materials are cooler than the pre-cooled environment, heat prefers transferring from the environment to the MCE material, which then recovers to the first stage ($+Q$).

One can estimate the MCE of a magnetic substance by experimental magnetization and specific-heat data with following the Maxwell relation: [188]

$$\left(\frac{\partial S_{\mathrm{M}}(M,T)}{\partial \mu_0 H} \right)_T = \left(\frac{\partial M(\mu_0 H, T)}{\partial T} \right)_{\mu_0 H}. \tag{2.48}$$

According to the above relation, the magnetic entropy ΔS_{M} can be deduced. Considering experimental data is usually discrete, the magnetic entropy ΔS_{M} can then numerically approximate the following difference equation

$$\Delta S_{\mathrm{M}}(T, \mu_0 H) = \mu_0 \sum_i \frac{M_{i+1} - M_i}{T_{i+1} - T_i} \Delta H_i. \tag{2.49}$$

Furthermore, with experimental temperature-dependent specific-heat data at different applied magnetic fields, the adiabatic temperature change ΔT_{ad} can be calculated by

$$\Delta T_{\mathrm{ad}} = \int_0^{\mu_0 H} \frac{T}{C_p(T, \mu_0 H)} \left(\frac{\partial M(\mu_0 H, T)}{\partial T} \right)_{\mu_0 H} d\mu_0 H. \tag{2.50}$$

The magnetocaloric effect (MCE) is an intrinsic nature of a magnetic material. As for a material displaying the MCE effect, thermal response to the application or removal of magnetic fields is maximized when the material is close to its magnetic ordering temperature. Thus, the materials considered for magnetic refrigeration would embrace a magnetic phase transition temperature near the temperature region of interest. Therefore, for refrigerators that are going to be used in the home, this interesting temperature should be room temperature [189, 190]. The temperature change can be further increased when the order parameter of the phase transition changes strongly within the temperature range of interest.

The magnitudes of the magnetic entropy and the adiabatic temperature changes strongly depend on the magnetic ordering process. The magnitude is usually small in

antiferromagnets, ferrimagnets, and spin glass systems but can be much larger for ferromagnets that undergo a ferromagnetic phase transition. First-order phase transitions are characterized by a discontinuity in the magnetization changes with temperature, resulting in latent heat. Second-order phase transitions do not have this latent heat associated with the phase transition. Though the MCE was firstly discovered in simple iron, further research on materials displaying MCE was concentrated on rare-earth and their alloys. One famous example with a sub-room temperature giant-MCE is the ternary alloy $Gd_5(Ge_{1-x}Si_x)_4$ [191]. One also needs to be aware that the development of this technology is very material-dependent and will likely not replace vapor-compression refrigeration unless significantly improved materials are discovered with cheap, abundant, and exhibit much larger MCE over a larger range of temperatures. Such materials need to show significant temperature changes under a field of two teslas or less, which means permanent magnets are also supposed to be integrated with a system of magnetic refrigeration.

CHAPTER 3

EXPERIMENTAL TECHNIQUES AND INSTRUMENTS

To finish the research in this thesis, I have used a variety of experimental techniques and instruments. In the present chapter, I introduce experimental procedures of material synthesis, in-house characterization methods and instruments, as well as neutron scattering theory and spectrometers I used. With the above experimental parts, basic physical properties of a certain strongly correlated electronic material could be obtained. A further in-depth understanding needs the explanation by theoretical modeling, which is elucidated in detail in chapter 4. Materials synthesis consists of polycrystalline synthesis (Section 3.1), single crystal growth by floating-zone method, and chemical vapor transport (Section 3.2). Moreover, a number of in-house characterizations I have used to obtain the detailed physical and chemical properties are listed (Section 3.3). These include physical property measurement system (PPMS), scanning electron microscope (SEM) and energy-dispersive X-ray spectroscopy (EDS), X-ray powder diffraction (XRPD), and X-ray Laue diffraction. Finally, experimental principles of neutron powder diffraction and inelastic neutron scattering are elucidated (Section 3.4), neutron scattering spectrometers I have used in this thesis are described as well.

3.1 Polycrsystalline synthesis

Polycrystalline samples are composed of small crystals (also called grains) whose crystallographic axes point to random orientations. Polycrystalline materials are easy to be synthesized, meanwhile, the production process is low-cost. Therefore, polycrystalline materials are popular in large amounts of engineering applications, including concrete, ceramic, batteries, *etc.* Besides, polycrystalline samples are usually treated as the precursor of single-crystal growth. Therefore, obtaining high-quality polycrystalline samples is very important for condensed matter science and modern industry.
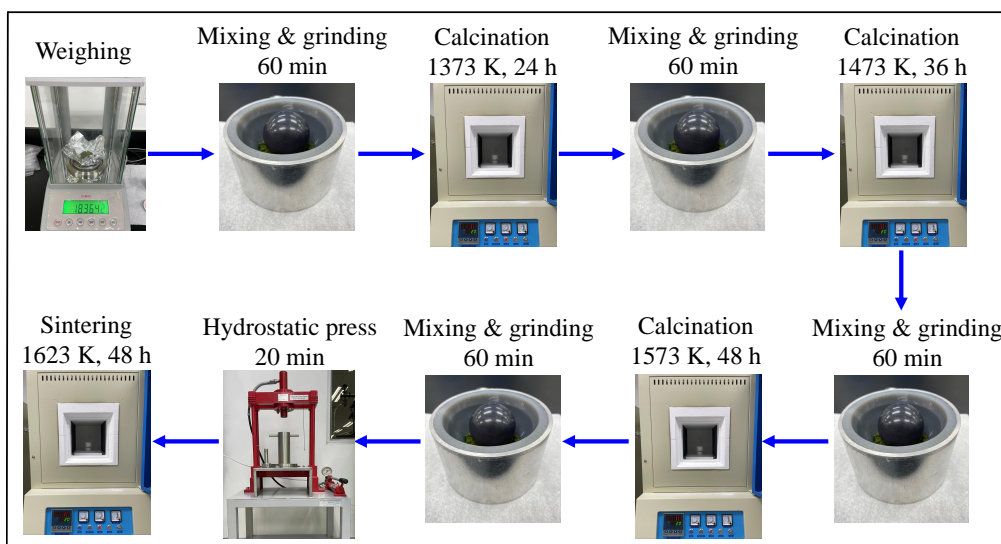
Figure 3.1: The processing route for the solid-state reaction of $GdMn_xCr_{1-x}O_3$ poly-crystalline sample.

Among various methods of polycrystalline synthesis, the high-temperature solid-state reaction method serves as a normal manner to synthesize polycrystalline materials. In this section, I introduce the detail of the solid-state reaction method with taking the preparation of polycrystalline samples of $GdMn_xCr_{1-x}O_3$ ($x = 0.1–1.0$) as an example. Results of X-ray diffraction are also illustrated to verify the phase purity of the present polycrystalline samples of $GdMn_xCr_{1-x}O_3$.

The present polycrystalline $GdMn_xCr_{1-x}O_3$ ($x = 0.1–1.0$) series compounds were synthesized with raw materials of Gd_2O_3 (Alfa Aesar, 99.9%), Cr_2O_3 (Alfa Aesar, 99.6%), and MnO_2 (Adamas-beta, 99%). Considering the raw materials, especially rare-earth oxides, may be deliquesced when they are exposed to air in a room-temperature environment. Hence, the raw materials need to be set in a drying oven with a temperature of around 423 K one day before weighing to acquire a chemical stoichiometry of the raw materials. A graphic description of detailed procedures is illustrated in Fig. 3.1. Since Cr_2O_3 has a high saturation vaporing pressure and is easy to evaporate at high temperatures, extra Cr_2O_3 with a ratio of about 5% of the original stoichiometry was added. After weighing, the raw materials were ground and mixed by a Vibratory Micro Mill (FRITSCH PULVERISETTE 0) for 60 min, a 50 mm-diameter ball made of agate was used for grinding. After ball milling, the mixture of raw materials was moved into
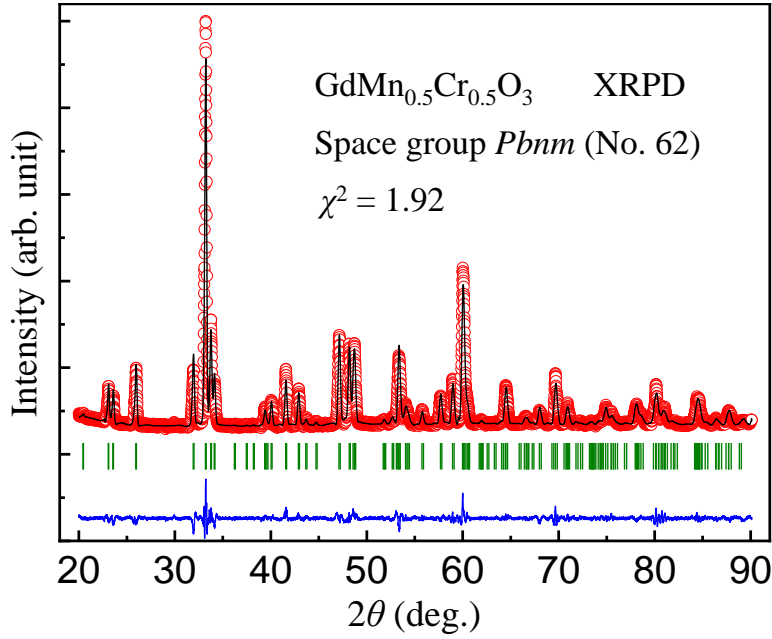
Figure 3.2: Profile matching of the XRPD data of $GdMn_{0.5}Cr_{0.5}O_3$ polycrystalline powder at room temperature shows no appearance of impurity phase within the detection accuracy.

an alumina crucible. The calcination was performed by a muffle furnace. Firstly, the mixture of raw materials experienced preliminary calcination with heating up to 1373 K and sustaining there for 24 hours. The resultants were milled with the same procedure as elucidated therein before. The powder sample was then calcined twice at 1473 K for 36 hours and at 1573 K for 48 hours with intermediate grinding and mixing after each firing. The final powder products were filled into balloons whose inner and outer surfaces were washed with water and dried in air. After filling in the resultants, the air in the balloons was evacuated by a dry vacuum pump. The balloons were tied while evacuating and pressed by a hydrostatic pressure at ~ 70 MPa. The pressed bulks were sintered at 1623 K for 48 hours. Finally, black dense polycrystalline bulk samples of $GdMn_xCr_{1-x}O_3$ were obtained.

XRPD was performed to confirm the phase purity of the present polycrystalline samples of $GdMn_xCr_{1-x}O_3$ ($x = 0.1$–1.0). The detailed principle of X-ray diffraction is illustrated in section 3.4. The FULLPROF Suite was used to refine all XRPD data of $GdMn_xCr_{1-x}O_3$. With the result of refinement, it is shown that the $GdMn_xCr_{1-x}O_3$ series polycrystalline samples crystallize into an orthorhombic phase with the $Pbnm$

54
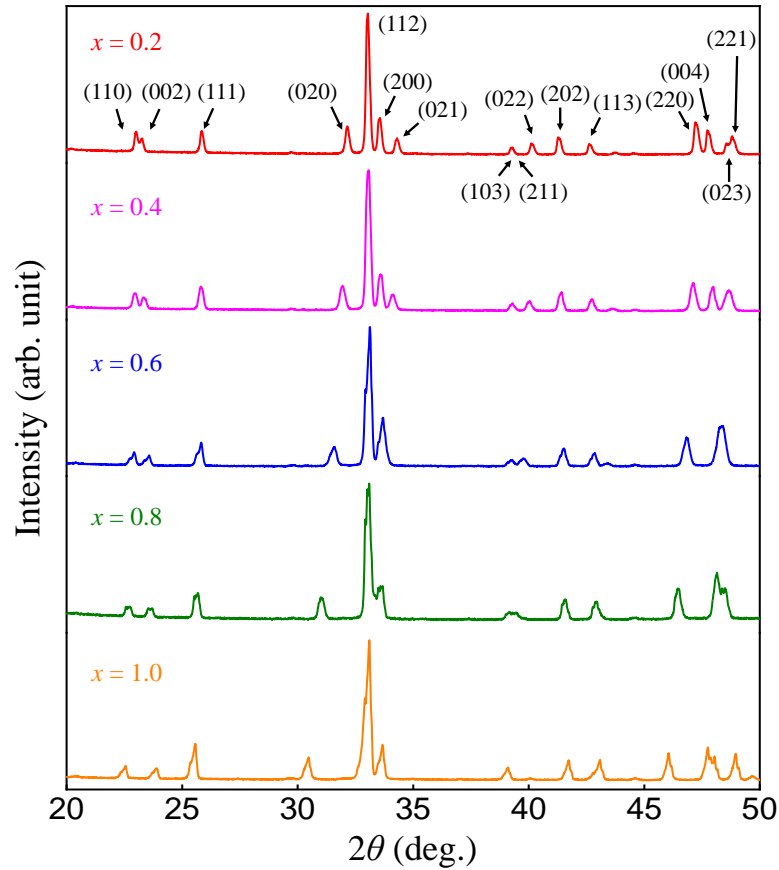
Figure 3.3: Room-temperature X-ray powder diffraction patterns of $GdMn_xCr_{1-x}O_3$ (x = 0.2, 0.4, 0.6, 0.8, 1.0) polycrystalline sample in a 2θ range of 20–50°. Miller indices (hkl) of the main reflectivity in the $Pbnm$ space group (No. 62) are also marked and accompanied by arrows pointing to corresponding Bragg peaks.

space group (No. 62). As a representative, the FULLPROF refinement result of $GdMn_{0.5}Cr_{0.5}O_3$ is displayed in Fig. 3.2, where observed (red circles) and calculated (black solid lines) XRPD patterns of a small amount of powder sample are shown, the vertical green bars mark the positions of nuclear Bragg reflections ($Pbnm$ space group), and the lower blue curve represents the difference between observed and calculated patterns. According to Fig. 3.2, it is evident that there is no impurity phase.

To compare the effect from different doping ratio of manganese, X-ray diffraction patterns of five compositions of polycrystalline $GdMn_xCr_{1-x}O_3$ (x = 0.2, 0.4, 0.6, 0.8, 1.0) are displayed in Fig. 3.3 with a 2θ range of 20–50°. In the XRPD pattern of the polycrystalline sample of $GdMn_{0.2}Cr_{0.8}O_3$, Miller indices (hkl) of the pronounced Bragg diffraction peaks were marked. With increasing x, i.e., the doping ratio of manganese, it is shown that the Bragg (1 1 0) peak and the Bragg (0 0 2) peak gradually
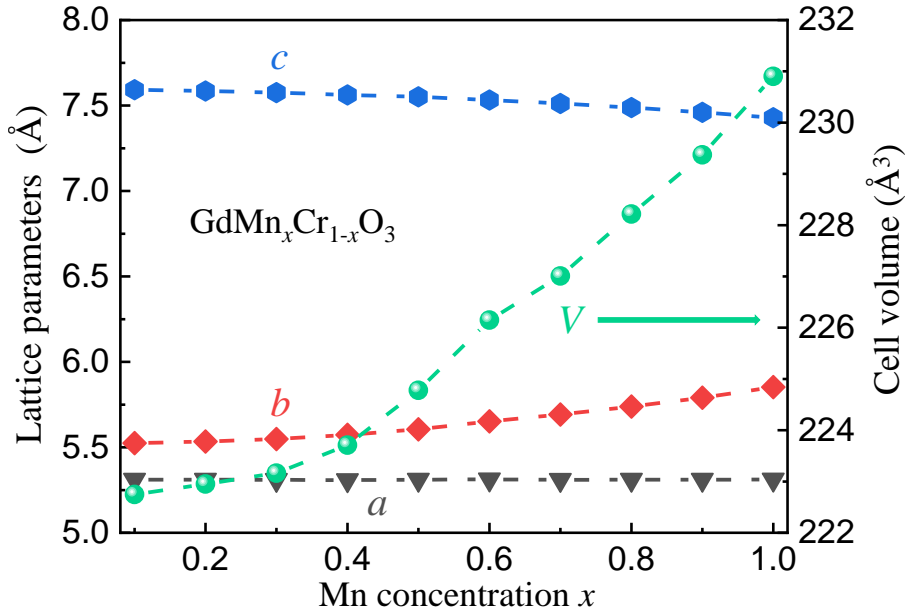
Figure 3.4: Room-temperature X-ray powder diffraction patterns of GdMn$_x$Cr$_{1-x}$O$_3$ (x = 0.2, 0.4, 0.6, 0.8, 1.0) polycrystalline sample in a 2θ range of 20–50°. Miller indices (hkl) of the main reflectivity in the $Pbnm$ space group (No. 62) are also marked and accompanied by arrows pointing to corresponding Bragg peaks.

shift apart from 23.22° and 23.45° for x = 0.1 to 22.60° and 23.95° for x = 1.0, respectively. Meanwhile, there also display gradual shifts of Bragg peaks of (0 2 0) and (0 2 2). With increasing x content from x = 0.1 to 1.0, the Bragg (0 2 0) peak shifts from 32.42° to 30.55°, and the Bragg (0 2 2) peak shifts from 40.40° to 39.20°, accompanied by merging with the Bragg (2 1 1) peak. Gradual shift with increasing content x also occurs in Bragg peaks of (2 2 0), (0 0 4), (0 2 3), and (2 2 1), in which (2 2 0) (from 47.50° to 46.20°), (0 2 3) (from 48.80° to 48.15°), and (2 2 1) (49.10° to 47.87°) show a gradual shift to a smaller 2θ area, while the Bragg (0 0 4) peak shifts from 47.95° to a larger 2θ value of 49.05°. The step-by-step shifts of Bragg peaks with increasing x content imply successful substitutional doping of manganese on chromium within the orthorhombic structure.

With the polycrystalline samples which are verified to be a pure phase, structural refinement was performed by FULLPROF Suite for x content ranging from 0.1 to 1.0. By using the $Pbnm$ space group (No. 62), a very good agreement between the experimental and theoretical XRPD patterns was achieved. In order to compare the effect of substitutional adulteration by manganese on crystallographic structure, lattice

parameters a, b, c, and cell volume V were extracted, as shown in Fig. 3.4. With increasing x content of manganese adulteration, lattice parameters and cell volume vary from $a = 5.3106(2)$ Å, $b = 5.5246(2)$ Å, $c = 7.5923(2)$ Å, $V = 222.748(11)$ Å^3 (x = 0.1) to $a = 5.3113(2)$ Å, $b = 5.8523(2)$ Å, $c = 7.4286(2)$ Å, $V = 230.903(13)$ Å^3 (x = 1.0). One interesting point is that the cell volume V increases smoothly firstly, and there occurs a rapid increase when the doping content x is beyond 0.4.

The present structural result on the series of polycrystalline samples of GdMn$_x$Cr$_{1-x}$O$_3$ (x = 0.1–1.0) proved that polycrystalline samples of RETMO compounds with good crystallization and pure phase can be obtained by the procedures of polycrystalline synthesis introduced in the present subsection.

3.2 Single crystal growth

In materials science, a single-crystal (also called monocrystalline) solid is a variety of materials, inside which the crystal lattice of the entire sample is continuous and unbroken to the edges of the sample, with no grain boundaries. Besides, an ordered three-dimensional arrangement of the atoms, ions, or molecules is repeated throughout the entire volume of a certain single-crystal sample. One can consider an amorphous structure as the opposite case of a single crystal, since there only exist short-range orders in amorphous materials. A transitional state of these two extremes is polycrystal.

Studies on single-crystal materials have enabled pronounced development both in science and precision technology. In the study of condensed matter physics, a single-crystal sample could give the intrinsic nature of a certain system. It is indispensable for certain experimental characterizations to carry out based on a single crystal, such as optics, excitations in three-dimensional reciprocal space, crystallographic anisotropy, *etc.* In technology, extensive applications have been realized based on single-crystal materials, one tremendous case is the semiconductor industry, which demands high-quality single-crystal silicon. Besides, single crystal materials are also widely used in optical engineering, sensors, photovoltaic industry, *etc.* The dramatic significance of high-quality single-crystal samples makes single-crystal growth procedures a tremen-

Figure 3.5: Laser diode FZ furnace at the University of Macau, Macao.

dous subject. Single crystal growth methods can usually be divided into four varieties, including melt, solid, vapor, and solution, according to what an artificial crystal could be grown. In the present section, I introduce two methods of single crystal growth, i.e., the floating-zone (FZ) technique and the chemical vapor transport (CVT) method that I used. Meanwhile, two varieties of compounds that I have grown are displayed as examples accompanied by their crystallographic structures.

3.2.1 Floating-zone method

In the present thesis, all of the single-crystal rare-earth chromate samples were grown by the FZ technique. One merit is that the FZ technique is a containerless method that prevents contamination from containers like crucibles. Moreover, the FZ technique could achieve the growth of single crystals with a centimeter scale and high-melting-point. The former enables certain experimental studies which demand samples with
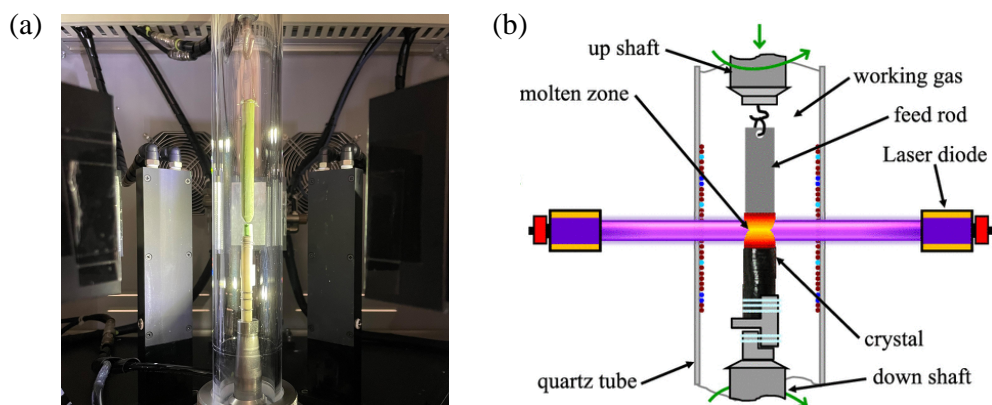
Figure 3.6: (a) A picture inside the laser diode FZ furnace before the growth of RECrO$_3$, and (b) a schematic of the vertical cross-section of the laser diode FZ furnace [192].

large mass, such as neutron scattering experiments. And the latter is especially significant for the growth of compounds, in which huge differences exist between the composition in the feed rod. Such a case can usually be evident at the beginning of growth due to an insufficient temperature.

More specifically, the FZ technique can be further separated based on a heat source. A well-known one is the mirror optical FZ technique which utilizes lamps whose radiation is focused by mirrors [74]. Another recently rising mode is the laser diode FZ technique (also named laser-heated pedestal growth) inside which a narrow region is heated. Unlike the former one, the laser diode FZ technique utilizes a powerful infrared laser as the radiation source. One promising advantage of the laser diode FZ technique is that the radiation is focused to the trajectory, making little volatile substance adhere on the inner side of the quartz tube since the intensity is so strong that it can hit the volatile substance from the trajectory. In contrast to the laser source, light in a mirror optical FZ furnace goes through a much wider region before focusing on the melting zone of crystal growth [193]. Hence, the radiation experiences an attenuation when it finally focuses on the crystal.

There is one laser diode FZ furnace (Model: LD-FZ-5-200W-VPO-PC-UM) in our lab at the University of Macau, Macao, as shown in Fig. 3.5. The furnace is equipped with five infrared lasers, whose power is 200 W with a wavelength of 975±5 nm. A light absorber is fixed in the direction of radiation of each laser, as shown in Fig. 3.6(a),

59
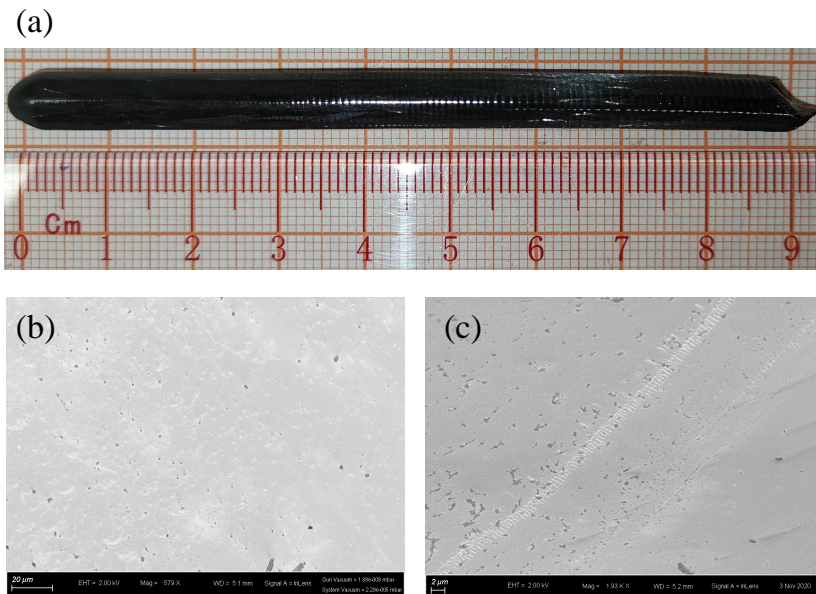
Figure 3.7: (a) One RECrO$_3$ crystal grown with the laser diode FZ technique at the University of Macau, Macao. SEM imagines the as-grown TmCrO$_3$ single crystal (b), and YCrO$_3$ single crystal (c).

two of the five absorbers are displayed. To illustrate the principle of the laser diode FZ technique, a schematic of the vertical cross-section of the laser diode FZ furnace is displayed in Fig. 3.6(b). Five lasers used as heat sources are installed at the same horizontal, which is collimated before single crystal growth. The radiation of the laser penetrates the quartz tube and focuses on the melting zone, which is located between the feed rod at the up shaft and the seed rod at the down shaft. The melting zone can be stabilized by surface tension, which is a material-dependent property. To control the pressure of the atmosphere and prevent leakage of volatile substances, single crystal growth works in a sealed quartz tube which can sustain a gas pressure up to 1 MPa. The air pressure inside the quartz tube should be evacuated at less than 5×10^{-3} Pa before each time of growth, selected gas is then pumped into the quartz tube to attain the required atmosphere condition. To reach a homogeneous temperature distribution accompanied by a steady melting zone of single crystal growth, the up shaft and down shaft usually rotate in opposite directions each other. The crystals of RECrO$_3$ were grown with a rotational speed range of 25-30 rpm/h. At the beginning of the growth, a super-necking method is utilized with a lowering speed of 3–6 mm/h for the seed rod and 2–3 mm/h for the feed rod. In this way, subsequent crystals can be grown
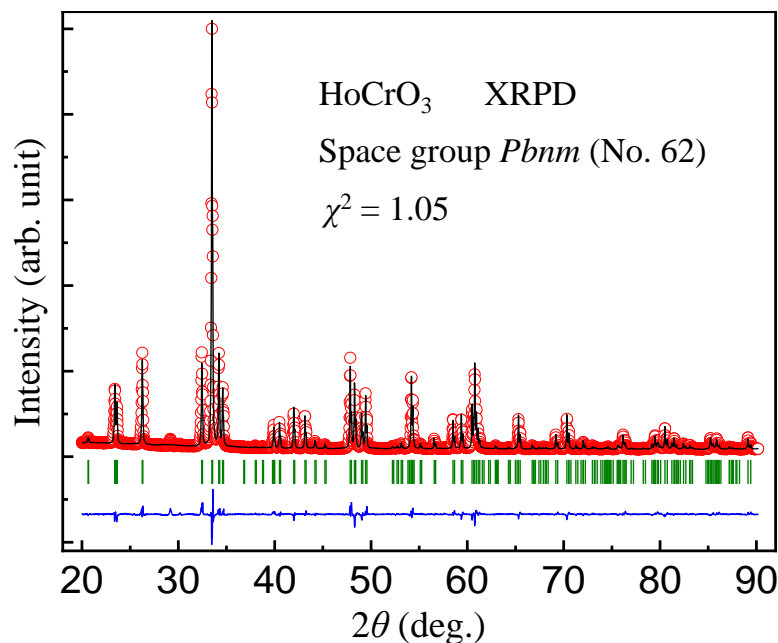
Figure 3.8: Profile matching of the XRPD data of a pulverized HoCrO$_3$ single crystal at room temperature shows no appearance of impurity phase within the detection accuracy.

based on a high-quality seed crystal. The most optimized speed of growth varies for different crystal types. For a compound having little volatilization near its melting point, usually, a slow speed of less than 5 mm/h can be used, like in the case of the single crystal growth of ferrites. However, for a compound whose compositions are volatile, such as chromates, a quick speed is then needed. In the present thesis, the RECrO$_3$ crystals were grown at speeds ranging from 5 mm/h to 15 mm/h. Moreover, by tuning the diameter of the feed rod and the speed difference between the up shaft and the down shaft, the diameter of as-grown crystals can be controlled.

Before the single crystal growth of RECrO$_3$ compounds, polycrystalline RECrO$_3$ powder with a homogenous phase was synthesized via the solid-state reaction method, as described in section 3.1. In the above procedure, I have used raw materials of Y$_2$O$_3$ (Alfa Aesar, 99.9%), Gd$_2$O$_3$ (Alfa Aesar, 99.9%), Tb$_2$O$_3$ (Alfa Aesar, 99.9%), Dy$_2$O$_3$ (Alfa Aesar, 99.9%), Ho$_2$O$_3$ (Alfa Aesar, 99.9%), Er$_2$O$_3$ (Alfa Aesar, 99.9%), Tm$_2$O$_3$ (Alfa Aesar, 99.9%), Yb$_2$O$_3$ (Alfa Aesar, 99.9%), Lu$_2$O$_3$ (Alfa Aesar, 99.9%), and Cr$_2$O$_3$ (Alfa Aesar, 99.6%). Fine powders with micro size were filled into clean balloons which were then shaped into cylindrical by an aluminum mold, and a following

61

high-temperature zone | low-temperature zone

transport agents & grown substance

transport agents
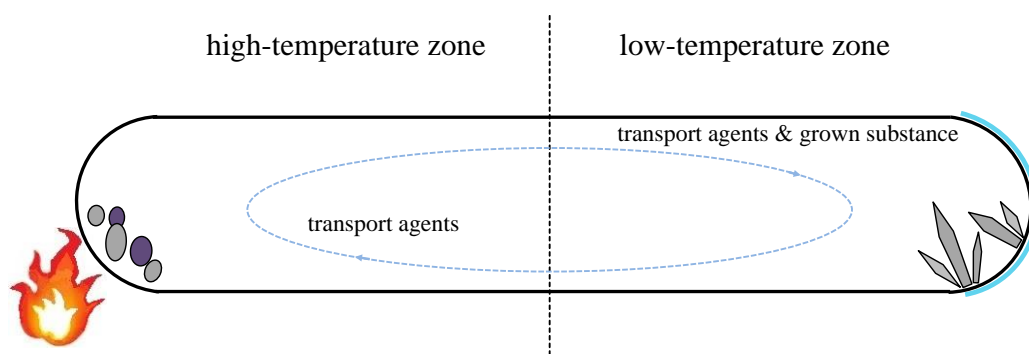
Figure 3.9: A schematic picture of single crystal growth by the CVT method. The evacuated can sealed quartz tube is situated at a furnace with a temperature gradient. During the growth of CVT, a cycle works with raw materials transferred from the hot end (T_1) to the cold end (T_2), leaving grown compounds at the cold end. The transport agent compound returns to the hot end and restarts a cycle then.

hydrostatic pressure of ~ 70 MPa. Considering the high saturation vapor pressure and intense volatilization of Cr_2O_3 compound, an extra 10–15% Cr_2O_3 was added at the final sintering of feed and seed rod.

As a representative, a picture of an as-grown $RECrO_3$ crystal is displayed in Fig. 3.7(a). To check the quality of the crystal grown by laser diode FZ technique, SEM imagines on the surface of as-grown $TmCrO_3$ and $YCrO_3$ single crystals were characterized within micron scale, as shown in Fig. 3.7(b) and Fig. 3.7(c), respectively. Striations of crystal growth can be observed evidently in the SEM images, and the surface behaves smoothly even in micron scale, implying a good quality of the as-grown single crystals. Furthermore, to confirm the phase purity of the $RECrO_3$ series crystals, XRPD was carried out at room temperature with carefully pulverized $RECrO_3$ single crystals. As one example, the FULLPROF refinement profile on the crystal structure of one pulverized $HoCrO_3$ single crystal is shown in Fig. 3.8. One can see an excellent agreement is achieved between the calculated and experimental XRPD patterns, meaning a pure phase of the as-grown $RECrO_3$ crystal by laser diode FZ technique. Detailed crystallographic parameters of $RECrO_3$ single crystals determined by XRPD are exhibited in chapter 5.
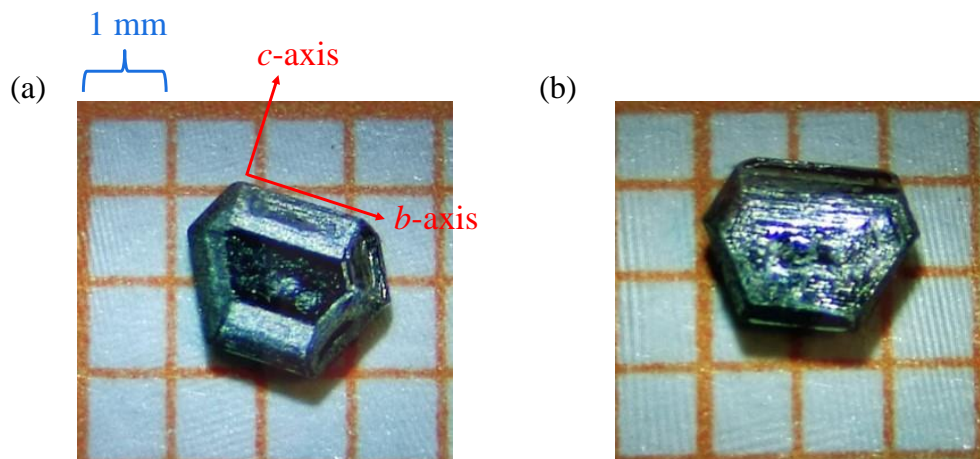
Figure 3.10: The front (a) and the back (b) of an as-grown CrP single crystal with the CVT method. The crystallographic b-axis and c-axis are marked within the $Pbnm$ space group (No. 62).

3.2.2 Chemical vapor transport

CVT method is another single-crystal-growth technique that was invented by Schäfer [194]. In the process, the solid phase compound is volatilized accompanied by a gaseous reactant, i.e., the transport agent. Gaseous substance deposits in the form of crystals somewhere cooler in the sealed tube. Similar to the flux method, crystals are usually grown with a natural crystallographic plane. One difference is a temperature gradient is necessary for single crystal growth by the CVT method. To realize a successful single crystal growth, an optimized temperature gradient and an appropriate transport agent are demanded [195]. Halogens and halogen compounds are two types of usual used transport agents. In the thesis, a chromium phosphide (CrP) single crystal has been grown with the CVT method, whose technological details is elucidated in the present subsection.

Iodine was chosen as the transport agent in the single crystal growth of CrP. Raw materials of chromium powder (Aladdin, 99.5%), iodine (Alfa Aesar, 99.5%), and red phosphorus (Aladdin, 98.5%) were used. Raw materials with a total mass of one gram were weighed in an argon glove box with a stoichiometric ratio of Cr:P:I = 1:1:1. The weighed raw materials were then ground with an agate pestle for 30 minutes in the argon glove box. The mixture was transferred into a quartz tube which was then sealed
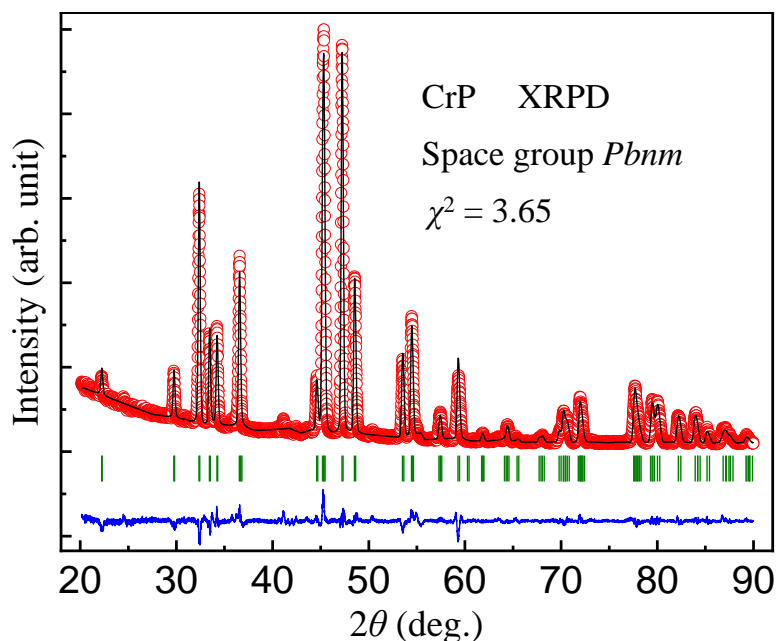
Figure 3.11: Profile matching of the XRPD data of CrP polycrystalline powder at room temperature shows no appearance of impurity phase within the detection accuracy.

at an evacuated pressure of $< 5 \times 10^{-3}$ Pa to prevent raw materials from oxidation. In order to perform single crystal growth of CrP by CVT method, the sealed quartz was moved into a furnace, in which a temperature gradient exists from one end to the other, as shown in Fig. 3.9. The high-temperature zone was kept at ~ 900 °C, and the low-temperature zone was kept at 800 °C for 7 days with a temperature decreasing rate of 150 °C/h. During the preservation, the transport agent (iodine) was gaseous due to its lower evaporating point than heating temperature and moved from the hot zone to the cold zone accompanied by carrying chromium and phosphorus. When arriving at the cold end, chromium and phosphorus were separated in the form of their compound, i.e., CrP. After that, iodine moved back to the hot end, and the cycle was completed followed by a fresh one.

After cooling down to room temperature, the quartz tube was opened in an argon glove box. Shinny metallic crystals crystallize at the hot end, as shown in Fig. 3.10. With a single-crystal X-ray diffractometer, it was determined that the as-grown single crystal crystallizes into an MnP-type structure [196], i.e. $Pbnm$ space group (No. 62), the crystallographic b axis and c axis are marked in Fig. 3.10(a). Furthermore, to confirm the phase purity of the as-grown CrP single crystal, XRPD was carried out by care-

Table 3.1: Structural parameters of a CrP single crystal obtained by FULLPROF refinements of XRPD data and from SCXD.

Structural parameters of a CrP single crystal		
(Orthorhombic, space group: $Pbnm$)		
	XRPD	SCXD
a (Å)	6.0050(1)	6.018(6)
b (Å)	5.3558(1)	5.379(5)
c (Å)	3.1151(1)	3.123(5)
V (Å^3)	100.187(4)	101.1(2)
Cr	4c: [0.1935(1), 0.0076(2), 0.25]	
B (Cr) (Å^2)	0.90(2)	
P	4c: [0.5646(2), 0.1865(2), 0.25]	
B (P) (Å^2)	1.11(3)	

The Wyckoff sites of all atoms are listed.

fully pulverizing small pieces of single crystals, and then refined with the FULLPROF suite. The $Pbnm$ space group was also utilized for structural refinement. The good agreement between the experimental and theoretical XRPD patterns demonstrates a $Pbnm$ space group of the crystal structure, as shown in Fig. 3.11. The structural parameters extracted from FULLPROF refinement and single crystal X-ray diffraction (SCXD) are listed in Table 3.1.

3.3 In-house characterizations

A physical property measurement system (PPMS) is an instrument for the characterizations of magnetization (DC and AC), heat capacity, resistivity, and thermal transport of a bulk/film accompanied by controlled temperature and magnet. Scanning electron microscope (SEM) is a non-destructive method to probe the surface morphology of a sample. The energy dispersive X-Ray Spectroscopy (EDS/EDX) is used to determine the elemental composition of a sample. X-ray diffraction is a quick method to determine the crystal structure of a certain material without destroying it. More specifically, it can be further divided into X-ray powder diffraction and X-ray Laue diffraction, the latter is for the determination of crystallographic axes and planes. Neutron scattering is a powerful technique to detect the crystal/magnetic structure and lattice/spin dynamics
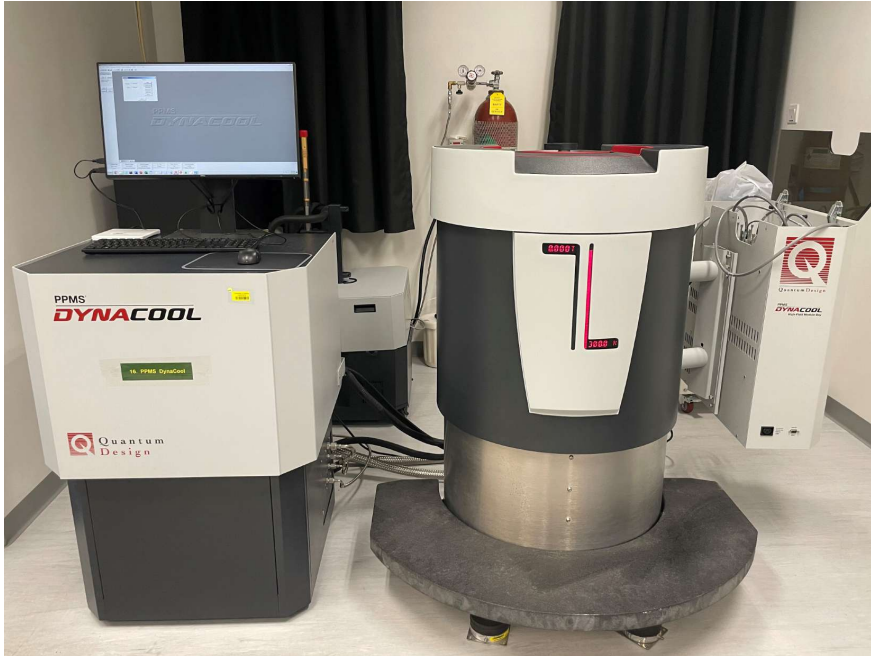
Figure 3.12: PPMS DynaCool instrument equipped at the University of Macau, Macao.

of a certain material.

In this section, I describe the instruments I have used in the thesis accompanied by the basic principles. Furthermore, I introduced the principles of neutron diffraction and inelastic neutron scattering, following which are an introduction to neutron scattering spectrometers that I have used in the thesis.

3.3.1 Physical property measurement

At the University of Macau, Macao, there is a PPMS DynaCool instrument, as shown in Fig. 3.12. The PPMS DynaCool instrument is an automated low-temperature and magnet system for physical property characterizations. Following a standard procedure, physical properties including specific heat, magnetic AC and DC susceptibility, and both electrical and thermal transport properties (Hall Effect, thermoelectric property, and Seebeck Effect) can be measured with controlled temperature (1.8–400 K) and external magnetic field (up to 14 T). Besides, a dilution refrigerator is used to perform measurements under an ultra-low temperature range of 0.05–4 K.

Heat capacity is measured with the thermal relaxation method, which measures the response of the sample after a heat perturbation. To attain a better thermal conduc-

tance, a sample with a smooth surface is usually chosen and mounted on the micro-calorimeter platform of the heat-capacity puck. The platform is connected by four platinum threads with thermal conductance to the cryostat (Bath). To improve the thermal conductivity between the sample to be measured and the micro-calorimeter platform, Apiezon N grease is used for fixing the sample. To extract the specific-heat signal from the background, the puck with an appropriate amount of the Apiezon N grease is supposed to be solely measured, i.e., the specific heat of the addenda. The absolute specific heat of the sample is obtained by subtracting the addenda signal from the raw specific-heat data, i.e., the sum of specific-heat data coming from the sample and addenda. The conventional electrical resistivity can be measured with the standard four-probe method by the ETO option of the PPMS DynaCool. The sample is mounted on a commercial sample puck from Quantum Design. The measurement of AC and DC magnetization employs a vibrating sample magnetometer. The sample is usually mounted on a sample holder made of quartz, here GE low-temperature varnish is employed for fixing the sample. To prevent the sample from leaving the sample holder under high magnetic fields, it is better to bind up the sample with a few layers of Teflon film.

3.3.2 Scanning electron microscope and energy-dispersive X-ray spectroscopy

SEM and EDS allow for a quick targeted analysis of sample surfaces. These techniques are widely used for material surface analysis, investigation of product failures, reverse engineering, contaminant identification, solder joint analysis, *etc.*

Since their commercial development in the 1950s, SEM and EDS comprise what has long been a tremendous tool for surface analysis in materials science and technology [197]. An SEM is a type of electron microscope that detects images of the sample surfaces. In contrast to a normal optical microscope which utilizes light for imaging, an SEM employs electrons—essentially translating electron interactions into an optical signal. The electron beam scans a raster pattern, then an image can be recognized by combining the position of the beam and the intensity of detected signals. EDS is a

Figure 3.13: SEM instrument equipped at the University of Macau, Macao.

technique for elemental analysis and chemical composition determination, associated with SEM. EDS is based on the emission of a specimen characteristic X-ray. A beam of high-energy charged electrons focuses on the investigated sample. An electron from a higher binding energy electron level falls into the core hole with emitting an X-ray whose energy is the difference between the electron level binding energies. EDS analysis gives a spectrum that displays the peaks correlated to the elemental composition of the investigated sample. At the University of Macau, there is an SEM instrument (ZEISS) collocated with an EDS instrument, as shown in Fig. 3.13.

3.3.3 X-ray diffraction

After Wilhelm Roentgen discovered X rays in 1895, William Henry Bragg and his son William Lawrence Bragg pioneered the determination of crystal structure by X-ray diffraction methods, beginning the history of investigation on the nature of crystal structure [198]. Then in 1912, Max Theodor Felix von Laue proposed a three-dimensional extension of Bragg's Law and obtained the Laue equations, according to which the Laue diffractometer was developed to determine the crystallographic axes of a solid crystal [199]. In crystals, typical interatomic distances are about $\sim$ 2-3 Å, making X-ray an appropriate radiation source for the detection of crystal structures.
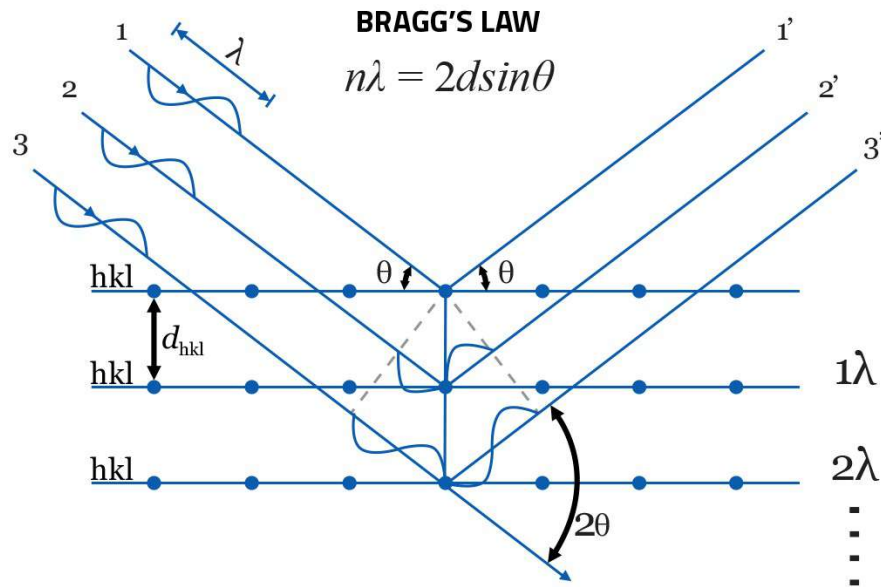
Figure 3.14: Schematic illustration of Bragg's law [202].

So far, the X-ray diffraction technique has been a widely used tool for the structural examination of solids and thin films [200]. To get better resolution and beam intensity of X-ray, synchrotron light sources are developed [201]. In the present part, principles of how to determine the crystal structure with XRPD are elucidated, as well as the determination of crystallographic axes by Laue X-ray diffraction.

3.3.3.1 X-ray powder diffraction

XRPD is the mostly used in-house tool to characterize the crystal structure of crystalline materials. It has so many merits like little time duration, non-destruction on samples, and almost no limitation on the form of samples.

After performing an XRPD, one can obtain a curve of intensity versus 2θ, as the illustrations in sections 3.1 and 3.2. Atomic distances and peak positions are related by the well-known Bragg's Law, whose schematic illustration is displayed in Fig. 3.14. In this process, X-rays that hit on the crystal are elastically scattered by the sets of planes with Miller indices (hkl). The path difference for beam 1 and beam $n + 1$ equals the length of the wavelength multiple n, i.e.

$$n\lambda = 2d_{hkl}sin\theta, \tag{3.1}$$

in which each Miller index can be solved in a certain crystalline material. The other significant parameter for determining the crystal structure is the integrated intensity of diffracted beam, it gives the form [203]

$$I_{hkl} = p_{hkl} A_\theta L_\theta P_\theta K |F_{hkl}|^2 + I_b. \tag{3.2}$$

In this equation, p_{hkl} is the multiplicity factor, which arises from the fact that there will be several equivalent sets of hkl planes, i.e., sharing identical d_{hkl} and F^2 values but with different orientations. For example, in the cubic structure, it has a multiplicity factor of $p_{100} = 6$ (100, $\bar{1}$00, 010, 0$\bar{1}$0, 001, 00$\bar{1}$) and $p_{111} = 8$ (111, 11$\bar{1}$, 1$\bar{1}$1, $\bar{1}$11, 1$\bar{1}\bar{1}$, $\bar{1}$1$\bar{1}$, $\bar{1}\bar{1}$1, $\bar{1}\bar{1}\bar{1}$). A_θ is the angle-dependent absorption, it gives the form of [203]

$$A_\theta = 1 - e^{-2\mu\tau/sin\theta}, \tag{3.3}$$

where τ is the traveling distance through the material, and μ is the absorption coefficient. For a wavelength of 1.54 Å, τ is 61 μm in NaCl and 4 μm in lead. L_θ and P_θ denote the Lorenz factor and polarization factor, respectively. Usually, the Lorenz factor and polarization factor can be expressed in a form of their combination, i.e., Lorenz-polarization factor

$$Lp = \frac{1 + cos^2\theta}{sin2\theta}. \tag{3.4}$$

In general, the effect of the Lp factor is to reduce the intensity at intermediate angles and enhance the intensity in forward and backward directions. K is the scaling factor for the normalization of experiment integrated intensities with absolute calculated intensities. F_{hkl} is the structure factor that determines the amplitude and phase of the diffracted beams

$$F_{hkl} = \sum_j^n g_j t_j f_j e^{[-2\pi i(hx_j + ky_j + lz_j)]}, \tag{3.5}$$

where the sum is over all atoms in the unit cell, x_j, y_j, and z_j are the positional coordi-

70

Figure 3.15: X-ray diffractometer equipped at the University of Macau, Macao.

nates of the j-th atom, g_j is the occupation factor of the j-th atom, t_j is the temperature factor, and f_j is the scattering factor of the j-th atom. F_{hkl} is the vector sum of waves from all atoms within the unit cell, and $(hx_j + ky_j + lz_j)$ is always an integer. A zero diffracted intensity for a group of diffracted beams is called a systematic absence. The structure form factor is the most important parameter of the integrated intensity, and a comparison of the experimental and calculated structure factors is a common aim of X-ray analysis of the crystal structure. In general, one can also simplify the integrated intensity as $I \propto |F_{hkl}|^2$. After summarizing the above terms, the integrated intensity can be expressed as

$$I_{hkl} = (1 - e^{-2\mu\tau/sin\theta})\frac{1 + cos^2\theta}{sin2\theta}K|F_{hkl}|^2 + I_b, \tag{3.6}$$

where I_b represents the intensity coming from the background.

The XRPD data shown in the present thesis was collected by the X-ray diffractometer at the University of Macau, Macao, as shown in Fig. 3.15. To acquire the information on crystal structure, Rietveld analysis of the XRPD data was carried out

71

with the FULLPROF Suite [204]. The pseudo-Voigt function was employed to fit the Bragg peak shape, and it shows a good description of most peaks. The pseudo-Voigt function can be expressed as follows

$$I_{2\theta} = I_{hkl}[\eta L(2\theta - 2\theta_0) + (1 - \eta)G(2\theta - 2\theta_0)], \tag{3.7}$$

where $L(2\theta - 2\theta_0)$ and $G(2\theta - 2\theta_0)$ denote the appropriate normalized Lorentz and Gaussian functions, respectively. Besides, the peak shape factor U, V, and W are composed into one function to fit the full width at half maximum (FWHM), which is described by H. The H parameter gives the form

$$H = U tan^2\theta + V tan\theta + W, \tag{3.8}$$

where U, V, and W are peak-shape parameters that can be refined according to experimental XRPD data. The refinement of all parameters is performed in a least-squares procedure, including lattice parameters, scaling factor, background, peak-width parameters, instrument parameter, preferred orientation, atomic positions, and B factors. After refinement, there are several R values to evaluate the fit: R-structure factor (R_F), R-Bragg factor (R_B), R-pattern factor (R_p), R-weighted pattern factor (R_{wp}), the expected R-value (R_{exp}), the goodness of fit (χ^2) [205].

R-weighted pattern factor:

$$R_{wp} = \left\{ \frac{\sum\limits_i w_i[y_i(\text{obs}) - y_i(\text{calc})]^2}{\sum\limits_i w_i[y_i(\text{obs})]^2} \right\}^{1/2}; \tag{3.9}$$

expected R-value:

$$R_{exp} = \left\{ \frac{N - P}{\sum\limits_i w_i[y_i(\text{obs})]^2} \right\}^{1/2}; \tag{3.10}$$
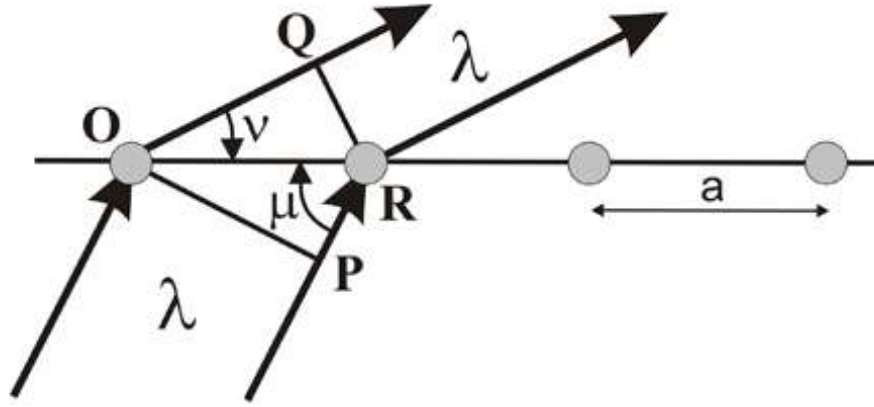
Figure 3.16: Schematic illustration of the Laue equations [206].

the goodness of fit:

$$\chi^2 = \frac{\sum\limits_{i} w_i [y_i(\text{obs}) - y_i(\text{calc})]^2}{N - P} = \frac{R_{\text{wp}}^2}{R_{\text{exp}}^2}, \tag{3.11}$$

where $\sum\limits_{i}$ represents the summation over the N points in the considered range, $w_i = 1/\sigma[y_i(\text{obs})]$ is the weighing factor, $y_i(\text{obs})$ is the observed counts, $y_i(\text{calc})$ is the calculated counts, and P is the number of refined parameters. Although X-ray diffraction has shown a lot of advantages, one disadvantage is that X-ray hardly interacts with light elements, such as hydrogen and oxygen. To determine these light elements one needs to utilize neutron diffraction, which is introduced in section 3.4.

Moreover, when the goal is to refine magnetic structures with neutron diffraction in a magnetic unit cell larger than the crystallographic cell, the unit cell parameters need to be changed accordingly, as well as the coordinates of atoms. The magnetic Bragg peaks are usually distinguished by a precise comparison between neutron powder diffraction patterns below and above the ordering temperature of magnetic moments. And the appropriate magnetic structure is determined with a careful attempt of all permissible magnetic models.

3.3.3.2 X-ray Laue diffraction

To understand the principle of Laue diffraction equations, one just needs to extend the diffraction equation to three-dimensional cases. The Laue equations are equivalent to
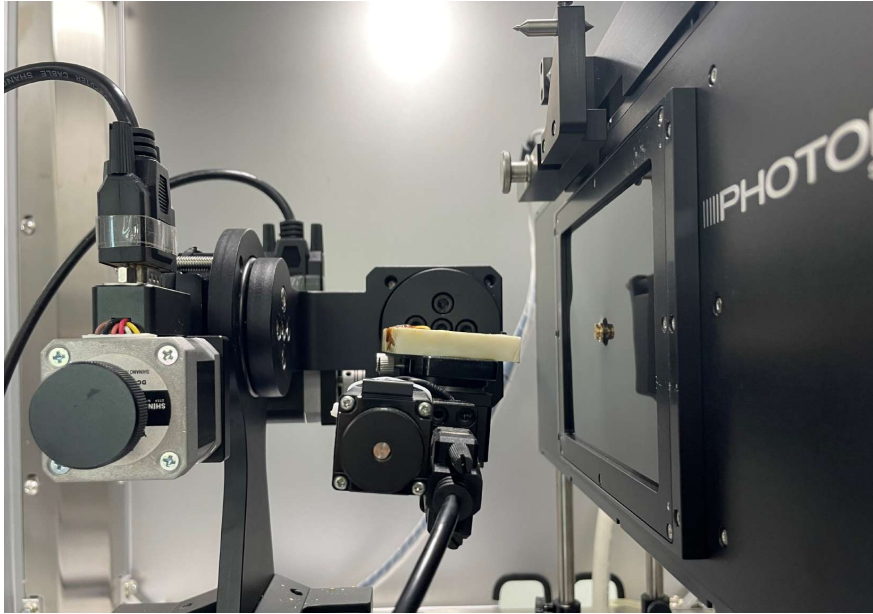
Figure 3.17: X-ray Laue diffractometer equipped at the University of Macau, Macao.

Bragg's law. The only difference is that the Laue equations are vector equations while Bragg's law is in a form that is easier to be solved, but both tell the same things.

Treating a one-dimensional lattice as an example, as shown in Fig. 3.16, OP is the wavefront of a set of plane waves, and it was scattered (diffracted) by the row of atoms and becomes another wavefront QR propagating at the other side. If the scattered wavefront QR can be observed, the two sets of waves are in phase then, the difference between the two paths is then expressed as

$$OQ - PR = l\lambda, \tag{3.12}$$

where the difference of paths between the waves OP and QR should be an integer number (l) multiplying the wavelength (λ). Considering the diffraction angle μ and ν, Eq. 3.12 can be reinterpreted as

$$a(cos\nu - cos\mu) = l\lambda, \tag{3.13}$$

where a represents the interatomic distance. If popularizing the above relations to a three-dimensional case whose lattice parameters are a, b, and c, one then has the same

74
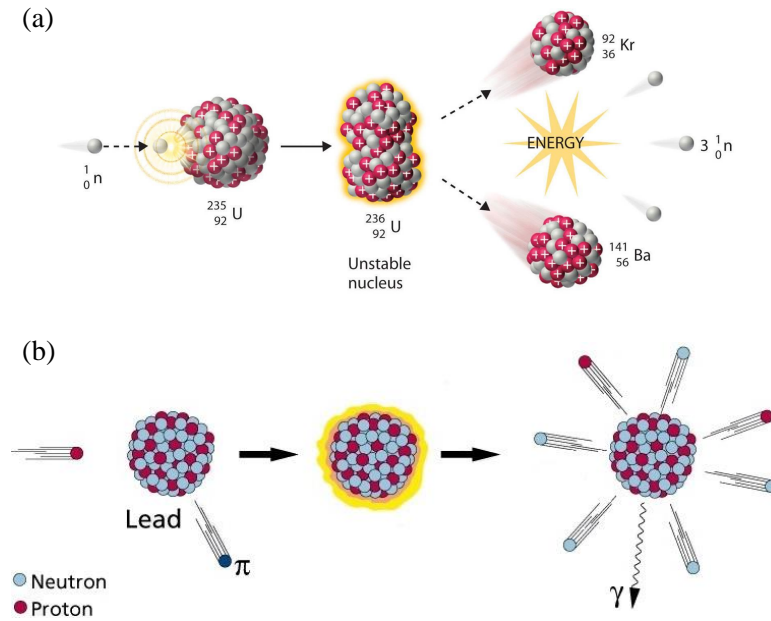
Figure 3.18: Schematic illustration of nuclear fission (a) and spallation (b).

relation as Eq. (3.13) but in three directions

$$a(cos\nu_1 - cos\mu_1) = l\lambda;$$ (3.14)

$$b(cos\nu_2 - cos\mu_2) = m\lambda;$$

$$c(cos\nu_3 - cos\mu_3) = n\lambda;$$

where l, m, and n are all integer numbers, and the above relations are called Laue equations. At the University of Macau, there is one X-ray Laue diffractometer as shown in Fig. 3.17, with which, as-grown crystals could be aligned and mounted in a precisely known crystallographic orientation. This is a prerequisite for single-crystal neutron scattering experiments.

3.4 Neutron scattering techniques

Since the discovery of neutrons by James Chadwick in 1932, people have opened the gate to the new world of atomic nuclei [207]. Neutrons have achieved tremendous development in science, technology, and medicine, and implemented vast applications in the nuclear power industry, boron neutron capture therapy, high energy physics, condensed matter physics, *etc.* As a unique probe, the neutron scattering technique has

Table 3.2: Properties of neutrons, whose β-decay lifetime, mass, charge, spin, magnetic moment, energy, confinement radius, and quark structure are listed below.

Parameters of neutrons	
β-decay lifetime τ	885.9(9) s
mass m	1.675×10^{-27} kg
charge q	0
spin S	$\hbar/2$
magnetic moment μ_n	$\gamma \cdot \mu_N$
energy $\hbar\omega$	$mv^2/2 = \hbar^2 k^2/2m$
confinement radius	0.7 fm
quark structure	udd

($\gamma = 1.91$, $\mu_N = 5 \times 10^{-27}$ J/T)
For "thermal" neutrons (300 K), $\hbar\omega = 25$ meV, $\lambda = 1.8$ Å, $v = 2200$ m/s.

risen to be a powerful tool to study the crystal structure, magnetic structure, elementary excitations, residual stresses, and nanostructure in material science and engineering. In the present section, firstly I introduce the generation of the neutron beam, and the principles of the neutron scattering technique, including elastic neutron scattering (ENS) and inelastic neutron scattering (INS). Then, neutron scattering spectrometers that I have employed in the thesis are elucidated in the following part.

To carry out neutron scattering experiments, one needs a neutron beam from neutron sources, which could provide neutron radiation with various energy and intensities. So far, neutron sources are mainly separated into two types: One is based on a research reactor, which uses U-235 fuel rods. A neutron beam can then be generated from nuclear fission, as shown in Fig. 3.18(a). Usually, energy deposited per useful neutron in a reactor-type neutron source is about ~ 180 MeV, which is much higher than that of a spallation neutron source. Moreover, the resolution could be more easily tailored to experimental demands, except for hot neutrons with which monochromator crystals and choppers are less effective. The other type is the spallation neutron source, which is a new-generation neutron source. It employs a combination of negative-hydrogen-ion linear accelerator and proton synchrotron accelerator, with which protons are accelerated to an energy level of $E \sim$ GeV and hit on target materials (usually
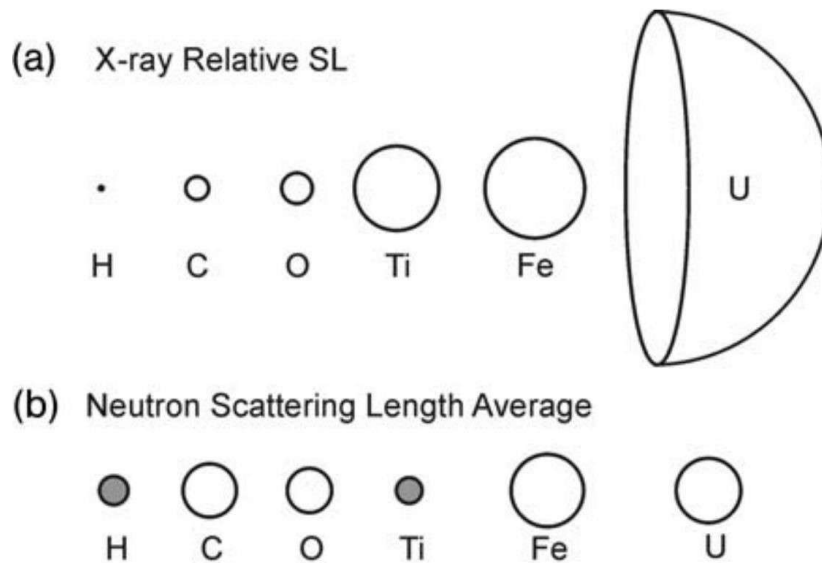
Figure 3.19: Scattering lengths of some typical elements for X-rays (a) and neutrons (b), averaged over the natural isotope distribution [208].

lead, uranium, or tungsten), from which neutrons are generated. A schematic illustration of neutron spallation is depicted in Fig. 3.18(b). As a new-generation neutron source, spallation sources use a pulse-mode neutron beam rather than Maxwellian. Besides, it has a high flux with about $\sim 10^{17}$ n/cm^2·s, which is of two magnitudes higher than that from reactors. At the early stage of both these two mechanisms, i.e., nuclear fission and spallation, fast neutrons with an energy scale of $\sim$ MeV are generated. Such a high energy scale of fast neutrons makes them very hard to interact with nuclei in condensed matter. To enable nuclear power application and neutron science, thermal neutrons are a necessity. Consequently, neutron moderators are employed to produce thermal neutrons with an energy level of ~ 1 eV.

Some of the intrinsic properties of neutrons are listed in Table 3.2, whose detailed illumination based is as follows:

(1) Neutrons directly interact with nuclei rather than electrons, thus, the scattering length seen by neutrons does not depend on nuclear charge numbers. Compared with X-rays and electrons, neutrons are more sensitive to light atoms, such as hydrogen and oxygen. A schematic of the scattering cross section of neutrons/X-rays with different elements is depicted in Fig. 3.19.

(2) Neutrons are electrically neutral, leading to no Coulomb interaction with elec-
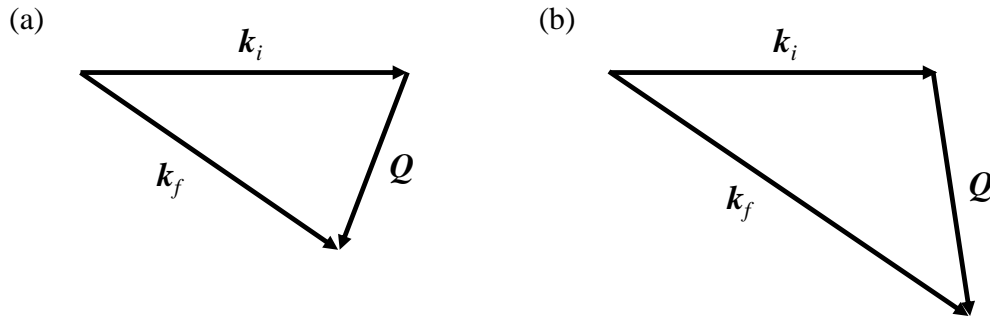
Figure 3.20: Schematic of (a) elastic and (b) inelastic neutron scattering. k_i and k_f denote wave vectors of neutrons of the incident and final states, respectively. Q denotes the wave vector transfer.

trons, making them penetrate much deeper than X-rays and electrons. Hence, neutrons give the properties of bulk, instead of surface merely. As a result, it is easy for neutrons to penetrate types of equipment for sample environments, enabling one to study the properties of a certain material under external fields or at low temperatures.

(3) The energy of neutrons is about a few to dozens of meV, which corresponds to a neutron wavelength of a few angstroms, coinciding with the scale of lattice parameters and most elementary excitations in solids. Besides, since energy and momentum can be distinguished simultaneously, the neutron scattering technique could be the method of choice for disentangling quasi-particle excitations, e.g., spin-wave excitation dispersion, and phonon dispersion.

(4) Neutrons have a spin of $S = 1/2$, enabling a magnetic moment of μ_N. So, neutrons could interact with the magnetic moments of magnetic materials. Such a feature makes neutrons a unique probe for static magnetic structure and spin dynamics.

(5) Neutrons interact weakly with materials, making neutron scattering a non-destructive method for understanding the information of matters. The weak interactions can be approximately described by linear response theory and perturbation theory, enabling a comparison between theoretical and experimental results.

Totally speaking, the above unique properties make neutron scattering technique the method of choice for multiple subjects comprising condensed matter physics, engineering, biological science, batteries, etc.

Depending on whether there is energy gain/loss, neutron scattering could be further

divided into elastic neutron scattering and inelastic neutron scattering, whose geometrical illuminations are depicted in Fig. 3.20(a) and (b), respectively. The relation of momentum transfer is given with

$$Q = k_f - k_i, \tag{3.15}$$

and the energy transfer is

$$E = \hbar\omega_i - \hbar\omega_f = \frac{\hbar k_i^2}{2m} - \frac{\hbar k_f^2}{2m}. \tag{3.16}$$

In the following part, the basic principles of the neutron scattering technique are introduced. Firstly, some terminologies of scattering are defined as follows. Φ is the total number of incident neutrons per cm^2 per second, and σ is the total number of neutrons scattered per second/Φ. In a scattering process, one has a cross-section with the solid angle of $d\Omega = sin\theta d\theta d\varphi$. Then, the differential scattering cross section can be formulated as $d\sigma/d\Omega$ = number of neutrons scattered into $d\Omega$ per second/$\Phi d\Omega$, and the partial differential cross section can be given as $d^2\sigma/d\Omega dE$ = number of neutrons scattered into $d\Omega$ & dE per second.

Usually, the deduction of scattering cross section starts from Fermi's golden rule, that can be given with [209]

$$\frac{d^2\sigma}{d\Omega d\omega} = \left(\frac{m}{2\pi\hbar^2}\right)^2 \frac{k_f}{k_i} \sum_{\lambda_i, \sigma_i} \sum_{\lambda, \sigma} p_{\lambda_i} p_{\sigma_i} \tag{3.17}$$

$$\left| \langle k_f \sigma_f \lambda_f | U(r) | k_i \sigma_i \lambda_i \rangle \right|^2 \cdot \delta(\hbar\omega + E_i - E_f),$$

where wave vector k_i, spin state σ_i, and energy E_i denote the initial state of scattering, i.e., incident neutron. Wave vector k_f, spin state σ_f, and energy E_f denote the final state. p_σ is the probability of polarization. The law of energy conservation in the scattering process is described by the δ function. $U(r)$ is the interacting operator between neutrons and the sample. Considering they are interacted by short-range nuclear forces, which is tiny compared with the typical neutron wavelength, $U(r)$ can be

Figure 3.21: BT-1 beamline at NIST, Gaithersburg [210].

approximated as the Fermi pseudo-potential [209]

$$U(r) = \frac{2\pi\hbar^2}{m} \sum_j b_j \delta(r - R_j), \tag{3.18}$$

where b_j is the nuclear scattering length, R_j is the coordinate of the j-th scattering nucleus in the system, and $(r - R_j)$ represents the distance between the incident neutron and the j-th nucleus. With the Fourier transform, the scattering potential of many bound nuclei can be then given with

$$U(r) = \sum_j b_j e^{iQ \cdot R_j}. \tag{3.19}$$

Depending on elastic or inelastic scattering, Fermi's golden rule can be then simplified.

3.4.1 Neutron powder diffraction

3.4.1.1 Principles of neutron diffraction

Since the structural scattering process in neutron diffraction is similar to that of X-ray diffraction, I start from the principles of magnetic elastic scattering directly. In elastic scattering, the initial state is actually the same as the final state. Consequently, the differential cross section of elastic scattering can be simplified as

$$\left(\frac{d\sigma}{d\Omega}\right)_{coh} = N\frac{(2\pi)^3}{v_0}\sum_{\tau}|F_N(Q)|^2 \cdot \delta(Q-\tau), \tag{3.20}$$

where N is the number of unit cells in the crystalline sample, $F_N(Q)$ is the structure factor, that can then be expressed as

$$F_N(Q) = \sum_{d} b_d e^{iQ\cdot d - W_d(Q)}, \tag{3.21}$$

where b_d and d are the coherent scattering length and the position of a particular nucleus, respectively. W_d is the Debye-Waller factor that accounts for the thermal motions of atoms. After ignoring the thermal fluctuations of atoms, the magnetic Bragg peaks $I_M(Q)$ can be further simplified as follows

$$I_M(Q) \propto p^2 n^2 \mu^2 sin^2\beta|F_N(Q)|^2, \tag{3.22}$$

where μ represents the ordered magnetic moment of the system.

3.4.1.2 High Resolution Powder Diffractometer: BT-1

The BT-1 beamline is a high-resolution neutron powder diffractometer located at the National Institute of Standards and Technology (NIST) [211]. This spectrometer is mainly used for carrying out neutron powder diffraction (NPD) experiments for crystallographic study by the Rietveld method or determination of the magnetic structure of magnetic materials. BT-1 is a 32 detector spectrometer that can perform with three dif-

Figure 3.22: GPPD beamline at CSNS, Dongguan [212].

ferent monochromators and two different incident Soller collimators. Thus, the spectrometer response can be tailored to adjust the needs of the experiment. Moreover, the BT-1 beamline is able to run accompanied by sample environments of heating, cryostat, and magnet, enabling a neutron scattering data collection at a wide temperature range from 0.3 to 2000 K, or under external magnetic fields. While for NPD experiment at room temperature, a six-position sample changer can be utilized to increase efficiency.

3.4.1.3 General neutron diffractometer: GPPD

The general purpose powder diffractometer (GPPD) is a pulsed neutron source based neutron powder diffractometer at the China Spallation Neutron Source (CSNS) [212]. This neutron powder diffractometer provides high-resolution, good-intensity experimental data of NPD, with which one can study crystallographic and magnetic structures. GPPD has multiple bank detectors, and at high-angle detectors, the resolution could be better than 0.2%. Fig. 3.22 shows the GPPD beamline at the target station. So far, the neutron flux on GPPD at the sample position can reach the order of 10^7 n/(s·cm^2).

3.4.2 Inelastic neutron scattering

3.4.2.1 Principles of inelastic neutron scattering

Here the cases of non-polarized inelastic neutron scattering are introduced. With only considering the spin scattering from magnetic identical ions which have localized electrons, Eq. 3.18 can then be expressed as [209]

$$\frac{d^2\sigma}{d\Omega d\omega} = (\gamma r_0)^2 \frac{k_f}{k_i} F^2(Q) e^{-2W(Q)} \sum_{\alpha,\beta} \left(\delta_{\alpha\beta} - \frac{Q_\alpha Q_\beta}{Q^2} \right) S^{\alpha\beta}(Q,\omega), \quad (3.23)$$

where $S^{\alpha\beta}(Q,\omega)$ is the dynamical scattering function, that can be further given with

$$S^{\alpha\beta}(Q,\omega) = \frac{1}{2\pi\hbar} \sum_{j,j'} \int_{-\infty}^{\infty} e^{iQ\cdot(R_j - R_{j'})} \langle S_j^\alpha(0) S_{j'}^\beta(t) \rangle e^{-i\omega t} dt, \quad (3.24)$$

where $\langle S_j^\alpha(0) S_{j'}^\beta(t) \rangle$ is the thermal average of the time-dependent spin operator. It is given by van Hove, meaning the probability that the j'-th ion located at $R_{j'}$ has a certain magnetic moment at the starting time and the j-th ion located at R_j has another moment. What the neutron scattering experiment measures are the Fourier transform of the correlation function, which is also what we need for describing a magnetic system. The van Hove expression is related to the fluctuation-dissipation theorem. Thus, $S^{\alpha\beta}(Q,\omega)$ can then be expressed as

$$S^{\alpha\beta}(Q,\omega) = \frac{N\hbar}{\pi(1 - e^{-\hbar\omega/k_B T})} Im\chi^{\alpha\beta}(Q,\omega), \quad (3.25)$$

where N is the total number of magnetic ions, $Im\chi^{\alpha\beta}(Q,\omega)$ is the imaginary part of the dynamical spin susceptibility. In neutron scattering experiments, neutrons generate a magnetic field $H^\beta(Q,\omega)$, which depends on wave vector and frequency, and probes the response from samples. The response is given with

$$M^\alpha(Q,\omega) = Im\chi^{\alpha\beta}(Q,\omega) H^\beta(Q,\omega). \quad (3.26)$$
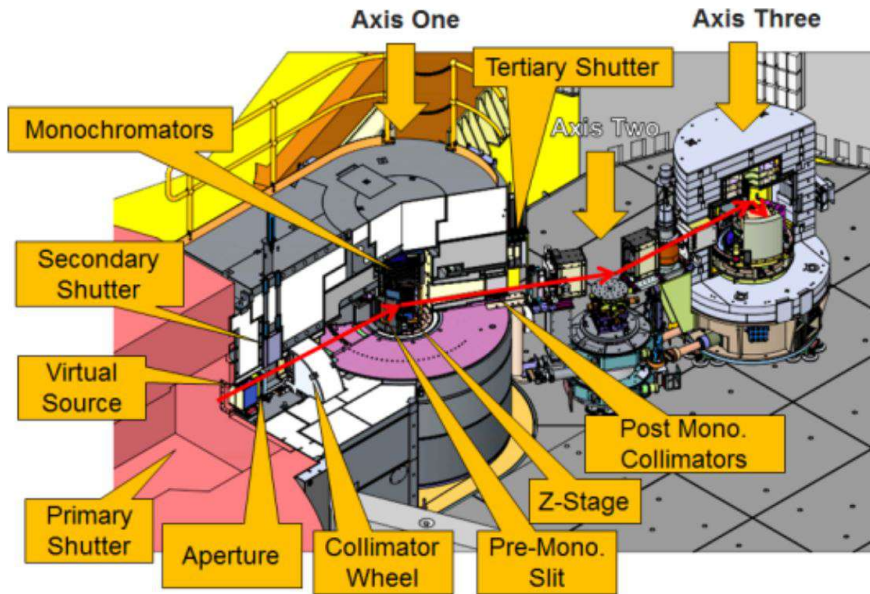
Figure 3.23: The triple-axis cold neutron spectrometer - SIKA at ANSTO, Lucas Height [213].

From above deduction on principles of neutron scattering technique, one may be able to understand that elastic neutron scattering actually tells people where the atoms are (crystal structure and magnetic structure). While inelastic neutron scattering tells people what atoms do (phonon, magnon, and other dynamical properties) in a system.

3.4.2.2 Cold neutron triple-axis spectrometer: SIKA

Triple-axis spectrometer was invented by Bert Brockhouse at Chalk River, and he was awarded the Nobel Prize in physics for his contribution to neutron science. The triple-axis spectrometer named SIKA at Australian Nuclear Science and Technology Organisation (ANSTO) is a new cold-neutron triple-axis spectrometer receiving neutrons from the Australian Light-water reactor, ANSTO [213]. Moreover, SIKA is equipped with a large double-focusing pyrolytic graphite monochromator, a multiblade pyrolytic graphite analyzer, and a multi-detector system. SIKA is an ideal spectrometer to study spin and lattice dynamics, elastic scattering on crystals, novel excitations, *etc.* at low temperatures with external magnetic fields due to its integration of good energy and momentum resolution, low background, high neutron flux, and a wide dynamic range.
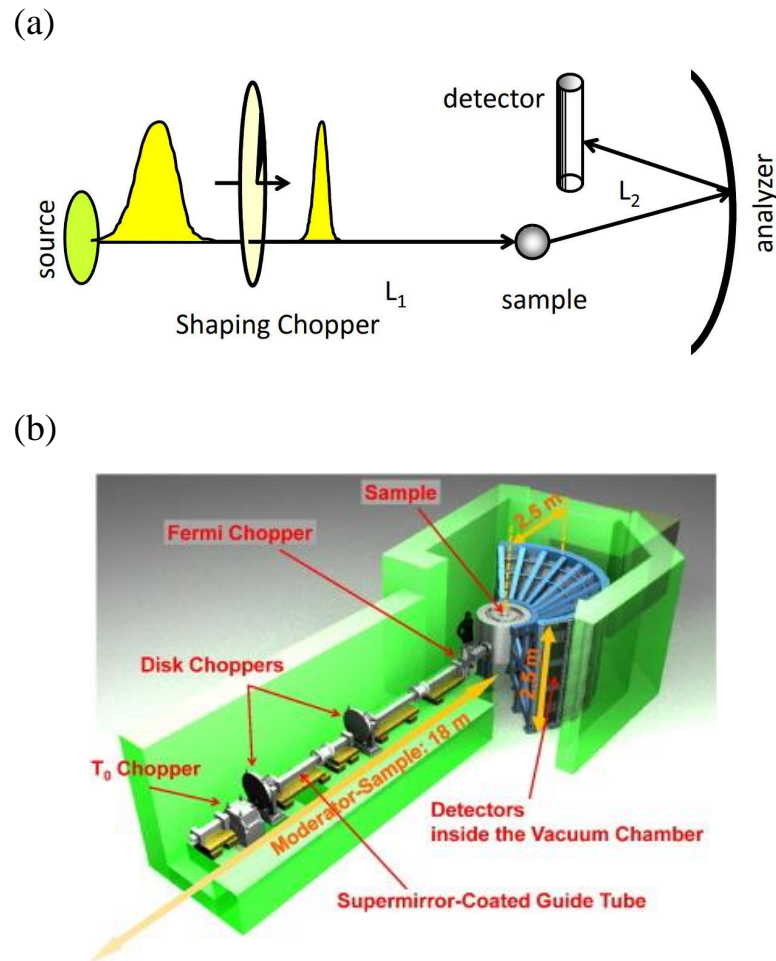
Figure 3.24: (a) Illustration of an inverted geometry instrument with a shaping chopper. (b) Layout of 4SEASONS at J-PARC, with long position sensitive detectors installed in the vacuum tank [214].

3.4.2.3 4D-Space Access Neutron Spectrometer: 4SEASONS

4SEASONS is a high-intensity medium-resolution thermal neutron Fermi-chopper spectrometer at the Materials and Life Science Experimental Facility (MLF), Japan Proton Accelerator Research Complex (J-PARC) [214]. It can efficiently detect even weak inelastic scattering signals coming from novel spin and lattice excitations in solids. The spectrometer can provide a high counting rate accompanied by neutron energy of 300 meV and moderate resolution ($\Delta E/E_i > 5\%$ at $E = 0$ meV). Before experiments, a user could use the $Horace$ code and simulate the E-Q space with varying rotation angles. The Fermi chopper rotates with certain particular frequencies, from which one can choose the most appropriate one according to the experimental requirement. Then,

for a given frequency, a neutron scattering experiment with multi-incident energies can be performed by the repetition rate multiplication method. Compared with traditional chopper spectrometers, 4SEASONS may enable efficient data collections. It is equipped with versatile instrumental technologies, e.g., an elliptic-shaped converging neutron guide, a wide area position sensitive detector comprising long-length (2.5m) ^{3}He tubes are arranged cylindrically in the vacuum scattering chamber.

CHAPTER 4

THEORETICAL MODEL

In the thesis, experiments were carried out to study the basic physical properties consisting of crystal structure, susceptibility, magnetic structure, specific heat, spin dynamics, *etc.* To implement an in-depth understanding of the intrinsic nature of rare-earth chromates, systematic theoretical calculations are significantly necessary. In the present chapter, I elucidate the theoretical methods that I have used in the thesis. In section 4.1, the basic knowledge of density functional theory is expressed, as well as some relative theoretical development on strongly correlated electronic systems. In section 4.2, I introduce linear spin-wave theory (LSWT), which is used to explain spin-wave dispersions collected by INS experiment.

4.1 Density functional theory

First-principles calculations based on density functional theory (DFT) are now an important means of quantum chemical calculation method in the fields of condensed matter, atomic and molecular physics, chemistry, biological macromolecules, *etc.* As an ab-initio calculation method, it merely works according to the principle of quantum mechanics, instead of empirical methods. As long as the basic parameters of the atomic information and lattice structure are inputted, DFT calculations are able to give the intrinsic properties of a certain system, e.g. electronic structure, magnetic moments, total energy of the system, and dielectric behaviors. Although sometimes the calculation results by DFT may not agree perfectly with experimental results, it is admitted that the DFT method is a significant route to provide some key physical clues, helping one understand the intrinsic nature of macroscopic phenomena

However, since the DFT method treats the electrons as submerging in a "sea" of electrons, i.e., mean-field approximation, which unfortunately underestimates the exchange interaction between electrons. A smaller band gap is then given by DFT cal-

culation, especially in strongly correlated electronic systems or RETMO compounds. To solve such issues, semi-empirical methods are proposed to compensate the on-site Coulomb interaction, i.e., DFT+U approach, in systems where localized $3d/4f$ orbitals are embedded in an elongated s-p state.

In the present section, an introduction to the DFT method is expressed by starting from the application of quantum mechanics on many-body real materials. Firstly, the Born-Oppenheimer approximation is introduced, then the Hartree-Fock method which uses the self-consistent method is included. Later, the concept of treating electrons as charge density is elucidated starting from the Thomas-Fermi model, to Hohenberg-Kohn theorems, and finally to Kohn-Shan equations. Moreover, Jacob's ladder is elucidated for one to understand the evolution of exchange-correlation functionals. I then elucidate the principle of the DFT+U approach, which is a modified model for strongly correlated electronic systems. It is worth mentioning that the DFT method is one of the most outstanding achievements in the theoretical chemistry area, and amounts of branches have been developed based on the DFT. The present part just aims to exhibit a simple introduction to the development of the DFT by omitting detailed theoretical deductions and branched models on certain specific issues.

4.1.1 Born-Oppenheimer approximation

In the early twenty century, it was well found that classical mechanics displays poor descriptions of the kinetics of microscopic particles. That centuries-old problem appeared less overwhelming after the gradual building of quantum mechanics by a series of physicists, including Max Planck, Niels Bohr, Albert Einstein, Louis de Broglie, Werner Heisenberg, Erwin Schrödinger, Paul Dirac, Wolfgang E. Pauli, Enrico Fermi, *etc.* Then, the kinetics of a microscopic particle can be precisely given by the Schrödinger equations

$$\hat{H}|\Psi\rangle = i\hbar\frac{\partial}{\partial t}|\Psi\rangle, \tag{4.1}$$

88

with separating the time variable, the time-independent (stationary) Schrödinger equation then reads

$$\hat{H}|\Psi\rangle = E|\Psi\rangle, \tag{4.2}$$

where E is the eigenvalue, $\hat{H}$ is the Hamiltonian of the system, and $|\Psi\rangle$ is the eigenfunction. In this way, $|\Psi\rangle$ contains all kinetic information of a microscopic particle. Nevertheless, there are no accurate solutions for real systems except the hydrogen atom up to now. And there exist Avogadro number-magnitude atoms in a real solid, making the solution of its Schrödinger equation an absolutely unsolvable puzzle. To simplify the question, we need to treat the real system with a series of reasonable approximations.

To separate the electronic motions and the ionic motions, the Born-Oppenheimer approximation (BOA) is proposed [215]. In a system including atoms and electrons, the time-independent Schrödinger equation reads

$$\hat{H}|\Psi(r, R)\rangle = (T_e + T_N + V_{ee} + V_{NN} + V_{eN})|\Psi(r, R)\rangle = E|\Psi(r, R)\rangle, \tag{4.3}$$

where T_e and T_N denote the kinetic energy terms of electrons and nuclei, respectively. V_{ee}, V_{NN}, and V_{eN} denote the terms of electron-electron, nucleus-nucleus, and electron-nucleus interactions, respectively. $|\Psi(r, R)\rangle$ denotes the vibration-electron wavefunction which depends on electronic coordinate r and nuclear coordinate R. In an atomic unit, the Hamiltonian is expressed in detail as

$$\hat{H} = -\sum_i \frac{1}{2}\nabla_i^2 - \sum_p \frac{1}{2M_p}\nabla_p^2 + \sum_{j<i} \frac{1}{r_{ij}} + \sum_{p<q} \frac{Z_p Z_q}{r_{pq}} - \sum_{p,i} \frac{Z_p}{r_{pi}}, \tag{4.4}$$

where p and q mark different atomic nuclei, i and j mark different electrons, M and m denote nuclear mass and electronic mass, respectively.

Since the mass ratio between nuclei and electrons is larger than 1836 (m_p/m_e), electrons could be treated adiabatically following the nuclear motion in a dynamical

sense, and the electrons adopt instantaneously to the motion of nuclei without needing a finite relaxation time [216]. Therefore, the adiabatic separation between electrons and nuclei acts as a reasonable approximation. $|\Psi(r,R)\rangle$ in Eq. (4.3) can be then expressed as the linear product between the wavefunctions of electrons and nuclei

$$|\Psi(r,R)\rangle = |\Psi_e(r,R)\rangle \otimes |\Psi_N(R)\rangle, \qquad (4.5)$$

the Hamiltonian of nuclei can be ignored since the kinetic energy of nuclei T_N is smaller than that of T_e with a factor of M/m. The repulsion potential between nuclei can be treated as a constant, which only affects the eigenvalue rather than affecting the eigenfunction. Then the Hamiltonian of electrons merely contains the kinetic energy term and potential term of electrons. In the atomic unit, it could be written as

$$\hat{H}_e = T_e + V_{ee} + V_{eN} = -\sum_i \frac{1}{2}\nabla_i^2 + \sum_{j<i} \frac{1}{r_{ij}} - \sum_{p,i} \frac{Z_p}{r_{pi}}, \qquad (4.6)$$

the repulsion energy between nuclei can be introduced after solving the kinetics of electrons.

4.1.2 Hartree-Fock method

With the BOA, next question is to solve electronic wavefunctions in many-electron system. Due to the existence of electron-electron interactions, it will be complicated to solve the many-body question of electrons. In 1927, Douglas Hartree proposed that the total electronic wavefunction of an N-electron system could be expressed as the product of each electronic wavefunction by treating $V_{ee} = 0$ [217]. This is the so-called Hartree Product, which reads

$$|\Psi_{\text{HP}}(r_1, r_2, ..., r_N)\rangle = |\phi(r_1)\phi(r_2)...\phi_N(r_N)\rangle. \qquad (4.7)$$

It is admitted that omitting the electron-electron interactions is not a good approximation, but people need to start from something. There is one apparent drawback

of the above form: the principle of antisymmetry of the wavefunction is neglected. Since electrons are Fermions, spin is also supposed to be considered rather than only containing the space coordinate. To overcome this issue, John C. Slater proposed the Slater determinant to describe the anti-symmetry nature of electronic wavefunctions in 1929 [218]. It is worth mentioning that the determinant form of one-particle orbitals was firstly used by Heisenberg and Dirac in 1926. Since spin is introduced, the coordinate needs to be changed as the form of space-spin generic coordinate, i.e., $q = \{r, \omega\}$, where ω is the spin coordinate. To make it be distinguished easily, the notation is changed from the spatial orbital $\phi(r)$ to a spin orbital $\chi(q)$. The wavefunction of an N-electron system in Slater determinant reads

$$|\Psi\rangle = \frac{1}{\sqrt{N!}} \begin{vmatrix} \chi_1(q_1) & \chi_2(q_1) & \cdots & \chi_N(q_1) \\ \chi_1(q_2) & \chi_2(q_2) & \cdots & \chi_N(q_2) \\ \vdots & \vdots & \ddots & \vdots \\ \chi_1(q_N) & \chi_2(q_N) & \cdots & \chi_N(q_N) \end{vmatrix} = |\chi_1, \chi_2, \cdots, \chi_N\rangle \quad (4.8)$$

in which electrons are indistinguishable. According to the rule of linear algebra, a minus would be generated if interchanging two electronic coordinates q_i and q_j. Besides, the determinant would be equal to zero if putting two electrons in the same orbital simultaneously. Such a rule just behaves identical to the Pauli exclusion principle, making the Slater determinant an ideal form for electronic wavefunctions.

With wavefunctions of the Hartree-Fock theory, the next work is to examine the Hamiltonian [219, 220]. The Hamiltonian expresses an independent particle model, which is indeed a simpler model compared with Kohn-Sham's DFT model, but it provides a good beginning to develop the method of self-consistent field equation. In this part, I will focus on the key point of Hartree-Fock theory with omitting some complex mathematical deductions of the variational method on the Lagrange Function.

Before everything, the single-electron operator can be defined as follows

$$h(i) = -\frac{1}{2}\nabla_i^2 - \sum_p \frac{Z_p}{r_{pi}}, \quad (4.9)$$

and the two-electron operator $v(i, j)$ reads

$$v(i, j) = \frac{1}{r_{ij}}, \tag{4.10}$$

with ignoring the constant term of nuclei-nuclei interaction, the electronic Hamiltonian in Eq. (4.6) can be then expressed as

$$\hat{H}_e = h(i) + v(i, j), \tag{4.11}$$

With the Hartree-Fock wavefunction of Slater determinant, the energy expectation in the framework of quantum mechanics reads

$$E_e = \langle \Psi | \hat{H}_e | \Psi \rangle, \tag{4.12}$$

where a better Ψ can be obtained by optimizing the parameters to minimize the energy expectation, and the true molecular orbital could be found in such a way. Then, the molecular orbitals could be mathematically acquired by a linear combination of a series of basis sets (also called basis functions). Slater-type orbitals (STO) and Gaussian-type orbitals (GTOs) are two varieties of basis functions that are often utilized as atomic orbital basis sets. This is the well-known linear combination of atomic orbital (LCAO) method.

In terms of electronic integrals, the Hartree-Fock energy of E_e can be then re-written as

$$E_{\text{HF}} = \sum_i \langle i | h | i \rangle + \frac{1}{2} \sum_{ij} ([ii|jj] - [ij|ji]), \tag{4.13}$$

here the single-electron integral is defined as

$$\langle i | j \rangle = \int dq_1 \chi_i^*(q_1) \chi_j(q_1), \tag{4.14}$$

and the two-electron integral is defined as

$$[ij|kl] = \int dq_1 dq_2 \chi_i^*(q_1)\chi_j(q_1)\frac{1}{r_{12}}\chi_k^*(q_2)\chi_l(q_2). \tag{4.15}$$

The spin orbitals which minimize the energy could be given by the Hartree-Fock method. Here, it is assumed that the orbitals of χ are orthogonal, i.e. $\langle i|j\rangle = \delta_{ij}$. With the variational procedure, Lagrange's method of undetermined multipliers is utilized to solve the extremum. A functional L is then defined as

$$L[\{\chi_i\}] = E_{\mathrm{HF}}[\{\chi_i\}] - \sum_{ij} \epsilon_{ij}(\langle i|j\rangle - \delta_{ij}), \tag{4.16}$$

where ϵ_{ij} denotes undetermined Lagrange multipliers, $\langle i|j\rangle$ is defined in the above text. With the variational method, it could be then set as

$$\delta L = \delta E_0[\{\chi_i\}] - \sum_{ij} \epsilon_{ij}\delta\langle i|j\rangle = 0, \tag{4.17}$$

The detailed algebraic process of the variational deduction is omitted, after that one can arrive at the Hartree-Fock equations:

$$h(q_1)\chi_i(q_1) + \sum_{j\neq i} \left[\int dq_2 |\chi_j(q_2)|^2 r_{12}^{-1} \right] \chi_i(q_1) \tag{4.18}$$

$$-\sum_{j\neq i} \left[\int dq_2 \chi_j^*(q_2)\chi_i(q_2)r_{12}^{-1} \right] \chi_j(q_1) = \epsilon_i \chi_i(q_1),$$

where ϵ_i is the energy eigenvalue of the corresponding orbital χ_i. The first term in square brackets in Eq. (4.18) denotes the Coulomb interaction between the orbital χ_i and the charge distribution of other electrons. The Coulomb term in the Hartree-Fock equations is a mean-field model, it reads

$$J_j(q_1) = \int dq_2 |\chi_j(q_2)|^2 r_{12}^{-1}, \tag{4.19}$$

The second term in square brackets in Eq. (4.18) is the exchange term, which is a

quantum mechanical effect between identical particles and does not have a classical homology. It has a similar mathematical expression as the Coulomb term, but spin orbitals of χ_i and χ_j are interchanged with each other. The exchange term reads

$$\sum_{j\neq i}\left[\int dq_2\chi_j^*(q_2)\chi_i(q_2)r_{12}^{-1}\right]\chi_j(q_1) \tag{4.20}$$

after acting on an arbitrary spin orbital χ_i, the exchange term can be re-written as

$$K_j(q_1)\chi_i(q_1) = \left[dq_2\chi_j^*(q_2)r_{12}^{-1}\chi_i(q_2)\right]\chi_j(q_1), \tag{4.21}$$

With the above operators of the Coulomb term and the exchange term, the Hartree-Fock equations become

$$\left[h(q_1) + \sum_{j\neq i}J_j(q_1) - \sum_{j\neq i}K_j(q_1)\right]\chi_i(q_1) = \epsilon_i\chi_i(q_1), \tag{4.22}$$

where it is easy to prove that the Coulomb term and the exchange term have following relations

$$J_i(q_1)\chi_i(q_1) - K_i(q_1)\chi_i(q_1) = 0, \tag{4.23}$$

Hence, the limitation of the summation in Eq. (4.22) could be canceled, and the Hartree-Fock equations become

$$\left[h(q_1) + \sum_{j}J_j(q_1) - \sum_{j}K_j(q_1)\right]\chi_i(q_1) = \epsilon_i\chi_i(q_1), \tag{4.24}$$

where we have the Fock operator

$$f(q_1) = h(q_1) + \sum_{j}J_j(q_1) - \sum_{j}K_j(q_1), \tag{4.25}$$

with which the Hartree-Fock equations further read

$$f(q_1)\chi_i(q_1) = \epsilon_i\chi_i(q_1), \tag{4.26}$$

which has the formation of an eigenvalue equation, but one needs to be aware that both J and K operators depend on molecular orbitals. Therefore, the actual Hartree-Fock equations are quite complex, and there is no accurate analytic solution to the equations. To solve the equations one can only take the iteration method, i.e., Hartree-Fock self-consistent-field (HFSCF) equations. The HFSCF method has a very profound effect on the progress of quantum chemistry computation, is also the foundation of semi-empirical quantum chemistry method and many-body perturbation method.

In the usual process, the i-th molecular orbital can be expanded by atomic orbital basis function $\tilde{\chi}$ as follows

$$\chi_i = \sum_{m=1}^{K} C_{mi}\tilde{\chi}_m, \tag{4.27}$$

where K is the number of basis functions of the basis set, making C_{mi} a K-dimension vector. The matrix element can be expressed as

$$S_{mn} = \int dq_1 \tilde{\chi}_m^*(q_1)\tilde{\chi}_n(q_1), \tag{4.28}$$

$$F_{mn} = \int dq_1 \tilde{\chi}_m^*(q_1)f(q_1)\tilde{\chi}_n(q_1), \tag{4.29}$$

One then has the matrix form, i.e., the Hartree-Fock-Roothaan equations

$$\sum_n F_{mn}C_{ni} = \epsilon_i \sum_n S_{mn}C_{ni}, \tag{4.30}$$

which can be further simplified as

$$\mathbf{FC} = \epsilon\mathbf{SC}, \tag{4.31}$$

where ϵ is a diagonal matrix of the energy eigenvalues ϵ_i. if comparing with an eigen-

value equation, one may find there exists one more term, i.e., the overlap matrix **S**. To make **S** vanish one could perform a transformation to realize an orthogonal basis.

The Hartree-Fock equations can be solved numerically (exact Hartree-Fock), or they can be solved in the space spanned by a set of basis functions (Hartree-Fock-Roothan equations). In either case, one needs to note that the solutions depend on the orbitals. Hence, we need to guess some initial orbital and then optimize the input orbital according to the deviation from the input circle by circle. For this reason, Hartree-Fock is called a self-consistent-field (SCF) approach. From the above deduction, one may understand that the correlation term is abandoned in the Hartree-Fock theory, and there exist $3N$ variables in an N-electron system, it is complex work to solve it precisely. Nonetheless, with suitable hybrid exchange-correlation functional, the Hartree-Fock method is widely utilized in atomic and molecular physics and provides a good description.

4.1.3 The Hohenberg–Kohn theorem and the Kohn-Sham equations

Before discussing the main theory of density functional theory, it is necessary to talk about the Thomas-Fermi (TF) model, which treats electronic density ρ as a variable. The TF model is formulated by Llewellyn Thomas and Enrico Fermi in 1927 [221, 222]. With including the classical expressions of the electron-electron and electron-nucleus interactions, the total energy of the TF model can be written as

$$F^{\text{TF}}[\rho] = T^{\text{TF}}[\rho] + V_{ee}[\rho] + V_{eN}[\rho], \tag{4.32}$$

where the total kinetic energy of all electrons of the system can be given with

$$T^{\text{TF}}[\rho] = \frac{3}{10}(3\pi^2)^{\frac{2}{3}} \int \rho^{\frac{3}{5}}(r) dr^3. \tag{4.33}$$

The TF model has many drawbacks, the most notorious one is that it treats electrons as uniform electronic gas. However, it is admitted that the TF model is usually deemed as the precursor of the density functional theory.

96

The Hohenberg–Kohn (HK) theorems define the theoretical basement of the density functional theory [223]. The first HK theorem, i.e., HK theorem - I defines:

The expectation of any physical observable of a many-electron system is a unique functional of electron density ρ.

And the HK theorem - II defines:

With the variational method, the precise ground state density ρ_0 is the one that minimizes the total energy E_0.

The HK theorem - I can be proved as follows [223]:

Firstly, the Hamiltonian of a many-body system can be given as

$$\hat{H} = T + V_{ee} + V_{\text{ext}}, \tag{4.34}$$

in which V_{ext} represents the external potential of the system, and the electronic Hamiltonian is

$$F = T + V_{ee}, \tag{4.35}$$

F is the same for all N-electron systems, and what differs is the external potential V_{ext}. The energy functional $E[\rho]$ can then be expressed as

$$E[\rho(r)] = \int \rho(r) V_{\text{ext}} dr + F[\rho(r)]. \tag{4.36}$$

If we assume there exist two distinctive external potentials of V_{ext} and V'_{ext}, giving rise to the same electronic density $\rho_0(r)$. Meanwhile, two different wavefunctions Ψ and Ψ' are given by the Hamiltonian $\hat{H}$ and $\hat{H}'$. Then, with the variational method and Eq. (4.35), one can have the following deduction

$$E_0 < \langle \Psi' | \hat{H} | \Psi' \rangle = \langle \Psi' | \hat{H}' | \Psi' \rangle + \langle \Psi' | \hat{H} - \hat{H}' | \Psi' \rangle \tag{4.37}$$

$$= E'_0 + \int \rho_0(r)(V_{\text{ext}} - V'_{\text{ext}}) dr \tag{4.38}$$

where E_0 and E'_0 are the groundstate energies of $\hat{H}$ and $\hat{H}'$, respectively. With the

above relation, one then has

$$E_0 + E_0' < E_0' + E_0, \tag{4.39}$$

which is evidently a paradox. Hence, a certain external potential is exclusively determined by the ground state electron density.

The proof of HK theorem - II is as follows [223]:

Since $\rho(r)$ determines V_{ext}, N and V_{ext} then determine $\hat{H}$ and hence Ψ. This implies both Ψ and the expectation of $\hat{F}$ are functionals of $\rho(r)$, which can be expressed as

$$F[\rho(r)] = \langle \psi | \hat{F} | \psi \rangle. \tag{4.40}$$

With an external potential V_{ext}, the ground state electronic density is then uniquely determined, and the corresponding energy functional is $E_V[\rho(r)]$. Then for another electronic density $\rho(r)'$

$$E_V[\rho(r)'] = \int n'(r) V_{\text{ext}} dr + F[\rho(r)'], \tag{4.41}$$

with the variational theorem, one has

$$\langle \psi' | \hat{F} | \psi' \rangle + \langle \psi' | V_{\text{ext}} | \psi' \rangle > \langle \psi | \hat{F} | \psi \rangle + \langle \psi | V_{\text{ext}} | \psi \rangle, \tag{4.42}$$

in which ψ is the wavefucntion of the groundstate electronic density $\rho(r)$, Eq. (4.42) is thus expressed as

$$\int n'(r) V_{\text{ext}} dr + F[\rho(r)'] > \int n(r) V_{\text{ext}} dr + F[\rho(r)], \tag{4.43}$$

then HK theorem - II is acquired as

$$E_V[\rho(r)'] > E_V[\rho(r)]. \tag{4.44}$$

98

The HK theorems give the basis of density functional theory. Nevertheless, to calculate a real system, one still needs an operable method. One year later in 1965, the well-known Kohn-Sham equations are developed [224].

The single-electron Kohn-Sham equations were developed by Walter Kohn and his postdoctor Lu Jeu Sham [224]. To focus on the meaning and operations of the Kohn-Sham equations, I omit the variational deduction and directly go to the Kohn-Sham equations, which can be expressed as [225]

$$\left[\frac{\hbar^2}{2m}\nabla^2 + V_{\text{ext}}(r) + e^2 \int \frac{n(r')}{|r-r'|} + \frac{\delta E_{\text{xc}}(r)}{\delta n(r)}\right]\psi_i(r) = \epsilon_i\psi_i(r), \qquad (4.45)$$

where the first term is the kinetic energy term of a single electron, the second term denotes the interactions between the single electron and nuclei, and the third term is the Hartree potential, which represents the Coulomb repulsion between the single electron and all electrons. While the final term is the exchange-correlation energy. In this way, the first three items can be precisely solved, and the exchange-correlation term contains all of the dirty things, i.e., unknown interacting terms. Eq. (4.45) can then be simplified as

$$\left[\frac{\hbar^2}{2m}\nabla^2 + V_{\text{ext}} + V_{\text{H}} + V_{\text{xc}}\right]\psi_i(r) = \epsilon_i\psi_i(r). \qquad (4.46)$$

Another merit of the Kohn-Sham equations is that people do not need to deal with the wavefunction with $3N$ variables of the Schrödinger equations. As an alternative, one just needs to get the exact electronic density functional $\rho(r)$, reducing the calculation workload to large extent. To understand the wavefunction of a many-body system, an iteration algorithm works as follows:

(1) Inputting an original, and tentative charge density $\rho(r)$;

(2) Solving the Kohn-Sham equations determined by the tentative charge density $\rho(r)$, then acquiring the single-electron wavefunction $\psi_i(r)$;

(3) Calculating the charge density determined by the Kohn-Sham single-electron wavefunction, i.e. $\rho_{\text{KS}}(r) = 2\sum_i \psi_i^*(r)\psi_i(r)$;

(4) Comparing the obtained charge density $\rho_{\text{KS}}(r)$ with the input charge density $\rho(r)$ in step (1), if their deviation is accepted within a specified accuracy, $\rho_{\text{KS}}(r)$ is then the ground state charge density, which can then be used to calculate the total energy. And if not, the tentative charge density needs to be corrected somehow.

The above procedures define how the self-consistent method of DFT works. However, the difficulty in the process is how to determine the E_{xc}. At the early stage of the DFT theory, the E_{xc} of local density approximation (LDA) was also constructed. It was so named because it uses an elementary volume with uniform density to describe the E_{xc}. After the LDA, a general gradient approximation (GGA) was then developed. Compared with the LDA, the GGA comprises more physical information. The subsequent development of the E_{xc} is just like a clamber on a ladder. In this process, more things are put into the higher-level E_{xc}. And this is the so-called Jacob's ladder on exchange-correlation energy [226], whose destiny is to get close to the chemical accuracy, as plotted in Fig. 4.1.

4.2 Linear spin-wave model

In this section, a spin model is established. Not only Heisenberg exchange interaction but also DM interaction and single-ion anisotropic terms are included to explain the spin-wave dispersions in a canted antiferromagnet. Under a rotating frame, the Holstein-Primakoff (HP) transformation is used to bosonize the spin Hamiltonian. After that, a Fourier transformation is performed to transform the Hamiltonian from real space to momentum space. The Bogoliubov transformation is utilized to diagonalize the spin Hamiltonian, and corresponding coefficients and eigenvalues are then deduced.

4.2.1   Spin Model

J. P. Van der Ziel *et. al.* has done a theoretical analysis by an approximation that ignores spin canting [227]. However, such a big approximation neglects the important DM interaction and can never describe the INS results of such a non-collinear
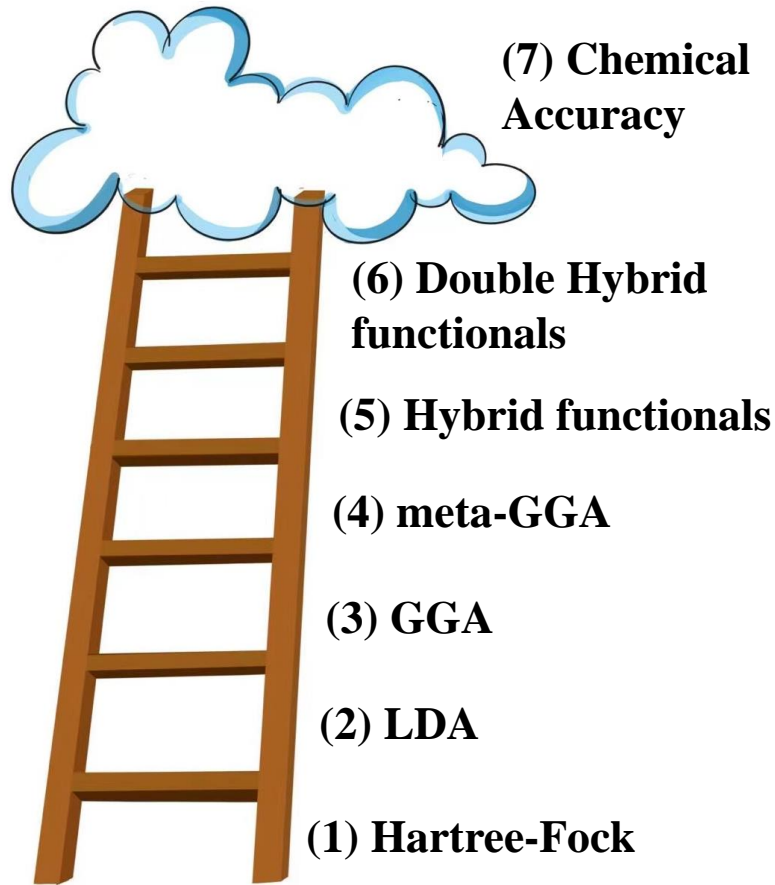
Figure 4.1: The Jacob's ladder of exchange-correlation functionals of density functional theory.

AFM spin system perfectly. Hence, DM interaction is required to be introduced in the Heisenberg model, considering the canted spins. Taking a linear spin-wave approximation, the magnon dispersions are obtained. By fitting the INS data, it is able to extract parameters of the magnetic exchange interaction and antisymmetric exchange interaction, i.e., DM interaction.

Before writing down a detailed Hamiltonian, it is convenient to transform the spin components from a laboratory frame $\mathbf{S} = (S^a, S^b, S^c)$ into a rotating frame [228, 229]. To avoid ambiguity, the spins along the $+c$ direction of the $Pnma$ space group are marked with spin up $\uparrow$, and those along the $-c$ direction are marked with spin down $\downarrow$.

For a Cr^{3+} ion with spin up, the transformation of the spin operator is

$$
\mathbf{S}_\uparrow = \begin{pmatrix} 1 & 0 & 0 \\ 0 & 1 & 0 \\ 0 & 0 & 1 \end{pmatrix} \begin{pmatrix} 1 & 0 & 0 \\ 0 & \cos\phi & \sin\phi \\ 0 & \sin\phi & \cos\phi \end{pmatrix} \begin{pmatrix} S^x \\ S^y \\ S^z \end{pmatrix},
\qquad (4.47)
$$

while for a spin down Cr^{3+} ion, we have

$$
\mathbf{S}_\downarrow = \begin{pmatrix} -1 & 0 & 0 \\ 0 & 1 & 0 \\ 0 & 0 & -1 \end{pmatrix} \begin{pmatrix} 1 & 0 & 0 \\ 0 & \cos\phi & \sin\phi \\ 0 & \sin\phi & \cos\phi \end{pmatrix} \begin{pmatrix} S^x \\ S^y \\ S^z \end{pmatrix},
\qquad (4.48)
$$

where $\phi = \arccos(0.979) \approx 11.8°$ is the canting angle of spin moments in $YCrO_3$. It is noted that (S^x, S^y, S^z) represents a coordinate system in which spins are parallel to the z-axis but $\mathbf{S}_{\uparrow,\downarrow} = (S^a, S^b, S^c)$ is written in laboratory coordinate. This rotation transformation is nothing but to make it clear to calculate in the rectangular coordinate system.

4.2.2 Heisenberg model

Having established the rotation transformation of spin operators, an AFM Heisenberg model is then built, including DM interactions, which are generally used in non-collinear AFM spin system. The Hamiltonian is described as

$$
\hat{H} = \sum_{i,j} J_{ij}\mathbf{S}_i \cdot \mathbf{S}_j + \hat{H}_{\text{DM}} - J_s \sum_i (S_i^z)^2.
\qquad (4.49)
$$

The first term is a general AFM Heisenberg model with five defined exchange interaction parameters, i.e., J_1–J_5. Usually, it is supposed to anticipate that $J_1, J_2 > 0$ for antiparallel spins while $J_3, J_4, J_5 < 0$ for parallel spins. The third term is the single-ion Ising anisotropy term [230], which leads to a spin gap in the spin spectrum, noting that $(S_i^z)^2$ is used instead of $(S_i^c)^2$ for convenience.

The DM interactions, which connect two spins between a third O^{2-} ion and will

destroy the time-inversion symmetry to lead to a canting structure, as given by [106]

$$\hat{H}_{\mathrm{DM}} = -\sum_{\langle i,j \rangle} \mathbf{D}_{ij} \cdot (\mathbf{S}_i \times \mathbf{S}_j), \tag{4.50}$$

where $\langle i,j \rangle$ refers to nearest-neighbor interaction.

By analysis of symmetry, the vector $\mathbf{D}_{ij}$ can be immediately distributed into two types, $\mathbf{D}_{1ij}$ denotes the interactions within the ac-plane and $\mathbf{D}_{2ij}$ denotes the bonds on the b-axis. According to the symmetry of the YCrO$_3$ compound ($Pnma$, No. 62), it is easy to find that all of the $\mathbf{D}_{1ij}$ have the same absolute value $|D_1| = |\mathbf{D}_{1ij}|$, and all of the $\mathbf{D}_{2ij}$ also have the same absolute value $|D_2| = |\mathbf{D}_{2ij}|$. Thus, the DM interactions can be simplified as two parameters. Since the DM interactions have been separated into two parts, they can be expressed as

$$\hat{H}_{\mathrm{DM}} = -\sum_{\langle i,j \rangle \in ac} \mathbf{D}_{1ij} \cdot (\mathbf{S}_i \times \mathbf{S}_j) - \sum_{\langle i,j \rangle \in b} \mathbf{D}_{2ij} \cdot (\mathbf{S}_i \times \mathbf{S}_j). \tag{4.51}$$

The next work is to get the directions of $\mathbf{D}_{1ij}$ and $\mathbf{D}_{2ij}$. In the theory of antisymmetric exchange, the orientations of $\mathbf{D}_{ij}$ are obtained by [108, 231]

$$\mathbf{D}_{ij} \propto \mathbf{r}_i \times \mathbf{r}_j, \tag{4.52}$$

where $\mathbf{r}_i$ and $\mathbf{r}_j$ are the vectors from a non-magnetic ion (O^{2-}) to the two magnetic ions (Cr^{3+}) that create an antisymmetric exchange interaction via this non-magnetic ion. To avoid ambiguity, it is defined that

$$\mathbf{D}_{\alpha ij} = D_\alpha \frac{\mathbf{r}_{i\uparrow} \times \mathbf{r}_{j\downarrow}}{|\mathbf{r}_{i\uparrow} \times \mathbf{r}_{j\downarrow}|}, \tag{4.53}$$

where $\alpha = 1, 2$ and it is required that the orientations must come from a vector product that magnetic moments with spin up $\uparrow$ times magnetic moments with spin down $\downarrow$. In this way, the orientations are obtained with the sign of D_α being arbitrary. Such as the orientations of DM interactions in YCrO$_3$, in which there exist 4 different directions

of $\mathbf{D}_{1ij}$ and 2 different directions of $\mathbf{D}_{2ij}$. As there is a mirror parallel to ac plane, $\mathbf{D}_{2ijy} = 0$ is reasonable according to Moriya's rule [106].

4.2.3 Spin-wave energy and spectra

After building a spin Hamiltonian with 8 parameters, composed of 5 for magnetic exchange interaction, 2 for DM interactions, and 1 for the single-ion Ising anisotropy term, the magnon spectra can be obtained with the diagonalization on the Hamiltonian. Taking $YCrO_3$ as an example, a unit cell contains 4 magnetic ions with a non-collinear AFM structure, it is natural of anticipating 4 spin-wave branches.

To simplify, an LSWT model is used to solve the spin Hamiltonian. Under the framework of LSWT, the HP transformation is used to bosonize the Hamiltonian [232], noting that the spin components have been transformed into the rotating frame,

$$S_i^{\dagger} = \sqrt{2S - a_i^{\dagger} a_i}\, a_i,\ S_i^{-} = a_i^{\dagger}\sqrt{2S - a_i^{\dagger} a_i},\ S_i^{z} = S - a_i^{\dagger} a_i, \tag{4.54}$$

where $a_i^{\dagger} a_i$ is a particle-number operator $\hat{N}_i$ of magnon. In general, only the low-energy states are considered at low temperature, in which $\langle a_i^{\dagger} a_i \rangle / 2S$ is so small that $\sqrt{2S - a_i^{\dagger} a_i} \approx \sqrt{2S}$ is a good approximation. Thus, the Hamiltonian has only a quadratic form,

$$\hat{H} = E_0 + \hat{H}_2, \tag{4.55}$$

where

$$E_0 = 4NS^2[(\sin^2 \phi - \cos^2 \phi)(J_1 + 2J_2) \tag{4.56}$$
$$+ \sin 2\phi(D_{1x} + 2D_{2x}) + J_3 + 4J_4 + J_5 - J_s],$$

is the classical ground state energy and $\hat{H}_2$ is a quadratic term. By minimizing the

classical ground state energy, a non-zero canting angle is given with

$$\tan(2\phi) = -\frac{D_{1x} + 2D_{2x}}{J_1 + J_2}. \tag{4.57}$$

This formula explains the existence of non-zero ϕ.

It is noted that $\hat{H}_2$ contains operators $a_{i\beta}^\dagger$ and $a_{i\beta}$, where i indicates the cell index and $\beta = 1, 2, 3, 4$ represents 4 different ions in this cell.

Then a Fourier transformation is defined as

$$
\begin{cases}
a_{i\beta} = \frac{1}{\sqrt{N}} \sum_{\mathbf{k}} e^{i\vec{k}\cdot\vec{R}_{i\beta}} a_{\beta\mathbf{k}}, & \beta = 1, 2, \\
a_{i\beta} = \frac{1}{\sqrt{N}} \sum_{\mathbf{k}} e^{-i\vec{k}\cdot\vec{R}_{i\beta}} a_{\beta\mathbf{k}}, & \beta = 3, 4,
\end{cases} \tag{4.58}
$$

where different rules for spin up and spin down points have been used to simplify the calculation, making no change to the results.

After Fourier transformation, the quadratic Hamiltonian in momentum space is obtained. A systematic Bogoliubov transformation is essential to diagonalize H_2, and the dispersion relations are obtained [233]. It is noted that the existence of non-collinear spin makes the process complex, and a numerical solution is required.

In the following part, the Bogoliubov transformation is utilized to diagonalize the spin Hamiltonian. After a Fourier transformation, the quadratic Hamiltonian reads,

$$H_2 = a^\dagger H_{\text{eff}} a, \quad H_{\text{eff}} = \begin{pmatrix} A & B \\ B^* & A^* \end{pmatrix}, \tag{4.59}$$

where $a^\dagger = (a_{1\mathbf{k}}^\dagger, a_{2\mathbf{k}}^\dagger, a_{3,-\mathbf{k}}^\dagger, a_{4,-\mathbf{k}}^\dagger, a_{1,-\mathbf{k}}, a_{2,-\mathbf{k}}, a_{3\mathbf{k}}, a_{4\mathbf{k}})$ is a matrix of operators while A and B are both 4×4 matrices, which satisfy $A^\dagger = A$ and $B^\top = B$.

A and B are given by

$$A = \begin{pmatrix} t_1 & \Gamma_{3\mathbf{k}} & \Gamma_{2\mathbf{k}} & \Gamma_{1\mathbf{k}} \\ & t_2 & \Gamma_{1\mathbf{k}} & \Gamma'_{2\mathbf{k}} \\ & & t_1 & \Gamma_{3\mathbf{k}} \\ & & & t_2 \end{pmatrix}, \tag{4.60}$$

$$B = \begin{pmatrix} 0 & 0 & \xi_{2\mathbf{k}} & \xi_{1\mathbf{k}} \\ & 0 & \xi^*_{1\mathbf{k}} & \xi_{2\mathbf{k}} \\ & & 0 & 0 \\ & & & 0 \end{pmatrix}, \tag{4.61}$$

with the definitions

$$t_1 = (J_1 + 2J_2)\cos 2\phi - 4J_4 - J_3(1 - \cos k_z) \tag{4.62}$$
$$-J_5(1 - \cos k_x) + J_s - D_{1x}\sin 2\phi - 2D_{2x}\sin 2\phi,$$

$$t_2 = (J_1 + 2J_2)\cos 2\phi - 4J_4 - J_3(1 - \cos k_z) \tag{4.63}$$
$$-J_5(1 - \cos k_x) + J_s - D_{1x}\sin 2\phi - 2D_{2x}\sin 2\phi,$$

$$\Gamma_{1\mathbf{k}} = -\gamma_{1\mathbf{k}}\left(J_1\sin^2\phi + \frac{1}{2}D_{1x}\sin 2\phi\right), \tag{4.64}$$

$$\Gamma_{2\mathbf{k}} = -\gamma_{2\mathbf{k}}\left(J_2\sin^2\phi + \frac{1}{2}D_{2x}\sin 2\phi + iD_{2y}\sin\phi\right), \tag{4.65}$$

$$\Gamma'_{2\mathbf{k}} = -\gamma_{2\mathbf{k}}\left(J_2\sin^2\phi + \frac{1}{2}D_{2x}\sin 2\phi - iD_{2y}\sin\phi\right), \tag{4.66}$$

$$\Gamma_{3\mathbf{k}} = J_4\gamma_{3\mathbf{k}}, \tag{4.67}$$

$$\gamma_{1\mathbf{k}} = \cos\frac{k_y}{2}, \tag{4.68}$$

$$\gamma_{2\mathbf{k}} = \cos\frac{k_x}{2}\cos\frac{k_z}{2}, \tag{4.69}$$

$$\gamma_{3\mathbf{k}} = 4\cos\frac{k_x}{2}\cos\frac{k_y}{2}\cos\frac{k_z}{2}, \tag{4.70}$$

and

$$\xi_{1\mathbf{k}} = \gamma_{1\mathbf{k}}\left(-J_1\cos^2\phi + \frac{1}{2}D_{1x}\sin 2\phi - iD_{1z}\cos\phi\right), \tag{4.71}$$

$$\xi_{2\mathbf{k}} = -J_2\gamma_{2\mathbf{k}}\cos^2\phi + \frac{1}{2}\gamma_{2\mathbf{k}}D_{2x}\sin 2\phi - 2iD_{2z}\cos\phi\sin\frac{k_x}{2}\sin\frac{k_z}{2}. \tag{4.72}$$

106

It is noted that the constant terms created by commutation relations have been left out.

Then, a systematic Bogoliubov transformation is taken to diagonalize the Hamiltonian [233]. We define a bosonic matrix

$$
\eta = \begin{pmatrix} I_{4\times4} & 0 \\ 0 & -I_{4\times4} \end{pmatrix}.
\tag{4.73}
$$

Also, ηH_{eff} is diagonalized. Finally, the eigenvectors are orthonormalized. The quasiparticles of magnon are $\alpha = Ta = (\alpha_{1\mathbf{k}}^\dagger, \alpha_{2\mathbf{k}}^\dagger, \alpha_{3,-\mathbf{k}}^\dagger, \alpha_{4,-\mathbf{k}}^\dagger, \alpha_{1,-\mathbf{k}}, \alpha_{2,-\mathbf{k}}, \alpha_{3\mathbf{k}}, \alpha_{4\mathbf{k}})$, where T satisfies

$$
T^\dagger H_{\text{eff}} T = \Lambda, \quad T^{-1} = \eta T^\dagger \eta.
\tag{4.74}
$$

Hence, the Bogoliubov transformation coefficients and eigenvalues are obtained.

In order to reproduce the INS experiment on the spin-wave dispersions of this noncollinear antiferromagnet, the dynamic structure factor is calculated as follows [209, 230],

$$
S^{\alpha,\beta}(\mathbf{k}, \omega) = \frac{1}{2\pi\hbar} \int_{-\infty}^{\infty} dt e^{-i\omega t} \langle S_{\mathbf{k}}^\alpha S_{-\mathbf{k}}^\beta(t) \rangle,
\tag{4.75}
$$

where $\alpha, \beta = a, b, c$ are components in the laboratory frame. The INS cross section is actually a combination of the dynamic structure factor with momentum-dependent prefactors according to the experimental settings. For simplicity, our intensity for the INS spectrum is expressed as

$$
I \propto \sum_{\alpha,\beta} (\delta_{\alpha\beta} - \tilde{k}_\alpha \tilde{k}_\beta) S^{\alpha,\beta}(\mathbf{k}, \omega),
\tag{4.76}
$$

where $\tilde{k}_\alpha, \tilde{k}_\beta$ are components of the normalized wave vector.

CHAPTER 5

CRYSTAL GROWTH ENGINEERING, STRUCTURAL EVOLUTION, AND THE WEAK FERROMAGNETISM IN ANTIFERROMAGNETIC MATRIX FROM T-E ORBITAL HYBRIDIZATION IN SINGLE-CRYSTAL RECRO$_3$

5.1 Introduction

Multiferroics have attracted tremendous attention due to the possible coexistence of ferroelectricity and magnetic order in the past decades. Such kind of materials offers great potential for the development of multi-functional devices in information storage [108, 234, 235, 236]. Perovskite-type ABO$_3$ oxides are one exciting class of multiferroic materials [237, 238, 239], in which there exists the possibility of tuning magnetic and/or ferroelectric orders by potential structural distortions, for example, the tilting of BO$_6$ oxygen octahedra [159], the A-site induced ionic distortion [63, 240], and the tilting of BO$_5$ blocks in hexagonal perovskites [241]. Rare-earth (RE) based transition-metal (TM) RETMO$_3$ perovskites display many interesting physical phenomena besides multiferroics, in which possible unpaired $4f$ and $3d$ electrons could have strong couplings [74, 242]. The interaction between RE- and TM- sites may induce spin-phonon coupling [243], magnetostriction effect [244], and the negative magnetization behavior [245]. Moreover, there exists a strong magnetoelectric coupling in some RETMO$_3$ materials like TbMnO$_3$ and HoMnO$_3$ compounds, and the DM interaction induced by specific magnetic orders was suggested to be responsible for the observed ferroelectric polar [105, 106, 131].

RECrO$_3$ orthochromates are another family of multiferroic materials. Below the Néel temperature of Cr^{3+} sublattices, ferroelectric polarizations were observed, and the magnetoelectric effect may exist in the family of orthochromates. Different phonon behaviors were observed between two types of RECrO$_3$ orthochromates with RE^{3+} = magnetic and non-magnetic ions, respectively, below the antiferromagnetic transition temperature T_N of Cr^{3+} sublattices, which indicates a coupling between phonons and

RE spins [246]. Moreover, it was suggested that the interactions of $3d$-$4f$ moments play an important role in producing electric polarization [246]. In RECrO$_3$ orthochromates, Cr^{3+} ($t_{2g}^3 e_g^0$) ions may enable a virtual charge transfer of t_{2g}^3-O-e_g^0 due to t_{2g}-e_g orbital hybridizations. This was suggested to be responsible for the dramatic change of superexchange interactions in Cr^{3+} sublattices [43, 122, 247]. The t-e orbital overlapping integrations can be tuned by structural distortions. Thus building a complete crystallographic database for the whole family of RECrO$_3$ orthochromates would be crucial for manipulating ferroelectricity and magnetism via structural distortions.

Since single crystals hold translational symmetry over macroscopic distances, they can provide reliable information about the structures and intrinsic properties. Extracting the intrinsic crystallographic information of RECrO$_3$ orthochromates requires high-quality single-crystal samples. Previously, the RECrO$_3$ single crystals were grown mainly by the flux method. One drawback of the method is that impurities may be introduced into the grown crystals by the flux itself [75], which influences strongly the structural, magnetic, and ferroelectric properties. Moreover, the grown single crystals were millimeters in size, which cannot satisfy the rigorous requirements in size and quality of some studies.

In the present chapter, successful single crystal growth of the family of RECrO$_3$ (RE = Eu, Gd, Tb, Dy, Y, Ho, Er, Tm, Yb, and Lu) compounds is realized by a laser-diode floating-zone (FZ) technique [248]. High-quality and large single crystals with centimeter size were obtained with the largest mass > 10 g. With the pulverized powdered samples, a systematic X-ray powder diffraction study is performed. The collected patterns were refined, and the crystallographic structure, lattice parameters, atomic positions, and isotropic Debye-Waller factors were finally extracted. The crystallography information was analyzed by taking into account the ionic radii of RE^{3+} ions and would provide the basis for further theoretical and experimental studies. Moreover, the results from in-house characterizations on grown single crystals are in agreement with those from our first-principles calculations. In the chapter, it is revealed that the RE-site tuned t-e hybridization process can induce FM interactions in

the main AFM matrix, shedding light on the coexistence of weak ferromagnetism with ferroelectric in orthochromates.

5.2 Methodology

Polycrystalline samples of $RECrO_3$ compounds were synthesized with conventional solid-state reaction, using raw materials of Cr_2O_3 (Alfa Aesar, 99.9%), Y_2O_3 (Alfa Aesar, 99.9%), Eu_2O_3 (Alfa Aesar, 99.9%), Gd_2O_3 (Alfa Aesar, 99.9%), Tb_4O_7 (Alfa Aesar, 99.9%), Dy_2O_3 (Alfa Aesar, 99.9%), Ho_2O_3 (Alfa Aesar, 99.9%), Er_2O_3 (Alfa Aesar, 99.9%), Tm_2O_3 (Alfa Aesar, 99.9%), Yb_2O_3 (Alfa Aesar, 99.9%), and Lu_2O_3 (Alfa Aesar, 99.9%). For the initial mixture of raw materials, additional $\sim$ 3–5% Cr_2O_3 was added. After twice calcinations (at 900 and 1100°, respectively, each for 18 h) and once sintering at 1300° for 12 h, pure phase $RECrO_3$ polycrystalline samples were obtained. It is stressed that before each firing step, we milled and mixed the resultant samples with a Vibrating Micro Mill (FRITSCH PULVERISETTE 0) for 1 h to ensure homogeneity. The polycrystalline $RECrO_3$ samples were treated additionally [248]. After that, cylindrical seed and feed rods were prepared with a hydrostatic pressure of $\sim$ 70 MPa. The rods were sintered at 1000° for 12 h for solidification. For both processes of calcination and sintering, the increasing and decreasing temperature speeds are 200 °C/h. The single crystals of $RECrO_3$ compounds have been grown with a laser-diode floating-zone (FZ) furnace (Model: LD-FZ-5-200WVPO-PC-UM) [248, 192]. The growth was under an argon condition with a pressure of 0.5–0.6 MPa. The argon gas was flowing constantly. The seed and feed rods rotate clockwise and counterclockwise, respectively, with a speed of 22 rotations per minute. The growth speed was 10–20 mm/h.

To study the crystalline structure, shiny pieces of $RECrO_3$ single crystals were chosen and carefully powdered with a Vibratory Micro Mill. The X-ray powder diffraction patterns were collected in a 2θ range of 20–90° with a step size of 0.02° on an in-house X-ray diffractometer (Rigaku, SmartLab 9 kW) employing cooper $K_{\alpha1}$ (1.54056 Å) and $K_{\alpha2}$ (1.54439 Å) with a ratio of 2:1 as the radiation. The X-ray powder diffrac-

tion patterns were collected at a voltage of 45 kV and a current of 200 mA at ambient conditions. The collected X-ray powder diffraction patterns were refined with the software of FULLPROF SUITE [204]. The Bragg-peak shape was modeled using a Pseudo-Voigt function. The background contribution was calculated with a linear interpolation between automatically-selected data points. Scale factor, lattice constants, background, peak profile shape, atomic positions, isotropic thermal parameter, and preferred orientation for all patterns were refined.

To determine the quality of the as-grown single crystals, a neutron Laue diffraction study was performed on the diffractometer, OrientExpress, located at ILL, Grenoble, France. Simultaneously, we simulated the recorded neutron Laue patterns along the three axes with the software OrientExpress [249] to confirm the quality of the grown crystals.

Magnetization was measured using the option of a vibrating sample magnetometer of Quantum Design physical property measurement system. Small $RECrO_3$ single-crystal samples (5–15 mg) were glued on a quartz sample holder with GE Varnish. The dc magnetization was measured at applied magnetic fields of 0, 50, and 100 Oe with ZFC and FC modes in a temperature range of 1.8–400 K. The magnetic-field-dependent hysteresis loops were measured from -14 to 14 T at different temperature points chosen within 1.8–300 K.

The first-principles calculations of $RECrO_3$ compounds were carried out within density functional theory. The exchange and correlation term in the Kohn-Sham equations was treated with the Perdew-Burke-Ernzerhof (PBE) and (PBE + U) functionals [250, 251, 252, 253] using the Vienna Ab-initio Simulation Package [254]. The core electrons were frozen, and the projected-augmented-wave method was used [255]. The Cr $3d4s$, RE (RE = Eu–Lu) elements $5p5d6s$, Y $4s4p5s5d$, and O $2s2p$ electrons were treated as valence electrons. It is well known that the $4f$ orbitals are tightly localized in comparison to the d orbitals. In the present chapter, one target is to unravel the effect of lattice variation on Cr^{3+}-O^{2-}-Cr^{3+} superexchange interactions, and the energy scale of RE^{3+}-RE^{3+} exchange interactions is about two magnitudes smaller

than that of Cr^{3+}-Cr^{3+}, hence the $4f$ electrons of lanthanide ions could be frozen reasonably. A Gaussian broadening of 0.05 eV was chosen. The set of plane-wave basis with an energy cutoff of 500 eV was used. Brillouin-zone integrations were performed with a Gamma-point-centered 7×7×5 Monkhorst-Pack k-point mesh [256]. The ionic relaxation was performed with a convergency criterion of 10^{-5} eV/primitive cell for each relaxation step and stopped moving when residual force < 0.01 eV/Å. A convergency accuracy of 10^{-6} eV per conventional cell was chosen for subsequent static self-consistent calculations.

Firstly the structures were optimized with collinear magnetic configurations of FM and A-type, C-type, and G-type AFM, to determine the magnetic ground state of each compound. Furthermore, to avoid an underestimation of the band gap, the Hubbard U value ($U_{\text{eff}} = U - J$) of each compound was calculated using the linear response ansatz [257, 258]. With appropriate Hubbard U value, static electronic self-consistent calculations were performed using the (PBE + U) method to obtain the exact total energy of the 4 magnetic states. The exchange parameters, J_i, under the classical Heisenberg model could be deduced with the energy mapping method, and so does T_{N}^{Cr} based on the MFA. Finally, the electronic structures of the RECrO$_3$ compounds were calculated by reading the charge density of ground state of the magnetic configurations.

5.3 Results and discussion

5.3.1 Crystal growth

Single-crystal materials hold translational symmetry of long-range building blocks, therefore, they provide reliable information on structures and properties of matters [74, 259, 260]. Exploring and optimizing the single crystal growth parameters are time-consuming and labor-intensive processes. We have for the first time grown large single crystals of the family of RECrO$_3$ (RE = Y, Eu, Gd, Tb, Dy, Ho, Er, Tm, Yb, and Lu) compounds. Photos of some representative as-grown single crystals were exhibited in Fig. 5.1(a)-(b), where the YbCrO$_3$ (Fig. 5.1(a), ∼ 7 cm in length) and LuCrO$_3$ (Fig. 5.1(b), ∼ 10 cm) crystals have a diameter of $\phi = 6$–8 mm and very shining sur-
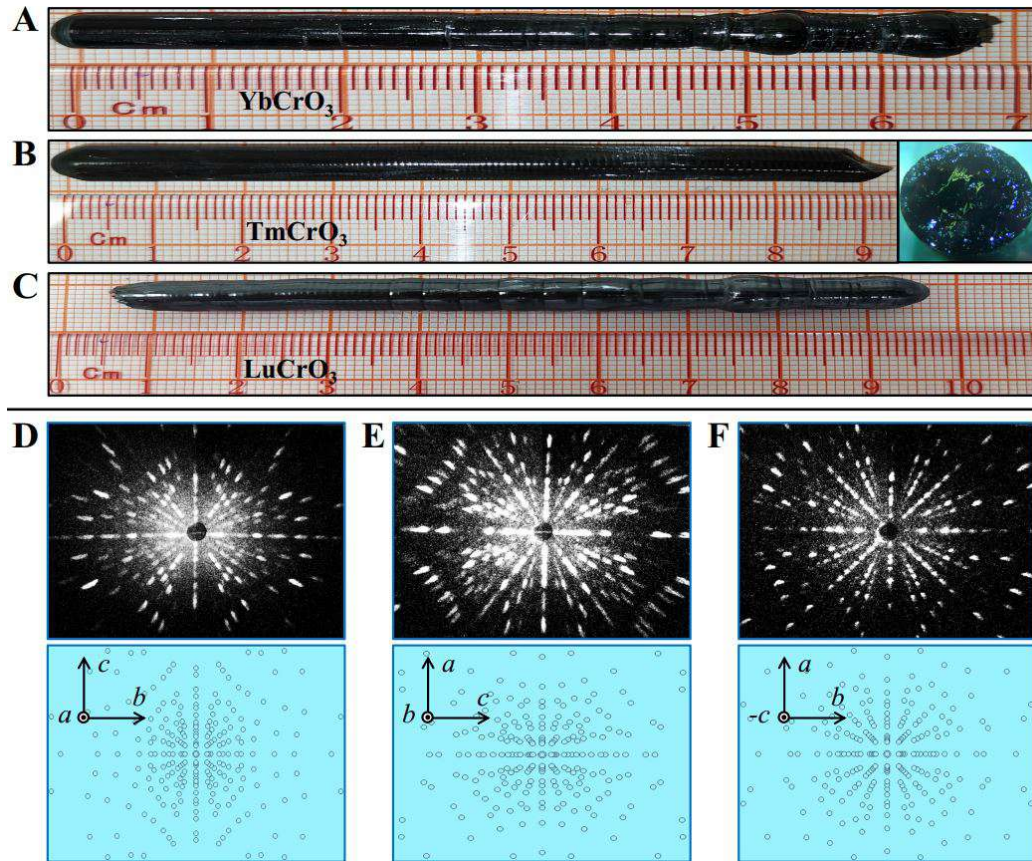
Figure 5.1: Photographs of single crystals of YbCrO$_3$ (a) and LuCrO$_3$ (b) as grown by a laser-diode floating-zone furnace. (c-e) Neutron Laue patterns of single-crystal YCrO$_3$ (top panel) and the corresponding theoretical simulations (bottom panel). The real-space lattice vectors are marked in the down panel, and the crystallographic a axis (c), b axis (d), and c axis (e) are perpendicular to the paper.

faces. So far, the largest single crystal we have grown is > 10 g for EuCrO$_3$. A China invention patent is also produced about crystal growths of RECrO$_3$ compounds [248].

The as-grown single crystals were studied on a neutron Laue diffraction. The top panel of Fig. 5.1(c)-(e) shows the monitored neutron Laue patterns of a YCrO$_3$ single crystal with the three axes perpendicular to the paper: a-axis (Fig. 5.1(c)), b-axis (Fig. 5.1(d)), and c-axis (Fig. 5.1(e)). All patterns display symmetric and very strong diffraction spots, indicating a good quality of the grown single crystal. As shown in the bottom panel of Fig. 5.1(c)-(e), the three patterns were theoretically simulated with the software OrientExpress [249], which further confirms the quality of the as-grown single crystals.
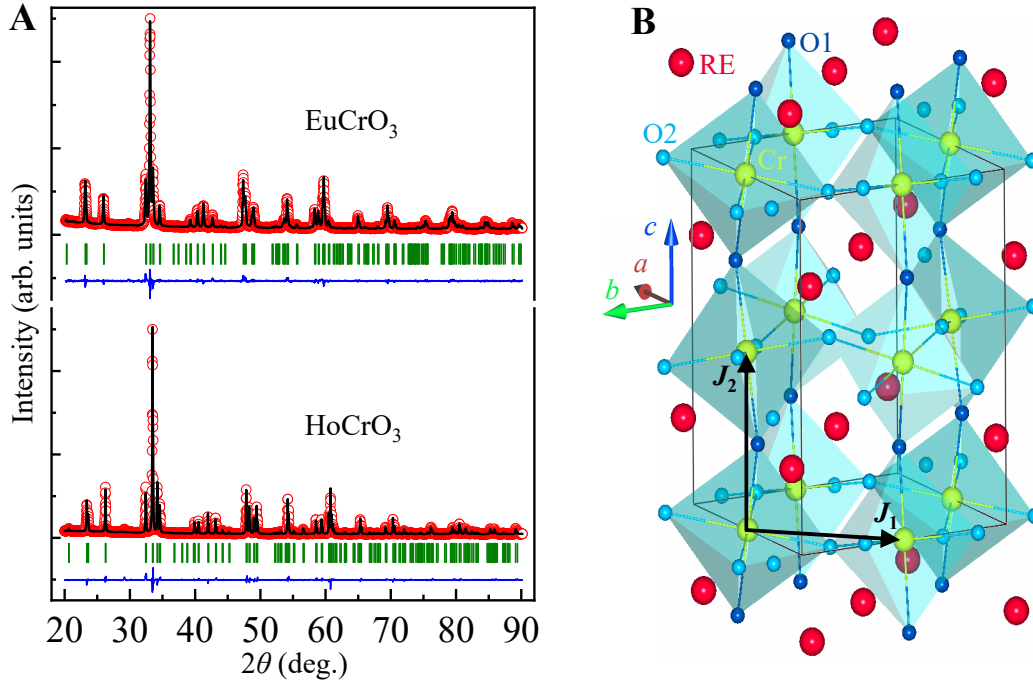
Figure 5.2: (a) Observed (circles) and calculated (solid lines) room-temperature X-Ray powder diffraction patterns of pulverized $RECrO_3$ (RE = Eu and Ho) single crystals. Vertical bars mark the positions of Bragg peaks. The bottom curves represent the difference between observed and calculated patterns. It is pointed out that the tiny peak located at $\sim 29.17°$ is from the impurity X-ray wavelength of copper K_β. (b) Refined crystal structure of $RECrO_3$ in one unit cell (solid lines) with the $Pbnm$ space group (No. 62). The RE, Cr, O1, and O2 ions are labeled. J_1 and J_2 represent the nearest-neighbor spin-exchange parameters within the ab plane and along the c axis, respectively.

5.3.2 structural evolution

To study the effect of RE^{3+} ions on structures of $RECrO_3$ (RE = Y, Eu–Lu) single crystals, X-ray powder diffraction measurements were carried out at room temperature. Figure 5.3 shows collected patterns as well as the corresponding structural refinements of four representative compounds $ErCrO_3$ (Figure 5.3(a)), $TmCrO_3$ (Figure 5.3(b)), $YbCrO_3$ (Figure 5.3(c)), and $LuCrO_3$ (Figure 5.3(d)). The collected patterns were indexed using an orthorhombic structure with the $Pbnm$ space group (No. 62). The Bragg peak shape and positions were carefully checked, there are no impurity peaks and detectable peak splitting. Therefore, the orthorhombic crystal system remains unchanged with RE^{3+} ions within the present experimental resolution. The small difference between collected and calculated X-ray powder diffraction patterns

114
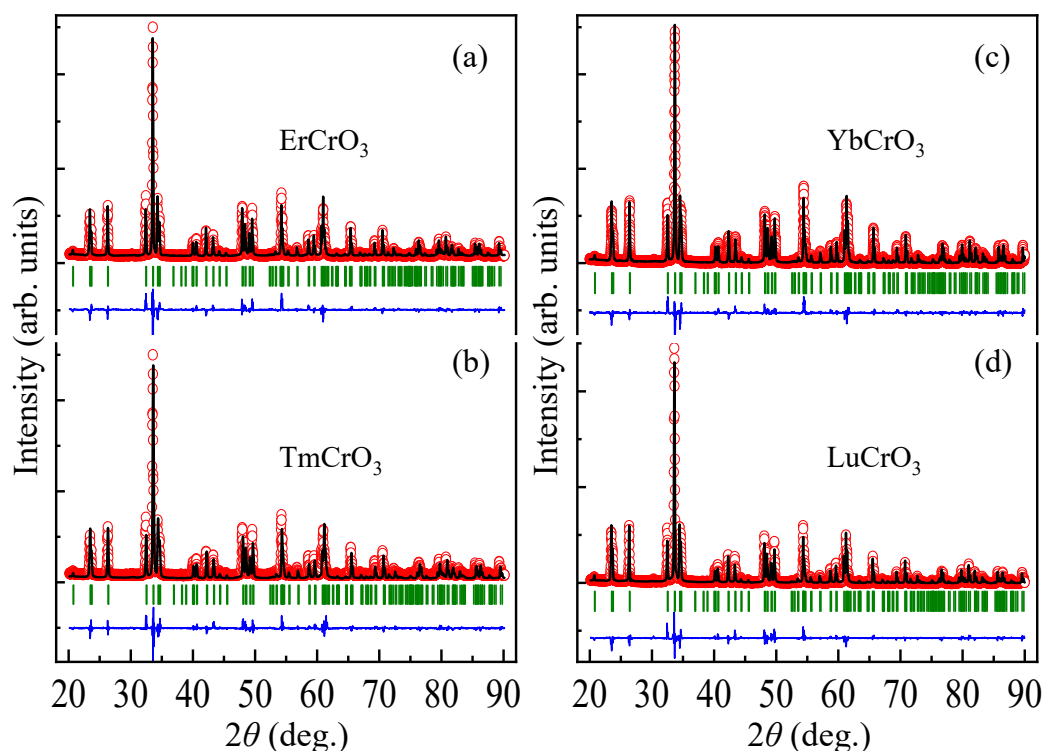
Figure 5.3: Observed (circles) and calculated (solid lines) room-temperature X-ray powder diffraction patterns of pulverized $ErCrO_3$ (a), $TmCrO_3$ (b), $YbCrO_3$ (c), and $LuCrO_3$ (d) single crystals. Vertical bars mark the positions of Bragg peaks. The bottom curves represent the difference between observed and calculated patterns.
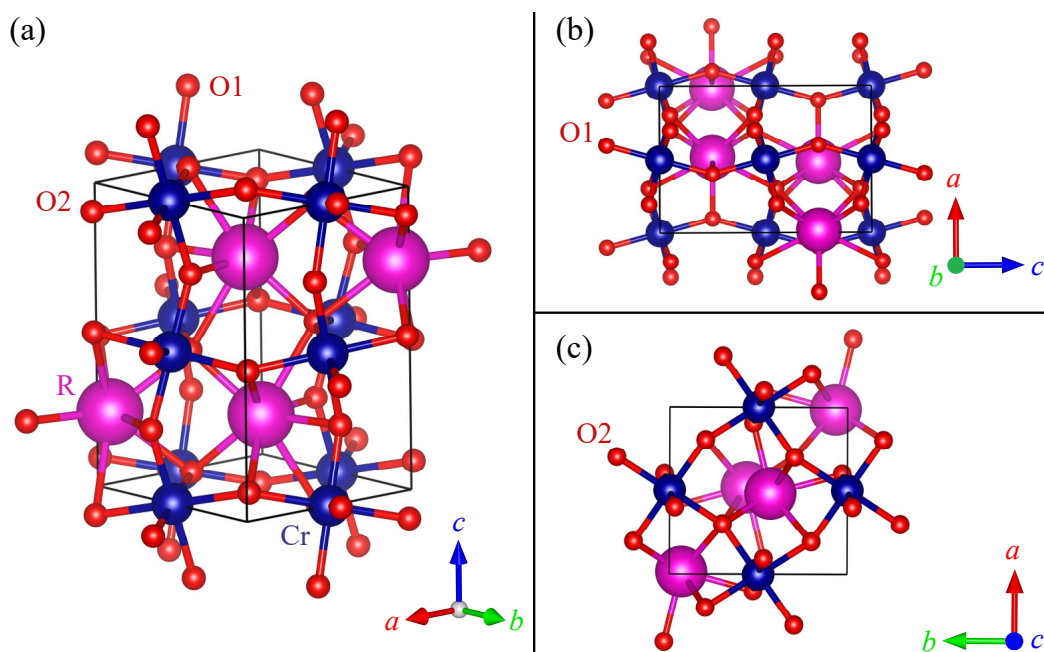
Figure 5.4: (a) Crystal structure of single-crystal $RECrO_3$ compounds in one unit cell (solid lines) of orthorhombic system with space group of $Pbnm$ (No. 62). Crystal structure of single-crystal $RECrO_3$ compounds projected into the ac plane (b) and the ab plane (c) for comparison. The RE (= rare earth), Cr, O1, and O2 ions are labeled.
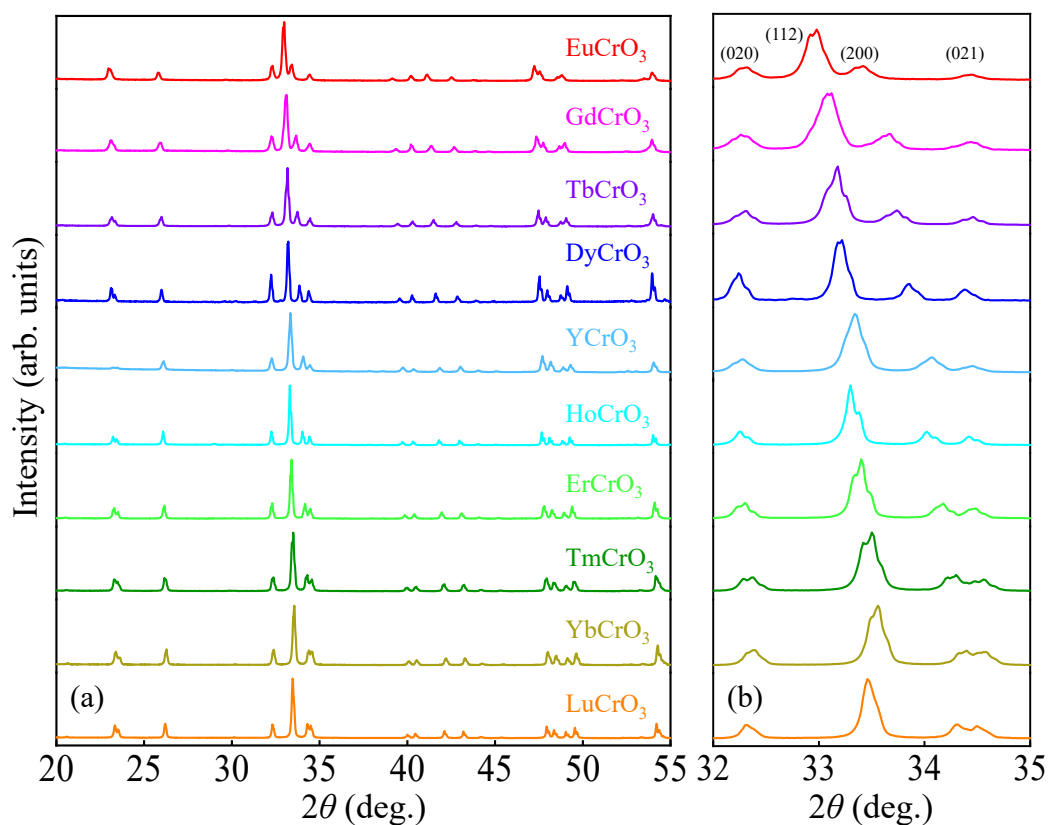
Figure 5.5: (a) Room-temperature X-ray powder diffraction patterns of pulverized RECrO$_3$ (R = Eu, Gd, Tb, Dy, Y, Ho, Er, Tm, Yb, and Lu) single crystals in a 2θ range of 20–55°. (b) For a clear comparison of the evolution of Bragg (0 2 0), (1 1 2), (2 0 0), and (0 2 1) reflections with RE ionic radius, we show the X-ray powder diffraction patterns in a small 2θ range of 32–35°.

(bottom curves in Figure 5.3) and the low values of the goodness of fit (Tables 5.1) further validate our refinements. The extracted unit cell of the orthorhombic structure was generated using the VESTA program [261] and displayed in 3D (Figure 5.4(a)) and 2D (*ac* plane, Figure 5.4(b); *ab* plane, Figure 5.4(c)) views. All extracted crystallographic information such as lattice constants and atomic positions was listed in Table 5.1.

Figure 5.5 displays the results of the X-ray powder diffraction study of single-crystal RECrO$_3$ (R = Y, Eu–Lu) compounds at room temperature. As shown in Fig. 5.5(a), we show the X-ray powder diffraction patterns in a 2θ range of 20–55°, covering the main Bragg peaks of the orthochromates. To monitor the evolution of the strongest Bragg reflections, the collected X-ray powder diffraction patterns in a 2θ range of 32–35° covering the Bragg positions of (0 2 0), (1 1 2), (2 0 0), and (0 2 1) peaks in space group of *Pbnm* (No. 62) were exhibited in Fig. 5.5(b). With decreasing ionic radius

Table 5.1: Refined structural parameters (lattice constants, unit-cell volume, atomic positions, thermal parameter B, and goodness of fit) of RECrO$_3$ (RE = Y, Eu, Gd, Tb, and Dy) compounds. The Wyckoff sites of all atoms were listed. IR = Ionic radii of RE^{3+} ions. The numbers in parenthesis are the estimated standard deviations of the (next) last significant digit.

Pulverized RECrO$_3$ single crystals

Orthorhombic, space group: $Pbnm$ (No. 62), $Z = 4$

	RE = Y	Eu	Gd	Tb	Dy	Ho	Er	Tm	Yb	Lu
IR (RE^{3+}) (Å)	1.040	1.087	1.078	1.063	1.052	1.041	1.030	1.020	1.008	1.001
a (Å)	5.2399(1)	5.3360(2)	5.3103(3)	5.2899(2)	5.2638(2)	5.2397(2)	5.2216(2)	5.2078(2)	5.1906(1)	5.1971(1)
b (Å)	5.5210(1)	5.5119(2)	5.5256(3)	5.5171(1)	5.5201(2)	5.5176(1)	5.5151(2)	5.5069(2)	5.5005(1)	5.5050(1)
c (Å)	7.5307(1)	7.6197(2)	7.6033(4)	7.5727(1)	7.5503(3)	7.5329(1)	7.5154(2)	7.4990(2)	7.4817(1)	7.4962(1)
V (Å^3)	217.857(5)	224.106(12)	223.102(18)	221.010(12)	219.386(16)	217.780(6)	216.424(11)	215.063(13)	213.607(6)	214.466(5)
$\alpha = \beta = \gamma$ (°)	90	90	90	90	90	90	90	90	90	90
RE (4c) x	-0.0165(2)	-0.0136(3)	-0.0132(4)	-0.0140(4)	-0.0144(8)	-0.0174(3)	-0.013(4)	-0.0171(3)	-0.0179(2)	-0.0181(3)
y	0.0660(1)	0.0546(1)	0.0589(2)	0.0607(2)	0.0617(4)	0.0658(2)	0.0669(2)	0.0680(2)	0.0696(1)	0.0688(2)
z						0.25				
B (Å^2)	1.91(2)	1.81(3)	1.84(4)	1.74(4)	1.14(9)	2.16(3)	1.62(5)	1.73(5)	1.61(3)	1.93(3)
Cr (4b) (x,y,z)					(0.0, 0.0, 0.5)					
B(Å^2)	2.11(4)	1.48(5)	2.29(8)	1.80(7)	3.09(19)	1.78(6)	2.14(9)	2.18(9)	2.11(6)	1.50(8)
O1 (4c) x	0.0957(9)	0.0692(16)	0.0982(19)	0.0713(20)	0.0465(56)	0.0961(16)	0.0740(24)	0.0875(23)	0.0841(16)	0.0856(23)
y	0.4741(8)	0.4846(11)	0.4800(18)	0.4876(14)	0.4937(28)	0.4720(13)	0.4816(17)	0.4763(18)	0.4786(12)	0.4815(18)
z						0.25				
B (Å^2)	1.17(7)	0.92(12)	1.31(18)	1.08(16)	1.69(40)	1.87(15)	0.92(12)	1.31(18)	1.08(16)	1.69(40)
O2 (8d) x	-0.3092(7)	-0.3014(12)	-0.3018(16)	-0.3010(15)	-0.3345(31)	-0.3049(13)	-0.3205(17)	-0.3225(17)	-0.3283(11)	-0.3137(17)
y	0.3023(7)	0.2983(11)	0.2938(16)	0.3023(14)	0.3544(25)	0.3090(11)	0.3251(15)	0.3184(16)	0.3247(10)	0.3046(16)
z	0.0554(5)	0.0462(8)	0.0542(10)	0.0518(9)	0.0312(22)	0.0491(8)	0.0487(11)	0.0470(11)	0.0450(8)	-0.0514(10)
R_{p}	8.81	3.51	3.43	3.79	5.03	4.11	5.33	4.84	6.43	5.54
R_{wp}	8.33	4.52	4.91	5.48	7.69	5.83	7.65	6.79	8.57	7.78
R_{exp}	9.60	4.43	3.43	4.25	2.99	5.66	4.60	4.17	4.92	5.25
χ^2	0.75	1.04	2.06	1.66	6.63	1.06	2.77	2.65	3.04	2.19
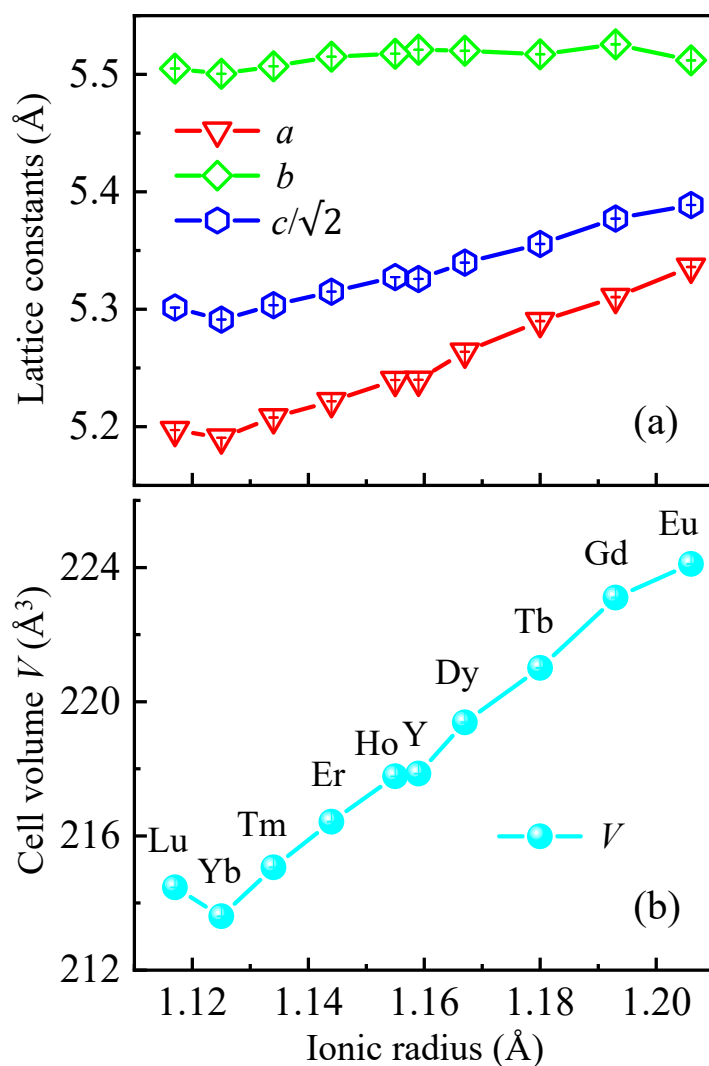
Figure 5.6: Effect of RE^{3+} cations on the lattice constants and unit-cell volume of RECrO$_3$ compounds. (a) lattice constants a, b, and c, (b) unit-cell volume V of RECrO$_3$ (RE = Eu, Gd, Tb, Dy, Y, Ho, Er, Tm, Yb, and Lu) single crystals.

(IR) of rare-earth cation, i.e., RE changes from Eu (IR = 1.087 Å) to Lu (IR = 1.001 Å), the 2θ value of the strongest Bragg (1 1 2) peak shifts from 33.12° (EuCrO$_3$) to 33.70° (YbCrO$_3$). Meanwhile, the 2θ values of Bragg (2 0 0) and (0 2 1) peaks shift from 33.56° and 34.58° (EuCrO$_3$) to 34.53° and 34.72° (YbCrO$_3$), respectively. The observed shifts of Bragg peak positions indicate changes in lattice constants and that different rare-earth cations produce different chemical pressures in RECrO$_3$ (RE = Y, Eu–Lu) orthochromates.

Figure 5.6 shows the ionic-radii dependent lattice parameters a, b, c, and unit-cell volume V of RECrO$_3$ (RE = Y, Eu–Lu) orthochromates, clearly displaying the effect

Table 5.2: To compare the change rate (slope) of unit-cell volume with RE ionic radius in RECrO$_3$ compounds, we calculated the first derivative of unit-cell volume with respective to RE^{3+} ionic radius for neighboring rare earths.

First derivative of unit-cell volume with respect to RE ionic radius ($\Delta V/\Delta r$)				
R change:	Lu $\to$ Yb	Yb $\to$ Tm	Tm $\to$ Er	Er $\to$ Ho	Ho $\to$ Y
$\Delta V/\Delta r$ (Å^2)	-122.714	161.778	136.100	123.273	19.250
R change:	Y $\to$ Dy	Dy $\to$ Tb	Tb $\to$ Gd	Gd $\to$ Eu	
$\Delta V/\Delta r$ (Å^2)	191.125	124.923	160.923	77.231	

of RE-site in RECrO$_3$ compounds on the crystallography. The ionic radii of RE^{3+} ions were taken with a coordination number of 8 and listed in Tables 5.1 [262]. As RE-site ionic radii increase from RE = Lu^{3+} to Eu^{3+}, lattice parameters of a, b, c, and unit-cell volume V change accordingly. As shown in Fig. 5.6(a), the lattice constants a and c almost increase linearly, except for RE^{3+} = Lu^{3+}. By contrast, the lattice constant b keeps approximately a constant. These changes in lattice constants jointly result in a linear increase in the unit-cell volume of RECrO$_3$ (except for RE^{3+} = Lu^{3+} ions) compounds (Fig. 5.6(b)). The slopes of the linear parts of lattice constants versus IR curves are 1.75(8) (along the a axis), 0.25(8) (along the b axis), and 1.66(7) (along the c axis), respectively. Therefore, with increasing RE^{3+} ionic radius, the lattice elongation along the a and c axes is almost the same, whereas, along the b axis, it decreases approximately by 83.5%, displaying an anisotropy. Meanwhile, the unit-cell volume V gets expansion at a rate of 131(4) Å^2 with RE^{3+} ionic radius.

As shown in Fig. 5.6, it is noted that lattice constants and unit-cell volume of RECrO$_3$ (RE = Y, Eu–Yb) single crystals get smaller and smaller as RE^{3+} ions vary from Eu^{3+} to Yb^{3+}. When RE^{3+} = Lu^{3+} ions, lattice parameters deviate upward from the linear curves of lattice parameters versus RE (= Y, Eu–Yb) ionic radii, i.e., the lattice parameters of LuCrO$_3$ are larger than those of YbCrO$_3$ compound. From the refined results of X-ray powder diffraction patterns, we get that the LuCrO$_3$ (IR of Lu^{3+} ions = 1.001 Å) single crystal has lattice parameters of a = 5.1971(1) Å, b = 5.5050(1) Å, c = 7.4962(1) Å, and V = 214.466(5) Å^3. By contrast, the YbCrO$_3$ (IR of Yb^{3+} ions

= 1.008 Å) single crystal has lattice parameters of a = 5.1906(1) Å, b = 5.5005(1) Å, c = 7.4817(1) Å, and V = 213.607(6) Å³. As is well known, the Yb^{3+} ion ($4f^{13}$, S = 1/2, L = 3, and J = 7/2) in $YbCrO_3$ compound has one unpaired f electron, therefore, it is magnetic. By contrast, the Lu^{3+} ion ($4f^{14}$, S = 0, L = 0, and J = 0) in $LuCrO_3$ compound has no unpaired electrons and thus is non-magnetic. Moreover, other RE^{3+} ions (RE = Eu, Gd, Tb, Dy, Ho, Er, and Tm) are also magnetic. Therefore, there exist stronger $3d$-$4f$ couplings in $RECrO_3$ (RE = Eu, Gd, Tb, Dy, Ho, Er, Tm, and Yb) compounds than that in $LuCrO_3$ compound. Thus, the anomaly of lattice parameters of the $LuCrO_3$ compound may be due to the disappearance of magnetostriction effect induced by $3d$-$4f$ interactions. This is in agreement with previous studies of single-crystal $YCrO_3$ where the formation of the canted antiferromagnetic structure in Cr^{3+} sublattices results in an additional shrinkage of the lattice parameters as temperature decreases [35, 263]. Previously, the temperature-dependent anisotropic magnetostriction constants, i.e., λ_{100} and λ_{111}, were written as $\lambda(T, B)/\lambda(0, 0) = \hat{I}_{5/2}(x)$, where $\hat{I}_{5/2}$ denotes the hyperbolic Bessel function and strongly depends on the $3d$-$4f$ couplings in RE-TM compounds [264]. Similarly, among rare-earth doped transition-metal $CoFe_{1.97}RE_{0.03}O_4$ (RE = La, Ce, Sm, Gd, Dy, Ho, Er, and Yb) spinel oxides, the largest maximum magnetostriction coefficient λ_{max} appears in the $CoFe_{1.97}RE_{0.03}O_4$ (RE = Yb) compound [265].

It is also essential to calculate the rate of unit-cell volume expansion of neighbor $RECrO_3$ compounds, i.e., $\Delta V/\Delta r$, the first derivative of unit-cell volume with respect to the ionic radius of rare earth. The resultant values of $\Delta V/\Delta r$ of $RECrO_3$ (RE = Y, Eu–Lu) single crystals were listed in Table 5.2. From Lu to Yb ions, $\Delta V/\Delta r$ is negative (–122.714 Å²). For other neighbor $RECrO_3$ compounds, the values of $\Delta V/\Delta r$ are all positive. Among the positive values of $\Delta V/\Delta r$, the smallest one equals 19.250 Å² when RE changes from Ho to Y; the largest $\Delta V/\Delta r$ = 191.125 Å² when RE changes from Y to Dy. It is pointed out that Y^{3+} ions are also non-magnetic. Shedding light on the $3d$-$4f$ coupling effect on structural, magnetic, and ferroelectric properties of $RECrO_3$ (RE = Eu, Gd, Tb, Dy, Y, Ho, Er, Tm, Yb, and Lu) compounds necessitates
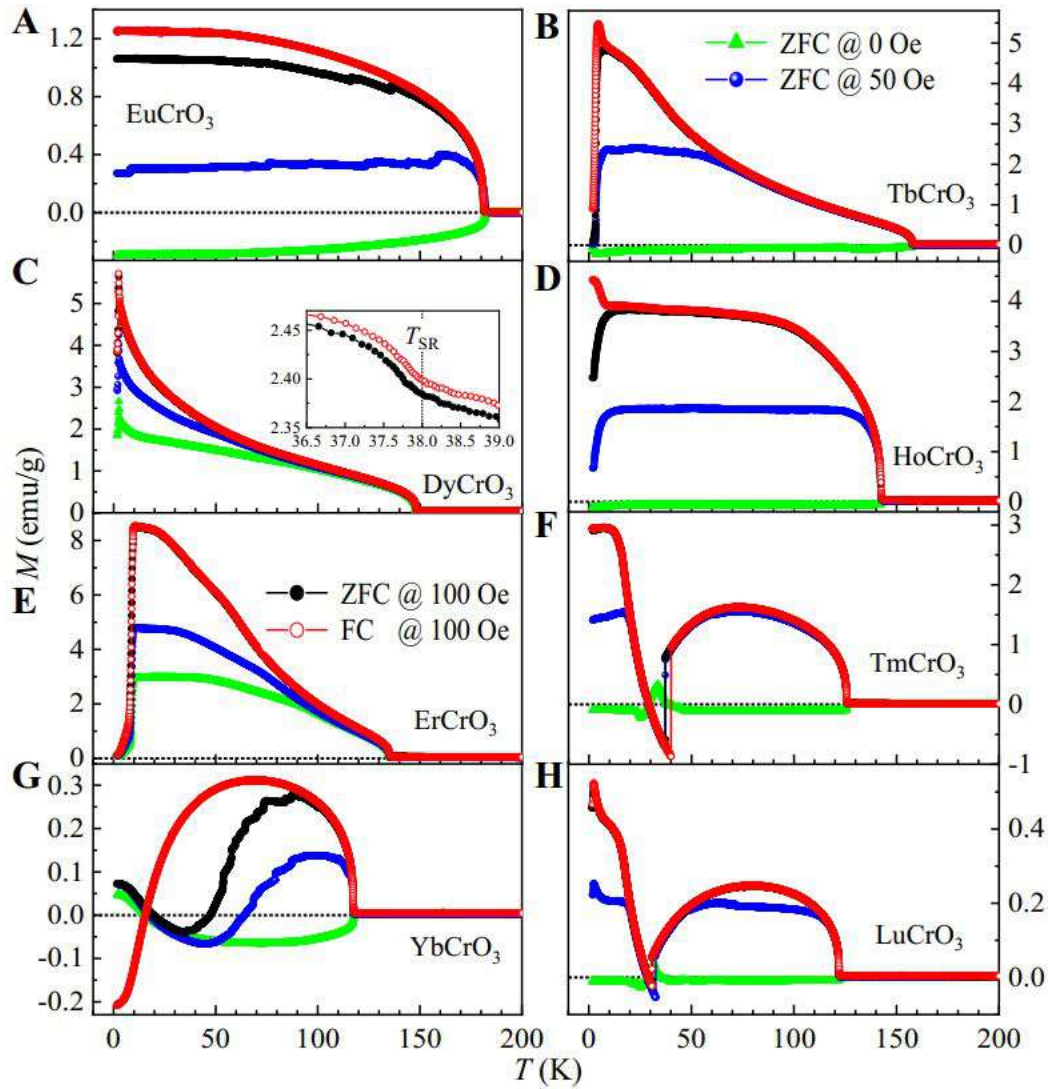
Figure 5.7: Magnetization as a function of temperature from 1.8–200 K measured at 0, 50, and 100 Oe: $EuCrO_3$ (a), $TbCrO_3$ (b), $DyCrO_3$ (c), $HoCrO_3$ (d), $ErCrO_3$ (e), $TmCrO_3$ (f), $YbCrO_3$ (g), and $LuCrO_3$ (h). We performed both zero-field and field-cooling measurements.

further controlled studies.

5.3.3 Magnetic properties

To clearly show features of dc magnetization in the vicinity of magnetic phase transitions, the temperature-dependent data in a temperature range of 1.8–200 K is presented as shown in Fig. 5.7. Magnetic hysteresis loops at the low-field regimes were displayed in Fig. 5.8; the isothermal field dependence of magnetization with the applied magnetic field from −14 to 14 T was supplemented in Fig. 5.9.

121

Table 5.3: Calculated theoretical quantum numbers of RE^{3+} ions in RECrO$_3$ single crystals based on Hund's rule: number of $4f$ ($4d$ for Y^{3+} ion) electrons, spin S, orbital L, total angular momentum J, Landé factors g_J, and the ground-state term $^{2S+1}L_J$. The values are listed about the measured (meas) ($\mu_{\text{eff-meas}}$) and theoretical (theo) effective PM moments ($\mu_{\text{eff-theo}}^{\text{Cr}} = g_J\mu_B\sqrt{S(S+1)} = 3.873\ \mu_B$, $\mu_{\text{eff-theo}}^{\text{RE}} = g_J\mu_B\sqrt{J(J+1)}$, and measured moment ($\mathcal{M}_{\text{meas}}$ per formula at 1.8 K and 14 T), and the theoretical saturation moments ($\mathcal{M}_{\text{sat-theo}}^{\text{Cr}} = g_J\mu_B S = 3\ \mu_B$, $\mathcal{M}_{\text{sat-theo}}^{\text{RE}} = g_J\mu_B J$, and $\mathcal{M}_{\text{sat-theo}}^{\text{total}} = \sqrt{(\mathcal{M}_{\text{sat-theo}}^{\text{RE}})^2 + (\mathcal{M}_{\text{sat-theo}}^{\text{Cr}})^2}$. The numbers in parenthesis are the estimated standard deviations of the (next) last significant digit.

$\mu_{\text{eff-theo}}^{\text{total}} = \sqrt{(\mu_{\text{eff-theo}}^{\text{RE}})^2 + (\mu_{\text{eff-theo}}^{\text{Cr}})^2}$, the measured

| RE^{3+} = | Y^{3+} | RECrO$_3$ single crystals | | | | | | | | |
		Eu^{3+}	Gd^{3+}	Tb^{3+}	Dy^{3+}	Ho^{3+}	Er^{3+}	Tm^{3+}	Yb^{3+}	Lu^{3+}
$4d^n$ ion	0									
$4f^n$ ions		6	7	8	9	10	11	12	13	14
S	0	3	7/2	3	5/2	2	3/2	1	1/2	0
L	0	3	0	3	5	6	6	5	3	0
J	0	0	7/2	6	15/2	8	15/2	6	7/2	0
g_J	–	–	2	1.5	1.33	1.25	1.2	1.167	1.143	–
$^{2S+1}L_J$	$^1S_0$	$^7F_0$	$^8S_{7/2}$	$^7F_6$	$^6H_{15/2}$	$^5I_8$	$^4I_{15/2}$	$^3H_6$	$^2F_{7/2}$	$^1S_0$
$\mu_{\text{eff-meas}}$ (μ_B)	3.95 [35]	6.44	8.40 [58]	10.51	11.35	11.03	10.20	8.35	5.63	4.98
$\mu_{\text{eff-theo}}^{\text{RE}}$ (μ_B)	0	0	7.937	9.721	10.646	10.607	9.581	7.561	4.536	0
$\mu_{\text{eff-theo}}^{\text{total}}$ (μ_B)	3.873	3.873	8.832	10.464	11.328	11.292	10.334	8.495	5.964	3.873
$\mathcal{M}_{\text{meas}}$ (μ_B)	~ 0.147 [35]	0.245(1)	6.43 [58]	6.248(1)	4.834(1)	3.999(1)	6.385(1)	2.868(1)	0.883(1)	1.197(1)
$\mathcal{M}_{\text{sat-theo}}^{\text{RE}}$ (μ_B)	0	0	7	9	10	10	9	7	4	0
$\mathcal{M}_{\text{sat-theo}}^{\text{total}}$ (μ_B)	3	3	7.616	9.487	10.440	10.440	9.487	7.616	5	3
T_N (K)	141.5(1) [35]	181.6(1)	169.3(1) [58]	157.9(1)	148.5(1)	143.2(1)	135.4(1)	125.9(1)	117.9(1)	122.3(1)
θ_{CW} (K)	−433.2(6)[35]	−450.4(15)	−20.33(4)[58]	−53.3(1)	−56.5(1)	19.6(1)	−30.0(1)	−90.6(4)	−17.4(1)	−110.4(2)

122
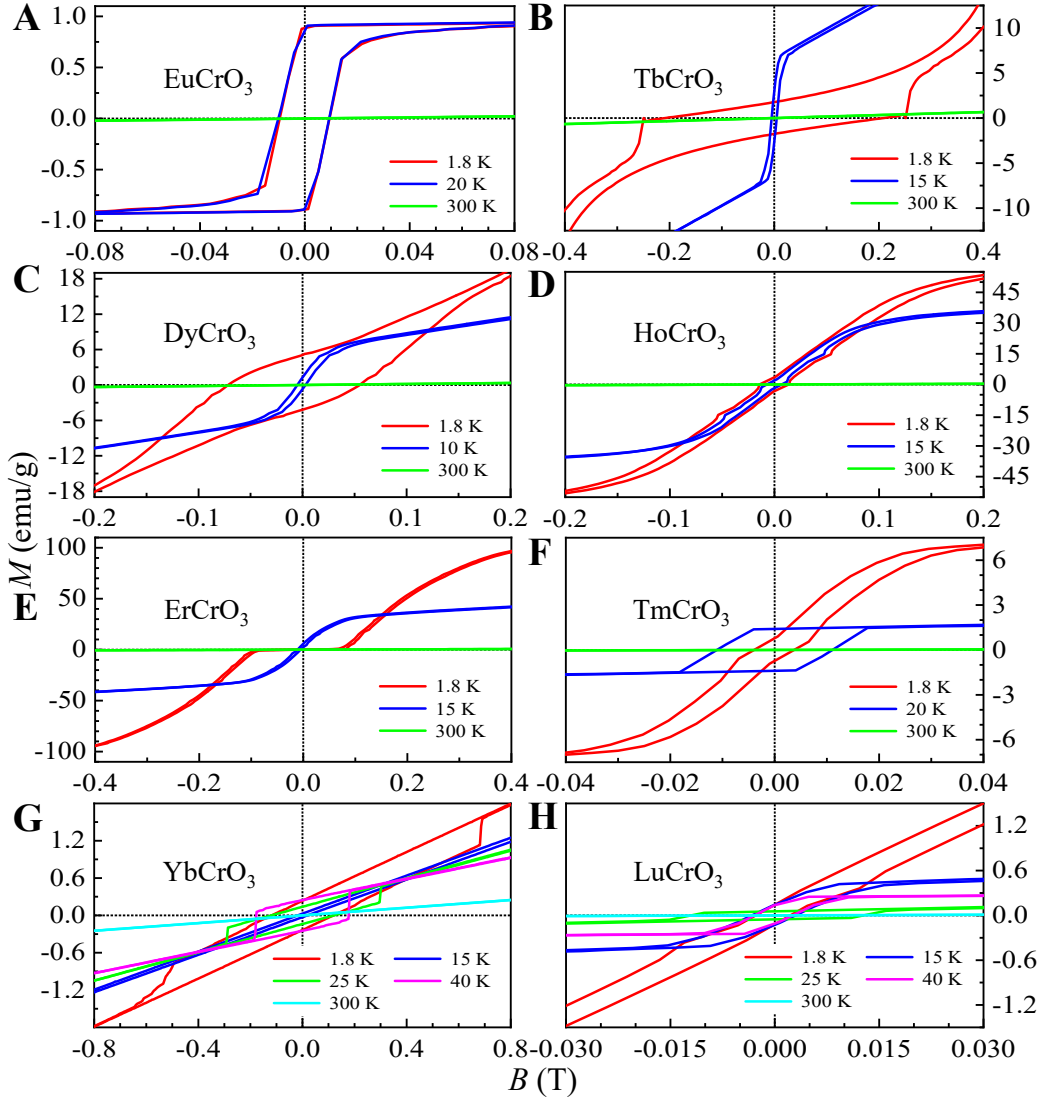
Figure 5.8: Magnetic hysteresis loops measured at low applied-magnetic fields with selected temperatures as shown: EuCrO$_3$ (a), TbCrO$_3$ (b), DyCrO$_3$ (c), HoCrO$_3$ (d), ErCrO$_3$ (e), TmCrO$_3$ (f), YbCrO$_3$ (g), and LuCrO$_3$ (h).

From the measured zero-field cooling (ZFC) magnetization data at 1000 Oe in a temperature range of 250–350 K, we calculated the inverse magnetic susceptibility $\chi^{-1} = B/M$, which can be well fit with the Curie-Weiss (CW) law for a pure PM state [63],

$$\chi^{-1}(T) = \frac{3k_B(T - \theta_{\text{CW}})}{N_{\text{A}}\mu_{\text{eff}}^2},\tag{5.1}$$

where $k_{\text{B}} = 1.38062 \times 10^{-23}$ J/K is the Boltzmann constant, θ_{CW} is the PM CW temperature, $N_{\text{A}} = 6.022 \times 10^{23}$ mol^{-1} is Avogadro's constant, and μ_{eff} is the effective

PM moment. The temperature-dependent magnetization data is fit by equation (5.1), to extract experimental values of the AFM transition temperature T_N^{Cr}, θ_{CW}, and $\mu_{\text{eff-meas}}$ of RECrO$_3$ single crystals. These measured values were listed in Table 5.3. For the RECrO$_3$ compounds, it is pointed out that both RE^{3+} and Cr^{3+} ions contribute to the effective PM moment. Therefore, the theoretical total effective PM moment is given with $\mu_{\text{eff-theo}}^{\text{total}} = \sqrt{(\mu_{\text{eff-theo}}^{RE})^2 + (\mu_{\text{eff-theo}}^{Cr})^2}$, where $\mu_{\text{eff-theo}}^{RE} = g\mu_B\sqrt{J(J+1)}$, and $\mu_{\text{eff-theo}}^{Cr} = g\mu_B\sqrt{S(S+1)} = 3.873\ \mu_B$ (where $S = 3/2$). The quantum numbers of RE^{3+} and Cr^{3+} ions are summarized, the values of $\mu_{\text{eff-theo}}^{RE}$ and $\mu_{\text{eff-theo}}^{\text{total}}$ are calculated as well. These were listed in Table 5.3 for a comparison to the experimental values.

In the following, the magnetic properties of RECrO$_3$ (RE = Eu, Tb, Dy, Ho, Er, Tm, Yb, and Lu) single crystals are presented one by one.

EuCrO$_3$

As shown in Fig. 5.7(a), EuCrO$_3$ presents a behavior of negative magnetization below T_N^{Cr} when the applied magnetic field B is absent. By contrast, with decreasing temperature at B = 50 Oe, the ZFC magnetization increases sharply below T_N^{Cr} within a very small temperature regime of ~ 1.2 K and then gets flatted down to 1.8 K. Compared to ZFC data, the field-cooling (FC) magnetization at 100 Oe increases by $\sim 18\%$ at 1.8 K. The magnetization data measured at 50 and 100 Oe resembles the features of a weak FM state. Based on these measurements, we determined $T_N^{Cr} = 181.6(1)$ K for the EuCrO$_3$ single crystal. Below T_N^{Cr}, EuCrO$_3$ enters into a canted AFM state probably due to the DM interactions between Cr^{3+} spin moments.

The field dependence of magnetization measured at 1.8 K was shown in Fig. 5.8(a), where clear magnetic hysteresis loops were observed at 1.8 K and 20 K, and there is almost no difference between them. A remanent magnetization $M_r \sim 0.91$ emu g^{-1} and a coercive field $B_c \sim 95$ Oe were determined. The magnetic hysteresis loop closes at ~ 867 Oe, after which the ZFC magnetization increases linearly as a function of the applied magnetic field with a slope of $dM/dB = 0.322(1)$ emu g^{-1} T^{-1} (Figure 5.9(a)). Based on this slope, supposing that the theoretical saturation magnetic moment of Cr^{3+}

ions $M_{\text{sat-theo}}^{\text{Cr}} = g_J \mu_B S = 3 \, \mu_B$, where $g_J = 2$ and $S = \frac{3}{2}$ for pure ionic Cr^{3+} ions as listed in Table 5.3, it is inferred that reaching a full magnetic saturation state requires $B \approx 203$ T. At 1.8 K and 14 T, a magnetization of $M_{\text{meas}} = 0.245(1) \, \mu_B/$Cr was obtained (Figure 5.9(a)), which equals $\sim 8.2\%$ of the theoretical value $M_{\text{sat-theo}}^{\text{total}} = 3 \, \mu_B/$Cr.

To avoid the effect of nonintrinsic magnetic contributions at low applied-magnetic fields, the ZFC magnetization data measured at 1000 Oe from 250–350 K was used for the CW fitting, which produces an effective PM moment $\mu_{\text{eff-meas}} = 6.44 \, \mu_B$ that is evidently much larger than the corresponding theoretical effective moment $\mu_{\text{eff-theo}}^{\text{total}}$ $= \sqrt{(\mu_{\text{eff-theo}}^{\text{RE}})^2 + (\mu_{\text{eff-theo}}^{\text{Cr}})^2} = 3.873 \, \mu_B$ (Table 5.3) and a CW temperature $\theta_{\text{CW}} = -450.4(15)$ K.

The present study indicates a possible existence of competition between FM and AFM exchange interactions. It is pointed out that all our data displays no indication of the formation of Eu^{3+} magnetic ordering at low temperatures, inconsistent with the previous study on polycrystalline $EuCrO_3$ samples [42]. This indicates that the $EuCrO_3$ single crystal holds a pure Eu^{3+} oxidation state, and there is no oxidation-state fluctuation for the Eu^{3+} ions.

TbCrO₃

$T_N^{\text{Cr}} = 157.9(1)$ K is determined for the $TbCrO_3$ single crystal as shown in Fig. 5.7(b). Below T_N^{Cr}, the ZFC magnetization at 0 Oe is negative, whereas the data measured at 50 and 100 Oe have a steady increase after a sharp enhancement around T_N^{Cr} within a temperature regime of ~ 0.56 K. With decreasing temperature, ZFC data measured at 100 Oe obviously exceeds the magnetization (measured at 50 Oe) at ~ 70 K. At ~ 7.7 K, a kink appears in the magnetization data measured at 50 and 100 Oe (ZFC at 50 and 100 Oe: downturn; FC at 100 Oe: upturn), suggesting the formation of a Tb^{3+} spin ordering. Below ~ 4.5 K, there exist a sharp decrease of the magnetization measured at $B = 50$ and 100 Oe and a sharp increase of the magnetization collected at 0 Oe. Below ~ 3 K, the ZFC magnetization measured at 0, 50, and 100 Oe approaches zero. Therefore, there exist very complicated magnetic phase transitions as a function

of temperature.

An apparent magnetic hysteresis loop was observed at 15 K (Fig. 5.8(b)), a temperature within $[T_N^{Tb}, T_N^{Cr}]$, with $M_r \sim 2.75$ emu g^{-1} and $B_c \sim 48$ Oe, indicating an appearance of the weak FM state of Cr^{3+} ions. When $T = 1.8$ K, both Tb^{3+} and Cr^{3+} spins order. It is interesting that we observed a parallelogram-shaped magnetic hysteresis loop with $M_r \sim 1.82$ emu g^{-1} and $B_c \sim 2500$ Oe (Fig. 5.8(b)). Compared to the magnetic hysteresis loop observed at 15 K, the bent parallelogram was stretched along the B axis and squeezed along the magnetization axis at 1.8 K. Such kind of twisted loop was not observed previously in either polycrystalline or single-crystalline (grown via the flux method) samples [172, 266], indicating a stronger coupling between Cr^{3+} and Tb^{3+} spins in our $TbCrO_3$ single crystal. As B increases, the magnetic hysteresis loop measured at 1.8 K gets a quick saturation at $B_s \sim 1.67$ T, while the one at 15 K increases smoothly and attains a plateau at ~ 6.8 T. At 1.8 K, a final magnetization $M_{meas} = 6.248(1)$ μ_B was reached at 14 T, which decreases by $\sim 34\%$ compared to the total theoretical saturation moment $M_{sat\text{-}theo}^{total} = 9.487$ μ_B as listed in Table 5.3.

The CW fitting results in $\mu_{eff\text{-}meas} = 10.51$ μ_B is almost the same as the theoretical total effective moment $\mu_{eff\text{-}theo}^{total} = 10.464$ μ_B. The CW temperature $\theta_{CW} = -53.3(1)$ K indicates a weak competition between FM and AFM interactions in the $TbCrO_3$ single crystal.

$TbCrO_3$ enters into a long-range canted AFM state of Cr^{3+} sublattices below T_N^{Cr} = 157.9(1) The possible long-range AFM order of Tb^{3+} sublattices is formed below $T_N^{Tb} \sim 7.7$ K. Strong coupling was observed between the spin orders of the Cr^{3+} and Tb^{3+} cations. In addition, a weak competition between the FM and AFM interactions of the Cr^{3+} cations was observed as well.

DyCrO$_3$

As shown in Fig. 5.7(c), the $DyCrO_3$ single crystal undergoes a magnetic phase transition from a PM state to a canted AFM phase at $T_N^{Cr} = 148.5(1)$ K, corresponding to the formation of the Cr^{3+} spin ordering. A kink appears at $T_{SR}^{Cr} \sim 38$ K (Fig. 5.7(c),
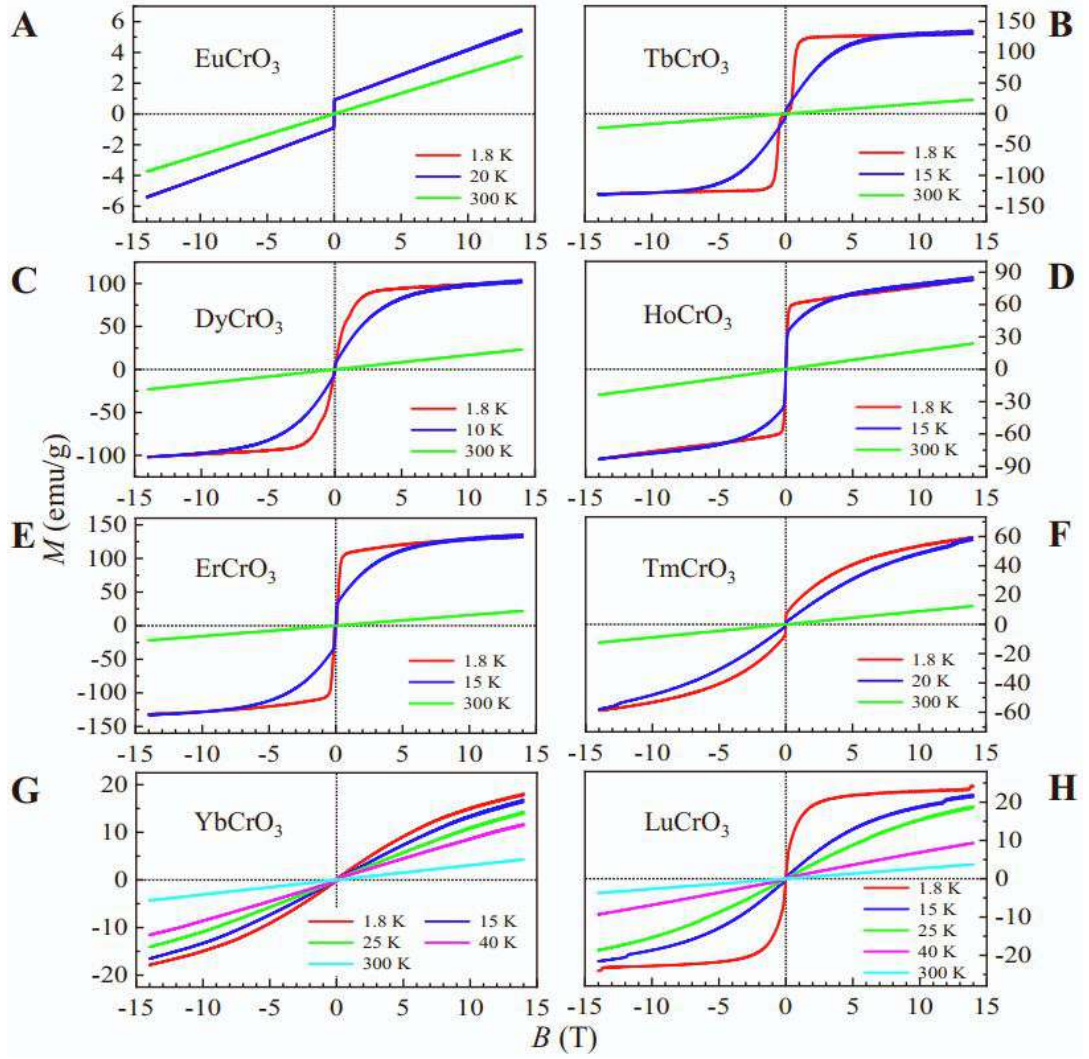
Figure 5.9: Applied magnetic-field dependent magnetization data in the whole studied field range from -14 to 14 T at selected temperatures, as shown: EuCrO$_3$ (a), TbCrO$_3$ (b), DyCrO$_3$ (c), HoCrO$_3$ (d), ErCrO$_3$ (e), TmCrO$_3$ (f), YbCrO$_3$ (g), and LuCrO$_3$ (h).

inset) in the magnetization measured at 0, 50, and 100 Oe, which is attributed to the spin reorientation of the Cr^{3+} spins. A similar observation was previously reported for DyCrO$_3$ single crystals grown by the flux method, where the appearance of the kink was believed to be caused by the spin reorientation of the Dy^{3+} spins [172]. Below T_N^{Cr}, the magnetization increases smoothly until the onset of a sharp enhancement at ~ 17 K, reaching a maximum at ~ 2.54 K and then followed by a quick reduction. Therefore, an AFM phase transition of the Dy^{3+} spins was observed at $T_N^{Dy} \sim 2.8$ K.

Isothermal magnetic hysteresis loops were observed at 1.8 ($M_r \sim 4.7$ emu g^{-1}; $B_c \sim 639$ Oe) and 10 K ($M_r \sim 1.1$ emu g^{-1}; $B_c \sim 41$ Oe) (Fig. 5.8(c)), confirming that the Cr^{3+} spins hold a canted AFM state. For the Dy^{3+} sublattices, it can be only

concluded that the spins form an AFM state. At both 1.8 and 10 K, the magnetization curves finally flat with $M_{\text{meas}} = 4.834(1)$ μ_{B} at 14 T (Figure 5.9(c)). This value is $\sim$ 53.7% less than the total theoretical saturation moment $M_{\text{sat-theo}}^{\text{total}} = 10.440$ μ_{B}, as listed in Table 5.3.

The CW fitting produces $\mu_{\text{eff-meas}} = 11.35$ μ_{B}, which is nearly equal to the theoretical value $\mu_{\text{eff-theo}}^{\text{total}} = 11.328$ μ_{B}. A CW temperature is given with $\theta_{\text{CW}} = -56.5(1)$ K (Table 5.3).

HoCrO$_3$

For the HoCrO$_3$ single crystal, T_{N}^{Cr} was determined to be 143.2(1) K (Fig. 5.7(d)). Below T_{N}^{Cr}, the ZFC magnetization at 0 Oe is negative, whereas, those at 50 and 100 Oe are positive and increased smoothly in the temperature regimes of $\sim$ 19 K (for 50 Oe) and $\sim$ 47 K (for 100 Oe) and then flatten until $T_{\text{N}}^{\text{Ho}} \sim 7.82$ K at which Ho^{3+} spins order antiferromagnetically. Below $\sim$ 2.4 K, all curves are flattened. When 2.4 K $< T < T_{\text{N}}^{\text{Ho}}$, the magnetization curves at ZFC (downturn) and FC (upturn) 100 Oe demonstrate an inverse trend; above T_{N}^{Ho}, they coincide. The degree of canting of the Cr^{3+} AFM structure determines the strength of the resulting ferromagnetism along the c axis. This prevents the formation of an AFM structure of the Ho^{3+} spins. The difference between the ZFC and FC magnetization at 100 Oe is controlled by the competition between Zeeman energy generated by the applied magnetic field and crystal field, AFM interaction strength of Ho^{3+} ions, and magnetic anisotropy [267].

At 1.8 and 15 K, magnetic hysteresis loops were observed in step-increasing mode, as shown in Fig. 5.8(d). Parameters of magnetism were extracted with $M_{\text{r}} \sim 3.5$ (1.8 K) and 1.9 (15 K) emu g^{-1}, and the corresponding $B_{\text{c}} \sim 140$ and 72 Oe, respectively. At 15 K, the magnetization increases linearly at $B \leq 618$ Oe and then proceeds smoothly into a plateau at $\sim$ 3.2 T; by contrast, at 1.8 K and $B \leq 1092$ Oe, the magnetization almost increases linearly with increasing magnetic field and then attains $M_{\text{meas}} =$ 3.999(1) μ_{B} at 14 T (Figure 5.9(d)). This value is only $\sim$ 38.3% of the theoretical value $M_{\text{sat-theo}}^{\text{total}} = 10.440$ μ_{B} as listed in Table 5.3.

The experimental effective magnetic moment is extracted with $\mu_{\text{eff-meas}} = 11.03$ μ_B, which is comparable to $\mu_{\text{eff-theo}}^{\text{total}} = 11.292$ μ_B, and $\theta_{\text{CW}} = 19.6(1)$ K. The previous study on polycrystalline $HoCrO_3$ sample shows $\mu_{\text{eff-meas}} = 11.55$ μ_B and $\theta_{\text{CW}} = -24.0$ K [268].

Obtaining evidence of short-range exchange interactions and magnetic fluctuations of Ho^{3+} spins reported previously by quasi-elastic and inelastic neutron scattering studies on $HoCrO_3$ powder samples [269, 270] necessitates more in-house characterizations with the as-grown $HoCrO_3$ single crystal.

ErCrO$_3$

As shown in Fig. 5.7(e), below $T_N^{\text{Cr}} = 135.4(1)$ K that is close to previous report value [271], there was a small sharp enhancement in the magnetization within ~ 0.72 K, which then increased smoothly until an onset of a sudden decrease at $T_{\text{SR}}^{\text{Cr}} \sim 9.7$ K. The decrease of magnetization is attributed to the spin reorientation transition of Cr^{3+} spins from Γ_4 to Γ_1, or the $\Gamma_1(0)$ spin configuration [272, 273]. Below $T_N^{\text{Er}} \sim 8$ K, the magnetization at 0, 50, and 100 Oe decreases linearly. No difference was found in the ZFC and FC magnetization at 100 Oe.

No magnetic hysteresis loop appeared in the M-B measurements (Fig. 5.8(e)), i.e., $M_r = 0$, and $B_c = 0$ for at 1.8, 15, and 300 K. In contrast, clear hysteresis loops were observed previously for polycrystalline $ErCrO_3$ samples [274]. For the magnetization curve at 1.8 K, a gate magnetic field of ~ 650 Oe exists. When $0 \leq B \leq B_{\text{gate}} = 650$ Oe, the magnetization increases linearly from 0 to ~ 0.45 emu g^{-1}. Then, it quickly flattened when $B \sim 0.617$ T and attains $M_{\text{meas}} = 6.385(1)$ μ_B at 14 T (Figure 5.9(e)).

The CW fitting results in an effective PM magnetic moment of 10.20 μ_B, in agreement with the theoretical value of 10.334 μ_B, and a CW temperature of $-30.0(1)$ K (Table 5.3).

TmCrO₃

As shown in Fig. 5.7(f), The as-grown TmCrO$_3$ single crystal was determined to be $T_{\mathrm{N}}^{\mathrm{Cr}}$ = 125.9(1) K, which is consistent with a previous study of polycrystalline TmCrO$_3$ [55, 275]. Below $T_{\mathrm{N}}^{\mathrm{Cr}}$, the ZFC magnetization at 0 Oe was found to be negative. The magnetization measured at 50 and 100 Oe is positive and increases sharply within ~ 1 K. This is because Cr^{3+} spins order into a canted AFM state of the Γ_2 configuration (F_x, C_y, G_z) [276, 275]. Upon further cooling, the magnetization increased smoothly until it reached a maximum at $T_{\mathrm{max}}^{\mathrm{Cr}} \sim 74$ K. After that, the magnetization reduces smoothly and attains negative values suddenly at $T_{\mathrm{SR}} \sim 37.2$ K (for ZFC at 50 and 100 Oe) and ~ 40.1 (for FC at 100 Oe), followed by a sharp increase with positive values appearing again at a compensation temperature $T_{\mathrm{comp}} \sim 28.72$ K. The sharp drop observed at $\sim$ 40.1 (for FC at 100 Oe) could be ascribed to the spin reorientation transition of Cr^{3+} ions accompanied by a 90° rotation of the spins, that is, from one crystallographic axis to another, probably because of the competition between anisotropic exchanges and single-ion anisotropy [267]. This feature becomes smooth in the polycrystalline samples [55, 275]. The present study reveals a reversal of the magnetization behavior. The ZFC and FC magnetization at 100 Oe nearly coincided with each other. This is different from the observations with polycrystalline TmCrO$_3$ [275]. A magnetic phase transition was observed at $T_{\mathrm{N}}^{\mathrm{Tm}} \sim 19.6$ K, which probably correlates with the AFM order of Tm^{3+} spins. This was not observed in polycrystalline TmCrO$_3$ samples [275, 55]. As shown in Fig. 5.8(f), different magnetic hysteresis loops were observed as follows: (i) At 20 K, a parallelogram-shaped loop with $M_{\mathrm{r}} \sim 1.4$ emu g^{-1} and $B_{\mathrm{c}} \sim$ 111 Oe. (ii) At 1.8 K, a twisted loop with $M_{\mathrm{r}} \sim 0.75$ emu g^{-1}, $B_{\mathrm{c}} \sim 38.2$ Oe. The magnetization reaches $M_{\mathrm{meas}} = 2.868(1)$ μ_{B} at 14 T (Figure 5.9(f), Table 5.3).

$\mu_{\mathrm{eff\text{-}meas}} = 8.35$ μ_{B} was obtained by CW fitting, which is almost identical to the calculated theoretical value $\mu_{\mathrm{eff\text{-}theo}}^{\mathrm{total}} = 8.495$ μ_{B}, and $\theta_{\mathrm{CW}} = -90.6(4)$ K (Table 5.3).

YbCrO₃

It was determined that $T_{\mathrm{N}}^{\mathrm{Cr}} = 117.9(1)$ K for the YbCrO$_3$ single crystal (Fig. 5.7(g)), which is the lowest magnetic phase transition temperature of Cr^{3+} sublattices among all rare-earth orthochromates. Below $T_{\mathrm{N}}^{\mathrm{Cr}}$, the ZFC magnetization at 0 Oe reduces sharply to negative values, whereas the magnetization measured at 50 and 100 Oe increases sharply and attains the maximum values at $T_{\mathrm{max}}^{\mathrm{Cr}} \sim 99.3$ K (for ZFC at 50 Oe), 86.3 K (for ZFC at 100 Oe), and 69.6 K (for FC at 100 Oe), followed by smooth decreases to negative values at compensation temperatures $T_{\mathrm{comp1}} \sim 63.7$ K (for ZFC at 50 Oe), 47.5 K (for ZFC at 100 Oe), and 15.5 K (for FC at 100 Oe). The magnetization measured at 0, 50, and 100 (ZFC) Oe reappeared at $T_{\mathrm{comp2}} \sim 15.5$ K (for ZFC at 0 Oe), 17.6 K (for ZFC at 50 Oe), and 19.5 K (for ZFC at 100 Oe), whereas the magnetization measured at FC 100 Oe still remains negative. Below $T_{\mathrm{N}}^{\mathrm{Yb}} \sim 7$ K, all the ZFC magnetization curves flatten [277]. Notably, a large difference exists between the curves of the ZFC and FC magnetization 100 Oe. The FC magnetization at 100 Oe resembles that observed in the polycrystalline samples [278].

No magnetic hysteresis loop appears in the ZFC M-B curves measured at 15 and 300 K, whereas, a magnetic hysteresis loop with a similar shape was observed at 1.8 K ($M_{\mathrm{r}} \sim 0.24$ emu g^{-1}; $B_{\mathrm{c}} \sim 1200$ Oe), 25 K ($M_{\mathrm{r}} \sim 0.14$ emu g^{-1}; $B_{\mathrm{c}} \sim 1200$ Oe), and 40 K ($M_{\mathrm{r}} \sim 0.25$ emu g^{-1}; $B_{\mathrm{c}} \sim 1780$ Oe) (Fig. 5.8(g)). The magnetization $M_{\mathrm{meas}} = 0.883(1)$ μ_{B} at 1.8 K and 14 T, which is merely $\sim 17.7\%$ of $M_{\mathrm{sat\text{-}theo}}^{\mathrm{total}} = 5$ μ_{B} (Figure 5.9(g), Table 5.3).

The CW fitting results in $\mu_{\mathrm{eff\text{-}meas}} = 5.63$ μ_{B}, which is slightly lower than the theoretical value $\mu_{\mathrm{eff\text{-}theo}}^{\mathrm{total}} = 5.964$ μ_{B}, and $\theta_{\mathrm{CW}} = -17.4(4)$ K (Table 5.3).

LuCrO₃

The LuCrO$_3$ single crystal exhibited magnetic behaviors similar to those observed in single-crystal TmCrO$_3$ (Fig. 5.7(h) and (f)). It was determined that $T_{\mathrm{N}}^{\mathrm{Cr}} = 122.3(1)$ K, $T_{\mathrm{max}}^{\mathrm{Cr}} \sim 79$ K (for ZFC and FC at 100 Oe), $T_{\mathrm{SR}} \sim 33$ K (for ZFC at 50 Oe) and 31 K (for ZFC and FC at 100 Oe), $T_{\mathrm{comp2}} \sim 28$ K (for all data), and $T_{\mathrm{N}}^{\mathrm{Lu}} \sim 2.3$ K

for the LuCrO$_3$ single crystal. No clear difference was observed in the ZFC and FC magnetization measured at 100 Oe. The LuCrO$_3$ single crystal demonstrated magnetic behaviors different from those of previous polycrystalline samples [279].

Magnetic hysteresis loops were observed as follows: 1.8 K ($M_r \sim 0.13$ emu g^{-1}; $B_c \sim 25$ Oe), 15 K ($M_r \sim 0.14$ emu g^{-1}; $B_c \sim 32$ Oe), 25 K ($M_r \sim 0.054$ emu g^{-1}; $B_c \sim 125$ Oe), and 40 K ($M_r \sim 0.12$ emu g^{-1}; $B_c \sim 28$ Oe) (Fig. 5.8(h)). The magnetization $M_{meas} = 1.197(1)$ μ_B at 1.8 K and 14 T is merely $\sim 39.9\%$ of $M_{sat\text{-}theo}^{total} = 3$ μ_B (Figure 5.9(h), Table 5.3).

The CW fitting results in $\mu_{eff\text{-}meas} = 4.98$ μ_B, which is 28.1% higher than the theoretical value $\mu_{eff\text{-}theo}^{total} = 3.873$ μ_B, and $\theta_{CW} = -110.4(2)$ K (Table 5.3).

The magnetic behaviors of single-crystal RECrO$_3$ are summarized as follows: (i) TbCrO$_3$, DyCrO$_3$, and ErCrO$_3$ display similar temperature dependencies; as do in TmCrO$_3$ and LuCrO$_3$ single crystals. (ii) DyCrO$_3$ and ErCrO$_3$ do not exhibit negative magnetization, whereas the others do. (iii) Reversal magnetic behaviors (positive $\rightarrow$ negative $\rightarrow$ positive) occur for TmCrO$_3$, YbCrO$_3$, and LuCrO$_3$ single crystals. (iv) There exist no indications of magnetic ordering of Eu^{3+} ions, which may require lower temperatures. (v) Obvious magnetic hysteresis loops were observed for RECrO$_3$, except for ErCrO$_3$. (vi) The measured magnetization at 1.8 K and high applied magnetic fields plateaus for RECrO$_3$ (RE = Tb, Dy, Ho, Er, and Lu) single crystals. (vii) The measured effective PM moments of EuCrO$_3$ and LuCrO$_3$ are not consistent the with theoretical values. (viii) The applied magnetic field of 14 T is far less to saturate RECrO$_3$ at 1.8 K. (ix) Only HoCrO$_3$ demonstrates a positive CW temperature. Finally, the complex and coupled magnetic phase transitions of RE^{3+} (except for Eu^{3+}) and Cr^{3+} ions were observed. Unraveling the nature of the magnetic phase transitions necessitates a neutron scattering study with modern scattering techniques [74].

5.3.4 First-principles calculations

Superexchange interactions between the neighboring spins of transition metals can be realized through VCT via intermediate O^{2-} ions. During this process, the tilting of the

Table 5.4: Calculated NN exchange parameters J_1 and J_2, as well as the ratio J_2/J_1, Néel temperature T_N^{MFA} based on the mean-field approximation, t-e orbital overlapping degree $I_{t_{2g\downarrow}-e_{g\uparrow}}$, and the ordered effective moment $M_{\mathrm{Cr}^{3+}}$ of Cr^{3+} ions in $\mathrm{RECrO_3}$ orthochromates.

Parameter	J_1	J_2	J_2/J_1	T_N^{MFA}	$I_{t_{2g\downarrow}-e_{g\uparrow}}$	$M_{\mathrm{Cr}^{3+}}$
(unit)	(meV)	(meV)		(K)	(states^2/eV)	(μ_B)
$\mathrm{EuCrO_3}$	-1.420	-1.390	0.98	245.7	-2.2104	2.933
$\mathrm{GdCrO_3}$	-1.330	-1.210	0.91	224.8	-2.2743	2.931
$\mathrm{TbCrO_3}$	-1.140	-0.940	0.82	186.5	-2.3571	2.929
$\mathrm{DyCrO_3}$	-1.050	-0.760	0.72	165.9	-2.4040	2.928
$\mathrm{YCrO_3}$	-0.990	-0.630	0.63	151.0	-2.4387	2.930
$\mathrm{HoCrO_3}$	-0.940	-0.430	0.46	134.3	-2.4602	2.928
$\mathrm{ErCrO_3}$	-0.850	-0.230	0.27	112.4	-2.5064	2.927
$\mathrm{TmCrO_3}$	-0.720	-0.120	0.17	90.2	-2.5396	2.926
$\mathrm{YbCrO_3}$	-0.690	-0.001	0.01	80.5	-2.5786	2.925
$\mathrm{LuCrO_3}$	-0.760	-0.046	0.06	91.3	-2.5394	2.925

oxygen octahedral corresponds to the change of the metal-oxygen-metal bond angles and may lead to t_{2g} and e_g orbital overlapping. This facilitates the hopping of $t_{2g\uparrow}$ electrons via the bridge of O^{2-} ions to occupy the empty e_g band and the interacting with filled $t_{2g\downarrow}$ electrons at the same site, that is, the intersite t-e orbital hybridization [43, 122]. In the framework of t-e hybridization, the superexchange parameter J consists of the two following parts [43]:

$$J = J^\pi - J^\sigma_{\mathrm{hb}}, \tag{5.2}$$

where J^π denotes AFM coupling via the VCT of t_{2g}^3-O-t_{2g}^3, and J^σ_{hb} represents FM coupling via the VCT of t_{2g}^3-O-e_g^2. Both processes are schematically depicted in Fig. 5.10(a) for Cr^{3+} ions. For example, for a half-filled transition metal like Fe^{3+} ($t_{2g}^3 e_g^2$), the effect of t-e hybridization on superexchange interactions may not be evident because the electron hoppings of Fe^{3+} ($t_{2g\uparrow}^3$)-O^{2-}-Fe^{3+} ($t_{2g\downarrow}^3$) and Fe^{3+} ($t_{2g\uparrow}^3$)-O^{2-}-Fe^{3+} ($e_{g\downarrow}^2$) themselves are AFM couplings already [43, 122]. In contrast, for less than half-filled $3d$ electrons like Cr^{3+} ions ($t_{2g}^3 e_g^0$) in $\mathrm{RECrO_3}$ compounds, the t-e orbital hybridiza-
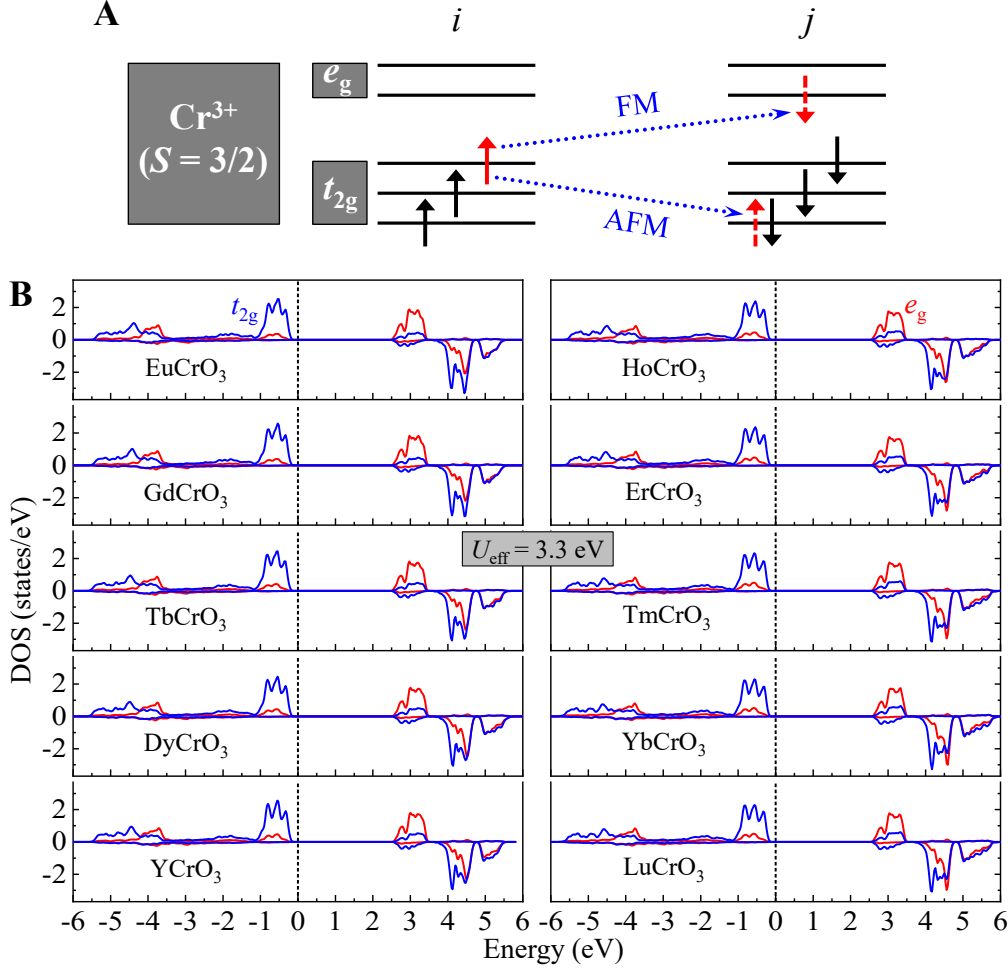
Figure 5.10: (a) Crystal field splitting of the fivefold degenerate d orbitals of Cr^{3+} ions ($3d^3$) in a cubic environment that splits the d-level into twofold degenerate e_g and threefold degenerate t_{2g} levels. The arrows represent the spins of chromium. We schematically show the virtual charge transfers, leading to FM and AFM states, respectively. (b) Calculated DOSs of t_{2g} and e_g orbitals (as marked) of Cr^{3+} ions in $RECrO_3$ (RE = Eu, Gd, Tb, Dy, Y, Ho, Er, Tm, Yb, and Lu) at $U_{eff} = 3.3$ eV. The positive and negative values denote high- and low-spin states, respectively. The vertical short-dotted lines at energy = 0 eV represent the Fermi level.

tion favors the VCT of Cr^{3+} ($t^3_{2g\uparrow}$)-O^{2-}-Cr^{3+} (e^0_g) [43, 280, 281]. Electron hopping of t^3_{2g}-O-e^0_g can increase the FM coupling component J^σ_{hb}. When RE^{3+} ions change from La to Lu in $RECrO_3$, the competition between the AFM (J^π) and the FM (J^σ_{hb}) components would probably result in a variation in T^{Cr}_N.

To quantitatively describe the Cr^{3+}-O^{2-}-Cr^{3+} superexchange interactions as well as the t_{2g}-e_g (t-e) orbital overlapping degree as a function of ionic radii of RE^{3+} ions, we calculated theoretically exchange parameters and electronic structures of $RECrO_3$ (RE = Y, Eu, Gd, Tb, Dy, Ho, Er, Tm, Yb, and Lu) compounds. We take into account
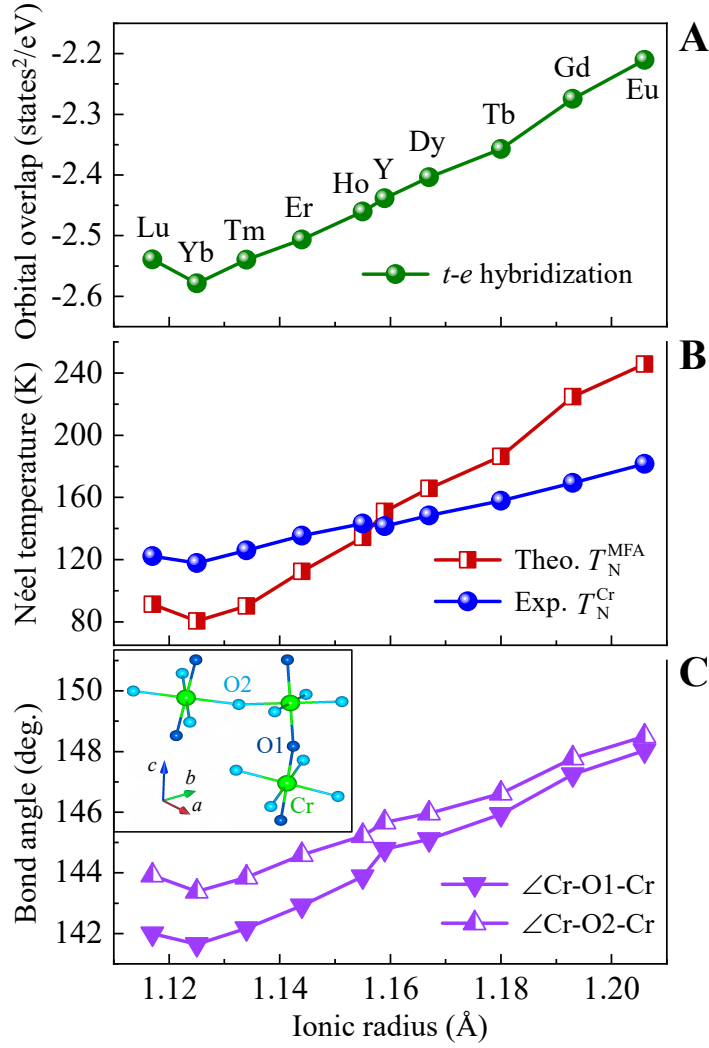
Figure 5.11: (a) Calculated t-e orbital overlapping degree ($I_{t_{2g\downarrow}-e_{g\uparrow}}$), (b) Experimental ($T_N^{Cr}$) and calculated ($T_N^{MFA}$) AFM transition temperatures, and (c) the theoretically optimized values of bond angles of $\angle$Cr-O1-Cr and $\angle$Cr-O2-Cr of RECrO$_3$ (RE = Eu, Gd, Tb, Dy, Y, Ho, Er, Tm, Yb, and Lu) compounds. The inset of **c** shows the geometry of the bond angles. The horizontal axis represents ionic radii of RE^{3+} ions.

mainly the nearest-neighbour (NN) exchange parameters of Cr^{3+} sublattices within the crystallographic ab plane (J_1) and along the c axis (J_2) as marked in Fig. 5.3(b). The values of J_1 and J_2 were extracted by the so-called energy mapping method with the four types (A-, C-, G-AFM, and FM) of magnetic structures. The total energy of each magnetic structure is obtained by DFT calculations, with projecting each collinear spin state onto the following spin Hamiltonian of a Heisenberg model

$$H = -\sum J_{ij} S_i \cdot S_j, \tag{5.3}$$

in which $J > 0$ represents FM interactions, and $J < 0$ denotes AFM couplings. With equation (5.3), one can solve J_1 and J_2 as [282, 283]

$$J_1 = (E_G + E_C - E_A - E_F)/8S^2, \quad \text{and} \tag{5.4}$$

$$J_2 = (E_G - E_C + E_A - E_F)/4S^2. \tag{5.5}$$

Thus, the Néel temperatures of RECrO$_3$ compounds can be calculated with the mean-field approximation (MFA) [282], i.e.,

$$T_N = \frac{2S(S+1)}{3k_B}(-4J_1 - 2J_2). \tag{5.6}$$

The density of states (DOSs) of the t_{2g} and e_g bands in RECrO$_3$ (RE = Y, Eu–Lu) compounds are calculated as shown as shown in Fig. 5.10(b), where the t-e orbital hybridization is obvious above the Fermi level. To depict the hybridization degree, the overlap of $t_{2g\downarrow}$ and $e_{g\uparrow}$ (Table 5.4) can be calculated via their DOS product over the corresponding energy region

$$I_{t_{2g\downarrow}-e_{g\uparrow}} = \int_{E_F}^{E_c} D_{t_{2g\downarrow}}(E) D_{e_{g\uparrow}}(E) dE, \tag{5.7}$$

where $D_{t_{2g\downarrow}}(E)$ and $D_{e_{g\uparrow}}(E)$ are the DOSs for $t_{2g\downarrow}$ and unoccupied $e_{g\uparrow}$ states of Cr^{3+} ions, respectively. E_F and E_c represent the Fermi level and cutoff energy of the $t_{2g\downarrow}$-$e_{g\uparrow}$ hybridization, respectively. With equation (5.7), the t-e hybridization in RECrO$_3$ orthochromates can be described (Table 5.4).

Different U_{eff}-value settings have a relative minor effect on the t-e hybridization; therefore, the calculations are based on the on-site Coulomb interactions between Cr^{3+} ions using a Hubbard U_{eff} = 3.3 eV derived under the framework of a linear-response ansatz, which gives a good agreement with the measured band gaps [284]. Meanwhile, the electron dispersions are not largely influenced by fixing U_{eff}, which assure the calculation of reliable t-e orbital hybridizations of RECrO$_3$ orthochromates by considering only the influence of RE^{3+} ions.

Based on foregoing discussions, the structural parameters of RECrO$_3$ orthochromates are optimized firstly. The calculations also indicate that the G-type AFM is the most stable magnetic structure for all the RECrO$_3$ orthochromates. Subsequently, we extracted the optimized values of J_1, J_2, Néel temperature T_N^{MFA}, and t_{2g}-e_g orbital overlapping degree $I_{t_{2g}-e_g}$ and listed them in Table 5.4. The calculated T_N^{MFA} coincides with the experimental T_N^{Cr} values (Table 5.3, Fig. 5.11(b)).

When RE^{3+} varies from Eu to Lu, the changes of the calculated $I_{t_{2g}-e_g}$ (Fig. 5.11(a)), T_N^{MFA} (Fig. 5.11(b)), and ∠Cr-O1-Cr and ∠Cr-O2-Cr (Fig. 5.11(c)) demonstrate a similar trend, indicating a strong correlation between them and a clear effect of RE^{3+} radii on the superexchange interactions. The calculated T_N^{MFA} coincided with the experimental T_N^{Cr} values. The average value ($\langle$∠Cr-O-Cr$\rangle$) of ∠Cr-O1(2)-Cr bond angles changes from $\langle$∠Cr-O-Cr$\rangle$ = 148.34° (EuCrO$_3$) to 142.81° (YbCrO$_3$), resulting in that the t-e hybridization ($I_{t_{2g}-e_g}$) changes from -2.2104 (EuCrO$_3$) to -2.5786 states^2/eV (YbCrO$_3$), and the corresponding T_N^{MFA} decreases from 245.7 (EuCrO$_3$) to 80.5 K (YbCrO$_3$). Therefore, the decreasing of the bond angles of ∠Cr-O1(2)-Cr facilitates the t-e hybridization by enhancing the FM component (J_{hb}^σ) within the entire superexchange interaction. Both the experimental and theoretical single-crystal studies produce the minimum AFM transition temperature for YbCrO$_3$ in the system (Fig. 5.11(b)), which is inconsistent with a previous study on polycrystal RECrO$_3$ samples where the minimum T_N and $\langle$∠Cr-O-Cr$\rangle$ occur to LuCrO$_3$ [122].

The present DFT calculations demonstrate that the magnetic anisotropy of Cr^{3+} sublattices can be tuned by RE^{3+} ions. The ratio of J_2/J_1 is a good parameter that inversely expresses anisotropy; it indeed reduces from $J_2/J_1 \sim 0.98$ (EuCrO$_3$) to $\sim$ 0.01 (YbCrO$_3$) as listed in Table 5.4 and strongly correlates with the values of bond angles of ∠Cr-O1(2)-Cr. As shown in Fig. 5.11(c), the angle of ∠Cr-O1-Cr is out of the ab plane (as schematically shown in the inset), and its value is smaller than that of ∠Cr-O2-Cr (within the ab plane). Therefore, it can be inferred that the VCT of $t_{2g\uparrow}^3$-O^{2-}-$t_{2g\downarrow}^3$ produces the major AFM spin interactions within the ab plane, whereas the VCT of $t_{2g\uparrow}^3$-O^{2-}-e_g^0 can generate FM couplings along the c axis. This is in good agreement with

the the previously proposed magnetic model: a canted AFM configuration with weak ferromagnetism along the c axis [227]. The difference between values of $\angle$Cr-O1(2)-Cr increases when RE^{3+} varies from Eu to Lu, indicating that the competition between in-plane AFM interactions and out-of-plane FM couplings becomes increasingly strong with an enhancement of FM interactions.

The largest difference between $\angle$Cr-O1-Cr and $\angle$Cr-O2-Cr occurs for YbCrO$_3$, leading to the smallest J_2/J_1 ratio (~ 0.01), and thus the largest magnetic anisotropy.

5.4 Conclusions

A series of RECrO$_3$ (RE = Y, Eu–Lu) single crystals have been grown with a laser-diode FZ furnace. The grown crystals are centimeter (gram)-scale with a good quality. Compared to previous ones grown by the flux method, The present RECrO$_3$ single crystals contain no impurity.

A systematic room-temperature X-ray powder diffraction study has been carried out on the as-grown single crystals. Structural refinements show that the RECrO$_3$ single crystals belong to orthorhombic crystal system with $Pbnm$ space group (No. 62). Lattice constants, unit-cell volume, atomic positions, and isotropic thermal parameters were extracted. Lattice parameters of a, b, c, and V display nearly a linear dependence on the ionic radii of RE (= Eu, Gd, Tb, Dy, Y, Ho, Er, Tm, and Yb) ions. There have been anomalies in lattice parameters of LuCrO$_3$ compound. These are ascribed to the fact that the Lu^{3+} ions are nonmagnetic and thus the magnetostriction effect resulting from $3d$-$4f$ couplings vanishes in LuCrO$_3$ compound. The evolutions of lattice constants display an anisotropy, thus showing that the elongations along the a and c axes remain almost the same and are much larger than that along the b axis.

Magnetization measurements were performed as functions of temperature and applied magnetic field on the grown single crystals, providing more reliable and intrinsic magnetic properties.

The t-e orbital hybridization was theoretically investigated by quantitatively calculating the t_{2g} and e_g orbital overlapping degree ($I_{t_{2g\downarrow}-e_{g\uparrow}}$) based on DOS calcula-

tions. As RE^{3+} ions change from Eu to Lu, the calculated AFM transition temperatures (T_N^{MFA}) demonstrate a similar trend with those determined experimentally (T_N^{Cr}). The changes in the $\angle$Cr-O1(2)-Cr bond angles strongly influence the weight factor of FM couplings (J_{hb}^{σ}) within the entire superexchanges interactions by (dis)favoring the VCT of $t_{2g\uparrow}^3$-O^{2-}-e_g^0. This may be the origin of the weak ferromagnetism appearing within the main AFM matrix of $RECrO_3$. The difference between $\angle$Cr-O1(2)-Cr bond angles results in a magnetic anisotropy between within the ab plane and along the c axis. The change of t-e hybridization coincides well with that of $\angle$Cr-O1(2)-Cr and that of T_N^{MFA}. The present research sheds light on the origin of the intriguing magnetism in the $RECrO_3$ system.

CHAPTER 6

NEUTRON POWDER DIFFRACTION AND INELASTIC NEUTRON SCATTERING STUDY ON SINGLE-CRYSTAL YCRO$_3$

6.1 Introduction

Most ferroelectric materials are perovskite-based oxides. In 1954, Looby and Katz replaced lanthanum in LaCrO$_3$ compound with yttrium during searching for new perovskite-type families and synthesized the YCrO$_3$ compound with an impurity of $\sim 2.5\%$ Cr$_2$O$_3$ using NaCl as the flux under a hydrogen atmosphere [26]. Based on the observation of a very weak extra Bragg peak, they indexed the X-ray powder-diffraction pattern with a monoclinic cell ($a = c = 7.61$ Å, and $b = 7.54$ Å) by doubling the fundamental perovskite unit cell [26]. One year later, the crystal structure was determined to be orthorhombic (with $Pbnm$ space group) with unit-cell constants $a = 5.238$, $b = 5.518$, and $c = 7.54$ Å [28]. This structure becomes more distorted as the pressure increases [285]. The lanthanide orthochromites of general formula RECrO$_3$ (RE = rare earth and Y) can be prepared by four different self-propagating high-temperature syntheses [286], i.e., the amorphous citrate precursor method [287], the conventional solid-state reaction method [74, 248], the hydrothermal synthesis [288], and the microwave-assisted technique [289].

Chemical substitution effect in the Y$_{1-x}$M$_x$CrO$_3$ (M = Mg, Ca, Sr, Ba) compound [290] and defect chemistry of the Ca-doped YCrO$_3$ compound [291] were investigated. The YCrO$_3$ compound in forms of bulk and thin film was suggested to be a candidate material for high-temperature thermistors [292, 293, 294]. Among the catalysts of ABO$_3$-type perovskite oxides (A = La, Y, Nd, Gd; B = Fe, Mn, Cr, Co) for the oxidation of 1,2-dichlorobenzene, the YCrO$_3$ compound was found to be the most active catalyst and was the only one that displayed no loss of its initial activity after several hours on stream [287]. The studies of nanocrystalline (un)doped YCrO$_3$ materials were reported [295, 296, 297]. The Nd-doped YCrO$_3$ nanoparticles display a semicon-

ducting feature and an enhanced dc conductivity as the Nd content increases, following the Dyre's free energy barrier model [297]. The magnetic configuration of the $YCrO_3$ compound below $T_N = 140$ K was proposed to be a canted antiferromagnetic (AFM) structure with antisymmetric spin superexchanges [298, 299, 300]. It was reported that there existed a spin reorientation of the Cr^{3+} moments in the $YCrO_3$ compound at ~ 60 K, corresponding to a rotation of the AFM easy axis [301]. Ferrimagnetism was found in the half-doped $YMn_{0.5}Cr_{0.5}O_3$ compound [302]. The magnetic interactions in bulk $YCrO_3$ compound were classified as classical three-dimensional isotropic Heisenberg universality according to the $ab\ initio$ calculations and Monte Carlo simulations based on a cubic structure with space group $Pm3m$ and lattice constant $a = 3.76$ Å [303]. To understand the ferroelectric anomaly occurring at ~ 473 K, the first-principles density functional theory calculations found that the noncentrosymmetric monoclinic structure (with space group $P2_1$) was the stablest one in view of its lowest energy [48]. The $YCrO_3$ compound was reported to be a relaxor ferroelectric material at about 450 K because of the local noncentrosymmetric structure [301]. The high-temperature magnetism (300–980 K) and crystallographic information (321–1200 K) were studied by a time-of-flight neutron powder diffraction [63], and it is of great interest that the structural information such as lattice constants, space group, bond angles, bond lengths, and the local distortion parameter have no response to the dielectric anomaly observed around 473 K [48]. Moreover, the DM interaction mechanism has been considered in the present thesis on our inelastic neutron scattering study of the $YCrO_3$ compound.

There has been a long-standing debate about the decision as to which structural symmetry is correct [26, 28, 63, 285, 287, 288], which necessitates a growth of the high-quality $YCrO_3$ single crystal [248, 304, 305, 306, 307] and a careful study of its crystalline and magnetic properties. Previously, small yttrium chromite single crystals with millimeter in size were grown from the PbF_2-B_2O_3 or the PbF_2-B_2O_3-KF flux in a platinum crucible [304, 305, 306].

In the present thesis, studies on the magnetization, crystal structure, thermal expansion, and local crystalline distortion of a pulverized $YCrO_3$ single crystal are car-

Table 6.1: Theoretical quantum numbers for $YCrO_3$ compound: spin S and the Landé factor g_J. We summarize the theoretical (theo) and measured (meas) (Fig. 6.1) values of effective (eff) chromium moment, μ_{eff}, and PM Curie temperature, θ_{CW}. R^2 represents the goodness of fit. $T_{\text{N}} = 141.5(1)$ K was extracted from our low-temperature (5–300 K) magnetization measurement. We also calculated the magnetic frustration factor f. The η factor is from Eq. (6.4). See detailed analyses in the text. The numbers in parenthesis are the estimated standard deviations of the last significant digit.

A $YCrO_3$ single crystal				
S		3/2		
g_J		2		
$\mu_{\text{eff\_theo}}\,(\mu_{\text{B}})$		3.873		
M versus T @ 0.3 T				
T (K)	300–400	400–540	540–640	640–750	750–980
$\mu_{\text{eff\_meas}}\,(\mu_{\text{B}})$	4.09(1)	3.97(1)	3.86(1)	3.70(1)	3.47(1)
θ_{CW} (K)	–331.6(1)	–290.3(1)	–245.7(2)	–172.0(2)	–64.8(2)
$f = |\theta_{\text{CW}}|/T_{\text{N}}$	2.34(1)	2.05(1)	1.74(1)	1.22(1)	0.46(1)
R^2	0.999	0.999	0.999	0.999	0.999
M versus $\mu_0 H$ @ T				
T (K)	300	500	700	900	
η	0.50(1)	0.63(1)	0.70(1)	0.72(1)	

ried out by PPMS DynaCool characterizations (300–980 K) and time-of-flight neutron powder-diffraction studies (321–1200 K). With the modified Brillouin function that includes a parameter η representing the degree of magnetic interactions and a CW law, the detailed magnetic parameters are uniquely determined such as the effective paramagnetic (PM) moment, PM CW temperature, the parameter η, and the frustration factor f to quantitatively understand the magnetism in $YCrO_3$ compounds. The space group of the crystal structure keeps $Pmnb$ in the entire temperature range. Anisotropic thermal expansion exists along the crystallographic a, b, and c axes with the largest incompressibility K_0 along the a axis, demonstrated by our fitting with the first-order Grüneisen function taking into account only the phonon contribution for an insulator. The Y, O1, and O2 ions show very large local distortion size Δ. The detailed local distortion modes of Y, Cr, O1, and O2 ions are extracted. It is noted that distinct atomic displacement and a large charge subduction exiting for the Y and O2 ions are indicative of their important roles in producing the dielectric anomaly of $YCrO_3$ compound.

Moreover, with a centimeter-sized YCrO$_3$ single crystal grown by a laser diode floating-zone (FZ) furnace [248], measurements are carried out on the chemical compositions, resistivity, and magnetization as functions of temperature and applied-magnetic field, heat capacity, time-of-flight neutron-powder diffraction based on a spallation neutron source, and single-crystal neutron diffraction based on a reactor. The chemical compositions of the grown YCrO$_3$ single crystal are nearly stoichiometric, and the YCrO$_3$ compound is a robust insulator.

With the inelastic neutron scattering (INS) study on a YCrO$_3$ single crystal and corresponding results. A Heisenberg model was build up, then details of the Heisenberg model was described. A linear spin wave theory was employed to solve Hamiltonian and get the results of dispersions. In subsection 6.3, I give the results of theoretical fit on the INS experimental data. Then, I discuss the results and provide the conclusions.

6.2 Methodology

Polycrystalline samples of YCrO$_3$ were prepared from stoichiometric mixtures of raw Y$_2$O$_3$ (ALFA AESAR, 99.9%) and Cr$_2$O$_3$ (ALFA AESAR, 99.6%) compounds by traditional solid-state reaction method [74]. After milling and mixing by a Vibratory Micro Mill (FRITSCH PULVERISETTE 0), the mixture was heated at 1000 °C for 24 h with an increasing and decreasing temperature speed of 200 °C/h in air to perform the process of pre-reaction. A similar heating procedure was carried out at 1100 °C. After that, the resultant green mixture was isostatically pressed into a ∼ 12 cm cylindrical rod with a pressure of 70 MPa. The rod was then sintered once at 1300 °C for 36 h in air. With above firing steps and milling and mixing with a ball of 50 mm in diameter after each heating process, we finally obtained a dense and homogenous pure polycrystalline YCrO$_3$ phase. High-quality single crystals of YCrO$_3$ were grown by the floating-zone (FZ) technique [74, 308] with a laser diode FZ furnace (Model: LD-FZ-5-200W-VPO-PC-UM) [248].

The DC magnetization was measured with a temperature increasing speed of 1 K/min at 0.3 T in the temperature range from 300 to 980 K on a Quantum Design

Physical Property Measurement System (PPMS DynaCool instrument). The M curves at 300, 500, 700, and 900 K versus applied magnetic field ($\mu_0 H$) up to 14 T were also recorded.

One as-grown YCrO$_3$ ($\sim$ 4 g) single crystal was pulverized with a Vibratory Micro Mill (FRITSCH PULVERISETTE 0), a time-of-flight neutron-powder diffraction study was performed on the POWGEN diffractometer (SNS, USA) from 12 to 1200 K at 0 T. The d band covers a range of 0.78–7.77 Å. The higher d band (1.7–7.77 Å) is able to monitor all magnetic Bragg reflections that are used to refine the low-temperature magnetic structure. Data from the lower d band (0.78–3.00 Å) give indication of all possible structural phase transitions. All collected time-of-flight neutron-powder diffraction data is analyzed with the software of FULLPROF SUITE. Single-crystal neutron diffraction was performed at the D23 diffractometer, located at the Institut Laue–Langevin (ILL), France. Inelastic neutron scattering experiment was carried out at the thermal neutron triple-axis-spectrometer - EIGER, located at the Paul Scherrer Institut (PSI), Swiss.

6.3   Results and discussion

6.3.1   High-temperature magnetism and crystallography in single-crystal YCrO$_3$

6.3.1.1 Magnetization versus temperature

To explore possible magnetoelectric coupling effect [309, 310] in a single-crystal YCrO$_3$ compound, a magnetization measurement was performed at DC field of 0.3 T from 300 to 980 K. That broad temperature regime is far above the weak ferromagnetic (FM) transition temperature, $\sim$ 140 K, so the magnetic anisotropy can be ignored. The temperature range covers the temperature point of $\sim$ 473 K, at which the dielectric anomaly was reported [48]. As shown in Fig. 6.1(a), The measured magnetization was transferred into magnetic moment μ_B per Cr^{3+} ion. With an increase of temperature, the magnetization decreases smoothly in the whole temperature range. The data

collected in pure PM state can be fit to

$$M = \frac{m}{T - \theta_{CW}},\qquad(6.1)$$

where m is a constant, and θ_{CW} is the PM CW temperature. The diamagnetism of Cr^{3+} ions is a temperature-independent constant, $\sim -1.1 \times 10^{-5}$ emu/mol [311], which is quite tiny so it can be neglected reasonably. Actually, the measured Cr^{3+} magnetization at 980 K and 0.3 T is equal to 4.33(1) emu/mol in this study, by far larger than its diamagnetism. The measured data was fit by the CW law, shown as the solid line in Fig. 6.1(a). This results in $\theta_{CW} = -264.0(1)$ K [Fig. 6.1(b)], and the goodness of fit $\chi^2 = 68.629$. As shown in Fig. 6.1, it is obvious that the fit is not comparable to the collected data, indicating that the CW temperature should have multiple components as a change in temperature. To confirm this, a constant, M_{Cr}, was included into the Eq. 6.1 to express the temperature-independent ordered magnetism of Cr^{3+} ions [51, 312], though the $YCrO_3$ compound stays in a pure PM state from 300 to 980 K. With the modified equation, the temperature-dependent magnetization data was fit and the resultant $M_{Cr} = -2.329(2)$ emu/mol, much smaller than the Cr^{3+} diamagnetism, which is physical nonsense.

The linear increase of the inverse magnetic susceptibility $\chi^{-1} = \frac{\mu_0 H}{M}$ with temperature in the pure PM state obeys well the molar susceptibility by CW law [308, 313, 314],

$$\chi^{-1}(T) = \frac{3k_B(T - \theta_{CW})}{N_A \mu_{eff}^2},\qquad(6.2)$$

where $k_B = 1.38062 \times 10^{-23}$ J/K is the Boltzmann constant, $N_A = 6.022 \times 10^{23}$ mol^{-1} is the Avogadro's number, and $\mu_{eff} = g\mu_B \sqrt{J(J+1)}$ is the effective PM moment. Here $J = S$ for the $YCrO_3$ compound. As shown in Fig. 6.2(a), the data in the temperature regimes of 300–400 K and 750–980 K (solid lines) was first fit, and they are extrapolated to the whole temperature range (dash-dotted lines). The two lines intersect at $T \sim 620$ K and are not able to cover all features of the data. In addition, there

145

Table 6.2: Refined lattice constants, unit-cell volume, atomic positions, isotropic thermal parameters (B), bond lengths, bond angles, and distortion parameter (Δ) of CrO6 octahedra, of the pulverized single-crystal $YCrO_3$ compound by the FULLPROF SUITE [204] with crystal structure ($Pmnb$) at 321, 750, and 1200 K.

	Pulverized $YCrO_3$ single crystal		
	(Orthorhombic, space group $Pmnb$, $Z = 4$)		
T (K)	321	750	1200
a (Å)	7.5332(3)	7.5615(3)	7.5976(3)
b (Å)	5.5213(2)	5.5280(2)	5.5367(3)
c (Å)	5.2418(2)	5.2636(2)	5.2921(2)
$\alpha(\beta, \gamma)$ (°)	90	90	90
V (Å^3)	218.02(1)	220.02(2)	222.61(2)
Y	$4c$	$4c$	$4c$
x	0.25	0.25	0.25
y	0.0689(8)	0.0675(9)	0.0649(10)
z	–0.0169(6)	–0.0155(7)	–0.0142(8)
B (Å^2)	4.4(13)	5.7(17)	5.4(19)
Cr	$4b$	$4b$	$4b$
(x, y, z)	(0, 0, 0.5)	(0, 0, 0.5)	(0, 0, 0.5)
B (Å^2)	3.8(12)	4.8(15)	4.5(16)
O1	$4c$	$4c$	$4c$
x	0.25	0.25	0.25
y	0.4654(7)	0.4660(9)	0.4668(10)
z	0.1053(8)	0.1039(9)	0.1017(11)
B (Å^2)	3.9(14)	5.2(18)	5.1(19)
O2	$8d$	$8d$	$8d$
x	0.0545(4)	0.0531(5)	0.0523(6)
y	0.3039(5)	0.3039(5)	0.3044(6)
z	–0.3082(5)	–0.3074(6)	–0.3070(7)
B (Å^2)	3.9(14)	5.2(18)	5.1(19)
Y-O11 (Å)	2.232(5)	2.238(6)	2.250(7)
Y-O12 (Å)	2.281(6)	2.291(7)	2.308(8)
Y-O21 (Å) ($\times 2$)	2.269(4)	2.282(5)	2.287(6)
Y-O22 (Å) ($\times 2$)	2.487(4)	2.507(5)	2.533(6)
<Y-O> (Å)	2.338(2)	2.351(2)	2.366(3)
Cr-O1 (Å) ($\times 2$)	1.972(1)	1.977(1)	1.983(2)
Cr-O21 (Å) ($\times 2$)	1.988(3)	1.989(3)	1.993(4)
Cr-O22 (Å) ($\times 2$)	1.999(3)	2.003(3)	2.010(3)
<Cr-O> (Å)	1.986(1)	1.990(1)	1.995(1)
$\angle$Cr-O1-Cr (°)	145.54(5)	145.98(6)	146.66(7)
$\angle$Cr-O2-Cr (°)	145.46(11)	145.96(12)	146.15(14)
Δ(Cr) ($\times 10^{-4}$)	0.306	0.285	0.329
R_p	7.83	7.44	6.88
R_{wp}	8.12	8.09	7.58
R_{exp}	4.49	4.31	4.06
χ^2	3.26	3.52	3.49

exists no anomaly in crystallographic information at 620 K as discussed below. There-fore, it is evident that χ^{-1} versus T obeys a piecewise linear function as shown in Fig. 6.2(b). Only if the inverse magnetic susceptibility was separated into five regimes, then it is able to model all features and fit well the data by Eq. 6.2. The corresponding fit results as well as the goodness of fit, R^2, are listed in Table 6.1. With increasing the temperature ranges, the measured effective PM moment, $\mu_{\text{eff\_meas}}$, decreases from 4.09(1) (300–400 K) to 3.47(1) μ_{B} (750–980 K), whereas the corresponding PM CW temperature, θ_{CW}, increases from –331.6(1) (300–400 K) to –64.8(2) K (750–980 K). In the temperature ranges of 300–400 K and 400–540 K, the measured effective PM moments $\mu_{\text{eff\_meas}} = 4.09(1)$ and 3.97(1) μ_{B}, respectively. Both values are larger than the calculated theoretical one $\mu_{\text{eff\_theo}} = 3.873$ μ_{B} supposing that all valence states are ionic and integer. The enhancement may be attributed to unquenched orbital angular momentum or the existence of local FM clusters with short-range spin interactions, i.e., magnetic polarons [127, 308, 315, 316]. In the temperature range 540–640 K, $\mu_{\text{eff\_meas}} = 3.86(1)$ μ_{B} is consistent with $\mu_{\text{eff\_theo}}$. At elevated temperature regimes of 640–750 and 750–980 K, $\mu_{\text{eff\_meas}}$ becomes smaller than $\mu_{\text{eff\_theo}}$. Based on these obser-vations, it is deduced that the above hypothesis on the formation of magnetic polarons is more reasonable. The increase of temperature easily destroys magnetic interactions, i.e., the forming ground of magnetic polarons.

It is interesting that in the whole studied temperature range, all deduced PM CW temperatures, θ_{CW}, are negative, indicating an AFM interaction, and largely deviated from the weak FM transition temperature $T_{\text{N}} = 141.5(1)$ K that was obtained from the magnetization study on the same single crystal at low temperatures of 5–300 K. The coappearance of AFM and FM phenomena may indicate a canted AFM state with strong magnetic frustration that can be characterized by a frustration parameter $f = \frac{|\theta_{\text{CW}}|}{T_{\text{N}}}$. The larger (than 1) the value of f, the stronger the corresponding magnetic frustration is [317]. As listed in Table 6.1, the f values are all larger than 1 except for the one in the temperature range 750–980 K, implying an existence of strong magnetic frustration and a complex low-temperature magnetic structure.
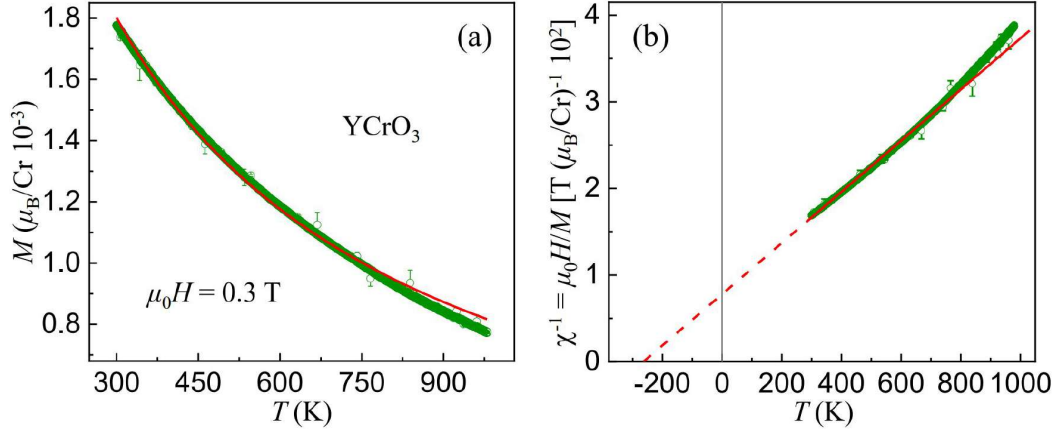
Figure 6.1: (a) Measured magnetization (M) of chromium ions in single-crystal YCrO$_3$ compound (circles) with an increase of temperature at $\mu_0 H = 0.3$ T ($\sim$ 40008 circles overlap each other so most of the error bars are embedded into the symbols). The solid line is a fit by Eq. (6.1) as described in the text. (b) Corresponding inverse magnetic susceptibility χ^{-1} (circles) of chromium ions in single-crystal YCrO$_3$ compound versus temperature. The solid line indicates a CW behavior of the data as described by Eq. (6.2) from 300 to 980 K, which was extrapolated to $\chi^{-1} = 0$ (dashed line) to show the PM Curie temperatures θ_{CW}.
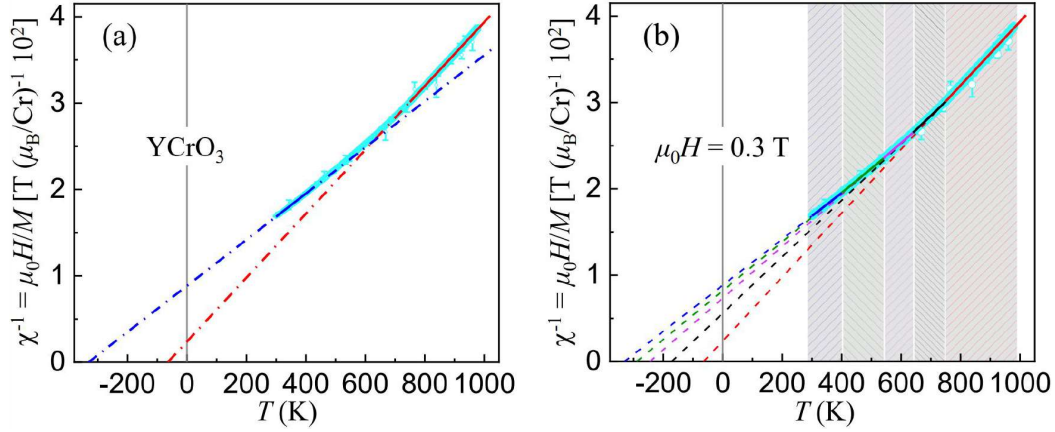
Figure 6.2: (a) Inverse magnetic susceptibility χ^{-1} (circles) of chromium ions in single-crystal YCrO$_3$ compound versus temperature. The solid lines indicate CW behaviors of the data as described by Eq. (6.2) at respective temperature regimes of 300–400 K and 750–980 K. They were extrapolated down to $\chi^{-1} = 0$ (dash-dotted lines) to show the PM Curie temperatures θ_{CW} and up to 1020 K (dash-dotted line). The fit results are listed in Table 6.1. (b) Inverse magnetic susceptibility χ^{-1} (circles) of chromium ions in single-crystal YCrO$_3$ compound versus temperature. The solid lines indicate CW behaviors of the data as described by Eq. (6.2) at respective temperature regimes of 300–400 K, 400–540 K, 540–640 K, 640–750 K, and 750–980 K. They were extrapolated to $\chi^{-1} = 0$ (dashed lines) to show the PM Curie temperatures θ_{CW}. The fit results are listed in Table 6.1.

The values of f for the REMnO$_3$ compounds were reported to be 10.1 (YMnO$_3$), 10.3 (LuMnO$_3$), and 7.8 (ScMnO$_3$) [318]. Within these compounds, the Mn ions form

148
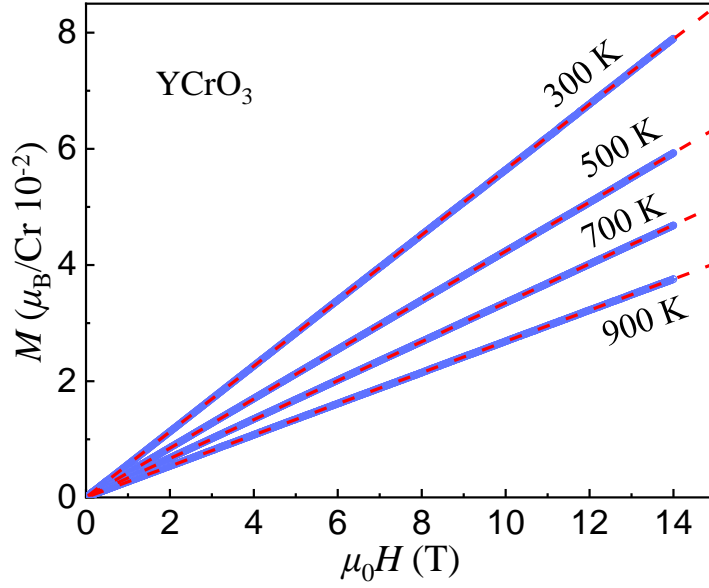
Figure 6.3: Measured magnetization per chromium ion in single-crystal YCrO$_3$ compound (circles) as a function of applied magnetic fields up to 14 T at 300, 500, 700, and 900 K. The dashed lines are fits to Eq. (6.3). See detailed analysis in the text. Error bars are standard deviations and embedded into the circles because collected data points (~ 1600) at respective temperatures overlap each other.

a triangular lattice in the hexagonal structure, therefore, there exists a geometrical spin frustration. It is pointed out that the crystallographic structure of YCrO$_3$ compound does not accommodate any geometric frustration [313, 314, 319, 320, 321]. The magnetic frustration in YCrO$_3$ compound originates from the observation of AFM and FM behaviors, which necessitates a determination of the detailed low-temperature magnetic structure.

6.3.1.2 Magnetization versus applied magnetic field

In this section, I mainly focus on the measurement of high-temperature (≥ 300 K) magnetic properties. As shown in Fig. 6.3, the magnetization was monitored as a function of applied magnetic field up to 14 T at 300, 500, 700, and 900 K with a small piece of randomly orientated single crystal (~ 14.91 mg). While increasing applied magnetic field, the magnetization increases linearly at all temperatures. The measured magnetic moment at 300 K and 14 T is 0.079(1) μ_B/Cr, mere $\sim 2.63\%$ of the theoretical saturated (sat) Cr^{3+} moment $\mu_{\text{sat\_theo}} = g_J S \mu_B = 3$ μ_B (Table 6.1).

For theoretically isolated atoms, the change of magnetization with applied mag-
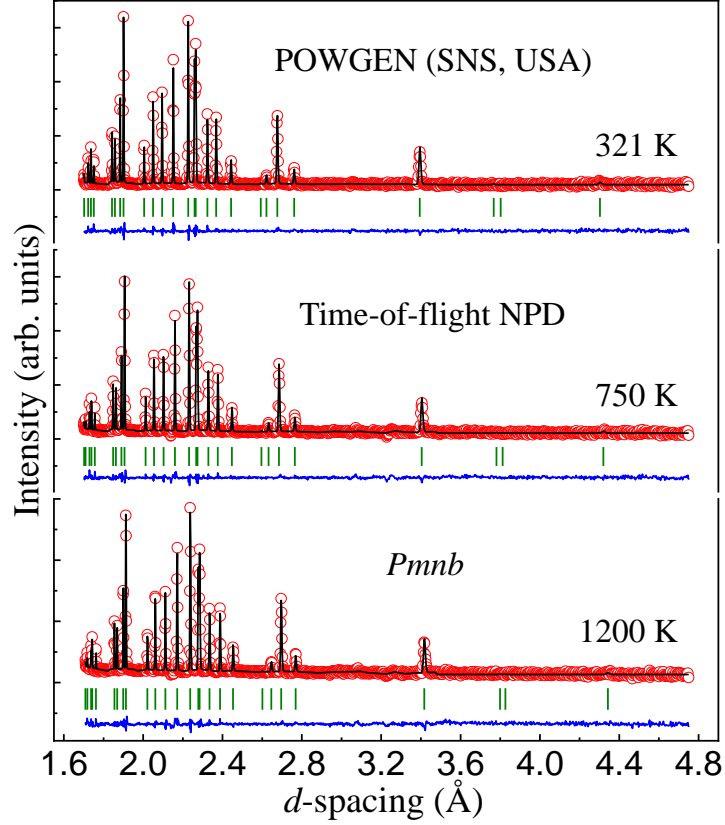
Figure 6.4: Observed (circles) and calculated (solid lines) time-of-flight neutron powder-diffraction patterns of a pulverized $YCrO_3$ single crystal, collected on the POWGEN diffractometer (SNS, USA) at 321, 750, and 1200 K. The vertical bars mark the positions of nuclear Bragg reflections ($Pmnb$ space group). The lower curves represent the difference between observed and calculated patterns.

netic field at high temperatures obeys a Brillouin function given by [322]

$$M(\mu_0 H) = \eta M_{theo}^{sat} B_J(x), with \qquad (6.3)$$

$$B_J(x) = \frac{2J+1}{2J} coth\left(\frac{2J+1}{2J}x\right) - \frac{1}{2J} coth\left(\frac{2J+1}{2J}x\right)$$

where $M_{theo}^{sat} = g_J J \mu_B = 3\ \mu_B$ is the theoretical value of the saturated mole moment, $J = \frac{3}{2}$ is the total angular momentum, and $x = \frac{g_J J \mu_B \mu_0 H}{k_B T}$. Equations (6.4) were used to fit the collected data as shown in Fig. 6.3 (dashed lines). The corresponding η values at respective temperatures are listed in Table 6.1. When $\eta = 1$, i.e., the theoretical case, there exists no magnetic exchange. With a decrease of temperature, spin interactions and the resultant magnetic order become possible. Since rotating and aligning spin moments of an antiferromagnet necessitate a very strong applied

150
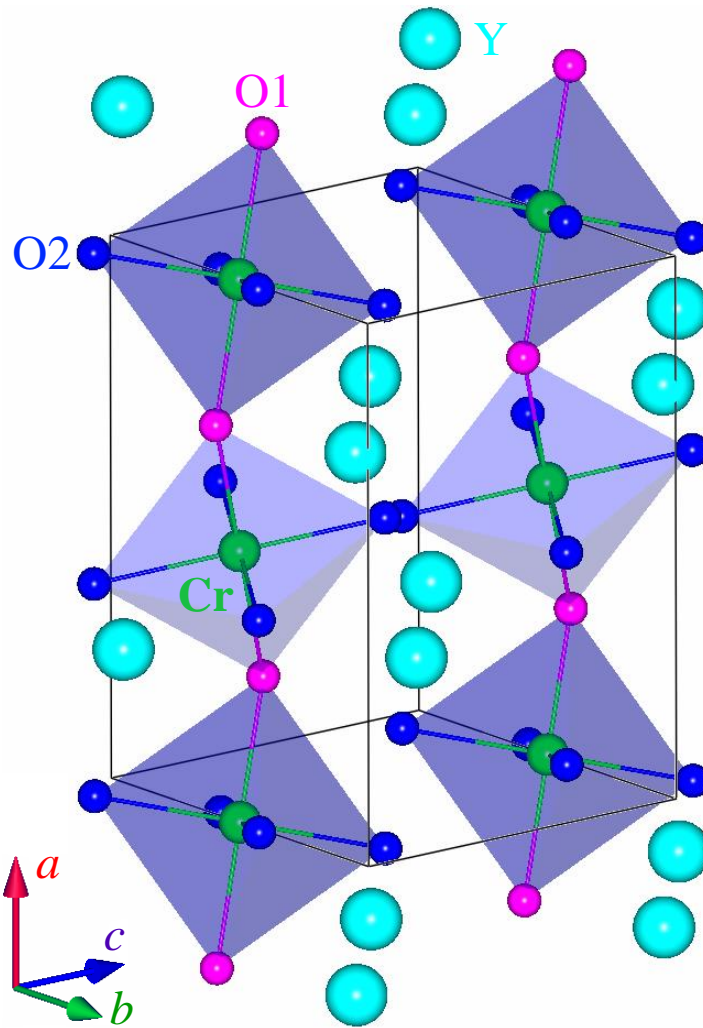
Figure 6.5: Crystal structure ($Pmnb$ space group) with one unit cell (solid line) of the YCrO$_3$ single crystal within the present experimental accuracy at the studied temperature regime of 321–1200 K. The solid balls were labeled as Y, Cr, O1, and O2 ions, respectively.

magnetic field, depending on detailed exchange parameters [267, 323, 324], measured magnetization will deviate from the value of the saturation moment, leading to the η value getting smaller than 1 and becoming smaller and smaller with an increase of AFM domains. As temperature decreases, the η values decrease, in agreement with the increase of f factors (Table 6.1).

6.3.1.3 Time-of-flight neutron powder diffraction

To explore possible structural phase transitions of YCrO$_3$ compounds above room temperature, a time-of-flight neutron powder-diffraction study was carried out from 321 to
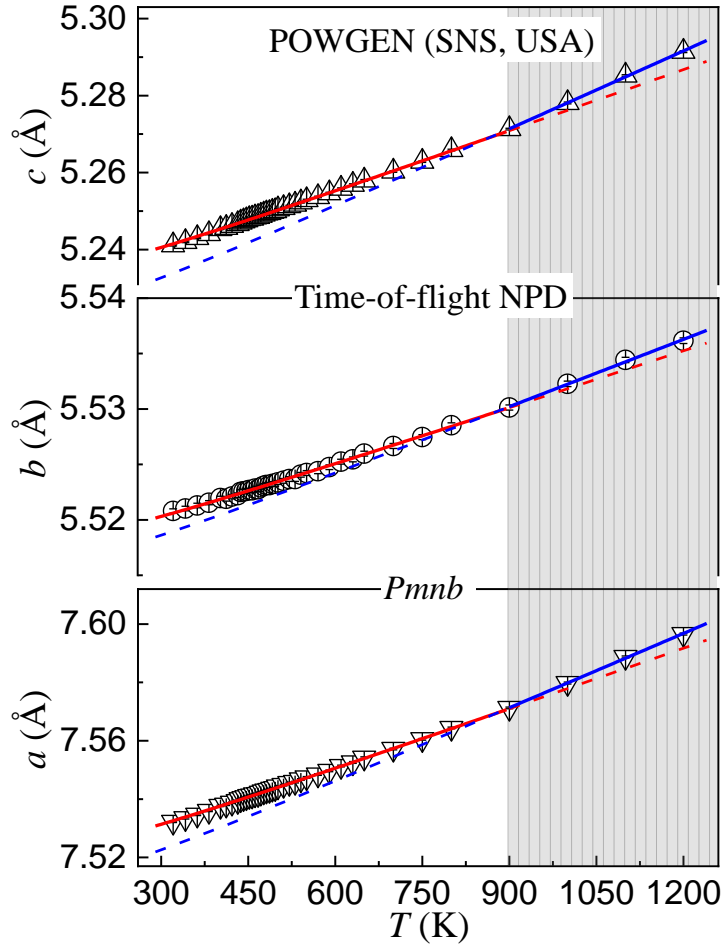
Figure 6.6: Temperature dependence of the lattice constants, a, b, and c, of the pulverized $YCrO_3$ single crystal (void symbols), which was extracted from our FULL-PROF [204] refinements based on the time-of-flight neutron powder-diffraction data collected on POWGEN diffractometer (SNS, USA) between 321 and 1200 K. The solid lines are theoretical estimates of the variation of structural parameters at the respective temperature regimes of 321–900 K and 900–1200 K, using the Grüneisen model [Eqs. (6.4) and (6.5)] with Debye temperature θ_D = 580 K, and extrapolated to the entire temperature range of 321–1200 K (dashed lines). Error bars are standard deviations obtained from our FULLPROF [204] refinements in the $Pmnb$ symmetry.

1200 K. Three representative neutron powder-diffraction patterns are shown in Fig. 6.4.

The Bragg peak shape was carefully checked, especially for the peaks located in the

low-d regime. All collected Bragg peaks were well indexed with the space group

$Pmnb$ (orthorhombic structure). No additional peak and possible peak splitting were

observed. Therefore, it could be concluded that within the present experimental ac-

curacy, there exists no structural phase transition for the $YCrO_3$ compound from 321

to 1200 K. The refined crystal structure in one unit cell was depicted in Fig. 6.5. The

refined structural parameters at 321, 750, and 1200 K, including lattice constants, unit-
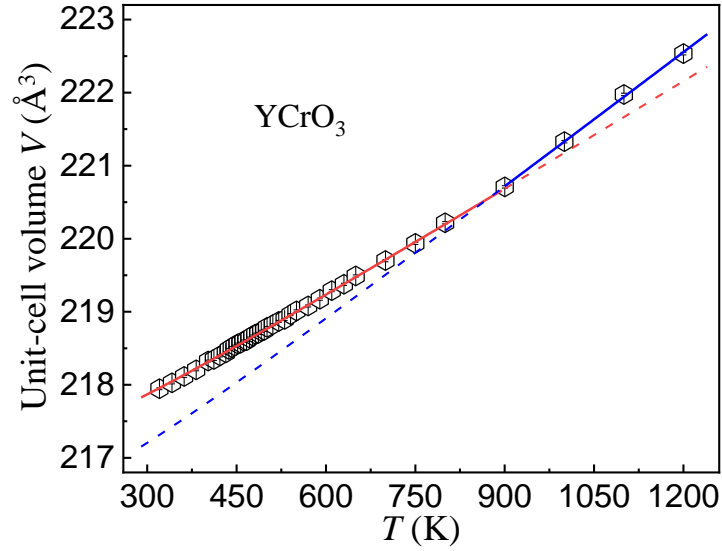
Figure 6.7: Temperature-dependent unit-cell volume, V, of the YCrO$_3$ single crystal (void symbols). This was extracted from our FULLPROF [204] refinements based on the time-of-flight neutron powder-diffraction data collected on POWGEN diffractometer (SNS, USA) between 321 and 1200 K. The solid lines are theoretical estimates of the variation of V within respective temperature regimes using the Grüneisen model [Eqs. (6.4) and (6.5)] with Debye temperature Θ_D = 580 K and extrapolated to the whole temperature range (dashed lines). Error bars are standard deviations obtained from our FULLPROF [204] refinements in the $Pmnb$ symmetry.

cell volume, atomic positions, and thermal parameters are all listed in Table 6.2, where the extracted bond lengths, bond angles, and the distortion parameter of CrO$_6$ octahedra are also displayed. The low values of the reliability factors validate the goodness of the refinements.

6.3.1.4 Anisotropic thermal expansion

Figure 6.6 shows the refined lattice constants, a, b, and c, at all temperatures from 321 to 1200 K. The corresponding change in unit-cell volume (V) was depicted in Fig. 6.7. For the insulating YCrO$_3$ compound, the contribution of lattice vibrations to the thermal expansion of the lattice configuration (ε) is much larger than that of electrons. Therefore, the temperature-dependent nonmagnetic contribution component of the thermal expansion is mainly from phonons. This can approximately be calculated based on the Grüneisen function at zero pressure with the first-order fashion [127, 325,

Table 6.3: Fit parameters of the lattice configuration ϵ (a, b, c, and V) of YCrO$_3$ compound with Eqs. (6.4) and (6.5), where $N = 5$ and $k_\mathrm{B} = 1.38062 \times 10^{-23}$ J/K, at the respective temperature regimes of 321–900 K and 900–1200 K (Figs. 6.6 and 6.7).

T (K)	321–900	900–1200
Θ_D (K)	580	580
ϵ_0^a (Å)	7.52180(2)	7.51080(7)
ϵ_0^b (Å)	5.51790(4)	5.51580(1)
ϵ_0^c (Å)	5.23320(3)	5.22330(5)
ϵ_0^V (Å^3)	217.190(1)	216.350(9)
K_0^a (Å/J)	$3.380(7) \times 10^{17}$	$4.160(5) \times 10^{17}$
K_0^b (Å/J)	$8.390(1) \times 10^{16}$	$9.910(8) \times 10^{16}$
K_0^c (Å/J)	$2.590(4) \times 10^{17}$	$3.300(8) \times 10^{17}$
K_0^V (Å^3/J)	$2.400(7) \times 10^{19}$	$3.000(2) \times 10^{19}$
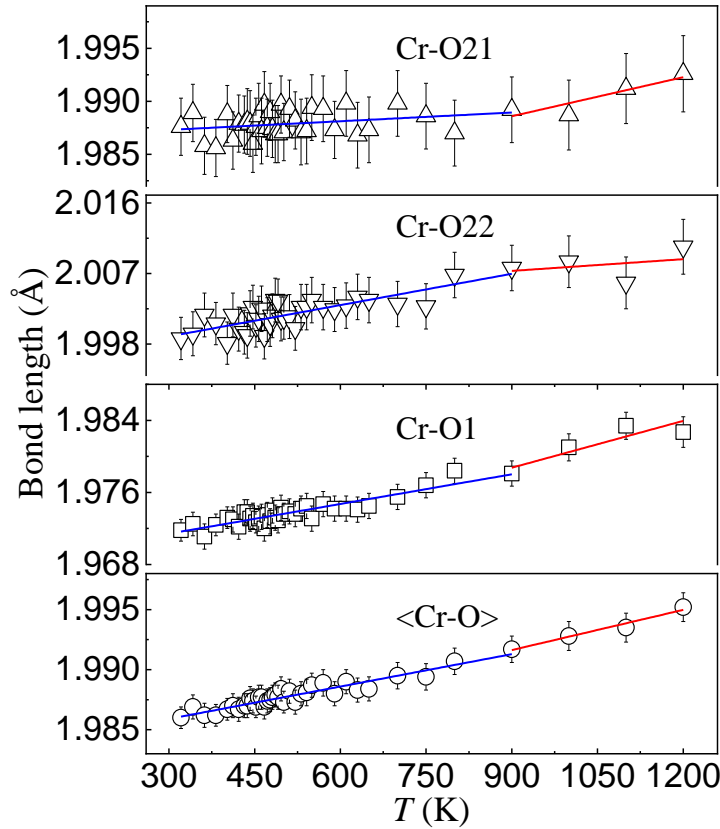
Figure 6.8: Temperature-dependent bond lengths of Cr-O1, Cr-O21, and Cr-O22 as well as the averaged bond length of Cr-O, i.e., <Cr-O>, of the single-crystal YCrO$_3$ compound (void symbols). This was extracted from our time-of-flight neutron powder-diffraction study. Error bars are standard (for the Cr-O1, Cr-O21, and Cr-O22 bond lengths) or combined (for the Cr-O bond length) deviations. Solid lines are linear fits.

326],

$$\epsilon(T) = \epsilon_0 + K_0 U, \qquad (6.4)$$

where ε_0 is the lattice configuration at 0 K, K_0 is a constant that reflects the incompressibility of the compound, and the internal energy U can be estimated based on the Debye approximations,

$$U(T) = 9Nk_{\mathrm{B}}T\left(\frac{T}{\Theta_{\mathrm{D}}}\right)\int_0^{\Theta_{\mathrm{D}}/T}\frac{x^3}{e^x - 1}dx, \qquad (6.5)$$

where $N = 5$ is the number of atoms per formula unit, and $\Theta_{\mathrm{D}} = 580$ K is the Debye temperature that can be determined by the upturn point of the $\varepsilon - T$ curve [127]. With the above Eqs. (6.4) and (6.5), the lattice configurations (a, b, c, and V) of YCrO$_3$ compound were fit in two temperature ranges of 321–900 K and 900–1200 K (solid lines). The fits were then extrapolated to the whole temperature regime (dashed lines) as shown in Figs. 6.6 and 6.7. The fit results are shown in Table 6.2. Within each temperature regime, as a whole, the temperature-dependent lattice configurations agree well with the theoretical estimations. However, at the boundary of the two temperature regimes, i.e., around 900 K, there exists an anomaly.

For lattice constants a, b, and c, the incompressibility K_0 in the temperature range 900–1200 K is larger than that in $T = 321$–900 K, which may be attributed to more developed phonon modes above 900 K. In both temperature regimes, $K_0^a > K_0^c > K_0^b$ indicates an anisotropic thermal expansion along the three crystallographic directions. This jointly results in the unit-cell volume expansion as shown in Fig. 6.7. $(K_{0(900-1200\mathrm{K})}^a - K_{0(321-900\mathrm{K})}^a)/(K_{0(321-900\mathrm{K})}^a) = 22.71\%$, $(K_{0(900-1200\mathrm{K})}^b - K_{0(321-900\mathrm{K})}^b)/(K_{0(321-900\mathrm{K})}^b) = 18.24\%$, and $(K_{0(900-1200\mathrm{K})}^c - K_{0(321-900\mathrm{K})}^c)/(K_{0(321-900\mathrm{K})}^c) = 27.80\%$, which implies that the temperature-dependent relative increase of K_0 is the largest one along the crystallographic c axis.

For the YMnO$_3$ compound, a clear structural phase transition with a change in space group from centrosymmetric $P6_3/mmc$ to $P6_3cm$ occurs at 1258(14) K [328,
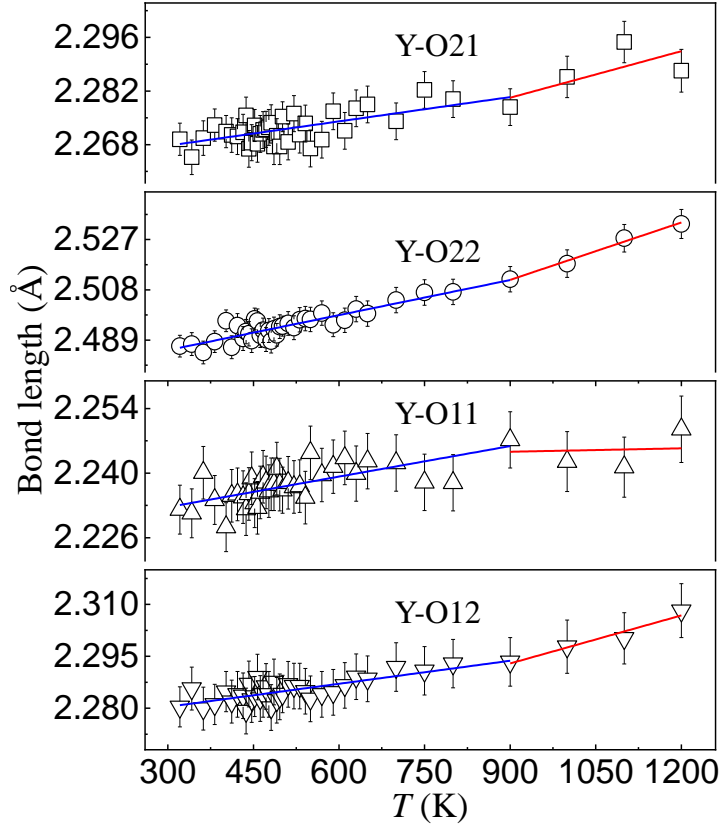
Figure 6.9: Lengths of Y-O11, Y-O12, Y-O21, and Y-O22 bonds of the single-crystal YCrO$_3$ compound versus temperature varying from 321 to 1200 K (void symbols), which was extracted from our time-of-flight neutron powder-diffraction study. Error bars are standard deviations. Solid lines are linear fits.

329, 330]. This structural phase transition temperature is much higher than its improper ferroelectricity transition temperature around 914 K and its AFM transition temperature around 76 K [318]. Clear anomalies were observed in the lattice constants a and c and unit-cell volume V as well as the distance between Y1 and Y2 ions, the displacements of O3 and O4 ions, the tilting angle of apical O1-Mn-O2, and the lengths of Y1-O bonds, accompanying the structural phase transition [328]. Moreover, an isosymmetric phase transition was found at $\sim$ 900 K, accompanied by a sharp decrease in polarization and anomalies in physical properties, which was attributed to a Y-O hybridization [328]. In our study, for the YCrO$_3$ compound, structural anomalies were observed in lattice configurations (a, b, c, and V) as well as Cr-O and Y-O bond lengths around 900 K (as shown below). However, no clear change in the space group was distinguished. The preservation of the $Pmnb$ space group of YCrO$_3$ compound may suggest that an isosymmetric structural phase transition happens around
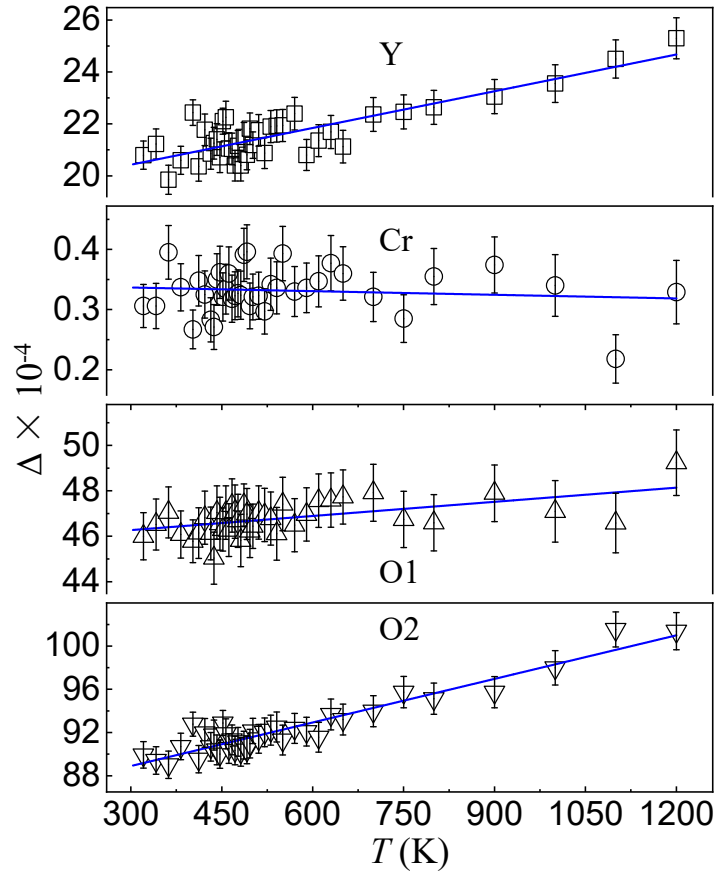
Figure 6.10: Temperature variation of the distortion parameter Δ of Y, Cr, O1, and O2 ions of the single-crystal $YCrO_3$ compound (void symbols), calculated by Eq. 6.6 from the refined structural parameters between 321 and 1200 K. The error bar was estimated based on the propagation law of errors [327]. The solid lines are tentative linear fits.

900 K [328, 331].

6.3.1.5 Bond lengths of Cr-O and Y-O

To analyze detailed local crystalline environments of Cr and Y ions in the $YCrO_3$ compound, we extracted and plotted the lengths of Cr-O21, Cr-O22, and Cr-O1 [Fig. 6.8] and Y-O21, Y-O22, Y-O11, and Y-O12 [Fig. 6.9] bonds. The averaged Cr-O bond length, i.e., $<$Cr-O$>$, was calculated and plotted in addition [Fig. 6.8]. We tentatively refined the bond lengths with a piecewise linear function in the entire temperature regime with two ranges of 321–900 K and 900–1200 K. As shown in Figs. 6.8 and 6.9, the fit results (shown as solid lines) clearly display an anomaly around 900 K, consistent with our observation in the lattice configurations of a, b, c, and V [Figs. 6.6 and 6.7]. From the temperature range of 321–900 K to 900–1200 K, the slope of the

157
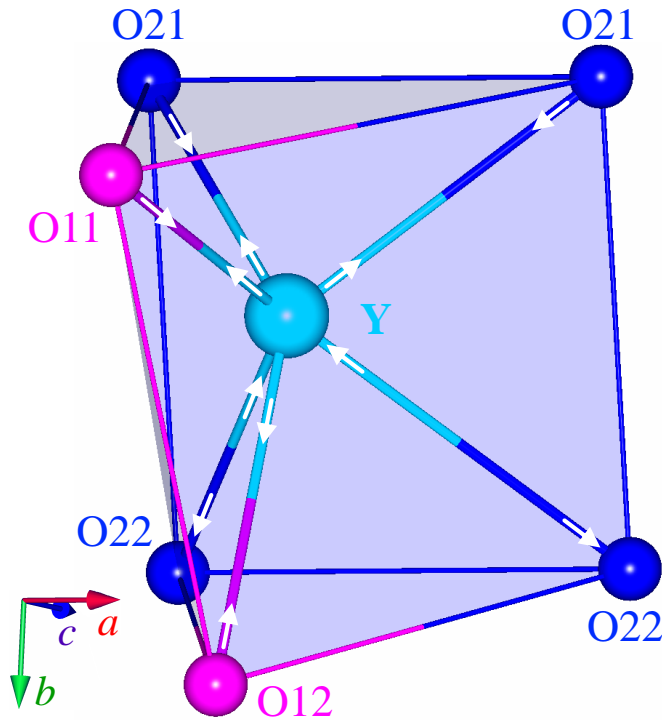
Figure 6.11: Local pentahedron environment of Y ions in the single-crystal YCrO$_3$ compound, which was extracted based on our FULLPROF refinements [204]. The Y, O11, O12, O21, and O22 ions are labeled as displayed. Detailed bond lengths of Y-O11, Y-O12, Y-O21 (×2), and Y-O22 (×2) are listed in Table 6.2. The arrows sitting on the Y-O bonds schematically show the deduced pentahedron distortion configuration.

bond length versus T curve obviously increases for the Cr-O21, Cr-O1, Y-O21, Y-O22, and Y-O12 bonds, e.g., for the Y-O22 bond, it increases from 4.42×10^{-5} to 7.23×10^{-5} Å/K, by $\sim 63.57\%$, whereas the slope sharply decreases for the Cr-O22 and Y-O11 bonds, e.g., for the Cr-O22 bond, it decreases by $\sim 62.59\%$.

By comparing all Cr-O and Y-O bonds, it was found that only the length of Cr-O21 bond increases in an inconspicuous way from 321 to 900 K, implying a small contribution to the thermal expansion of the lattice configuration. From 900 to 1200 K, the upturn of the lattice configuration (a, b, c, and V) was attributed to an increase of the lengths of Cr-O21, Cr-O1, Y-O21, Y-O22, and Y-O12 bonds. It is reasonable to deduce that the anisotropic thermal expansion in lattice constants a, b, and c is from different increases in lengths along the different directions of Cr-O and Y-O bonds.
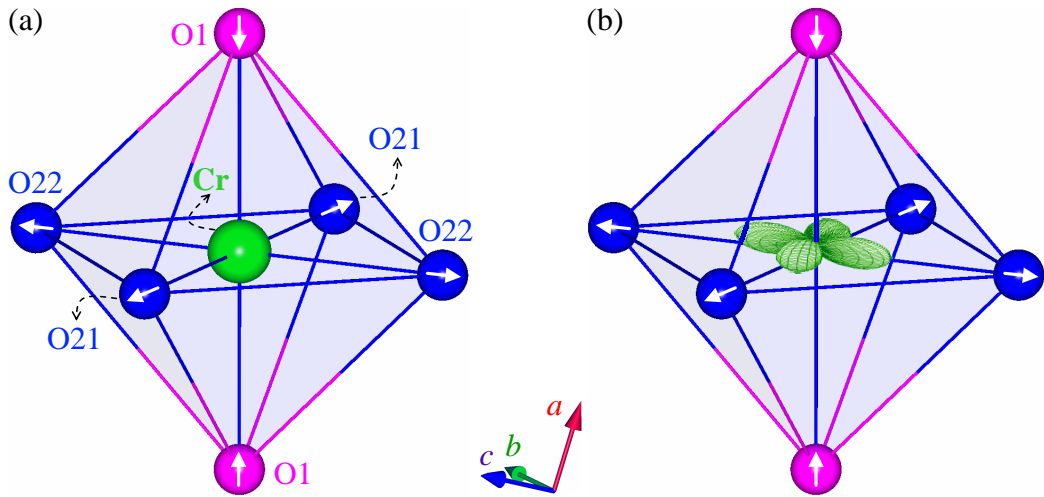
Figure 6.12: (a) Local octahedral environment of Cr ion in the single-crystal $YCrO_3$ compound, which was extracted based on our FULLPROF refinements [204]. The arrows drawn through the oxygen ions ($2\times$O1, $2\times$O21, and $2\times$O22) schematically show the deduced octahedral distortion mode. Representative refined bond lengths of Cr-O1, Cr-O21, and Cr-O22 at 321, 750, and 1200 K are listed in Table 6.2. (b) In such octahedral geometry, we schematically drew the approximate $3d_{yz}$ orbital shape in real space.
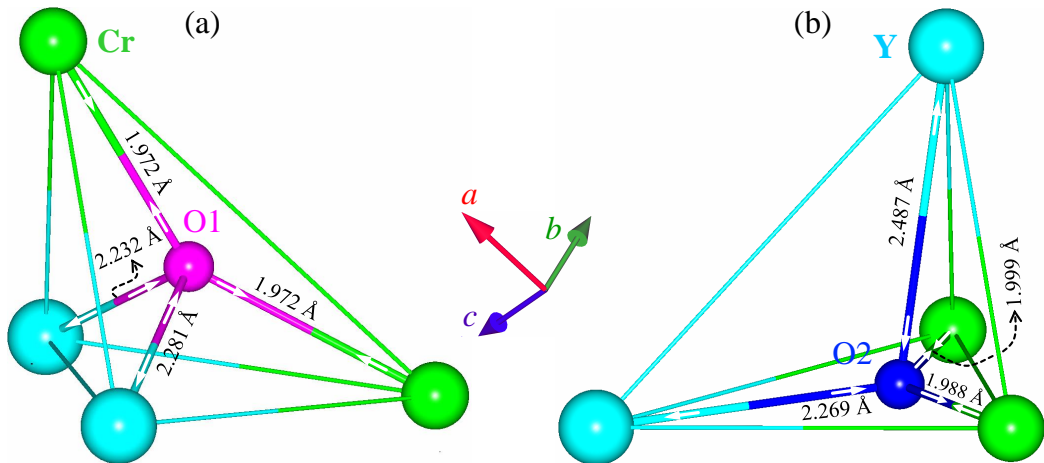
Figure 6.13: Local tetrahedral environments of O1 (a) and O2 (b) ions in the single-crystal $YCrO_3$ compound, which was extracted based on our FULLPROF refinements [204]. The Y, Cr, O1, and O2 ions are labeled as displayed. Detailed bond lengths of O1-Cr ($\times 2$), O1-Y, O2-Cr, and O2-Y at 321 K were marked. The arrows sitting on the O-Y and O-Cr bonds schematically show the deduced tetrahedral distortion modes.

6.3.1.6 Local distortion modes of Y, Cr and O ions

Identifying a detailed local crystalline environment is essential in determining electronic structure, spin configuration, orbital degeneracy and crystal field effect of $3d$-, $4d$-, $5d$-, or $4f$- compounds [74]. A quantitative measurement of the magnitude of

a local crystalline environment can be evaluated by the local distortion parameter Δ defined as [74, 159, 308, 332]

$$\Delta = \frac{1}{n} \sum_{i=1}^{n} \left(\frac{d_n - \langle d \rangle}{\langle d \rangle} \right), \tag{6.6}$$

where n is the coordination number, d_n is the bond length along one of the n coordination directions, and $\langle d \rangle$ is the averaged bond length. With Eq. 6.6, the local distortion parameter Δ was calculated as a function of temperature for the Y, Cr, O1, and O2 ions as shown in Fig. 6.10. For the $3d$ Cr^{3+} ions in single-crystal $YCrO_3$ compound, it is interesting that the local distortion parameter Δ keeps almost a constant in the whole temperature range, displaying no response to the previously reported dielectric anomaly [48]. The averaged Δ value of Cr^{3+} ions from 321 to 1200 K is of $\sim$ 3.3×10^{-5} that is approximately two orders of magnitude lower than that of $3d$ Kramers Mn^{3+} ions in the Jahn-Teller (JT) distorted regime of single-crystal $La_{\frac{7}{8}}Sr_{\frac{1}{8}}MnO_3$ compound [308]. This sharp comparison dramatically demonstrates the importance of local crystalline environment.

It is noted that the Y, O1, and O2 ions show huge Δ values, almost two orders of magnitude larger than that of Cr ions. At 321 K, $\Delta(O2) \approx 1.96\Delta(O1) \approx 4.32\Delta(Y)$ $\approx 293.89\Delta(Cr)$, indicating a significant local crystalline environmental effect of O2, O1, and Y ions on the property of a $YCrO_3$ compound. This urges us to figure out the local distortion modes of Y, Cr, and O ions, as schematically drawn in Figs. 6.11–6.13, respectively.

Figure 6.11 shows the local pentahedron environment of Y ions. It is worth mentioning that there are six Y-O bonds at the neighbor of the Y atom, i.e., with a coordination number 6, two Y-O1 and four Y-O2 bonds. Among them, $2 \times$ Y-O22 bonds are stretched, and Y-O11, Y-O12, and $2 \times$ Y-O21 bonds are shortened (Table 6.2). This results in both the O11-O21-O22-O12 planes being bent outward, shifting the charge weight center of Y ions upward, whilst holding the $2 \times$ O21 and the $2 \times$ O22 ions within one O21-O22-O22-O21 plane. The extracted pentahedron distortion mode of Y ion was schematically displayed by the arrows sitting on the six Y-O bonds.

160

The Cr ion in YCrO$_3$ compound has three electrons in the unfilled $3d$ shell, therefore, Cr^{3+} is a non-Kramers ion, in principle, without JT effect. That is why Cr^{3+} ions have a very small local distortion parameter Δ [Fig. 6.10]. From the refined Cr-O bond lengths as listed in Table 6.2, it could be deduced that the octahedral distortion mode of Cr^{3+} ions (coordination number: 6) in YCrO$_3$ compound, as shown in Fig. 6.12(a). This distortion mode, as schematically displayed by the arrows sitting on oxygen ions, results from stretched Cr-O21 and Cr-O22 and shortened Cr-O1 bonds, behaving like a cooperative JT distortion. The local crystalline environment of Cr^{3+} ions in YCrO$_3$ compound coincides with the t_{2g} orbital shapes (d_{xy}, d_{zx}, d_{yz}). As shown in Fig. 6.12(b), the $3d_{yz}$ orbital shape in real space was accommodated into the CrO$_6$ octahedron. Because the two Cr-O1/O21/O22 bonds locate along the plane/body diagonal direction and have the same length, the sum effect of electric-lattice interactions is canceled out. Therefore, within the present crystal symmetry, no displacement happens to the Cr ions.

Figure 6.13 illustrates the local distortion environments of O1 [Fig. 6.13(a)] and O2 [Fig. 6.13(b)] ions in single-crystal YCrO$_3$ compound. Both O1 and O2 ions have a coordination number 4, forming a tetrahedron. By comparing the refined Cr-O and Y-O bond lengths (referring to Table 6.2), two tetrahedral distortion modes could be deduced for the O1 and O2 ions, respectively, as displayed by the arrows sitting on the Cr-O and Y-O bonds. For example, for the O1 ions [Fig. 6.13(a)], the 2$\times$Cr-O bonds are shortened, whereas the two Y-O bonds are stretched. This pushes the O1 ions towards to the Cr ions. So do the O2 ions [Fig. 6.13(b)]. Within the two oxygen tetrahedrons, the longest Y-O bond is Y-O2 = 2.487(4) Å (at 321 K) as displayed in Fig. 6.13(b). This drives the O2 ions very close to the bottom Y-Cr-Cr plane, a large negative charge displacement. Compared to the O1 ions, the local crystalline environment of O2 ions is much more distorted in agreement with our calculations as shown in Fig. 6.10 where the local distortion parameter Δ of O2 ions is approximately two times larger than that of O1 ions.

The distortion parameter Δ, to some extent, is a criterion for what magnitude a

certain atom displaces with its surrounding ligands [74]. For example, Kramers ions usually show a JT distortion whose magnitude can be expressed by the size of the distortion parameter Δ. The JT effect occurring in $3d$ transition metal oxides can lead to the degeneracy of d orbitals accompanied by lowering the structural symmetry to release the electronic occupied energy. That can result in charge/orbital ordering and magnetic transition and may shed light on the colossal magnetoresistance effect [74, 333]. For $3d^3$ Cr^{3+} ions in $YCrO_3$ compounds, no JT effect is expected, and thus the distortion parameter Δ of Cr^{3+} ions is quite small, which is hard to break the centrosymmetry of the center Cr^{3+} ions, therefore, no ferroelectricity is expected from the Cr-sites. However, as shown in Figs. 6.11 and 6.13(b), the centrosymmetries of Y^{3+} and O_2^{2-} ions could be broken by their large local environmental distortions, which may induce the geometric ferroelectricity. Similar observation was also reported on the orthorhombic $GdCrO_3$ compound, in which the Gd^{3+} and O^{2+} ions move toward different directions and produce a huge charge density in the Gd-O bonds [240].

6.3.1.7 Bond valence states of Y, Cr and O ions

It is well known that bond valences are strongly correlated to bond distances, and some empirical relationships were previously proposed [204, 334, 335, 336]. With our refinements, we extracted the bond valence states (BVSs) of Y, Cr, and O ions as shown in Fig. 6.14. As temperature increases, the BVSs of Y, Cr, and O ions almost decrease linearly. The calculated BVS values for the Cr and O1 ions are 2.956(7)+ and 2.079(11)– at 321 K, close to the ideal 3+ and 2–, respectively. However, for the Y and O2 ions, the calculated BVS values, BVS(Y) = 2.636(15)+ and BVS(O2) = 1.757(8)–, differ largely from the respective perfect values of 3+ and 2– in pure ionic model. Therefore, there exit positive and negative charge displacements from Y and O2 ions that coincide with their strongly distorted local crystalline environments. In the $Pmnb$ symmetry, there are two non-equivalent crystallographic sites for the O1 and O2 ions. As shown in Fig. 6.14, the charge difference between O1 and O2 ions is approximate $0.317(15)e^-$ with ~ 21 standard deviations, indicative of a big degree of the charge
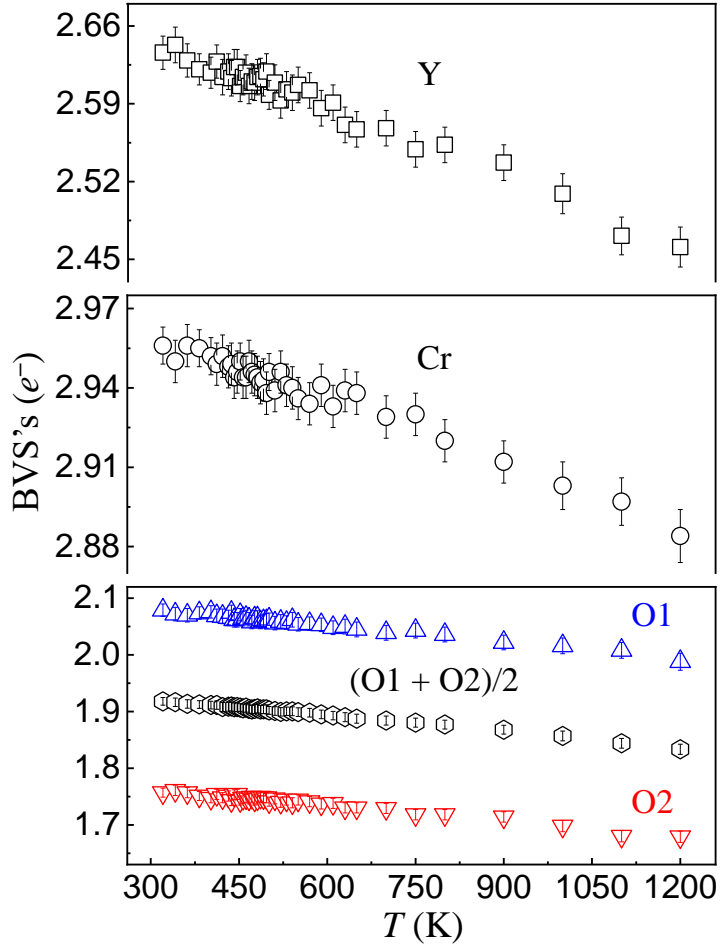
Figure 6.14: Temperature variation of the bond valence states (BVSs) of Y, Cr, O1, and O2 ions in the single-crystal YCrO$_3$ compound, calculated from our refined structural parameters between 321 and 1200 K by the FULLPROF SUITE [204]. For a clear comparsion, we also calculated the average BVSs of O1 and O2 ions, i.e., (O1 + O2)/2. Error bars are combined standard deviations.

disproportion. It is of interest to notice that the extracted charge difference between O1 and O2 ions is even much bigger than the charge difference between Mn^{3+} and Mn^{4+} ions in the charge/orbital ordered states of manganites [308, 337] where for the La$_{\frac{7}{8}}$Sr$_{\frac{1}{8}}$MnO$_3$ compound [308], the charge difference is 0.11(5) e^-, and for the half-doped Nd$_{\frac{1}{2}}$Sr$_{\frac{1}{2}}$MnO$_3$ [337] it is 0.16 e^-. It is thus reasonable to deduce that the Y and O2 ions play an important role in forming the dielectric anomaly of YCrO$_3$ compound.

Finally, the temperature-dependent isotropic thermal parameters B of Y, Cr, and O1/O2 (constrained to be the same) ions of YCrO$_3$ compound were present in Fig. 6.15 where almost no change exists from 321 to 1200 K within the experimental accuracy.

As is well known, the contribution of magnetism in YCrO$_3$ compound comes from
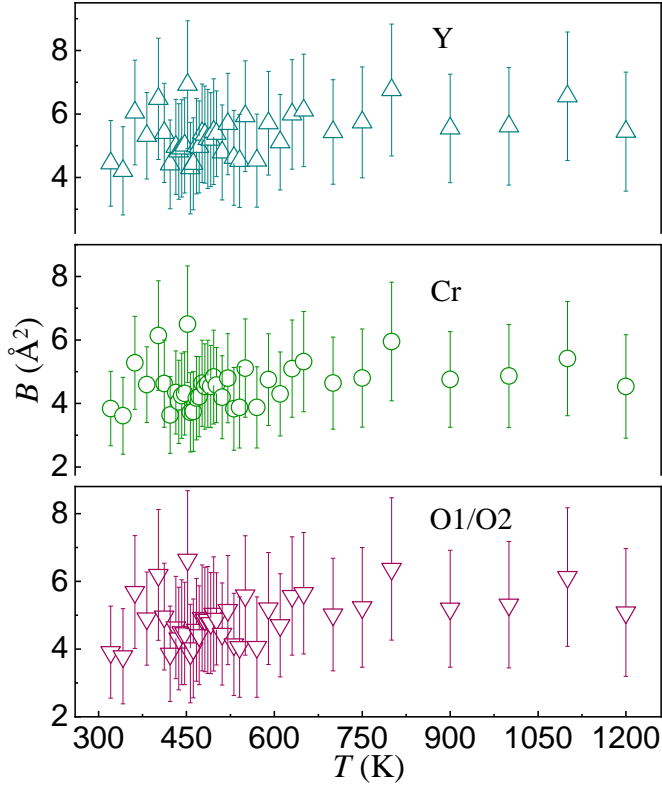
Figure 6.15: Temperature variation of the isotropic thermal parameters, B, of Y, Cr, O1, and O2 ions in the single-crystal $YCrO_3$ compound. During our FULLPROF [204] refinements, we constrained the B sizes of O1 and O2 ions to the same value. Error bars are standard deviations.

the Cr^{3+} ($3d^3$) ions supposing that the $YCrO_3$ compound forms pure ionic bonds and thus there is no magnetic contribution from oxygen sites [74, 308]. As in the foregoing discussion, the dielectric anomaly [48] of $YCrO_3$ compound may be ascribed to the obvious atomic displacement and charge subduction of Y and O2 ions. The Y^{3+} ion is nonmagnetic because the ground-state electronic configuration of neutral Y is $[Kr]4d^15s^2$. Therefore, the structural parameters extracted from our time-of-flight neutron powder-diffraction study don't display a response to the previously observed dielectric anomaly. On the other hand, that doesn't mean that there is no magnetoelectric coupling existing in $YCrO_3$ compound. To unravel this coupling necessitates measurements with extremely high applied magnetic fields. By comparison, the $YMnO_3$ compound belongs to a hexagonal symmetry with the structural building block of MnO_5, and its ferroelectric polarization is due to opposing unequal dipoles of the two Y sites as well as the tilting and distortion of the MnO_5 blocks [338, 241, 328].

The Gd^{3+} ($4f^7$) ions in $GdCrO_3$ compounds has a very strong magnetic contribution. It is expected that the Gd-Cr coupling in $GdCrO_3$ compounds is much stronger than the Y-Cr coupling in $YCrO_3$ compound. As foregoing remarks, the previously reported dielectric anomaly of $YCrO_3$ compound may be due to large atomic displacement and charge subduction of Y and O2 ions, whereas, only Cr ions contribute to its magnetism. That may be the reason why the structural parameters don't show any anomaly around 473 K.

It is stressed that the space group $Pmnb$ belongs to a centrosymmetric structure in which the sum of negative and positive charge shifts has to be zero. Our interesting observations, e.g., the extremely large local distortion parameter Δ of Y, O1, and O2 ions, the obvious displacement of Y and O2 ions and the charge subduction of Y and O2 ions, indicate that the actual structural symmetry of $YCrO_3$ compounds may be much lower than $Pmnb$. As a foregoing discussion, even though Kramers ions like Mn^{3+} theoretically and experimentally exhibit a larger local distortion, e.g., a JT/cooperative JT effect, than non-Kramers ions like Cr^{3+}, their detailed distortion modes can be the same, as demonstrated in this study. Additionally this distortion mode can even be applicable to the $4f$ ions [313].

6.3.2 Low-temperature crystallography, magnetism, heat capacity, and anisotropic magnetostriction effect in single-crystal YCrO₃

6.3.2.1 ICP-OES measurements

By quantitative ICP-OES measurements, we determined the chemical compositions of the studied single crystal as $Y_{0.97(2)}Cr_{0.98(2)}O_{3.00(2)}$. This implies that the resultant single crystals of $YCrO_3$ compound by the FZ method are nearly stoichiometric within the experimental accuracy. Therefore, during analyzing magnetization and time-of-flight neutron-powder diffraction data, the stoichiometry of the synthesized $YCrO_3$ samples was kept being the ideal one (i.e., 1:1:3).

Table 6.4: Theoretical quantum numbers of YCrO$_3$ compound: spin S, orbital L, total angular momentum J, as well as the ground-state term $^{2S+1}L_J$. Due to a quenching by the hosted crystal field, the actual orbital angular momentum $L = 0$ for the $3d$ ions in most cases, leading to the Landé factor $g_J = 2$. We also summarized the theoretical (theo.) and measured (meas.) [Fig. 2(b)] values of effective (eff) chromium moment μ_{eff}, PM Curie temperature θ_{CW}, theoretical saturation (sat) chromium moment $\mu_{sat.theo.}$, and AFM transition Néel temperatures (T_N) at $\mu_0 H = 0.01$ and 5 T. The refined chromium moment size ($\mu_{meas.}$) at 12 K with the AFM model as shown in Fig. 1 from our POWGEN study was listed. The numbers in parenthesis are the estimated standard deviations of the last significant digit.

A YCrO$_3$ single crystal	
$3d$ ion	Cr^{3+}
$3d^n$	3
S	3/2
L	3
$J = L - S$ (Hund's rule for free Cr^{3+})	3/2
$^{2S+1}L_J$	$^4F_{\frac{3}{2}}$
g_J (quenched $L = 0$, $J = S$)	2
$\mu_{eff\_theo.} = g_J[S(S+1)]^{\frac{1}{2}}$ (μ_B)	3.873
$\mu_{sat\_theo.} = g_J S$ (μ_B)	3
$\mu_{eff\_meas.}$ (μ_B)	3.95(2)
θ_{CW} (K)	–433.2(6)
T_N (at 0.01 T)	141.5(1)
T_N (at 5 T)	144.5(1)
$\mu_{meas.}$ (12 K, POWGEN) (μ_B)	2.45(6)

6.3.2.2 Resistivity measurements

An attempt was performed to measure possible resistivity in the YCrO$_3$ single crystals with a multimeter at room temperature. Unfortunately, it was beyond the maximum range (10^6 ohm) of the ohmmeter. In addition, the attempt to measure it by the standard four-probe method with our PPMS DynaCool system from 2 to 300 K was fruitless. Therefore, it could be concluded that the YCrO$_3$ compound is a robust insulator in our studied temperature range. A deeper understanding of the electronic states of conducting VO [339] and insulating YCrO$_3$ compounds necessitates more experimental work and theoretical band structure calculations. Perhaps both samples are the only two pure $3d^3$ compounds.
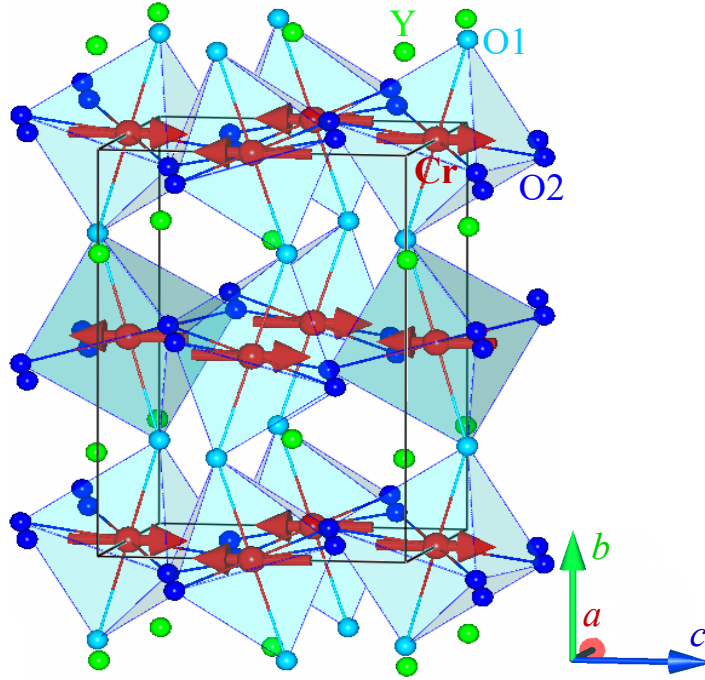
Figure 6.16: Orthorhombic crystal structure (with $Pnma$ space group) with one unit cell (solid lines) and the AFM structure in one AFM unit cell with the propagation vector at $\mathbf{k}$ = (1 1 0) below T_N = 141.5(1) K of the YCrO$_3$ single crystal. The arrows on the Cr ions represent the spins of chromium. Both the unit cells of orthorhombic and AFM structures are (a b c).
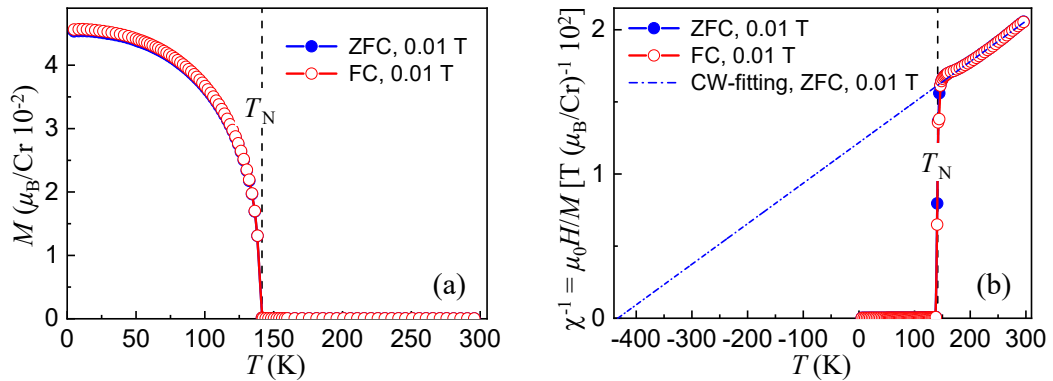
Figure 6.17: (a) ZFC and FC magnetization (M) of chromium ions in the single-crystal YCrO$_3$ compound as a function of temperature measured at $\mu_0 H = 0.01$ T. (b) Corresponding ZFC and FC inverse magnetic susceptibility χ^{-1} (circles) of chromium ions in the single-crystal YCrO$_3$ compound versus temperature. The dash-dotted line indicates a CW behavior of the ZFC data at elevated temperatures between 200 and 300 K, which was extrapolated to $\chi^{-1} = 0$ to show the PM Curie temperature θ_{CW}. The fit results were listed in Table 6.4. In (a) and (b), $T_N = 141.5(1)$ K labels the AFM transition temperature at $\mu_0 H = 0.01$ T, and the solid lines are guides to the eye.
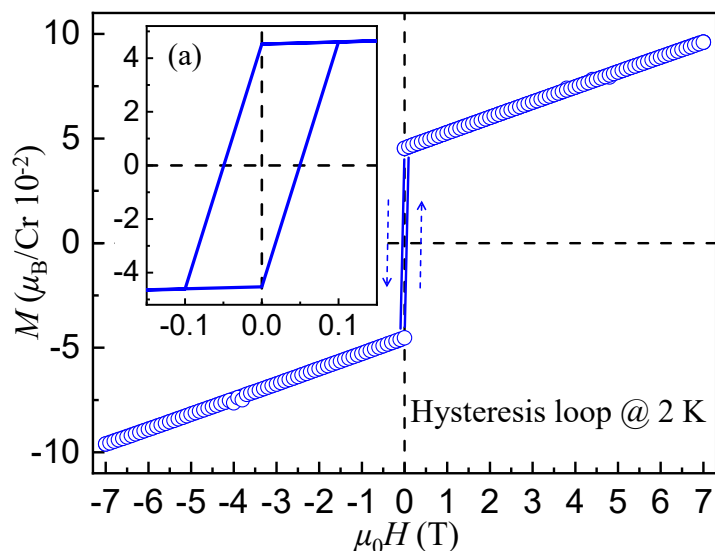
Figure 6.18: ZFC magnetic hysteresis loop of the single-crystal YCrO$_3$ compound measured at 2 K. Inset (a) is the enlarged image of the narrow loop.
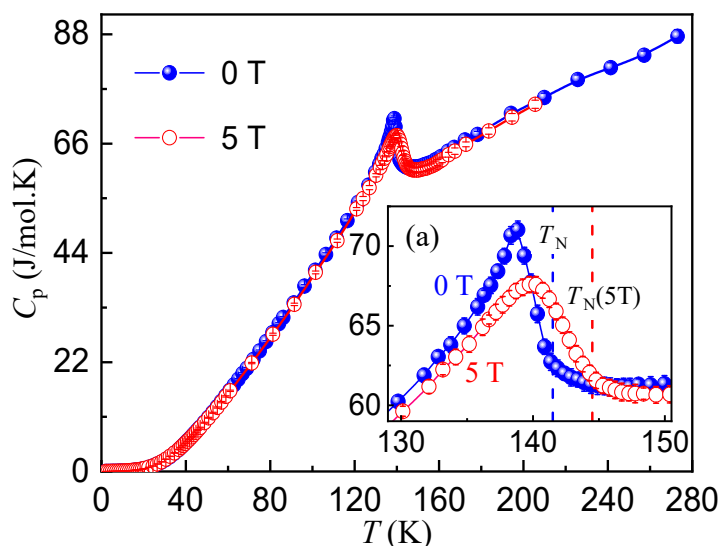
Figure 6.19: Heat capacities of the single-crystal YCrO$_3$ compound measured at 0 T (solid circles) and 5 T (void circles). The solid lines are guides to the eye. Inset (a) is the enlarged image around the AFM transition temperatures. The vertical dashed lines show the detailed transition temperatures at the fields of 0 and 5 T. Here, T_N (0 T) = 141.5(1) K at 0 T; by comparison, at 5 T, T_N (5 T) = 144.5(1) K. The solid lines are guides to the eye.

6.3.2.3 Magnetization versus temperature

Fig. 6.17(a) shows magnetization measurements of a small piece of randomly-orientated YCrO$_3$ single crystal. The unit of vertical axis was transferred into μ_B per Cr^{3+} ion. There exists no obvious difference between ZFC and FC data. Upon cool-
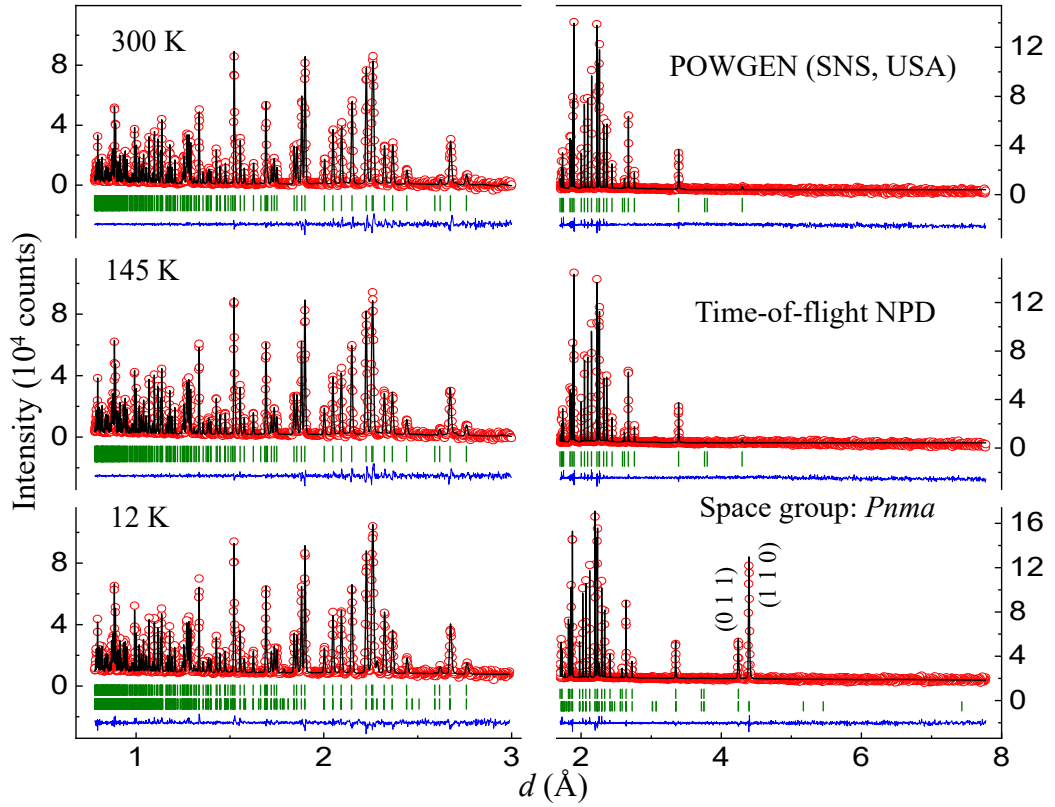
Figure 6.20: Observed (circles) and calculated (solid lines) time-of-flight neutron-powder diffraction (NPD) patterns of a pulverized $YCrO_3$ single crystal, collected from the POWGEN diffractometer (SNS, USA) at 12, 145, and 300 K. The vertical bars mark the positions of nuclear (up, $Pnma$ space group) and magnetic (down, P-1 space group) Bragg reflections, and the lower curves represent the difference between observed and calculated patterns.

ing, ZFC and FC magnetization curves measured at 0.01 T show very small values down to temperature $\sim$141.5 K, e.g., ZFC magnetization $= 4.860(4) \times 10^{-7}$ and $7.310(6) \times 10^{-7} \mu_B/Cr^{3+}$ at 295 and 142.3 K, respectively. Around 141.5 K, they increase sharply by $\sim 38\%$ in a small thermal range of ~ 5 K, followed by a smooth increase down to 5 K. This resembles the characteristic feature of a reasonable canted antiferromagnet and rules out the possibility for a ferrimagnet. At 5 K, ZFC magnetization $= 4.530(4) \times 10^{-2} \mu_B/Cr^{3+}$.

The inverse magnetic susceptibility $\chi^{-1} = \mu_0 H/M$ was calculated as shown in Fig. 6.17(b), where the nearly linear increase of χ^{-1} in the PM state at high temperatures obeys well the molar susceptibility via a CW law

$$\chi(T) = \frac{C}{T - \theta_{CW}} = \frac{N_A \mu_{eff}^2}{3k_B(T - \theta_{CW})},$$

(6.7)

169

Table 6.5: Refined including lattice constants, unit-cell volume, atomic positions, isotropic thermal parameters (B), bond lengths, bond angles, and the distortion parameter Δ of the pulverized $YCrO_3$ single crystal at 12, 145, and 300 K. The Wyckoff site of each ion and the goodness of fit were listed. The numbers in parenthesis are the estimated standard deviations of the last significant digit.

A pulverized $YCrO_3$ single crystal			
(Orthorhombic, space group $Pnma$ (No. 62), $Z = 4$)			
T (K)	12	145	300
a (Å)	5.5189(1)	5.5181(1)	5.5198(1)
b (Å)	7.5205(1)	7.5213(1)	7.5297(1)
c (Å)	5.2323(1)	5.2328(1)	5.2392(1)
$\alpha(\beta,\gamma)$ (°)	90	90	90
V (Å^3)	217.17(1)	217.18(1)	217.75(1)
Y($4c$) x	0.0682(4)	0.0672(1)	0.0665(1)
Y($4c$) y	0.25	0.25	0.25
Y($4c$) z	–0.0172(4)	–0.0177(1)	–0.0174(2)
Y($4c$) B (Å^2)	0.2	0.28(2)	0.47(2)
Cr($4b$) (x, y, z)	(0, 0, 0.5)	(0, 0, 0.5)	(0, 0, 0.5)
Cr($4b$) B (Å^2)	0.2	0.29(3)	0.39(3)
O1($4c$) x	0.4643(5)	0.4646(2)	0.4647(2)
O1($4c$) y	0.25	0.25	0.25
O1($4c$) z	0.1039(5)	0.1052(2)	0.1050(2)
O1($4c$) B (Å^2)	0.2	0.34(2)	0.51(2)
O2($8d$) x	0.3020(4)	0.3020(1)	0.3021(1)
O2($8d$) y	0.0539(2)	0.0538(1)	0.0536(1)
O2($8d$) z	–0.3065(4)	–0.3067(1)	–0.3066(1)
O2($8d$) B (Å^2)	0.2	0.34(2)	0.51(2)
Y-O11 (Å)	2.237(3)	2.231(1)	2.233(1)
Y-O12 (Å)	2.276(4)	2.286(1)	2.290(1)
Y-O21 (Å) (×2)	2.277(3)	2.272(1)	2.273(1)
Y-O22 (Å) (×2)	2.476(3)	2.479(1)	2.485(1)
<Y-O> (Å)	2.337(1)	2.337(1)	2.340(1)
Cr-O1 (Å) (×2)	1.967(1)	1.969(1)	1.971(1)
Cr-O21 (Å) (×2)	1.983(2)	1.983(1)	1.984(1)
Cr-O22 (Å) (×2)	1.992(2)	1.991(1)	1.993(1)
<Cr-O> (Å)	1.980(1)	1.981(1)	1.983(1)
∠Cr-O1-Cr (°)	145.81(3)	145.49(1)	145.53(1)
∠Cr-O2-Cr (°)	146.18(9)	146.18(3)	146.22(3)
Δ(Y) ($\times 10^{-4}$)	18.197	19.085	19.789
Δ(Cr) ($\times 10^{-4}$)	0.268	0.215	0.203
Δ(O1) ($\times 10^{-4}$)	47.429	47.743	47.930
Δ(O2) ($\times 10^{-4}$)	90.063	90.578	91.684
R_p	6.40	5.46	6.03
R_{wp}	9.33	3.67	3.74
R_{exp}	7.33	2.69	2.83
χ^2	1.62	1.86	1.75
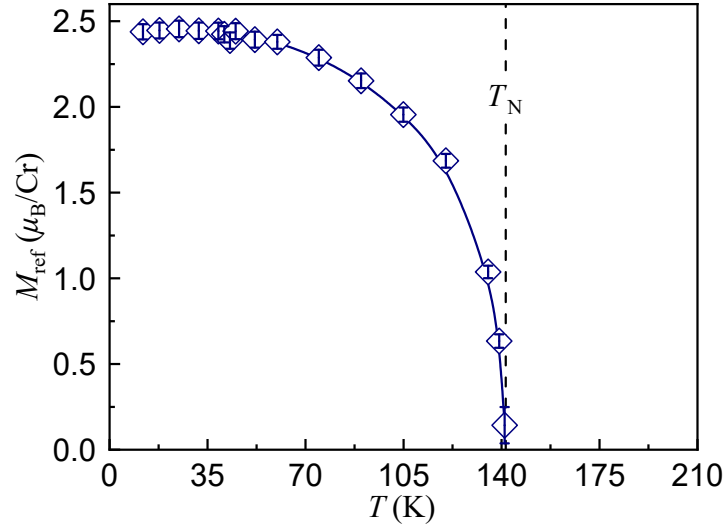
Figure 6.21: Refined chromium-moment size M_{ref} (at 0 T) of a pulverized YCrO$_3$ single crystal versus temperature by the software of FULLPROF SUITE [204]. The solid line is a guide to the eye. Error bars are standard deviations obtained from our FULLPROF refinements in the $Pnma$ symmetry. T_{N} = 141.5(1) K labels the AFM transition temperature at zero applied-magnetic field.
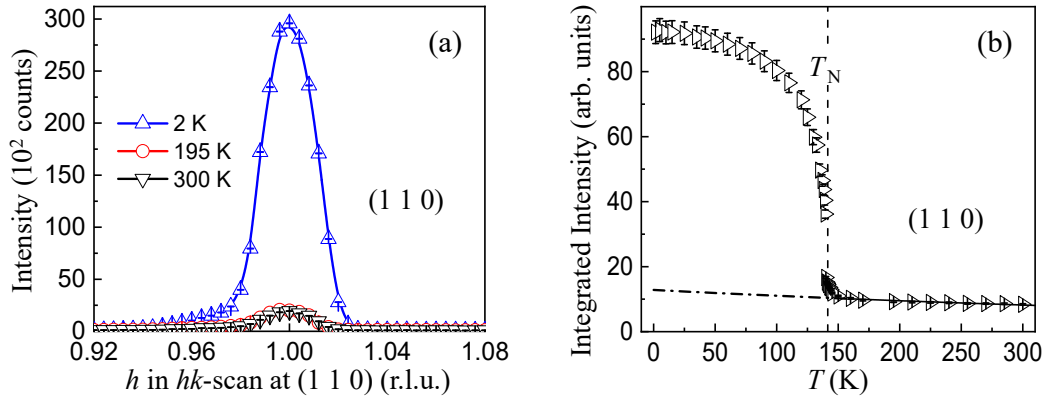
Figure 6.22: (a) Representative longitudinal scans of the magnetic Bragg (1 1 0) reflection at three temperatures of 2, 195, and 300 K, from the D23 (ILL, France) study on a YCrO$_3$ single crystal. The solid lines are guides to the eye. (b) Corresponding temperature-dependent integrated intensities of the magnetic Bragg (1 1 0) reflection. $T_{\text{N}} = 141.5(1)$ K labels the AFM transition temperature. The solid line was a fit to Eqs. (6.8) and (6.10) in the affiliated thermal regime. It was extrapolated to overall temperatures (dash-dotted line). The error bars in (a) and (b) are the standard deviations based on our measurements and fits.

where C is the Curie constant, θ_{CW} is the PM Curie temperature, $N_{\text{A}} = 6.022 \times 10^{23}$ mol^{-1} is the Avogadro's number, $\mu_{\text{eff}} = g\mu_{\text{B}}\sqrt{J(J+1)}$ is the effective PM moment, and $k_{\text{B}} = 1.38062 \times 10^{-23}$ J/K is the Boltzmann constant. The fit by Eq. 6.7 was shown as the dash-dotted line in Fig. 6.17(b). The fit parameters were listed in Table 6.4.

Figures 6.17(a) and 6.17(b) clearly indicate a sharp magnetic phase transition. The

magnetic phase transition temperature was determined as $T_N = 141.5(1)$ K. The resultant PM CW temperature $\theta_{CW} = -433.2(6)$ K, indicating an existence of strong AFM correlations. The frustrating parameter was calculated [313, 314, 317, 319, 320, 321], i.e., $f = |\theta_{CW}|/T_N = 3.061(5)$, which was consistent with the high-temperature magnetization study [248]. This value indicates that the low-temperature magnetic moments of Cr^{3+} ions in $YCrO_3$ compound are frustrated by competitive spin exchanges. As listed in Table 6.4, the extracted effective PM moment $\mu_{eff\_meas} = 3.95(2)$ μ_B, a little bit larger than the calculated theoretical value $\mu_{eff\_theo} = 3.873$ μ_B, which was acceptable within the present experimental accuracy.

6.3.2.4 Magnetization versus applied magnetic field

Figure 6.18 shows the measurement of magnetic hysteresis loop at 2 K. Figure 6.18(a) clearly exhibits the hysteresis loop whose shape is of a parallelogram. The loop locates in a magnetic field range of ~ -0.1 to 0.1 T with a coersive force of ~ 0.05 T and a residual magnetism of $\sim 4.54 \times 10^{-2}$ μ_B/Cr^{3+}. These small values demonstrate that the $YCrO_3$ compound is a soft canted antiferromagnet at low temperatures. At 2 K and 7 T, the measured ZFC magnetization $M = 9.603 \times 10^{-2} \mu_B/Cr^{3+}$. From 0.1 to 7 T, the measured magnetization almost increases linearly with $\chi = M/\mu_0 H = 7.24(1) \times 10^{-3}$ $\mu_B T^{-1}/Cr^{3+}$. We therefore estimated that reaching a complete magnetic saturation state, an applied-magnetic field $\mu_0 H \geq \sim 408$ T is required [267].

6.3.2.5 Heat capacity

Figure 6.19 shows the heat capacity measurements. At 0 T, with decreasing temperature, the measured heat capacity decreases until $T_N = 141.5$ K, followed by an appearance of a λ-shape peak. Below this, heat capacity continues to decrease and gets flat below ~ 24 K. The observation of the λ-shape peak indicates a phase transition. To reveal the nature of the phase transition, we measured heat capacity under an applied-magnetic field of 5 T. As shown in Fig. 6.19(a), at 5 T, it was noted that the intensity of the λ-shape peak was reduced, accompanied by a shift of the peak position from

~ 138.8 K (0 T) to an elevated temperature ~ 139.9 K (5 T). This is the characteristic feature of a canted antiferromagnet. Thus, the phase transition is magnetic rather than structural. It was determined that T_N (5 T) = 144.5(1) K, ~ 3 K higher than the T_N at 0 T. Quantitative analysis of the relationship between values of T_N and applied-magnetic-field strengths necessitates more measurements. It is pointed out that with the measurement of magnetization versus temperature, it is easy to determine the value of T_N. From heat capacity measurements, the phase transition temperature is at the temperature point at which a kink exists in the C_p–T curve as marked in Fig. 6.19(a).

Albeit that the magnetization and heat capacity measurements show FM behaviors below T_N, the net magnetic interaction strength inside YCrO$_3$ compound is of strongly AFM because θ_{CW} = –433.2(6) K, indicating a complex low-temperature magnetic structure.

6.3.2.6 *Time of flight neutron powder diffraction*

To make the nature of the observed weak ferromagnetism clear and explore possible structural phase transitions in the YCrO$_3$ single crystal, a time-of-flight neutron-powder diffraction study was carried out. The results were shown in Fig. 6.20. At the three temperatures as labeled, i.e., below (12 K), around (145 K), and above (300 K) the magnetic transition temperature (~ 141.5 K), all time-of-flight neutron-powder diffraction patterns were well indexed by an orthorhombic structure with the space group $Pnma$. There was no detectable peak splitting or an appearance of satellite reflections. This indicates that no structural phase transition occurs in the YCrO$_3$ single crystal as a function of temperature in the studied thermal regime. This is in agreement with our heat capacity measurements. Based on the observed magnetic Bragg (0 1 1) and (1 1 0) peaks, as labeled in the right-bottom of Fig. 6.20, an AFM model was established with the propagation vector at $\mathbf{k}$ = (1 1 0) and the moment directions along the crystallographic c axis. The extracted magnetic structure was schematically drawn in Fig. 6.16. It is pointed out that the magnetic (1 1 0) reflection is structurally forbidden by the space group $Pnma$. All possible canted AFM models were tried, unfortunately,

the corresponding FULLPROF refinements were not successful. The refined structural parameters were listed in Table 6.5. It is pointed out that for the refinement of the data at 12 K, the isotropic thermal parameters (B) of Y, Cr, O1, and O2 ions are constrained being the same as 0.2.

Within the present experimental accuracy, a G-type AFM structure can be determined as shown in Fig. 6.16, where the nearest-neighbor Cr^{3+} spins are aligned antiparallel. The directions of the AFM submoments are along with the crystallographic c axis, i.e., the direction with the smallest lattice constant. It is hard to determine the possible canting angle. It was suggested that including an SOC on the quenched Cr^{3+} ground state, an antisymmetric exchange interaction would cant the AFM moments along the crystallographic b axis, i.e., the direction with the largest lattice constant, according to the DM theory [75]. This leads to an appearance of the weak ferromagnetism.

Figure 6.21 shows the refined moment size of Cr^{3+} ions in the $YCrO_3$ single crystal, extracted from our time-of-flight neutron-powder diffraction study. As listed in Table 6.4, the refined moment size at 12 K is 2.45(6) μ_B, $\sim 82\%$ of the theoretical saturation moment (3 μ_B), in agreement with our conclusion that there exists a magnetic frustration in $YCrO_3$ compound and the studies with X-ray magnetic circular dichroism and absorption spectroscopies [303] where the computed values of spin and orbital moments are 2.38 μ_B and –0.094 μ_B, respectively, and that the total magnetic moment has little contribution from the orbital component. As temperature increases, the refined moment size remains a plateau up to ~ 50 K, followed by a gradual diminution with temperature upon warming until a radical disappearance around 141.5 K, the onset temperature of the AFM transition (Figs. 6.17 and 6.21). Above T_N (0 T) = 141.5 K, intensities of the two magnetic Bragg reflections were undetectable.

6.3.2.7 Single crystal neutron diffraction

An orientated $YCrO_3$ single crystal with the (H K 0) reciprocal-lattice vector in the scattering plane was used to perform a single-crystal neutron diffraction study on the
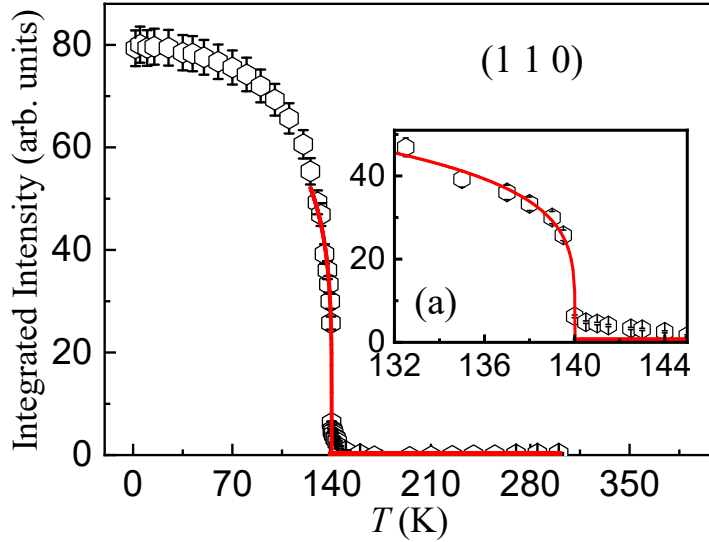
Figure 6.23: Subtracted integrated intensity from the pure magnetic contribution at the Bragg (1 1 0) peak position (void pentagons), to see detailed analysis in the text. Inset (a) shows the enlarged image around T_N from 132–145 K. The solid line was a fit to the power-law Eq. (6.11) in the affiliated thermal regime. The error bars are the propagated standard deviations based on our calculations.

D23 single-crystal diffractometer (ILL, France). Figure 6.22(a) shows some longitudinal scans of the magnetic Bragg (1 1 0) reflection. At 2 K (below T_N), a very strong peak was observed, indicating a formation of the AFM structure. At 195 and 300 K (above T_N), the intensity of the magnetic (1 1 0) peak decreased sharply but did not disappear. It is interesting that there still exists detectable intensity of the Bragg (1 1 0) peak above T_N. We ruled out the $\lambda/2$ contamination. As the foregoing remark, this reflection is forbidden by the space group $Pnma$. Therefore, the existence of the Bragg (1 1 0) reflection above T_N indicates that the actual crystalline structure of YCrO$_3$ compound may be lower than the orthorhombic structure with space group $Pnma$. Our studies also demonstrate that the scattering ability of a single crystal is much higher than that of the corresponding pulverized powder sample.

At 195 and 300 K, the observed Bragg (1 1 0) reflection forbidden structurally by the $Pnma$ symmetry was treated to be from a pure nuclear contribution. The temperature variation of this contribution depends mainly on the thermal dynamic vibrations of related atoms, i.e., Debye-Waller (DW) factors. The falloff of the temperature-weakened intensity at a certain scattering vector **Q** almost decays exponentially and

can be estimated by

$$I = I_0 e^{-2W(Q,T)}, \tag{6.8}$$

where the exponential part is the DW factor, and

$$2W(Q,T) = \frac{\hbar^2 Q^2}{2M} \int coth\left(\frac{\hbar\omega}{2k_{\mathrm{B}}T}\right) \frac{Z(\omega)}{\omega} d\omega, \tag{6.9}$$

where $\hbar = 1.054589 \times 10^{-34}$ J.s is the Planck constant divided by 2π, M is the atomic mass, and $Z(\omega)$ is the phonon density of states [340]. At high temperatures, it is given simply by

$$2W = \frac{3\hbar^2 Q^2}{M k_{\mathrm{B}} \Theta_{\mathrm{W}}^2} T, \tag{6.10}$$

where Θ_{W} is the effective Debye temperature [341]. Therefore, the DW factor was practically treated with a linear response to temperature, as verified in previous studies [159, 313, 332, 342]. The integrated intensities of the Bragg (1 1 0) reflection was fit above T_{N} to Eqs. (6.8) and (6.10), shown as the solid line in Fig. 6.22(b), and extrapolated the fit to the entire temperature range (shown as the dash-dotted line).

Furthermore, The corresponding nuclear component was subtracted from the total scattered intensity at the Bragg (1 1 0) peak position to extract the pure magnetic contribution below T_{N} as shown in Fig. 6.23. The resultant magnetic intensity above T_{N} is approximately zero within accuracy, which in turn supports the above subtraction. The extracted integrated intensity (I) of Bragg (1 1 0) reflection from the pure magnetic contribution can be fit to a power-law equation [343, 344]

$$I(T) = I_0 \left(\frac{|T - T_{\mathrm{N}}|}{T_{\mathrm{N}}}\right)^{2\beta}, \tag{6.11}$$

where T_{N} is the value of the Néel temperature, and β is the critical exponent. The fit with Eq. (6.11) to the extracted data in a narrow thermal range from 125 to 140 K, shown as the solid line in Fig. 6.23, produces a Néel temperature $T_{\mathrm{N1}} = 140.0(1)$ K,
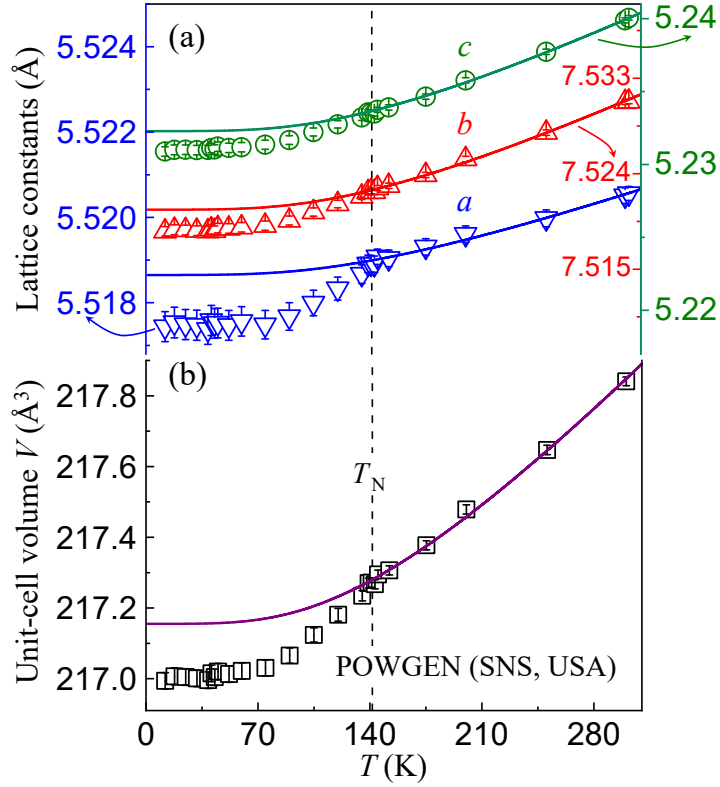
Figure 6.24: (a) Temperature-dependent lattice constants a, b, and c of a pulverized YCrO$_3$ single crystal. (b) Corresponding anomalous unit-cell volume V expansion with temperature. The solid lines in (a) and (b) are theoretical estimates of the variation of structural parameters using the Grüneisen model with Debye temperature of $\Theta_D = 580$ K that is the same value as the one reported previously [63]. $T_N = 141.5(1)$ K labels the AFM transition temperature. The error bars in (a) and (b) are the standard deviations obtained from the FULLPROF refinements with the $Pnma$ structural symmetry.

and the critical exponent $2\beta = 0.215(6)$, indicating a second-order type phase transition and probably two-dimensional Ising-like spin interactions existing within the reciprocal (1 1 0) scattering plane [343, 345]. The fitting procedure was as follow: First, we kept $I_0 = 80$ and $T_N = 141.5$ K and allowed β to vary; finally, all parameters were fit together. For comparison, the data was further fit in three temperature ranges of 125–140 K, 130–140 K, and 135–140 K. No clear differences exist in the values of the refined T_N and β, which validates our choice of the temperature range of 125–140 K for the final fitting.

As shown in Fig. 6.23(a), it is interesting to note that above T_{N1}, there exists weaker critical scattering over a range of temperature up to 145 K.
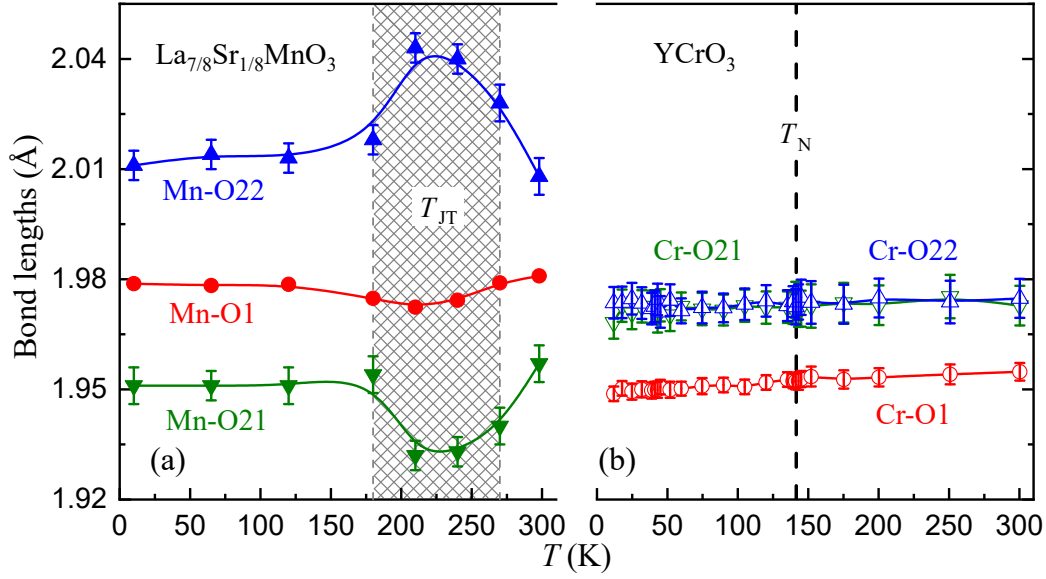
Figure 6.25:   (a) Three bond lengths of Mn-O1, Mn-O21, and Mn-O22 in the
$La_{\frac{7}{8}}Sr_{\frac{1}{8}}MnO_3$ single crystal [308] versus temperature. $T_{JT} \approx 180$–270 K denotes the
regime of the Jahn-Teller effect. (b) Corresponding bond lengths in the $YCrO_3$ sin-
gle crystal as a function of temperature from this study. $T_N = 141.5(1)$ K labels the
AFM transition temperature. The error bars in (a) and (b) were from our FULLPROF
refinements.

6.3.2.8 Anisotropic magnetostriction effect

The refined lattice parameters a, b, and c, as well as the unit-cell volume V, from
our time-of-flight neutron-powder diffraction studies were shown in Fig. 6.24 (void
symbols). Upon cooling, the refined (Re) a, b, c, and V almost shrink linearly down to
T_N at which a cusp appears.

As in the foregoing discussions, the $YCrO_3$ compound is an insulator. Thus, the
electronic contribution to the thermal expansion of its lattice configuration (ε) can be
neglected. The temperature variation of the nonmagnetic contribution component is
then mainly from phonons. This can approximately be estimated according to the
Grüneisen rules at zero pressure with a second-order fashion [346, 325, 326]

$$\varepsilon(T) = \varepsilon_0 + \varepsilon_0 \frac{U}{Q - BU}, \tag{6.12}$$

where ε_0 is the lattice parameter at 0 K, and the internal energy U can be calculated
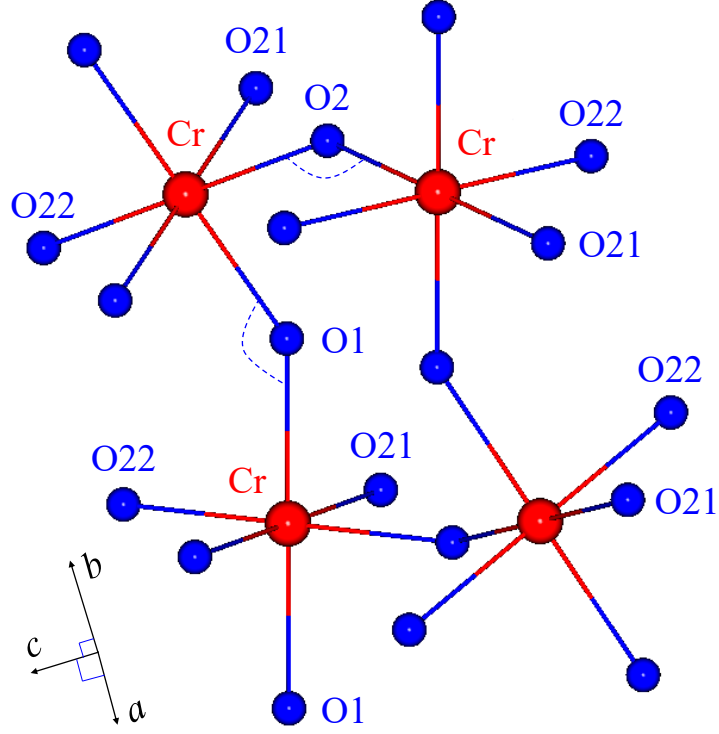
Figure 6.26: Schematic illustration of the three Cr-O bonds (Cr-O1, Cr-O21, and Cr-O22), as well as the two bond angles Cr-O-Cr (Cr-O1-Cr and Cr-O2-Cr) in the orthorhombic structure of a YCrO$_3$ single crystal. In this structural symmetry (with $Pnma$ space group), Cr ions in YCrO$_3$ compound have the same Wyckoff site, $4b$ (0 0 0.5), as that of the Mn ions in La$_{\frac{7}{8}}$Sr$_{\frac{1}{8}}$MnO$_3$ compound [74, 159, 332, 308].

with the Debye approximations

$$U(T) = 9Nk_{\mathrm{B}}T\left(\frac{T}{\Theta_{\mathrm{D}}}\right)^3 \int_0^{\frac{\Theta_{\mathrm{D}}}{T}} \frac{x^3}{e^x - 1}dx, \tag{6.13}$$

where $N = 5$ is the number of atoms per formula unit, and Θ_{D} is the Debye temperature. With Eqs. (6.4) and (6.5), the lattice parameters of YCrO$_3$ compound in the PM state (above $T_{\mathrm{N}} \approx 141.5$ K) were fit, and the fits were extrapolated to overall temperatures as shown in Fig. 6.24 (solid lines). For example, the fitting for the unit-cell volume V results in $V_0 \approx 217.14$ Å^3, $Q \approx 7.57 \times 10^{-18}$ J, and $B \approx$ –40.73. The different variations in a, b, and c below T_{N} in contrast to our theoretical estimates by the Grüneisen (Gr) law [326, 325] (solid lines), e.g., $\frac{a_{\mathrm{Re}}^{12K} - a_{\mathrm{Gr}}^{12K}}{a_{\mathrm{Gr}}^{12K}} \approx$ –2.73 $\times 10^{-4}$, $\frac{b_{\mathrm{Re}}^{12K} - b_{\mathrm{Gr}}^{12K}}{b_{\mathrm{Gr}}^{12K}}$ $\approx$ –2.19 $\times 10^{-4}$, and $\frac{c_{\mathrm{Re}}^{12K} - c_{\mathrm{Gr}}^{12K}}{c_{\mathrm{Gr}}^{12K}} \approx$ –2.67 $\times 10^{-4}$, indicate an anisotropic magnetostriction effect and that magnetic anisotropy exists in YCrO$_3$ compound. Below T_{N}, the magnetically-driven additional decreases of a, b, and c jointly result in an enhanced
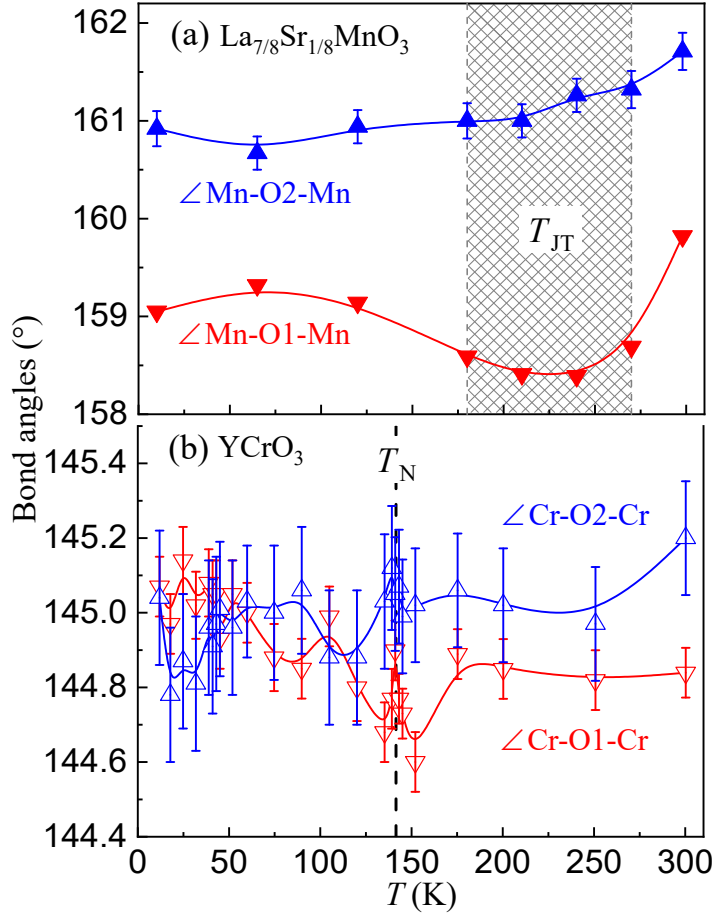
Figure 6.27: (a) Temperature-dependent bond angles of Mn-O1-Mn and Mn-O2-Mn in the $La_{7/8}Sr_{1/8}MnO_3$ single crystal [308]. $T_{JT} \approx 180$–270 K denotes the regime of the Jahn-Teller effect. (b) Temperature-dependent bond angles of Cr-O1-Cr and Cr-O2-Cr in the $YCrO_3$ single crystal from the present study. $T_N = 141.5(1)$ K labels the AFM transition temperature. The error bars in (a) and (b) are the standard deviations from refinements. The solid lines in (a) and (b) are guides to the eye.

sample contraction upon cooling, e.g., $\frac{V_{Re}^{12K} - V_{Gr}^{12K}}{V_{Gr}^{12K}} \approx -7.43 \times 10^{-4}$, signifying a magnetoelastic effect [346] and a localized nature of the t_{2g} moments, opposite the case in the GdSi metallic compound [347].

6.3.2.9 Comparison between t_{2g} $YCrO_3$ and e_g $La_{7/8}Sr_{1/8}MnO_3$ compounds

As shown in Fig. 6.25, it is of interest to compare the bond lengths of the $3d$ Mn^{3+}/Mn^{4+} ($e_g^1 t_{2g}^3 / e_g^0 t_{2g}^3$) ions in $La_{\frac{7}{8}}Sr_{\frac{1}{8}}MnO_3$ compound [308, 348] with those of the Cr^{3+} ($e_g^0 t_{2g}^3$) ions in $YCrO_3$ compound. The structural parameters of $La_{\frac{7}{8}}Sr_{\frac{1}{8}}MnO_3$ compound [308] were from a neutron-powder diffraction study on samples pulverized from a single crystal. This is thus comparable to the results from the present study. Both bond
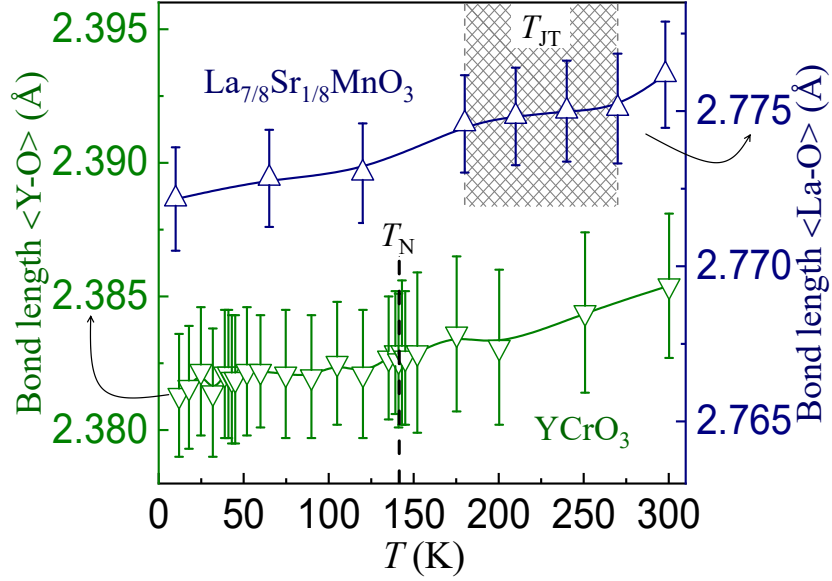
Figure 6.28: Comparison of the averaged bond lengths of Y-O in $YCrO_3$ (left, from the present study) and La-O in $La_{\frac{7}{8}}Sr_{\frac{1}{8}}MnO_3$ [308] (right) single crystals. $T_{JT} \approx 180$–270 K denotes the regime of the Jahn-Teller effect of $La_{\frac{7}{8}}Sr_{\frac{1}{8}}MnO_3$ compound. $T_N = 141.5(1)$ K labels the AFM transition temperature of $YCrO_3$ compound. The error bars are the calculated standard deviations. The solid lines are guides to the eye. It is clear that the bond length of $\langle Y\text{-}O \rangle$ is shorter than that of the $\langle La\text{-}O \rangle$ bond beyond statistics.

lengths of Mn-O21 and Mn-O22 [Fig. 6.25(a)] and the bond angle of Mn-O1-Mn [Fig. 6.27(a)] respond readily to the Jahn-Teller effect that occurs in $La_{\frac{7}{8}}Sr_{\frac{1}{8}}MnO_3$ compound within a temperature range of $\sim$ 180–270 K, whereas, those in $YCrO_3$ compound keep nearly constants, and both Cr-O bond lengths [Fig. 6.25(b)] and Cr-O-Cr bond angles [Fig. 6.27(b)] exhibit no response to the AFM transition, consistent with the fact that Cr^{3+} ions don't have the Jahn-Teller effect. The values of Cr-O1 bond lengths are similar to those of the Mn-O21, and Cr-O21 and Cr-O22 to Mn-O1 (Fig. 6.25).

As shown in Figs. 6.26 and 6.27, in contrast to the bond angle of Mn-O-Mn, $\angle$Cr-O-Cr decreases hugely by $\sim 15°$, which may correspond intimately to a possible lowering of the crystalline symmetry in the $YCrO_3$ single crystal. The relatively shorter bond length of $\langle Y\text{-}O \rangle$ (Fig. 6.28) introduces an immense mismatch between Y^{3+} and Cr^{3+} sites, leading to a huge chemical pressure and driving the subsequent rotating and tilting of the CrO_6 octahedra.
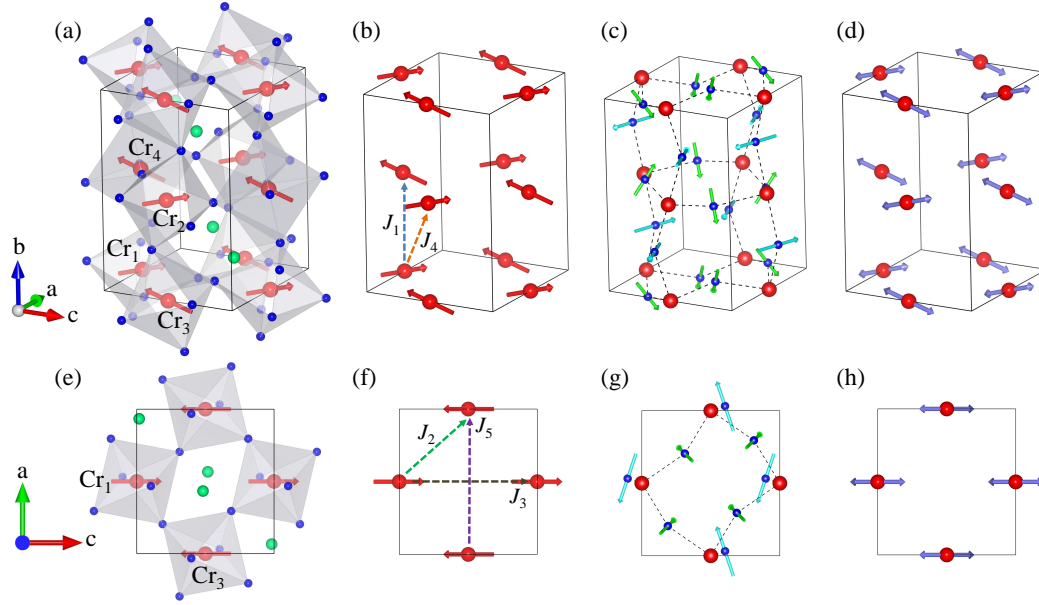
Figure 6.29: (a) Spin structure of YCrO$_3$ at 1.6 K in a conventional cell, in which Y, Cr, and O ions are labelled by green, red, and blue solid balls, respectively. The 4 magnetic ions in the unit cell are labeled by Cr1, Cr2, Cr3 and Cr4. (b) The exchange interactions J_1 and J_4 are defined in a conventional cell. (c) Dzyaloshinskii-Moriya (DM) interactions D_1 (green arrows) and D_2 (azure arrows) are defined. (d) Single-ion Ising anisotropic term on each Cr ions. Top view of b-axis of (e) spin structure at 1.6 K, (f) exchange interactions including J_2, J_3 and J_5, (g) DM interactions, (h) single-ion Ising anisotropic term.

6.3.3 Spin waves and magnetic exchange interactions in a spin-canted YCrO$_3$ antiferromagnet

It is also interesting to show the spectra in KL-plane at some constant energy, setting $H = 0$, shown in Fig. 6.33 and Fig. 6.34. We find the theoretical results fit INS data very well.

As there is an energy gap at $(0, 1, 1)$, the dispersions shown in intensities forms a series of concentric circles at low energies (see Fig. 6.33). But at higher energies, such as $E_i = 21$ meV in Fig. 6.34(b), the spectra show a square structure, which is very interesting. The good consistency between the experiment and theory at high energy confirms that the LSWT could describe the magnon excitaions well.

To unravel the nature of spin-wave excitations in YCrO$_3$, the INS experimental results were fit with the Heisenberg spin Hamiltonian based on above referred LSWT model. Exchange parameters of YCrO$_3$ are $SJ_1 = 3.0$, $SJ_2 = 2.0$, $SJ_3 = -1.2$, $SJ_4 = -0.4$, $SJ_5 = -1.2$, $SD_1 = -0.4$, $SD_2 = -0.3$, and $SJ_s = 0.32$ meV,
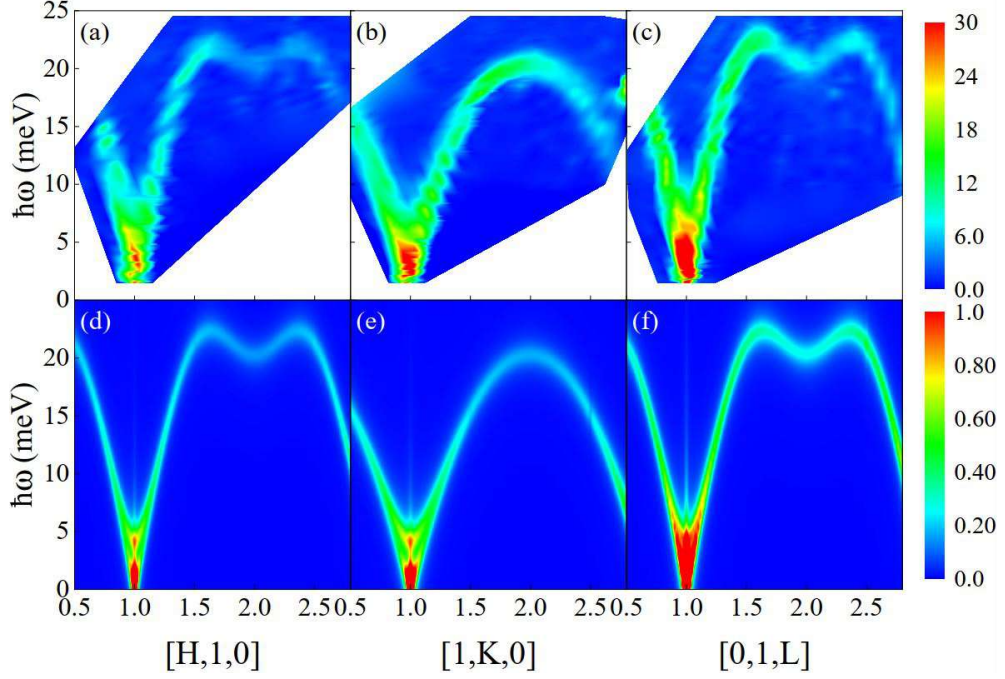
Figure 6.30: Spin wave spectra of INS in H, K and L directions. (a-c) are the measured spectra from INS experiments. (d-f) are the theoretical results. $\eta = 2$ meV is used in as a full width at half maximum (FWHM) for Delta function.

while $J > 0$ and $J < 0$ represent antiferromagnetic (AFM) and ferromagnetic (FM) exchange interactions respectively. Since the present LSWT model could describe the high energy spectrum well, it could be confirmed that the theoretical method is reliable. The fit parameters give $\phi = 2.7°$, which is much smaller than the measurement

With the present high-quality single crystal, an excellent agreement was achieved between the experimental INS data and the fit result. The present LSWT model with Heisenberg exchange J_1–J_5 and DM interaction gives $SJ_1 - SJ_2 = 1$ meV ($J_2/J_1 \sim$ 0.67), indicating an evident difference between the out-of-ac-plane and in-ac-plane NN Heisenberg exchange interactions in the YCrO$_3$ system. In contrast with previous reported INS study of YCrO$_3$ [227] and YFeO$_3$ [349], in which the Heisenberg exchange model was built with treating the nearest neighbouring (NN) Heisenberg exchange out-of-ac-plane (J_1) and the NN Heisenberg exchange in-ac-plane (J_2) as an identical type of exchange interaction.

We then proceed with understanding the quite large interlayer interaction J_1 in YCrO$_3$. According to the GKA rule [21, 22], the superexchange interaction in a transition-metal perovskite oxide strongly depends on the TM-O-TM bond angle and
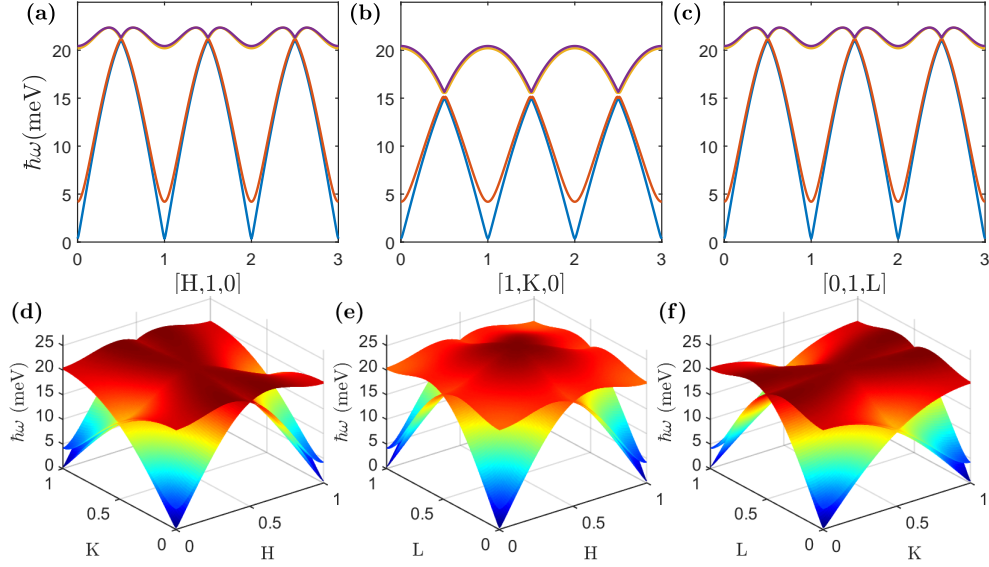
Figure 6.31: Theoretical results of spin wave dispersion relations alone k_x, k_y and k_z directions.

the TM-O bond length where TM stands as the transition-metal atoms. The T-O-T bond angle and T-O bond length could be remarked as θ and d, respectively. It was reported that the AFM interaction in transition-metal perovskite oxide can be precisely described by the formula $J \sim \cos^4(\omega/2)/d^7$ where $\omega = 180° - \theta$ [122, 350]. In the NPD study on YCrO$_3$, both the Cr-O-Cr bond angle and the Cr-O bond length could be extracted [35]. According to the NPD results collected at 12 K, a close values of θ ($\angle$Cr-O-Cr) were displayed between the J_1 and J_2 with $\theta_1 = 145.81°$ and $\theta_2 = 146.18°$. A smaller bond lengths of Cr-O bond were observed with $d_{\text{Cr-O}} = 1.967$ Å in the Cr-O-Cr pathway of J_1 than that of J_2. Since there exist two types of Cr-O bond in the Cr-O-Cr pathway of J_2, using the average value of them with $d_{\langle\text{Cr-O}\rangle} = 1.9875$ Å will mediate their difference. The GKA rule states that superexchange interactions are AFM where the VCT is between the overlapping orbitals that are half-filled, but they are FM where the VCT is from a half-filled to an empty orbital or from a filled to a half-filled orbital. With the above bond parameters, the formula $J \sim \cos^4(\omega/2)/d^7$ gives $J_2/J_1 \sim 0.93$, indicating an apparent difference exists between J_1 and J_2 even only considering the contribution from AFM part. Therefore, it will be a good treatment to separate the out-of-ac-plane and the in-ac-plane NN Heisenberg exchange interactions.

In practice, a much smaller value of $J_2/J_1 \sim 0.67$ was obtained by the LSWT fit on
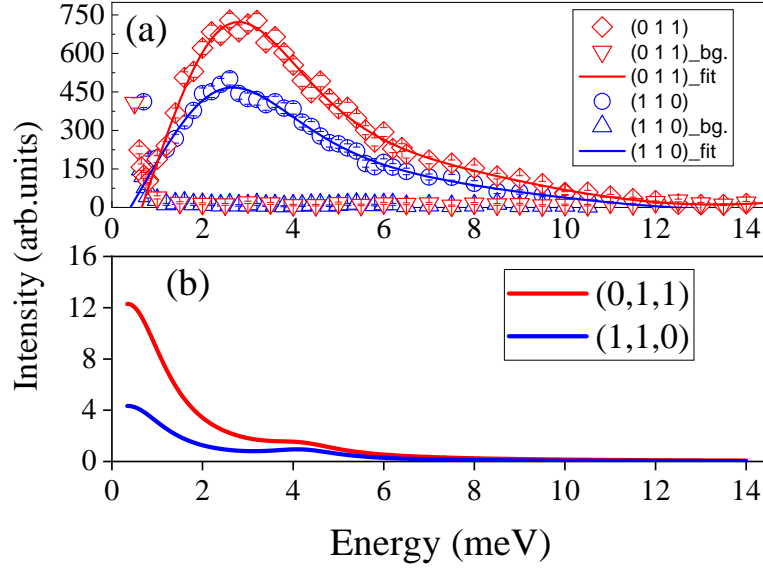
Figure 6.32: Energy dependence of intensities at momenta $(1,1,0)$ and $(0,1,1)$. (a) INS results. (b) Theoretical fits.

the INS result. This may imply the overall difference between exchange interactions of J_1 to J_2 cannot be fully described when merely considering the distinctions coming from angle and bond-length dependence on the AFM coupling. YCrO$_3$ has an $S =$ 3/2 Cr^{3+} ($t_{2g}^3 e_g^0$) state, where a t_{2g}-e_g orbital hybridization could exist in the Cr-O-Cr electron hopping process. Because of the empty e_g orbital, the ferromagnetic coupling will be enhanced to the overall superexchange of $J = J^\pi - J_{hb}^\sigma$, in which J^π and J_{hb}^σ stand as the Cr-O-Cr angle dependent AFM coupling and the FM coupling induced by t-e hybridization [43]. When looking back on the Cr-O-Cr bond parameters of YCrO$_3$, very close θ values were displayed between the Cr-O-Cr pathways of J_1 and J_2. But, there also exists a different d_{Cr-O} value with a compressed Cr-O bond at the pathway of J_1, indicating the d_{Cr-O} value may have a significant role on the change of t_{2g}-e_g orbital hybridization. This is totally different with the case of $S = 5/2$ Fe^{3+} ($t_{2g}^3 e_g^2$) for YFeO$_3$, in which no FM coupling could act on the overall superexchange interaction by the t_{2g}-e_g hybridization. Consequently, the Cr-O-Cr superexchanges need to be discriminated between the one out-of-ac-plane and the one in-ac-plane in perovskite orthochromite compounds.

In such a spin-canted antiferromagnet, the DM interactions, which represent the antisymmetric exchanges, have a big magnitude of $D_1 = -0.27$ meV and $D_2 = -0.2$
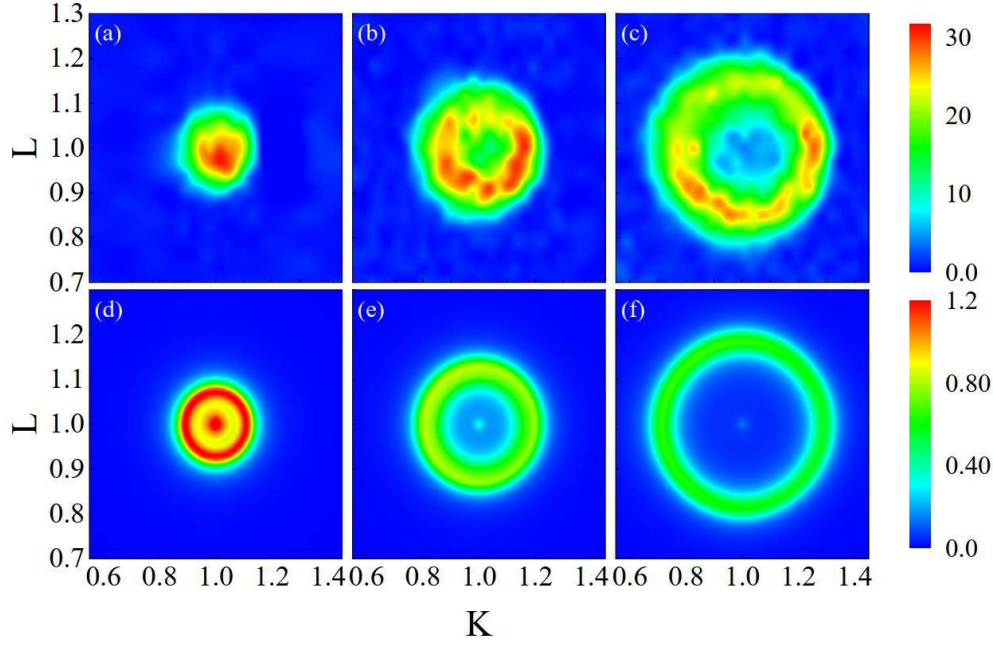
Figure 6.33: Spin wave spectra at $(0\ K\ L)$ plane. Constant energy cut are chosen as 4 (the first column), 7 (the second column) and 10 meV (the third column) at 1.6 K. (a-c) are experimentals while (d-f) are theoretical results.

meV. Such strong DM interactions compete with the isotropic Heisenberg exchanges, and cant the spin moments to minimize the energy of ground state, resulting in the observed spin-wave dispersion profile. Moreover, the DM interactions have the same order of magnitude as the Heisenberg exchange term, implying the SOC cannot be ignored in $YCrO_3$. There also exists single-crystal based INS study to unpuzzle the exchange interactions in the orthorhombic $YFeO_3$, while they treated the out-of-ac-plane and the in-ac-plane NN Heisenberg exchanges as one identical type J_1, and the $J_3 - J_5$ Heisenberg exchange in the present model were deemed as another identical interaction, i.e., the next-nearest-neignbouring (NNN) which was noted as J_2. In the precedent simplified model, the Heisenberg exchange parameters J_1 and J_2, the DM interaction parameters D_1 and D_2 were fit with $J_1 =$ –4.77 meV, $J_2 =$ –0.21 meV, $D_1 =$ –0.074 meV, and $D_2 =$ –0.028 meV [349]. The DM interaction was given with a energy scale of two-order magnitude smaller than the Heisenberg exchange term. Compared with the Heisenberg exchange the DM interaction is so tiny in $YFeO_3$.

In contrast, the $YCrO_3$ compound gives much stronger DM interactions than the $YFeO_3$ compound, demonstrating the existence of SOC in $YCrO_3$ compounds. Since

186
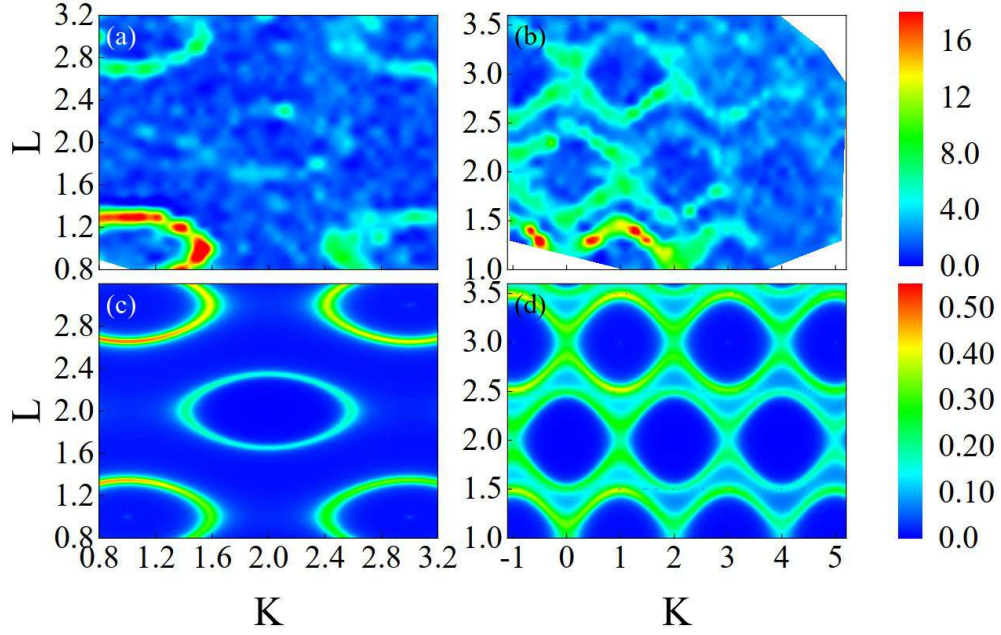
Figure 6.34: Spin wave spectra at (0 K L) plane. Constant energy cut are chosen as 17 (the first column) and 21 meV (the second column) at 1.6 K. (a) and (b) are experiments while (c) and (d) are our calculation results.

the asymmetric exchange interaction usually appears in noncentresymmetic structures [106], rather than centresymmteric structures like the orthochromates. It can be inferred that the actual crystal structure of the YCrO$_3$ compound might be lower than the orthorhombic structure. This result is consistent with the previous observation of ferroelectricity in the system [48]. In the precedent study of magnetization measurement on a YCrO$_3$ single crystal, the energy scale of the exchange field, the Dzyaloshinsky field, and the anisotropy field were evaluated with $H_E = 1.6 \times 10^6$ Oe, $H_D = 7 \times 10^4$ Oe, and $H_A = 2000$ Oe, respectively [298]. It should be admitted that the above evaluation were carried out under a very simplified model. A Heisenberg model, which could distinguish each NN and NNN exchange interaction, needs to be introduced, to precisely determine each exchange interaction in such a complex magnetic system. The existence of SOC in the YCrO$_3$ canted antiferromagnet makes it an ideal platform to manipulate the SOC by substitutional adulteration or other types of chemical pressure.

At the high energy region, as shown in Fig. 6.34(b), the spectra show an interesting square structure. In general, the spectra at high energy reflect more detailed messages about the interactions [351]. It was found that the special spectra from the appreciable

interlayer interactions, i.e., $SJ_1 = 3.0$ meV and a small absolute value $SJ_4 = -0.4$ meV. Such a space anisotropy causes a square profile in KL plane. The small spin gap of ~ 0.5 meV at (1,1,0) and (0,1,1) indicates a very tiny anisotropic Heisenberg exchange. In contrast, a much larger spin gap was exhibited in the INS experiment on the $YFeO_3$ compound, indicating a possibly stronger magnetic anisotropic exchange. Consequently, higher-order anisotropic Heisenberg terms need to be considered in the $YFeO_3$ compound [349]. This issue was also verified by a precedent study on the magnetization, in which the second- and fourth-order anisotropic term H_{K2} and H_{K4} were determined with $H_{K2} = 1.2 \times 10^3$ Oe and $H_{K4} = 2.6 \times 10^2$ Oe for $YFeO_3$, $H_{K2} = 8.8 \times 10^2$ Oe and $H_{K4} = 0$ for $YCrO_3$ [352]

6.4 Conclusions

To summarize, a $YCrO_3$ single crystal has been grown by a laser diode FZ method. Based on the as-grown single crystal, the high-temperature (300–980 K) magnetism and structural information (321–1200 K) of the $YCrO_3$ compound were quantitatively investigated. The high-temperature magnetization can only be fit by the CW law with multiple effective PM moments and multiple PM CW temperatures with strong magnetic frustration, implying a complicated low-temperature magnetic structure. The magnetization versus applied-magnetic-field curve obeys well the present modified Brillouin function with an inclusion of a factor η, denoting the strength of magnetic interactions. The crystal structure was refined with $Pmnb$ symmetry in the entire studied temperature range within the present experimental accuracy. Detailed structural information including lattice constants, unit-cell volume, atomic positions, thermal parameters, bond lengths, local distortion parameter, bond angles, local distortion modes, and BVSs, were extracted. The thermal expansions along the a, b, and c axes are anisotropic with an anomaly appearing around 900 K. This anomaly might be attributed to an isosymmetric structural phase transition. The local distortion parameter Δ of Cr ions is about two orders of magnitude lower than that of Y and O ions. It was found that both Y and O2 ions produce a clear atomic displacement and a large charge

deviation from theoretical ones. Thus, the present thesis suggests that the Y and O2 ions may play an important role in forming the previously reported dielectric anomaly of the YCrO$_3$ compound. The present results make YCrO$_3$ a particularly significant compound for theoretical and further experimental studies on t_{2g} physics. The magnetic structure and dielectric property would be further explored in combination with theoretical calculations.

With the as-grown single crystal, ICP-OES measurement gives a nearly stoichiometric chemical ratio of Y$_{0.97(2)}$Cr$_{0.98(2)}$O$_{3.00(2)}$. There are three electrons locating on the 3d t_{2g} orbitals of Cr^{3+} ions, therefore, the YCrO$_3$ compound is a robust insulator. Although the measurements of the applied-magnetic-field dependent heat capacity as well as the magnetization versus temperature and applied-magnetic field show the character of a very soft ferromagnet with a coersive force of ~ 0.05 T, the extracted PM CW temperature, $\theta_{CW} = -433.2(6)$ K, by the fit with a CW law is strongly negative with the frustrating parameter $f = |\theta_{CW}|/T_N = 3.061(5)$, and the measured magnetization at 2 K and 7 T is only $\sim 3.2\%$ of the theoretical saturation moment. These indicate that the spin moments of Cr^{3+} ions in YCrO$_3$ compound are magnetically frustrated. The consistency between the effective PM moment, $\mu_{\text{eff\_meas}} = 3.95(2)$ μ_B, and the theoretically-calculated value, $\mu_{\text{eff\_theo}} = 3.873$ μ_B, validates the results concluded in the framework of the CW-law fitting. By magnetization measurements, it could be determined that the magnetic phase transition temperature as $T_N = 141.5(1)$ K at an applied-magnetic field of 0.01 T. This is in agreement with the present neutron-powder and single-crystal diffraction studies. The magnetic transition temperature was pushed upward to T_N (5T) = 144.5(1) K at 5 T, increased by ~ 3 K.

With the neutron-powder diffraction study, it is able to established an AFM structure with the propagation vector at **k** = (1 1 0) and the same unit cell as that of the crystalline structure (with space group $Pnma$). The direction of the Cr^{3+} spin moments is along the crystallographic c axis. The refined moment size is 2.45(6) μ_B at 12 K, $\sim 82\%$ of the theoretical saturation value 3 μ_B. This is consistent with the fact that a magnetic frustration exists in YCrO$_3$ compound. By the fit on integrated in-

tensities of the magnetic Bragg (1 1 0) reflection extracted from the pure magnetic contribution with a power law, it was found that the Cr^{3+} spin interactions were probably two-dimensional Ising like within the reciprocal (1 1 0) scattering plane. Above $T_N = 141.5(1)$ K, the refined lattice constants a, b, and c as well as the unit-cell volume V, agree well with the Grüneisen rules at zero pressure with a second-order fashion. By comparison, below T_N, the lattice configuration (a, b, c, and V) deviates largely downward from the Grüneisen law, displaying an anisotropic magnetostriction effect along the crystallographic a, b, and c axes and a magnetoelastic effect with the unit-cell volume V. Especially, upon cooling, the sample contraction is enhanced below T_N.

In the whole studied temperature range of 12–302 K, no crystalline structural phase transition was observed with the neutron-powder diffraction study, whereas by the present single-crystal neutron diffraction study, the Bragg (1 1 0) peak was clearly observed above the magnetic phase transition temperature 141.5(1) K. This peak persists up to 300 K and is forbidden by the crystalline orthorhombic structure (with space group $Pnma$). This implies that the actual crystalline structure of $YCrO_3$ compound is probably lower than the present one. To figure out the reasons for a possible lowering of the structural symmetry in the $YCrO_3$ single crystal, the t_{2g} $YCrO_3$ and the e_g $La_{7/8}Sr_{1/8}MnO_3$ single crystals were compared. It is pointed out that with a limited number of the observed magnetic Bragg peaks, it is hard to determine the canting degree of the AFM Cr^{3+} spins. This can be addressed by a further time-of-flight single-crystal neutron-diffraction study. To determine the actual crystalline structure is not an easy job, but it would shed light on the dielectric anomaly of $YCrO_3$ compound.

Moreover, with a single-crystal $YCrO_3$ antiferromagnet with canted spin moments, an INS study on the spin-wave excitation spectra was carried out. The experimental INS result shows a spin gap at (1,1,0) and (0,1,1) of the magnon spectra with ~ 0.5 meV, evidencing a small magnetic anisotropy in the $YCrO_3$ compound. Hence, the present LSWT framework, in which the isotropic Heisenberg exchange predominates, is perceived as an ideal model for the $YCrO_3$ compound. The experimental spin-wave dispersion in the $YCrO_3$ compound can be well described by the LSWT model, which

is composed of the Heisenberg exchange J_1–J_5, the Dzyaloshinskii-Moriya interaction D_1 (in-ac-plane vector) and D_2 (out-of-ac-plane vector), and the single-ion Ising anisotropy term. Unlike the YFeO$_3$ compound, a dramatic difference with $J_2/J_1 \sim$ 0.67 was displayed in the YCrO$_3$ compound with S = 3/2 Cr^{3+} ($t_{2g}^3 e_g^0$) state between the out-of-ac-plane NN Heisenberg exchange interaction J_1 and the in-ac-plane NN Heisenberg exchange interaction J_2. This may imply the existence of the t_{2g}-e_g orbital hybridization. And the alteration of Cr-O bond length may significantly influence the FM coupling of the t_{2g}-e_g hybridization in a Cr-O-Cr superexchange. To precisely determine the values of each exchange interaction, a thorough Heisenberg exchange model distinguishing each exchange is supposed to be built, as introduced in the present Ph.D. thesis. To reproduce the magnon band successfully, a noticeable DM interaction value needs to be introduced, implying the existence of the SOC in the YCrO$_3$ canted antiferromagnet. The appreciable asymmetric exchange interaction may imply that the actual crystalline structure of the YCrO$_3$ system might be lower than the orthorhombic structure. To unravel this puzzle, a spallation neutron source based single-crystal diffraction needs to be then carried out. In the present thesis, the spin interactions of the YCrO$_3$ antiferromagnet were revealed with the comprehensive INS study, to shed light on the potential crystalline structure of the YCrO$_3$ compound, a candidate for multiferroic materials.

CHAPTER 7

MAGNETIC PHASE DIAGRAM AND MAGNETOCALORIC EFFECT IN SINGLE-CRYSTAL GDCRO$_3$

7.1 Introduction

The GdCrO$_3$ compound was initially synthesized in 1956 [28]. Its crystalline structure was proved to be orthorhombic with the space group $Pbnm$ and lattice constants a = 5.312 Å, b = 5.514 Å, and c = 7.611 Å [29]. Recently, the space group was determined to be $Pna2_1$ [240]. Later, its infrared and electronic absorption spectra were studied [353]. Although the GdCrO$_3$ single crystal grown with a flux method may contain ∼1% impurity, it was proposed that below ∼ 7 K, the ionic Cr^{3+} magnetic sublattice underwent a spin reorientation from the Γ_4 (G_x, A_y, F_z) to the Γ_2 (F_x, C_y, G_z) magnetic structure. This was driven by the formation of the Gd^{3+} magnetic sublattice and the Gd^{3+}-Cr^{3+} couplings [75, 354]. The behavior of negative magnetization with a minimum centered around 25 K was observed in a polycrystalline GdCrO$_3$ sample, which was ascribed to the interactions between paramagnetic (PM) Gd^{3+} moments and the canted Cr^{3+} antiferromagnetic (AFM) moments [355]. It was reported that the GdCrO$_3$ compound displayed an electric polarization of 0.7 μC/m^2 at E = 2.25 kV/cm, appearing simultaneously with the formation of the Cr^{3+} magnetic structure below $T_{\text{N-Cr}}$ [50]. The distortion in the GdCrO$_3$ structure was proposed to be associated with the off-center displacement of Gd atoms together with octahedral rotations via displacement of oxygen ions [240, 356]. Magnetic refrigeration has risen to become a new civilian refrigeration technology [357]. Besides the ferroelectric properties, the GdCrO$_3$ compound has attracted much attention and been believed to be a promising magnetorefrigerator material due to its high effective magnetic entropy change [51, 358, 359, 360].

In the present thesis, a GdCrO$_3$ single crystal was grown using laser diodes with the floating-zone (FZ) technique. The crystalline structure was characterized with a

room-temperature X-ray powder diffraction (XRPD) study. The magnetic properties were also studied with a physical property measurement system (PPMS DynaCool instrument, Quantum Design). Based on the measurements, the magnetocaloric effect (MCE) was studied, it was found that the $GdCrO_3$ single crystal investigated in this thesis displayed the highest magnetic entropy change among all $RECrO_3$ compounds (RE = $4f^n$ rare earths, $n = 7–14$). Moreover, the magnetic phase diagrams were built as a function of applied magnetic field around the magnetic phase transitions of Gd^{3+} and Cr^{3+} ions, shedding light on a further understanding of the nature of the intriguing magnetism.

7.2 Methodology

Polycrystalline samples of the $GdCrO_3$ compound were synthesized using the conventional solid-state reaction method [74, 159, 332]. Chemically stoichiometric raw materials of Gd_2O_3 (Alfa Aesar, 99.9%) and Cr_2O_3 (Alfa Aesar, 99.6%) were milled and mixed by a Vibratory Micro Mill (FRITSCH PULVERISETTE 0) with an addition of 5–10% Cr_2O_3 compound. The mixture was calcined twice at ambient air pressure: One time was at 1100 °C for 24 h, and the other was at 1200 °C for 36 h. $GdCrO_3$ single crystals were grown with a laser diode FZ furnace (model: LD-FZ-5-200W-VPO-PC-UM) [63, 192, 248].

A small piece of the single crystal was pulverized to check the phase purity, the room-temperature crystalline structure was determined with XRPD employing copper $K_{\alpha 1}$ (1.54056 Å) and $K_{\alpha 2}$ (1.544390 Å) with a ratio of 2:1 as the radiation. The XRPD pattern was collected at $2\theta = 20–90°$ with a step size of 0.02°. The software FULLPROF SUITE was used to refine the collected XRPD data [204]. To estimate the background contribution, the Bragg peak shape was modelled with a pseudo-Voigt function. Also, a linear interpolation was used between automatically selected data points. The refining parameters are scale factor, zero shift, background contribution, peak shape parameters, asymmetry, preferred orientation, lattice constants, and atomic positions.

The measurements of the dc magnetization and the specific heat were carried out on a PPMS DynaCool instrument using the vibrating sample magnetometry and the heat capacity options, respectively. The dc magnetization at an applied magnetic field of 500 Oe was measured with two modes at 1.8–300 K: One was after cooling with 0 Oe, i.e., zero-field cooling (ZFC), and the other was at $\mu_0 H = 500$ Oe, i.e., field cooling (FC). To clearly show the effect of applied magnetic field on magnetic structures of the two magnetic ions Gd^{3+} and Cr^{3+}, ZFC magnetization measurements at different fields as a function of temperature in two ranges (1.8–8 and 165–172 K) were performed. ZFC magnetization measurements from –14 to 14 T at different temperatures were carried out either in a mode of the magnetic hysteresis loop or as a function of increasing magnetic field. In order to gain the adiabatic temperature change, the specific heats at 1.8–300 K were measured at magnetic fields of 0, 0.5, 1, 2, 3, 5, 6, 8, 10, 12, and 14 T.

7.3 Results and discussion

7.3.1 Structural study

To study the crystalline structure of the present grown $GdCrO_3$ single crystal, a small piece of the $GdCrO_3$ single crystal was pulverized. An XRPD experiment was then carried out at room temperature. Figure 7.1(a) shows the collected and refined patterns. Within the present experimental accuracy, the data can be well indexed with space group $Pmnb$. The corresponding crystalline structure in one unit cell is exhibited in Fig. 7.1(b), and the refined structural information is listed in Table 7.1. The low values of the goodness of refinement validate the present FULLPROF refinements. The present refined room-temperature lattice constants of the pulverized $GdCrO_3$ single crystal are $a = 7.6041(3)$ Å, $b = 5.5255(2)$ Å, and $c = 5.3102(2)$ Å, consistent with previously reported values from a study with the polycrystalline $GdCrO_3$ compound [355].
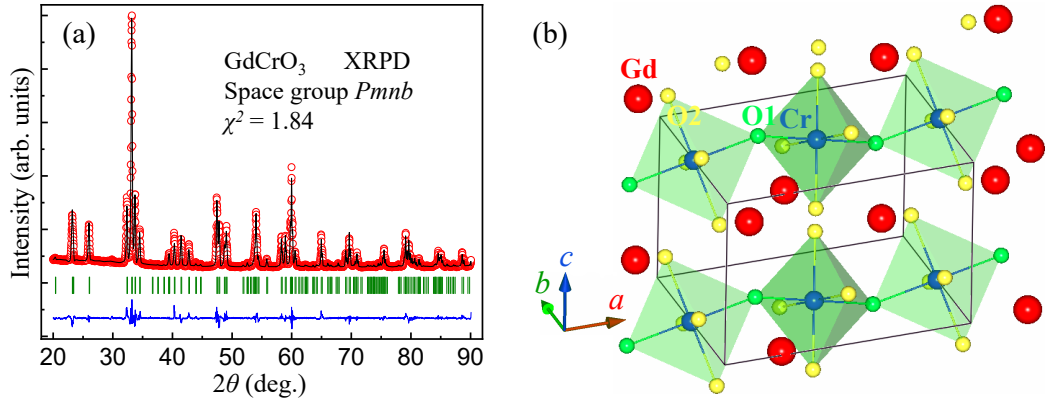
Figure 7.1: (color online) (a) Observed (circles) and refined (solid line) XRPD patterns collected with a pulverized GdCrO$_3$ single crystal at room temperature. Vertical bars mark the positions of Bragg peaks. The bottom curve represents the difference between observed and refined XRPD patterns. (b) Crystal structure of the GdCrO$_3$ compound in one unit cell (solid lines) with $Pmnb$ space group (No. 62). The Gd, Cr, O1, and O2 ions are labeled.

7.3.2 Magnetic phase transitions

Figure 7.2 shows the measured magnetization as a function of temperature. As shown on the left axis of Fig. 7.2(a), as temperature decreases from 300 to 1.8 K, there is a smooth increase in the magnetization with an anomaly appearing around $T_{\text{N-Cr}}$ [Fig. 7.2(d)]. At $T_{\text{N-Cr}}$, a small sharp increase was observed [Fig. 7.2(d)]. This is by far clearer in the inverse magnetic susceptibility χ^{-1}, as shown on the right axis of Fig. 7.2(a). The magnetization increases smoothly again until around 25 K. We observed a maximum at T_{SR} [Fig. 7.2(c)]. Upon further cooling, there exists a kink at $T_{\text{N-Gd}}$ [Fig. 7.2(c)]. These anomalies are attributed to magnetic phase transitions. The first anomaly is related to Cr^{3+} ions, and $T_{\text{N-Cr}} \approx 168.97$ K at 0.06 T. The second one is ascribed to the spin reorientation of Cr^{3+} ions due to the gradual formation of Gd^{3+} moments [75], and $T_{\text{SR}} \approx 6.74$ K at 0.02 T. Taking into account the fact that the ordering of $4f$ magnetic Gd^{3+} ions requires much lower temperatures [361, 362], the third one thus corresponds to the formation of a long-range-ordered Gd^{3+} magnetic structure, and $T_{\text{N-Gd}} \approx 2.33$ K at 0.02 T. The inverse magnetic susceptibility χ^{-1} in a pure PM state observes well with the CW law

$$\chi^{-1}(T) = \frac{3k_{\text{B}}(T - \theta_{\text{CW}})}{N_{\text{A}}\mu_{\text{eff}}^2}, \tag{7.1}$$

195

Table 7.1: Refined structural parameters, including lattice constants, unit-cell volume V, atomic positions, and goodness of refinement, from room-temperature XRPD with a pulverized $GdCrO_3$ single crystal (orthorhombic, $Pmnb$ space group, No. 62, $Z = 4$). The Wyckoff sites of all atoms are listed. We kept the atomic occupation factors (OCs) during FULLPROF refinements. The numbers in parentheses are the estimated standard deviations of the last significant digit. $R_p = 3.28$, $R_{wp} = 4.64$, $R_{exp} = 3.43$, and $\chi^2 = 1.84$.

a (Å)	b (Å)	c (Å)	V (Å^3)	$\alpha(= \beta = \gamma)$ (deg)	
7.6041(3)	5.5255(2)	5.3102(2)	223.12(2)	90	
Atom	Site	x	y	z	OCs
Gd	$4c$	0.25	0.0588(2)	0.0151(3)	0.5
Cr	$4b$	0.00	0.00	0.50	0.5
O1	$4c$	0.25	0.4705(19)	0.1146(19)	0.5
O2	$8d$	0.0530(10)	0.2784(17)	–0.2935(16)	1.0

where $k_B = 1.38062 \times 10^{-23}$ J/K is the Boltzmann constant, θ_{CW} is the PM CW temperature, $N_A = 6.022 \times 10^{23}$ mol^{-1} is Avogadro's constant, and $\mu_{eff} = g\mu_B \sqrt{J(J+1)}$ is the effective PM moment. The magnetization in the temperature range of 200—300 K ($> T_{N\text{-}Cr} > T_{N\text{-}Gd}$) was fit to Eq. (7.1). The fit was then extrapolated down to $M(\theta_{CW}) = 0$, as shown on the right axis of Fig. 7.2(a). This results in an effective PM moment $\mu_{eff} = 8.40(9)$ μ_B and a PM CW temperature $\theta_{CW} = -20.33(4)$ K. It is stressed that these values correlate with the PM behaviors of both Gd^{3+} and Cr^{3+} ions. Here, the extracted $\mu_{eff} = 8.40(9)$ μ_B is a little larger than the previously reported value of ~ 8.2 μ_B from a study with the polycrystalline $GdCrO_3$ compound [288], indicating a better quality of the single-crystal $GdCrO_3$ sample. For Gd^{3+} ions (shell $4f^7$, quantum numbers $S = \frac{7}{2}$, $L = 0$, and $J = \frac{7}{2}$), the size of the theoretical (theo.) effective PM moment is 7.94 μ_B, while for Cr^{3+} ions, $\mu_{eff\_theo.} = 3.873$ μ_B [63], therefore, $\mu_{eff\_theo.} = \sqrt{7.94^2 + 3.873^2}$ $\mu_B = 8.834$ μ_B for the $GdCrO_3$ compound. This theoretical value is $\sim 5.17\%$ larger than the corresponding experimental value of 8.40(9) μ_B, which indicates that vacancies probably exist in the Gd and/or Cr atomic sites. The magnetic frustration parameter $f = \frac{|\theta_{CW}|}{T_N}$ was calculated schematically [63]; for Cr^{3+} ions at 0.05 T, $f_{Cr} \approx 0.12$. Compared with the $YCrO_3$ compound within which the Y^{3+} ions are nonmagnetic and $f_{Cr} \approx 3.06$ [35], the competing degree of AFM and
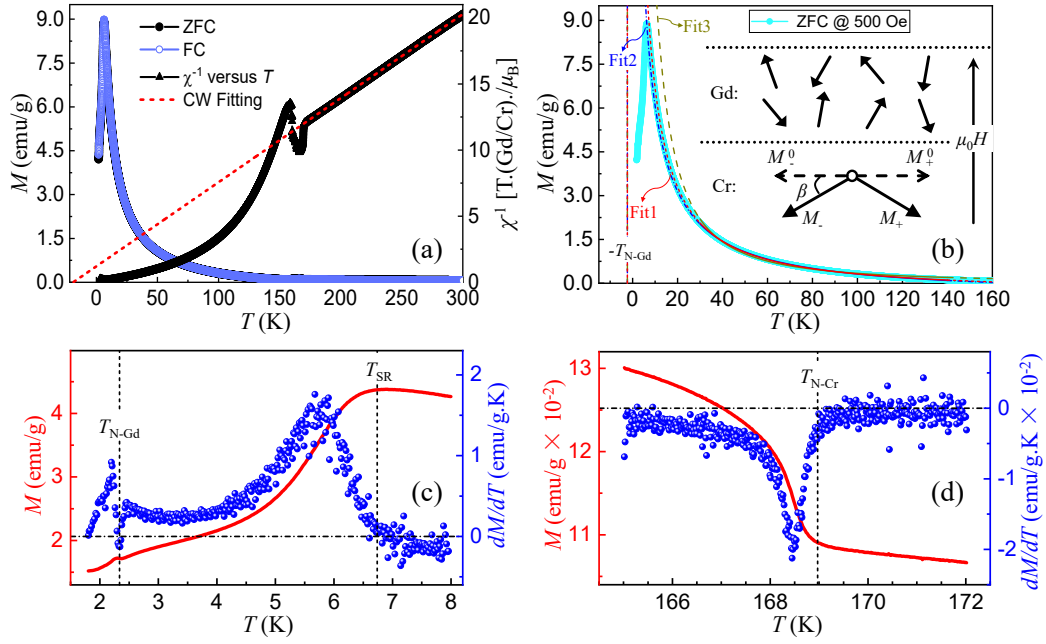
Figure 7.2: (color online) Representative magnetization measurements of a small piece of GdCrO$_3$ single crystal with random crystallographic orientations. (a) ZFC (solid circles) and FC (void circles) magnetization M (left axis) and the corresponding ZFC inverse magnetic susceptibility χ^{-1} (solid triangles; right axis) at an applied magnetic field of 500 Oe as a function of temperature in the range of 1.8–300 K. The dashed line represents the fit with a CW law. (b) ZFC M versus temperature (solid circles) measured at 500 Oe from 1.8 to 160 K. The solid lines denote fit 1 [with Eq. (7.3)], fit 2 [with Eq. (7.2)], and fit 3 [with Eq. (7.3)] in the temperature range of 30–140 K. They were extrapolated to the whole temperature regime [–$T_{\text{N-Gd}}$, 160 K] and are shown as the short-dashed line (fit 1), dash-dotted line (fit 2), and long-dashed line (fit 3). The inset schematically shows spin configurations of Gd^{3+} and Cr^{3+} ions within 30–140 K. See details in the text. (c) ZFC M (left axis), as well as the corresponding dM/dT (right axis), versus temperature in the range of 1.8–8 K at 200 Oe. $T_{\text{N-Gd}}$ points out the magnetic transition temperature of Gd^{3+} ions, which was defined as the temperature point where the slope of the M-T curve is minimum. T_{SR} indicates the spin reorientation (SR) temperature of Cr^{3+} ions, which was defined as the temperature point from which the slope of the M-T curve changes from negative to positive upon cooling. (d) ZFC M (left axis) and its slope dM/dT (right axis) versus temperature in the range of 165–172 K at an applied magnetic field of 600 Oe. $T_{\text{N-Cr}}$ implies the magnetic transition temperature of Cr^{3+} ions, which was defined as the temperature point at which a kink appears in the slope of the M-T curve upon cooling.

ferromagnetic interactions in GdCrO$_3$ compound is much weaker. The introduction of magnetic Gd^{3+} ions in the GdCrO$_3$ compound has a strong effect on the magnetic structure of Cr^{3+} ions, in agreement with the appearance of T_{SR}.

To analyze individually the PM behavior of Gd^{3+} ions, the magnetization data in the temperature range of 30–140 K was taken. This thermal range was within the

Table 7.2: Fit values of the parameters M_{BG} and γ while modelling the temperature-dependent ZFC magnetization data of the GdCrO$_3$ single crystal (measured at 7–30 K and 500 Oe) with Eq. 7.3. The whole temperature range was divided into five regimes (see details in the text). During the refinements, $m = 114.17(51)$ emu K/g and $\theta_{\mathrm{CW}} = -2.33$ K were fixed. The numbers in parentheses are the estimated standard deviations of the last significant digit.

T regime (K)	7–10	10–15	15–20	20–25	25–30
M_{BG} (emu/g)	1.312(12)	0.050(8)	–0.239(10)	–0.306(12)	–0.329(15)
γ	1.229(1)	1.144(1)	1.122(1)	1.115(1)	1.112(2)

interval $(T_{\mathrm{N\text{-}Gd}}, T_{\mathrm{N\text{-}Cr}})$ (Fig. 7.2), far above $T_{\mathrm{N\text{-}Gd}}$ (to ensure that Gd^{3+} ions were indeed in a PM state) and $\sim$20 K below $T_{\mathrm{N\text{-}Cr}}$ (to weaken the effect of ordered Cr^{3+} ions as much as possible). The data was first tentatively fit with

$$M = M_{\mathrm{BG}} + \frac{m}{T - \theta_{\mathrm{CW}}}, \tag{7.2}$$

where M_{BG} is the contribution from background (BG) magnetization that includes actual BG magnetization from the instrument and sample holder, as well as the glue, the temperature-independent diamagnetism components of the Gd^{3+} and Cr^{3+} ions, and the temperature-independent net magnetization of the Cr^{3+} magnetic sublattice, and m is a constant. Similar modeling strategies were used previously [75, 51, 173, 355, 363]. The values of the diamagnetism of Gd^{3+} and Cr^{3+} ions are $\sim -2.0 \times 10^{-5}$ and $\sim -1.1 \times 10^{-5}$ emu/mol [311], respectively, which could be neglected reasonably. Since the Gd^{3+} magnetic sublattice seems to form a long-range AFM order below $T_{\mathrm{N\text{-}Gd}}$, most likely, the frustration parameter of Gd^{3+} ions $f = \frac{|\theta_{\mathrm{CW}}|}{T_{\mathrm{N}}^{\mathrm{Gd}}} \approx 1$, from which it can be deduced with $\theta_{\mathrm{CW}}^{\mathrm{Gd}} \approx -T_{\mathrm{N}}^{\mathrm{Gd}} \sim -2.33$ K. By forcing $\theta_{\mathrm{CW}}^{\mathrm{Gd}} = -2.33$ K, the data was refined with Eq. (7.2), $M_{\mathrm{BG}} = -0.473(33)$ emu/g and $m = 80.823(22)$ emu K/g were then obtained, and the resultant fit is shown as fit2 in Fig. 7.2(b). It is worth noting that in Eq. (7.2), the net magnetization of the Cr^{3+} magnetic sublattice is supposed to be temperature independent, which is true only at low temperatures. For example, achieving this stage for the YCrO$_3$ single crystal, it requires temperatures at least below ~ 50
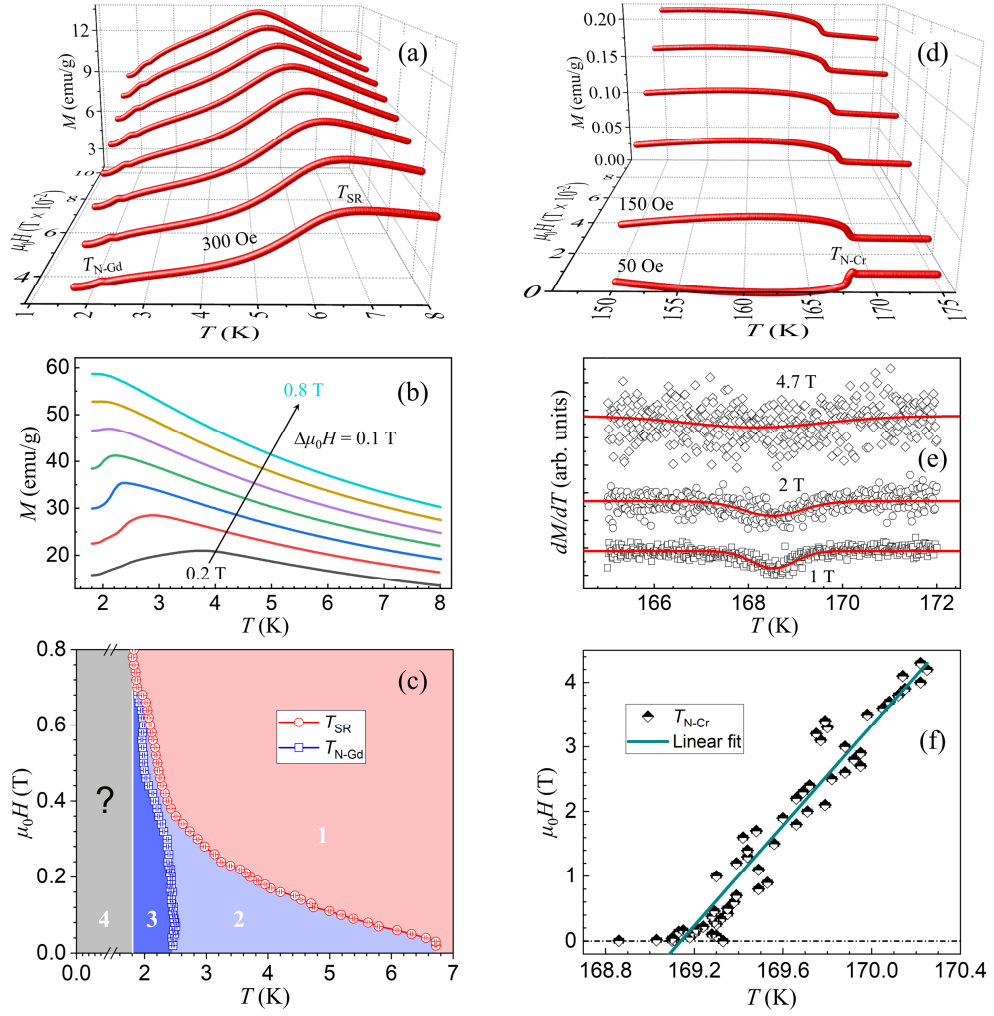
Figure 7.3: (color online) ZFC M as a function of temperature from 1.8 to 8 K at applied magnetic fields of (a) 300–1000 Oe with a step size of 100 Oe and (b) 0.2–0.8 T with $\Delta\mu_0 H = 0.1$ T. (c) Applied magnetic-field- and temperature-dependent phase diagram of $T_{N\text{-}Gd}$ and T_{SR}. (d) ZFC M versus temperature from 150 to 175 K at applied magnetic fields of 50, 150, 400, 600, 800, and 1000 Oe. (e) Slope dM/dT (symbols) of the M-T curve at 1, 2, and 4.7 T. The solid lines are fits with a modified Gaussian function, as guides to the eye. (f) $T_{N\text{-}Cr}$ as a function of applied magnetic field (symbols). We fit tentatively the data with a linear function (solid line).

K [35].

For ferromagnets, it has been proved that the temperature-dependent magnetic susceptibility observes a power law $\chi_0^{-1} \propto (T - T_C)^\gamma$ at temperatures slightly above the Curie temperature T_C, where the exponential parameter γ usually acts as a criterion for distinguishing the Heisenberg system ($\gamma = \frac{4}{3}$) from the Ising one ($\gamma = \frac{5}{4}$) [364, 365]. When $\gamma = 1$, it correlates with the CW model that is derived from the molecular-field theory; when $\gamma > 1$, it becomes a modified nonlinear formula that relates to the short-
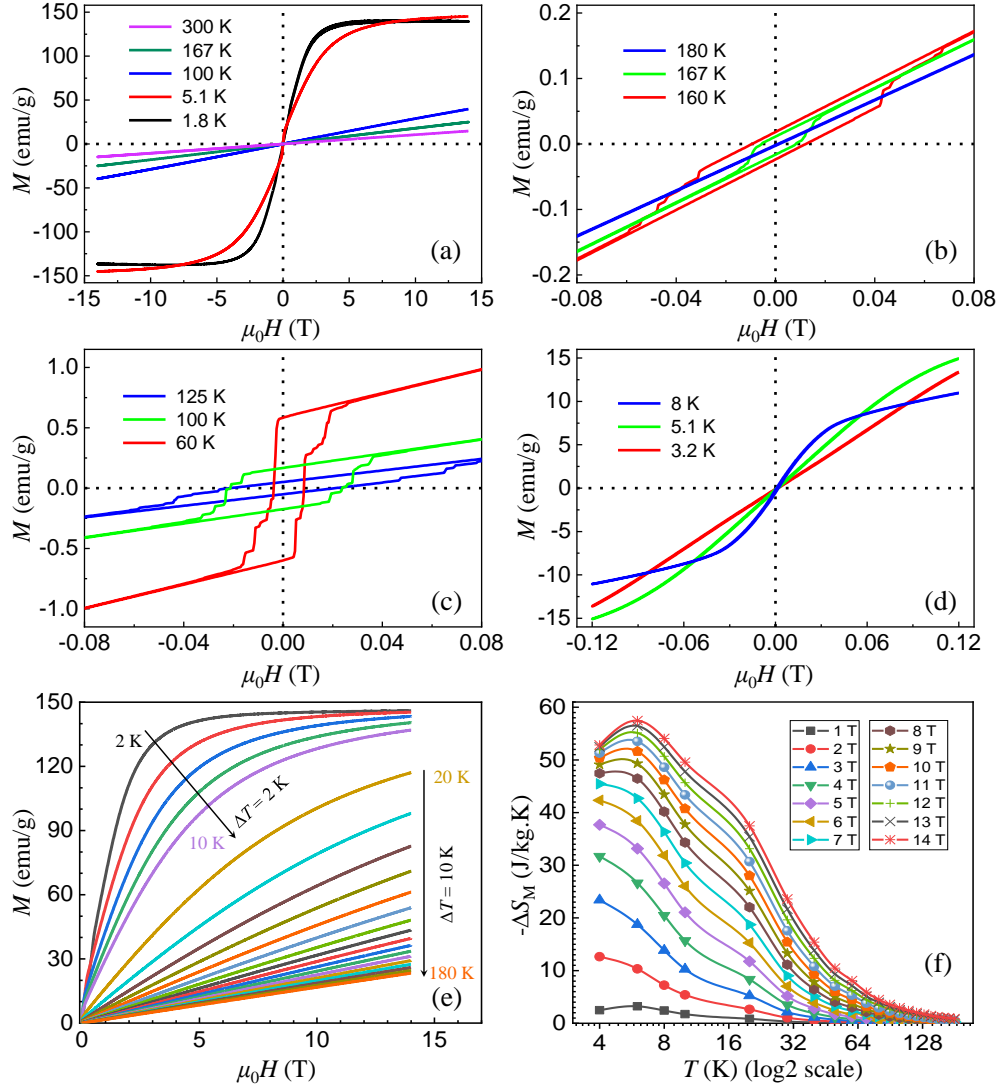
Figure 7.4: (color online) (a)-(d) Representative ZFC isothermal magnetization versus applied magnetic field. (a) The field range is from –14 to 14 T, and the studied temperature points are at 1.8, 5.1, 100, 167, and 300 K. The measured temperature points are (b) 160, 167, and 180 K, (c) 60, 100, and 125 K, and (d) 3.2, 5.1, and 8 K. For (b–d), the magnetic fields are from –1.2 to 1.2 T. (e) Representative ZFC magnetization as a function of applied magnetic field in the range of 0–14 T at temperatures of 2–10 K (step size of 2 K) and 10–180 K (step size of 10 K). (f) Extracted magnetic entropy versus temperature in the thermal range of 4–180 K (with $\log_2$ scale) at $\mu_0 H = 1$–14 T with an interval of 1 T. The solid lines are guides to the eye.

range spin correlations during the formation of the spin order [366, 367]. For antiferromagnets, there also exists a power-law model in describing the staggered magnetic susceptibility $\chi(Q) \propto \alpha(T - T_N)^{-\gamma}$ below T_N [368]; when $\alpha = 1$, one may get the best fit [369].

Since $T_{N\text{-Gd}}$ (2.33 K) $\ll T_{N\text{-Cr}}$ (168.97 K), when the magnetic structure of Cr^{3+} ions
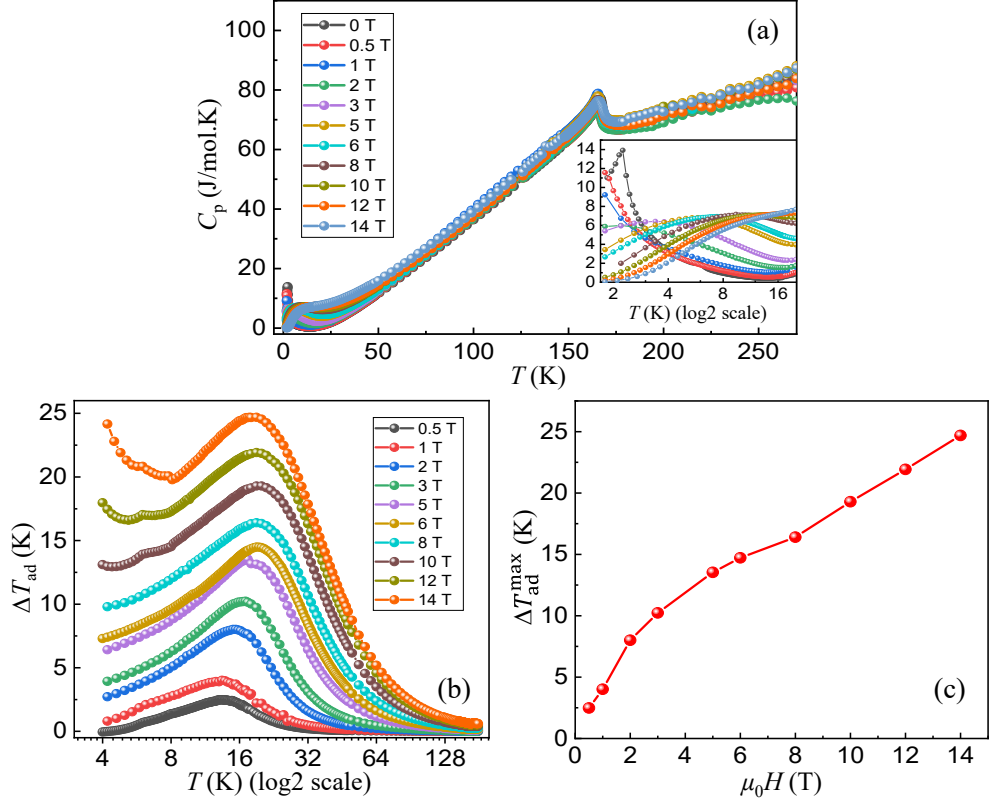
Figure 7.5: (color online) (a) Temperature-dependent specific heat measured at applied magnetic fields of 0–14 T. The inset exhibits specific heats within the temperature range of 1.8–20 K with a log2 scale. (b) Temperature-dependent adiabatic temperature change ΔT_{ad} with applied magnetic fields from 0.5 to 14 T. (c) Maximum of adiabatic temperature change $\Delta T_{\mathrm{ad}}^{\mathrm{max}}$ versus applied magnetic field. In (a)–(c), the solid lines are guides to the eye.

is established below $T_{\mathrm{N\text{-}Cr}}$, the staggered magnetization could induce short-range Gd^{3+} magnetic orders due to possible Gd^{3+}-Cr^{3+} couplings [360, 370, 371]. To model these complicated magnetic behaviors, Eq. (7.2) was modified to

$$M = M_{\mathrm{BG}} + \frac{m}{(T - \theta_{\mathrm{CW}})^{\gamma}}, \tag{7.3}$$

where γ is a parameter representing both the short-range correlations of Gd^{3+} ions and the temperature-dependent component of the net magnetization of the Cr^{3+} magnetic sublattice. This could be enhanced by the formation of magnetic polarons due to Gd^{3+}-Cr^{3+} ionic couplings [127, 372]. Following strategies were taken for refinements in the thermal range of 30–140 K: (i) First, $M_{\mathrm{BG}} = 0$ was kept and m and γ were then refined, which resulted in $m = 618.1(12)$ emu K/g, and $\gamma = 1.6219(5)$, and the

fitting result is shown as fit 3 in Fig. 7.2(b). (ii) While releasing M_{BG}, m, and γ, they were refined simultaneously, leading to $M_{\text{BG}} = -0.359(22)$ emu/g, $m = 114.17(51)$ emu.K./g, and $\gamma = 1.108(1)$, the best fit [fit 1 in Fig. 7.2(b)]. This best refinement is supported by the following facts: (i) $T = 30$ K is a little above the temperature point at ~ 24.51 K at which a kink appears in the slope of the $M - T$ curve and from where ZFC M increases sharply upon cooling due to the formation of AFM Gd^{3+} sublattice moments. (ii) While extrapolating these fits to the temperature range from –2.33 to 160 K [Fig. 7.2(b)], the calculated values of $M(T)$ [dash-dotted line (fit 2) and long-dashed line (fit 3)] deviate too much from the measured data below 30 K and above 140 K. It is noted that for the best fit, fit 1, the refined M_{BG} is still negative, which is much smaller than the values of diamagnetism of Gd^{3+} and Cr^{3+} ions, and $\gamma > 1$. As shown in the inset of Fig. 7.2(b), one possible configuration of spin moments for 30–140 K is as follows (i) The magnetic Gd^{3+} ions stay in a PM state; that is, all spins are theoretically aligned randomly with potential short-range correlations induced possibly by the formation of the magnetic order of Cr^{3+} ions. (ii) The formed Cr^{3+} AFM sublattice moments (M_+ and M_-) are canted downward from their AFM axis $M_+^0 M_-^0$ with an angle of β so that the net Cr^{3+} and Gd^{3+} moments are in opposite directions, leading to a negative value of M_{BG}. It is pointed out that mere the applied magnetic field of 500 Oe itself is hard to make an AFM canting [267] and produce such a large net negative magnetization from the Cr^{3+} magnetic sublattice, consistent with the formation of a canted AFM Cr^{3+} structure.

To gain in-depth understanding of the two magnetic transitions occurring at 2.33 and 6.74 K, we further fit the temperature-dependent (from 7 to 30 K) ZFC magnetization data using Eq. 7.3. The m value in Eq. 7.3 is determined by the CW constant. Therefore, the parameters of m and θ_{CW} were fixed (Table 7.2), and only M_{BG} and γ were released for the fits. To explore the detailed temperature-dependent values of M_{BG} and γ, we divided the temperature range of 7–30 K into five regimes, i.e., 7–10, 10–15, 15–20, 20–25, and 25–30 K. The fit results are listed in Table 7.2. It is noted that as temperature decreases from 30 to 7 K, the value of γ increases, consistent with

Table 7.3: Comparison of the MCE in different RECrO$_3$ compounds (RE = $4f^n$ rare earths, n = 7–14). Here PC = polycrystal, SC = single crystal, FZM = floating-zone method, FLM = flux method, T = temperature, Lit. = the literature, and TS = this study.

Compound	$4f^n$	Form	$-\Delta S_M$ (J/kg K)			$\Delta \mu_0 H$ (T)	T (K)	Ref.
			From Lits.	From TS	Improved			
LaCrO$_3$		PC	0.1699	3.75	2107%	5	~37.1	[373]
GdCrO$_3$	7	SC (FZM)		57.47		14	6	TS
GdCrO$_3$	7	SC (FLM)	29.5	35.52	20.4%	4	3	[51]
GdCrO$_3$	7	PC	41.24	49.96	21.1%	9	3.8	[359]
TbCrO$_3$	9	SC (FLM)	5.0	11.97	139.4%	2	~4.5	[172]
DyCrO$_3$	10	PC	10.85	28.70	164.5%	4	5	[374]
HoCrO$_3$	11	PC	7.2	18.72	160%	7	20	[375]
ErCrO$_3$	12	PC	10.7	22.88	113.8%	7	15	[274]
TmCrO$_3$	13	PC	4.6	16.6	260.8%	5	~13.4 K	[275]
YbCrO$_3$	14	PC	~1.91	18.23	854.5%	5	~12.33	[18]

the hypothesis that there exist short-range AFM orders of Gd^{3+} ions above $T_{\text{N-Gd}}$. It is more interesting that the value of M_{BG} changes from negative (15–30 K) to positive (7–15 K). This sign change most likely indicates that the AFM axis of Cr^{3+} ions rotates, consistent with the observed spin-reorientation transition.

7.3.3 Magnetic phase diagrams

Figure 7.3 shows the measurements of magnetization as a function of temperature at different applied magnetic fields. The values of $T_{\text{N-Gd}}$ and T_{SR} were determined as shown in Fig. 7.2(c). The indications of $T_{\text{N-Gd}}$ and T_{SR} were clearly observed at 300–1000 Oe [Fig. 7.3(a)]. With increasing applied magnetic field, the values of $T_{\text{N-Gd}}$ and T_{SR} shift to lower and lower temperatures [Figs. 7.3(b) and 7.3(c)]. Temperature-dependent magnetization curves around T_{SR} were previously measured at 0, 50, 500, and 1000 Oe [75, 51]. Unfortunately, due to the presence of impurities [75, 51], the indication of the SR transition disappeared when the strength of applied magnetic field was stronger than 1000 Oe, and the kink indicative of the AFM transition of Gd^{3+}

ions at $\sim$2.3 K did not appear [51]. By comparison, our study clearly shows both features with the high-quality GdCrO$_3$ single crystals. This makes us confident to deeply explore the detailed magnetic phase diagram.

As shown in Fig. 7.3(c), above $\sim$0.68 T, the value of $T_{\text{N-Gd}}$ combines with that of T_{SR}, and the indication of $T_{\text{N-Gd}}$ is indistinguishable; above $\sim$0.8 T, the signature of T_{SR} disappears, indicating that there exist applied-magnetic-field-driven magnetic phase transitions [267]. We therefore divided the magnetic phase diagram [Fig. 7.3(c)] into four regimes. Within the regime 1, the ions of magnetic Cr^{3+} form a long-range ordered AFM structure with a small canting [Fig. 7.2(b)]. With decreasing temperature and increasing applied magnetic field, the AFM easy axis $M_+^0 M_-^0$ of Cr^{3+} magnetic ions changes from one direction to another (regime 2), depending on the competing degree between anisotropic exchange and single-ion anisotropic energies of Cr^{3+} ions as previously predicated theoretically [267]. While further decreasing temperature, the long-range magnetic order of Gd^{3+} ions forms (regime 3). Regime 4 has not been explored yet owing to the technique limitation. The applied magnetic field shifts $T_{\text{N-Gd}}$ to lower temperatures, resembling the behavior of a normal antiferromagnet. It is abnormal that the applied magnetic field also suppresses the values of T_{SR}, which necessitates a further hot-neutron scattering study to solve this puzzle. It is pointed out that the magnetic phase diagram of applied magnetic field and temperature [Fig. 7.3(c)] was compiled with the measurements of magnetization, which strongly depends on the relative magnetic contributions of Gd^{3+} and Cr^{3+} ions [355].

As shown in Fig. 7.3(d), at 50 Oe, the $M - T$ curve behaves like an antiferromagnet. Upon cooling, the magnetization increases obviously at $T_{\text{N-Cr}} = 168.86(2)$ K, reaches a maximum at 168.40(2) K, and subsequently decreases sharply and then becomes negative at 167.99(2) K, followed by a smooth decrease until $\sim$162 K. After that, the magnetization increases again and becomes positive at $\sim$149.73 K. A Similar magnetic reversal was also observed in TmCrO$_3$ [275, 66], EuCr$_{0.85}$Mn$_{0.15}$O$_3$ [363], and YbCrO$_3$ [272] compounds. By contrast, above 150 Oe, the values of the measured magnetization always remain positive [Figs. 7.3(d) and 7.3(e)], and the magnetization

in the temperature range from ~140 K to $T_{\text{N-Cr}}$ becomes larger and larger with increasing applied magnetic field, so that the kink indicative of the appearance of $T_{\text{N-Cr}}$ [Fig. 7.2(d)] gets weaker and weaker and finally disappears above ~4.3 T [Figs. 7.3(e) and 7.3(f)]. The kink may be buried in the higher magnetization signal induced by higher applied magnetic fields, or its disappearance might indicate a meltable magnetic state. Utilizing the method shown in Fig. 7.2(d), we determined the values of $T_{\text{N-Cr}}$ as a function of applied magnetic field, as shown in Fig. 7.3(f). The applied magnetic fields enhance the values of $T_{\text{N-Cr}}$, consistent with the hypothesis that below $T_{\text{N-Cr}}$ the magnetic Cr^{3+} ions order with a canted AFM structure.

Figure 7.4(a) shows the ZFC magnetization as a function of applied magnetic field from –14 to 14 T at marked temperatures. At 1.8 K, the magnetization increases almost linearly from 0 to ~2 T and then approaches towards a saturation magnetic state above ~4 T. At 5.1 K, the saturated magnetization at 14 T is ~4% higher than that at 1.8 K, consistent with the formation of a Gd^{3+} magnetic structure below $T_{\text{N-Gd}}$. We transferred the unit of magnetization from emu per gram into μ_B per chemical formula unit ($GdCrO_3$) and found that the values of the saturation moments under 14 T were ~6.43 μ_B (at 1.8 K) and ~6.69 μ_B (at 5.1 K). These values are a little smaller than the theoretical saturation moment of Gd^{3+} ions, i.e., $g_J J = 7\ \mu_B$, consistent with the foregoing discussions that the Gd^{3+} ions in the $GdCrO_3$ compound form a long-range magnetic order. To check a possible magnetic hysteresis effect, we measured the magnetization from –1.2 to 1.2 T in detail as temperature decreased from 180 to 3.2 K [Figs. 7.4(b)-7.4(d)]. As shown in Fig. 7.4(b), no hysteresis loop was observed at 180 K. Upon cooling, it appears at 167 K (below $T_{\text{N-Cr}}$), consistent with the hypothesis that the Cr^{3+} ions in the $GdCrO_3$ compound form a canted AFM structure. Upon further cooling down to 60 K [Fig. 7.4(c)], the magnetic hysteresis effect gets more and more obvious with enhanced remanent magnetization. As shown in Fig. 7.4(d), at 8 K, the hysteresis loop becomes very small, and the magnetization shows a nonlinear field dependence, a characteristic feature of ferromagnetism or a short-range AFM state [314, 267]. At 5.1, 3.2, and 1.8 K (below T_{SR}), the magnetic hysteresis loops are indistinguishable.

This may indicate that the canting degree of Cr^{3+} magnetic sublattice becomes very small or a magnetic phase transition for Cr^{3+} ions from the canted to a collinear AFM structure exists.

7.3.4   Magnetocaloric effect

To study the MCE of our grown $GdCrO_3$ single crystals, we measured field-dependent magnetization from 0 to 14 T at temperatures indicated in Fig. 7.4(e). The magnetic entropy change $-\Delta S_M$ can be calculated by

$$|\Delta S_M(T, \mu_0 H)| = \mu_0 \sum_i \frac{M_{i+1} - M_i}{T_{i+1} - T_i} \Delta H_i, \tag{7.4}$$

where $|\Delta S_M|$ is the absolute value of the magnetic entropy change, μ_0 is the permeability of vacuum, M_{i+1} and M_i represent measured values of magnetization at temperatures of T_{i+1} and T_i, respectively, and ΔH_i is the differential element of the applied magnetic field. Based on Eq. (7.4), we calculated the values of $-\Delta S_M$ of the single-crystal $GdCrO_3$ compound, and the results are shown in Fig. 7.4(f). It is clear that below 9 T, the value of $-\Delta S_M$ reaches a maximum at $\sim$4 K; above 9 T, the maximum point shifts to an elevated temperature $\sim$6 K. For example, at 6 K and 14 T, $-\Delta S_M \approx$ 57.47 J/kg K, which decreases rapidly upon warming. With a field change of $\Delta \mu_0 H$ = 9 T, we calculated the magnetic entropy change $-\Delta S_M$ = 49.11 J/kg K at 4 K for the single-crystal $GdCrO_3$ sample. This value is $\sim$19.1% higher than the value 41.24 J/kg K measured with a polycrystalline $GdCrO_3$ sample under the same conditions at 3.8 K [359]. We compared the magnetic entropy changes of $GdCrO_3$ single crystals grown with two different methods: One was the flux method, where $-\Delta S_M$ = 29.5 J/kg K with $\Delta \mu_0 H$ = 4 T at 3 K [51]; the second one was the laser-diode-heated FZ technique from the present study where $-\Delta S_M \approx$ 35.52 J/kg K (extrapolated) with the same values of $\Delta \mu_0 H$ and temperature, an improvement of approximately 20.4%. It is obvious that the single-crystal $GdCrO_3$ compound synthesized by the FZ method [192, 248, 63] shows a much stronger MCE than the polycrystalline samples, and is even much better than the $GdCrO_3$ single crystal grown by the flux method [51]. In Ta-

ble 7.3, we further compare our results with those from other RECrO$_3$ compounds. For example, at 20 K and 7 T, we calculate $-\Delta S_{\mathrm{M}} \approx 18.72$ J/kg K for the GdCrO$_3$ single crystal. This is $\sim$160% larger than that of the HoCrO$_3$ compound, 7.2 J/kg K [375]. We also compared our results with those from other studies on DyCrO$_3$ [374], ErCrO$_3$ [274], etc., as listed in Table 7.3. This demonstrates that the single-crystal GdCrO$_3$ compound with enhanced MCE is a promising material for potential application in magnetic refrigerators.

With our measured temperature-dependent specific-heat data at different applied magnetic fields, as shown in Fig. 7.5(a), the adiabatic temperature change ΔT_{ad} can be calculated according to [376, 377]

$$\Delta T_{\mathrm{ad}} = \int_0^{\mu_0 H} \frac{T}{C_p(T, \mu_0 H)} \frac{\partial M}{\partial T}\bigg|_{\mu_0 H} d\mu_0 H. \tag{7.5}$$

We calculated the temperature dependence of ΔT_{ad} as well as the applied magnetic-field-dependent maximum $\Delta T_{\mathrm{ad}}^{\mathrm{max}}$, as shown in Figs. 7.5(b) and 7.5(c), respectively. Figure 7.5(b) shows an applied-magnetic-field-driven enhancement of ΔT_{ad} when $\mu_0 H \geq$ 10 T. The grown GdCrO$_3$ single crystal in this study holds large values of adiabatic temperature change, e.g., $\Delta T_{\mathrm{ad}}^{\mathrm{max}} \approx 16.40$ K at 8 T and 24.69 K at 14 T. The $\Delta T_{\mathrm{ad}}^{\mathrm{max}}$ value of the single-crystal GdCrO$_3$ compound is much larger than that of other Gd-based perovskites such as GdMnO$_3$ and GdAlO$_3$ [377]. It is also larger than that of some lanthanide-based oxides such as EuHo$_2$O$_4$ ($\Delta T_{\mathrm{ad}}^{\mathrm{max}} \approx 12.7$ K) and EuDy$_2$O$_4$ ($\Delta T_{\mathrm{ad}}^{\mathrm{max}} \approx 16$ K) [378].

7.4 Conclusions

In summary, we have investigated the structural and magnetic properties of the GdCrO$_3$ single crystal. The collected XRPD pattern was well indexed with the space group $Pmnb$, from which we extracted the lattice constants and atomic positions. The magnetization data at 500 Oe from 200 to 300 K agree well with the CW law, which results in a PM CW temperature $\theta_{\mathrm{CW}} = -20.33(4)$ K and an effective PM moment

8.40(9) μ_B. Taking into account both the temperature-dependent and -independent net-magnetization of Cr^{3+} ions, we can fit well the magnetization data at 30–140 K. We clearly observed the indications of the formation of the canted AFM structure of Cr^{3+} ions at $T_{N\text{-}Cr}$, the spin reorientation of Cr^{3+} moments at T_{SR}, and the formation of a long-range-ordered Gd^{3+} magnetic structure at $T_{N\text{-}Gd}$. We have constructed the magnetic phase diagrams of $T_{N\text{-}Cr}$, T_{SR}, and $T_{N\text{-}Gd}$ as a function of applied magnetic field and proposed magnetic configurations in the corresponding temperature regimes. The magnetic phase diagrams of $T_{N\text{-}Gd}$ and $T_{N\text{-}Cr}$ are consistent with the corresponding magnetic structures, whereas, the magnetic phase diagram of T_{SR} seems to be abnormal. When $T_{SR} < T < T_{N\text{-}Cr}$, obvious magnetic hysteresis loops were observed. Below T_{SR}, the hysteresis loop becomes very weak, probably indicating a decrease in the canting degree of the Cr^{3+} magnetic structure or a phase transition from the canted to a collinear AFM structure. We calculated the magnetic entropy change $-\Delta S_M$. For example, $-\Delta S_M \approx 35.52$ J/kg K at $\Delta\mu_0 H = 4$ T and 3 K, an improvement of $\sim 20.4\%$ compared with that of the $GdCrO_3$ single crystal grown by the flux method [51]. We summarized the MCE of $RECrO_3$ compounds (RE = $4f^n$ rare earths, $n = 7$–14) and found that our grown $GdCrO_3$ single crystal displayed the highest value of magnetic entropy change and an enhanced adiabatic temperature change. This indicates that the single-crystal $GdCrO_3$ compound is a potential candidate for magnetic cooling.

The natural Gd atom is a very strong neutron absorber. Therefore, uniquely determining the interesting magnetic structures, as well as the magnetic phase-transition diagrams explored in this study, necessitates a single-crystal neutron-diffraction study with a hot neutron source.

CHAPTER 8

SUMMARY AND OUTLOOK

In the final chapter of the present PhD Thesis, I am going to summarize the methodologies, and the main results on the rare-earth chromate single crystals. A series of $RECrO_3$ single crystals with RE = Y, Eu, Gd, Tb, Dy, Ho, Er, Tm, Yb, Lu were studied. Moreover, possible future works are also discussed here.

Chapter 3:

In this chapter, I summarise experimental methods that I utilise in the thesis, accompanied with the corresponding principles. Firstly, I introduce the solid state reaction method with which pure phase polycrystalline powder sample is obtained. Employing the laser-diode FZ method, a series of high-quality rare-earth chromate single crystals have been grown successfully, including $RECrO_3$ (RE = Y, Eu, Gd, Tb, Dy, Ho, Er, Tm, Yb, Lu). Besides, with the CVT method, I have also grown high-quality CrP single crystal.

To characterize the as-grown single crystals, in-house characterizations are performed with various experimental instruments including Physical Property Measurement System, scanning electron microscope and energy-dispersive X-ray spectroscopy, X-ray diffractometer, and X-ray Laue diffractometer. The principles of X-ray diffraction and structural refinement are also elucidated. Furthermore, I introduce the principles of neutron scattering with a division of elastic and inelastic scattering. The neutron spectrometers that I have utilised are also displayed.

Chapter 5:

With the as-grown single crystals, various types of in-house characterizations were performed including Physical properties measurement, scanning electron microscope and energy-dispersive X-ray spectroscopy, X-ray diffractometer, and X-ray Laue diffractometer. A systematic room-temperature X-ray powder diffraction study was carried out on the grown single crystals. Structural refinements show that the $RECrO_3$ single

crystals belong to orthorhombic crystal system with space group of $Pbnm$ (No. 62). Lattice constants, unit-cell volume, atomic positions, and isotropic thermal parameters were extracted. We performed magnetization measurements as functions of temperature and applied magnetic field on the grown single crystals, providing more reliable and intrinsic magnetic properties.

Also, I studied theoretically the t-e hybridization by calculating quantitatively the t_{2g} and e_g orbital overlapping degree ($I_{t_{2g\downarrow}-e_{g\uparrow}}$) based on DOS calculations. As RE^{3+} ions change from Eu to Lu, the trend of theoretically-calculated AFM transition temperatures is in agreement with that of our experimentally-determined ones ($T_{\text{N-Cr}}$). The changes of the out-of- and in-plane bond angles of $\angle$Cr-O1(2)-Cr strongly influence the weight factor of FM couplings (J_{hb}^{σ}) in the whole superexchanges interactions by (dis)favoring the VCT of t_{2g}^3-O^{2-}-e$_g^0$, which may be the origin of the weak ferromagnetism appearing within a main AFM matrix in the RECrO$_3$ system.

Chapter 6:

Neutron powder diffraction study was carried out at a temperature range from 12 K to 1200 K.

I have quantitatively investigated the high-temperature (300—980 K) magnetism and structural information (321—1200 K) of a single-crystalline YCrO$_3$ compound. The high temperature magnetization can only be fit by the CW law with multiple effective PM moments and multiple PM CW temperatures with strong magnetic frustration, implying a complicated low temperature magnetic structure. The crystal structure was refined with $Pmnb$ symmetry in the entire studied temperature range within the present experimental accuracy. Detailed structural information including lattice constants, unit-cell volume, atomic positions, thermal parameters, bond lengths, local distortion parameter, bond angles, local distortion modes, and BVSs, were extracted.

With the neutron powder diffraction at low temperature, we have established an AFM structure with the propagation vector at **k** = (1 1 0) and the same unit cell as that of the crystalline structure (with space group $Pbnm$). The direction of the Cr^{3+} spin moments is along the crystallographic c axis. The refined moment size is 2.45(6)

μ_{B} at 12 K, ~82% of the theoretical saturation value 3 μ_{B}. This is consistent with the fact that a magnetic frustration exists in YCrO$_3$ compound. By fitting integrated intensities of the magnetic Bragg (1 1 0) reflection extracted from the pure magnetic contribution with a power law, we found that the Cr^{3+} spin interactions were probably two-dimensional Ising like within the reciprocal (1 1 0) scattering plane. Moreover, an anisotropic magnetostriction effect is observed along the crystallographic a, b, and c axes and a magnetoelastic effect with the unit-cell volume V.

To precisely determine the values of each exchange interaction, an inelastic neutron scattering experiment was carried out based on a YCrO$_3$ single crystal. A thorough Heisenberg exchange model distinguishing each exchange was built. The dramatic difference between J_1 and J_2 is deemed as a evidence of the existence of $t_{2\mathrm{g}}$-e_{g} orbital hybridization. To reproduce the magnon band successfully, a noticeable DM interaction value needs to be introduced, implying the existence of a strong SOC effect in the YCrO$_3$ antiferromagnet.

Chapter 7:

The structural and magnetic properties of the GdCrO$_3$ single crystal was carried out. The collected XRPD pattern was well indexed with the space group $Pbnm$, from which I extracted the lattice constants and atomic positions. The magnetization data at 500 Oe from 200 to 300 K agree well with the CW law, which results in a PM CW temperature Θ_{CW} = –20.33(4) K and an effective PM moment 8.40(9) μ_{B}. Taking into account both the temperature-dependent and -independent net-magnetization of Cr^{3+} ions, we can fit well the magnetization data at 30–140 K. We clearly observed the indications of the formation of the canted AFM structure of Cr^{3+} ions at $T_{\mathrm{N\text{-}Cr}}$, the spin reorientation of Cr^{3+} moments at T_{SR}, and the formation of a long-range-ordered Gd^{3+} magnetic structure at $T_{\mathrm{N\text{-}Gd}}$.

Furthermore, the magnetic phase diagrams of $T_{\mathrm{N\text{-}Cr}}$, T_{SR}, and $T_{\mathrm{N\text{-}Gd}}$ were constructed as a function of applied magnetic field and proposed magnetic configurations in the corresponding temperature regimes. The magnetic phase diagrams of $T_{\mathrm{N\text{-}Gd}}$ and $T_{\mathrm{N\text{-}Cr}}$ are consistent with the corresponding magnetic structures, whereas, the magnetic

phase diagram of T_{SR} seems to be abnormal. When $T_{\text{SR}} < T < T_{\text{N-Cr}}$, obvious magnetic hysteresis loops were observed. Below T_{SR}, the hysteresis loop becomes very weak, probably indicating a decrease in the canting degree of the Cr^{3+} magnetic structure or a phase transition from the canted to a collinear AFM structure. We calculated the magnetic entropy change $-\Delta S_{\text{M}}$. For example, $-\Delta S_{\text{M}} \approx 35.52$ J/kg K at $\Delta \mu_0 H = 4$ T and 3 K, an improvement of $\sim 20.4\%$ compared with that of the $GdCrO_3$ single crystal grown by the flux method.

Apart from the discussed issues in the thesis, the determination on the magnetic structure of $RECrO_3$ compounds is a difficult job, especially the exact values of magnetic moment along each crystallographic axis. To precisely address above issue, neutron single-crystal diffraction is necessary. An evaluation on the magnetic Bragg peaks may help us understand the nature of magnetism. Moreover, inelastic neutron scattering study on the spin dynamics of RE^{3+} spins is another interesting work. It is also of significance to make a comparison with $REAlO_3$, to reavel the effect from Cr^{3+} internal magnetic field on the magnetic behavior of Kramers/non-Kramers ion. In addition, since the physics of $t_{2\text{g}}$-e_{g} hybridization in Cr^{3+} ($t_{2\text{g}}^3 e_g^0$) state is unravelled by ab-initio calculation, it is interesting to manipulate the competition between FM and AFM coupling in certain chromates, to generate more novel quantum states.

REFERENCES

[1] S. H. Simon, The Oxford Solid State Basics. Oxford: Oxford University Press, 2013.

[2] B. Keimer and J. E. Moore, "The physics of quantum materials," Nat. Phys., vol. 13, pp. 1045–1055, 2017.

[3] D. W. Murphy et al., "New superconducting cuprate perovskites," Phys. Rev. Lett., vol. 58, pp. 1888–1890, 1987.

[4] D. Khomskii, "Classifying multiferroics: Mechanisms and effects," Physics, vol. 2, p. 20, 2009.

[5] H. J. Zhao, W. Ren, Y. Yang, J. Íñiguez, X. M. Chen, and L Bellaiche, "Near room-temperature multiferroic materials with tunable ferromagnetic and electrical properties," Nat. Commun., vol. 5, p. 4021, 2014.

[6] Y. Zhang, Y.-W. Tan, H. L. Stormer, and P. Kim, "Experimental observation of the quantum hall effect and berry's phase in graphene," Nature, vol. 438, no. 7065, pp. 201–204, 2005.

[7] B. A. Bernevig and S.-C. Zhang, "Quantum spin hall effect," Phys. Rev. Lett., vol. 96, p. 106 802, 2006.

[8] A. Catuneanu, Y. Yamaji, G. Wachtel, Y. B. Kim, and H.-Y. Kee, "Path to stable quantum spin liquids in spin-orbit coupled correlated materials," npj Quantum Mater., vol. 3, p. 23, 2018.

[9] R. C. Sousa and I. L. Prejbeanu, "Non-volatile magnetic random access memories (MRAM)," C. R. Phys., vol. 6, pp. 1013–1021, 2005.

[10] C. Hobbs et al., "Fermi level pinning at the polysi/metal oxide interface," in 2003 Symposium on VLSI Technology. Digest of Technical Papers, IEEE, 2003, pp. 9–10.

[11] L. J. Geerligs, D. V. Averin, and J. E. Mooij, "Observation of macroscopic quantum tunneling through the coulomb energy barrier," Phys. Rev. Lett., vol. 65, pp. 3037–3040, 1990.

[12] J. Wang et al., "Epitaxial $BiFeO_3$ multiferroic thin film heterostructures," Science, vol. 299, pp. 1719–1722, 2003.

[13] T. Kimura, T. Goto, H. Shintani, K. Ishizaka, T. Arima, and Y. Tokura, "Magnetic control of ferroelectric polarization," Nature, vol. 426, pp. 55–58, 2003.

[14] B. B. Van Aken, T. Palstra, A. Filippetti, and N. A. Spaldin, "The origin of ferroelectricity in magnetoelectric $YMnO_3$," Nat. Mater., vol. 3, pp. 164–170, 2004.

[15] P. Sahlot, A. Jana, and A. M. Awasthi, "Exchange bias in multiferroic $Ca_3Mn_2O_7$ effected by dzyaloshinskii-moriya interaction," AIP Conf. Proc., vol. 1942, p. 130 009, 2018.

[16] C.-W. Nan, M. I. Bichurin, S. Dong, D. Viehland, and G. Srinivasan, "Multiferroic magnetoelectric composites: Historical perspective, status, and future directions," J. Appl. phys., vol. 103, p. 031 101, 2008.

[17] X. Duan, J. Huang, B. Xu, and S. Liu, "A two-dimensional multiferroic metal with voltage-tunable magnetization and metallicity," Mater. Horiz., vol. 8, pp. 2316–2324, 2021.

[18] G. N. P. Oliveira, "Local probing spinel and perovskite complex magnetic systems," Ph.D. dissertation, Universidade do Porto, Porto, 2017.

[19] S. Naray-Szabo, "Die strukturen von verbindungen ABO_3 'schwesterstrukturen.'," Naturwissenschaflen, vol. 31, p. 466, 1943.

[20] G. H. Jonker and J. H. Van Santen, "Ferromagnetic compounds of manganese with perovskite structure," Physica, vol. 16, pp. 337–349, 1950.

[21] J. B. Goodenough, "Theory of the role of covalence in the perovskite-type manganites $[La, M(II)]MnO_3$," Phys. Rev., vol. 100, pp. 564–573, 1955.

[22] J. Kanamori, "Superexchange interaction and symmetry properties of electron orbitals," J. Phys. Chem. Solids, vol. 10, pp. 87–98, 1959.

[23] P. W. Anderson, "Antiferromagnetism. Theory of superexchange interaction," Phys. Rev., vol. 79, pp. 350–356, 1950.

[24] P. W. Anderson, "New approach to the theory of superexchange interactions," Phys. Rev., vol. 115, pp. 2–13, 1959.

[25] H. L. Yakel, "On the structures of some compounds of the perovskite type," Acta Cryst., vol. 8, pp. 394–398, 1955.

[26] J. T. Looby and L. Katz, "Yttrium chromium oxide, a new compound of the perowskite type," J. Am. Chem. Soc., vol. 76, pp. 6029–6030, 1954.

[27] S. Geller, "Crystal structure of gadolinium orthoferrite, $GdFeO_3$," J. Chem. Phys., vol. 24, pp. 1236–1239, 1956.

[28] S. Geller and E. A. Wood, "Crystallographic studies of perovskite-like compounds. I. Rare earth orthoferrites and YFeO$_3$, YCrO$_3$, YAlO$_3$," Acta Crystallogr., vol. 9, pp. 563–568, 1956.

[29] S. Geller, "Crystallographic studies of perovskite-like compounds. IV. Rare earth scandates, vanadites, galliates, orthochromites," Acta Crystallogr., vol. 10, pp. 243–248, 1957.

[30] W. C. Koehler and E. O. Wollan, "Neutron-diffraction study of the magnetic properties of perovskite-like compounds LaBO$_3$," J. Phys. Chem. Solids., vol. 2, pp. 100–106, 1957.

[31] I. Weinberg and P. Larssen, "Electron paramagnetic resonance and antiferromagnetism in LaCrO$_3$," Nature, vol. 192, pp. 445–446, 1961.

[32] N. Shamir, H. Shaked, and S. Shtrikman, "Magnetic structure of some rare-earth orthochromites," Phys. Rev. B, vol. 24, pp. 6642–6651, 1981.

[33] T. Yamaguchi, "Theory of spin reorientation in rare-earth orthochromites and orthoferrites," J. Phys. Chem. Solids, vol. 35, pp. 479–500, 1974.

[34] N. Kojima, I. Tsujikawa, and K. Tsushima, "Optical investigations of rare-earth orthochromites. I. TmCrO$_3$," J. Phys. Soc. Jpn., vol. 54, pp. 4794–4803, 1985.

[35] Y. Zhu et al., "Crystalline and magnetic structures, magnetization, heat capacity, and anisotropic magnetostriction effect in a yttrium-chromium oxide," Phys. Rev. Mater., vol. 4, p. 094 409, 2020.

[36] H. Wang et al., "Competition of ferromagnetism and antiferromagnetism in Mn-doped orthorhombic YCrO$_3$," J. Magn. Magn. Mater., vol. 535, p. 168 022, 2021.

[37] L. M. Daniels et al., "Structures and magnetism of the rare-earth orthochromite perovskite solid solution La$_x$Sm$_{1-x}$CrO$_3$," Inorg. Chemi., vol. 52, pp. 12 161–12 169, 2013.

[38] R. Shukla et al., "Multifunctional nanocrystalline CeCrO$_3$: Antiferromagnetic, relaxor, and optical properties," J. Phys. Chem. C, vol. 113, pp. 12 663–12 668, 2009.

[39] J. D. Gordon, R. M. Hornreich, S. Shtrikman, and B. M. Wanklyn, "Magnetization studies in the rare-earth orthochromites. V. TbCrO$_3$ and PrCrO$_3$," Phys. Rev. B, vol. 13, pp. 3012–3017, 1976.

[40] F. Bartolomé, J. Bartolomé, M. Castro, and J. J. Melero, "Specific heat and magnetic interactions in NdCrO$_3$," Phys. Rev. B, vol. 62, pp. 1058–1066, 2000.

[41] M. Tripathi, R. J. Choudhary, D. M. Phase, T. Chatterji, and H. E. Fischer, "Evolution of magnetic phases in $SmCrO_3$: A neutron diffraction and magnetometric study," Phys. Rev. B, vol. 96, p. 174 421, 2017.

[42] M. Taheri et al., "Magnetic structure, magnetoelastic coupling, and thermal properties of $EuCrO_3$ nanopowders," Phys. Rev. B, vol. 93, p. 104 414, 2016.

[43] J.-S. Zhou et al., "Intrinsic structural distortion and superexchange interaction in the orthorhombic rare-earth perovskites $RCrO_3$," Phys. Rev. B, vol. 81, p. 214 115, 2010.

[44] M. Taheri et al., "Structural, magnetic, and thermal properties of $Ce_{1-x}Eu_xCrO_3$ orthochromite solid solutions," Phys. Rev. B, vol. 99, p. 054 411, 2019.

[45] R. B. Venugopal, P. B. Vittal, R. G. Narsinga, F. C. Chou, and B. D. Suresh, "Magnetization reversal in $PrCrO_3$," Adv. Mat. Res., vol. 1086, pp. 96–100, 2015.

[46] Y. Zhu et al., "Crystal growth engineering and origin of the weak ferromagnetism in antiferromagnetic matrix of orthochromates from t-e orbital hybridization," iScience, vol. 25, p. 104 111, 2022.

[47] M Eibschütz, R. Cohen, and L. Van Uitert, "The hyperfine structure of Sm^{149} in $SmFeO_3$ and $SmCrO_3$," J. phys., Colloq., vol. 32, pp. C1–922, 1971.

[48] C. R. Serrao, A. K. Kundu, S. B. Krupanidhi, U. V. Waghmare, and C. N. R. Rao, "Biferroic $YCrO_3$," Phys. Rev. B, vol. 72, p. 220 101, 2005.

[49] A. Indra et al., "Magnetoelectric coupling and exchange bias effects in multiferroic $NdCrO_3$," J. Phys.: Condens. Matter, vol. 28, p. 166 005, 2016.

[50] B. Rajeswaran, D. I. Khomskii, A. K. Zvezdin, C. N. R. Rao, and A. Sundaresan, "Field-induced polar order at the Néel temperature of chromium in rare-earth orthochromites: Interplay of rare-earth and cr magnetism," Phys. Rev. B, vol. 86, p. 214 409, 2012.

[51] L. H. Yin, J. Yang, X. C. Kan, W. H. Song, J. M. Dai, and Y. P. Sun, "Giant magnetocaloric effect and temperature induced magnetization jump in $GdCrO_3$ single crystal," J. Appl. Phys., vol. 117, p. 133 901, 2015.

[52] K. Tsushima, T. Tamaki, and Y. Yamaguchi, "Magnetization process in $DyCrO_3$," AIP Conf. Proc., vol. 24, pp. 69–70, 1975.

[53] A. M. Kadomtseva et al., "Magnetic properties of $DyCrO_3$," Sov. Phys. JETP, vol. 92, pp. 179–189, 1987.

[54] E. F. Bertaut and J. Mareschal, "Etude de la structure magnetique des chromites d'erbium et de neodyme par diffraction neutronique," Solid State Commun., vol. 5, pp. 93–97, 1967.

[55] L. Wang, G. H. Rao, X. Zhang, L. L. Zhang, S. W. Wang, and Q. R. Yao, "Reversals of magnetization and exchange-bias in perovskite chromite $TmCrO_3$," Ceram. Int., vol. 42, pp. 10 171–10 174, 2016.

[56] Deepak, A. Kumar, and S. M. Yusuf, "Intertwined magnetization and exchange bias reversals across compensation temperature in $YbCrO_3$ compound," Phys. Rev. Mater., vol. 5, p. 124 402, 2021.

[57] M. Kajiura, K. Aoyagi, and T. Tamaki, "Exciton absorption lines in antiferromagnetic $LuCrO_3$," J. Phys. Soc. Jpn., vol. 39, pp. 1572–1578, 1975.

[58] Y. Zhu et al., "Enhanced magnetocaloric effect and magnetic phase diagrams of single-crystal $GdCrO_3$," Phys. Rev. B, vol. 102, p. 144 425, 2020.

[59] E. F. Bertaut, J Mareschal, and G. F. De Vries, "Etude par diffraction neutronique de la structure magnetique du chromite de terbium," J. Phys. Chem. Solids, vol. 28, pp. 2143–2154, 1967.

[60] A. Ghosh, A. Pal, K. Dey, S. Majumdar, and S. Giri, "Atypical multiferroicity of $HoCrO_3$ in bulk and film geometry," J. Mater. Chem. C, vol. 3, pp. 4162–4167, 2015.

[61] K. R. S. Preethi Meher, A. Wahl, A. Maignan, C. Martin, and O. I. Lebedev, "Observation of electric polarization reversal and magnetodielectric effect in orthochromites: A comparison between $LuCrO_3$ and $ErCrO_3$," Phys. Rev. B, vol. 89, p. 144 401, 2014.

[62] G. N. P. Oliveira, R. C. Teixeira, R. P. Moreira, J. G. Correia, J. P. Araújo, and A. M. L. Lopes, "Local inhomogeneous state in multiferroic $SmCrO_3$," Sci. Rep., vol. 10, p. 4686, 2020.

[63] Y. Zhu et al., "High-temperature magnetism and crystallography of a $YCrO_3$ single crystal," Phys. Rev. B, vol. 101, p. 014 114, 2020.

[64] M. El Amrani, M. Zaghrioui, V. T. Phuoc, F. Gervais, and N. E. Massa, "Local symmetry breaking and spin–phonon coupling in $SmCrO_3$ orthochromite," J. Magn. Magn. Mater., vol. 361, pp. 1–6, 2014.

[65] L. H. Yin et al., "Electric dipoles via Cr^{3+} (d^3) ion off-center displacement in perovskite $DyCrO_3$," Phys. Rev. B, vol. 98, p. 054 301, 2018.

[66] K. Yoshii and N. Ikeda, "Dielectric and magnetocaloric study of $TmCrO_3$," J. Alloys Compd., vol. 804, pp. 364–369, 2019.

[67] Y. Zhu, K. Sun, S. Wu, J. Xia, and H.-F. Li, "A comprehensive review on the ferroelectric orthochromates: Syntheses, properties, and applications," Coord. Chem. Rev., under review, 2022.

[68] Z. J. Feng, Y. X. Xu, and C. L. Zeng, "Preparation and high temperature performances of $DyCrO_3$-based coatings on a ferritic stainless steel interconnect material," J. Power Sources, vol. 235, pp. 54–61, 2013.

[69] Z. Hou, F. Chen, J. Wang, C. P. François-Xavier, and T. Wintgens, "Novel $Pd/GdCrO_3$ composite for photo-catalytic reduction of nitrate to N_2 with high selectivity and activity," Appl. Catal. B, vol. 232, pp. 124–134, 2018.

[70] R. Ullah, M. A. Ali, G Murtaza, A. Mahmood, and S. M. Ramay, "An investigation of structural, elastic, mechanical, electronic, magnetic and thermoelectric properties of ferromagnetic half metallic $EuCrO_3$," Mat. Sci. Semicon. Proc., vol. 122, p. 105 487, 2021.

[71] H. Ueda, H. Mitamura, T. Goto, and Y. Ueda, "Successive field-induced transitions in a frustrated antiferromagnet $HgCr_2O_4$," Phys. Rev. B, vol. 73, p. 094 415, 2006.

[72] M. Matsuda et al., "Spin–lattice instability to a fractional magnetization state in the spinel $HgCr_2O_4$," Nat. Phys., vol. 3, pp. 397–400, 2007.

[73] J. B. Philipp et al., "Structural and doping effects in the half-metallic double perovskite A_2CrWO_6 (A = Sr, Ba, and Ca)," Phys. Rev. B, vol. 68, p. 144 431, 2003.

[74] H. Li, "Synthesis of CMR manganites and ordering phenomena in complex transition metal oxides," Ph.D. dissertation, Forschungszentrum Jülich, Jülich, 2008.

[75] A. H. Cooke, D. M. Martin, and M. R. Wells, "Magnetic interactions in gadolinium orthochromite, $GdCrO_3$," J. Phys. C: Solid State Phys., vol. 7, p. 3133, 1974.

[76] Y. Tokura and N. Nagaosa, "Orbital physics in transition-metal oxides," Science, vol. 288, pp. 462–468, 2000.

[77] E. Dagotto and Y. Tokura, "Strongly correlated electronic materials: Present and future," MRS Bull., vol. 33, pp. 1037–1045, 2008.

[78] E. Dagotto, "Complexity in strongly correlated electronic systems," Science, vol. 309, pp. 257–262, 2005.

[79] P. Curie, "Sur la symétrie dans les phénomènes physiques, symétrie d'un champ électrique et d'un champ magnétique," J. Phys. Theor. Appl., vol. 3, pp. 393–415, 1894.

[80] P. Debye, "Bemerkung zu einigen neuen versuchen über einen magneto-elektrischen richteffekt," Zeitschrift für Physik, vol. 36, pp. 300–301, 1926.

[81] G. A. Smolenskii, A. I. Agranovskaya, and V. A. Isupov, "New ferroelectrics of complex composition: Pb_2MgWO_6, $Pb_3Fe_2WO_9$ and Pb_2FeTaO_6," Sov. Phys. Solid State, vol. 1, pp. 907–908, 1959.

[82] I. E. Dzyaloshinskii, "On the magneto-electrical effects in antiferromagnets," Sov. phys. JETP, vol. 10, pp. 628–629, 1960.

[83] H. Schmid, "Multi-ferroic magnetoelectrics," Ferroelectrics, vol. 162, pp. 317–338, 1994.

[84] M. M. Vopson, "Fundamentals of multiferroic materials and their possible applications," Crit. Rev. Solid State Mater. Sci., vol. 40, pp. 223–250, 2015.

[85] Y. Tokunaga, Y. Taguchi, T. Arima, and Y. Tokura, "Electric-field-induced generation and reversal of ferromagnetic moment in ferrites," Nat. Phys., vol. 8, pp. 838–844, 2012.

[86] J. van den Brink and D. Khomskii, "Multiferroicity due to charge ordering," J. Phys. Condens. Matter, vol. 20, p. 434 217, 2008.

[87] C. Ederer and N. A. Spaldin, "A new route to magnetic ferroelectrics," Nat. Mater., vol. 3, pp. 849–851, 2004.

[88] J. X. Zhang et al., "Microscopic origin of the giant ferroelectric polarization in tetragonal-like $BiFeO_3$," Phys. Rev. Lett., vol. 107, p. 147 602, 2011.

[89] J. F. Scott, C. A. Araujo, B. M. Melnick, L. D. McMillan, and R. Zuleeg, "Quantitative measurement of space-charge effects in lead zirconate-titanate memories," J. Appl. Phys., vol. 70, pp. 382–388, 1991.

[90] G. L. Smith et al., "PZT-based piezoelectric mems technology," J. Am. Ceram. Soc., vol. 95, pp. 1777–1792, 2012.

[91] N. A. Spaldin and M. Fiebig, "The renaissance of magnetoelectric multiferroics," Science, vol. 309, pp. 391–392, 2005.

[92] N. Ikeda et al., "Ferroelectricity from iron valence ordering in the charge-frustrated system $LuFe_2O_4$," Nature, vol. 436, pp. 1136–1138, 2005.

[93] D. V. Efremov, J. Van Den Brink, and D. I. Khomskii, "Bond-versus site-centred ordering and possible ferroelectricity in manganites," Nat. Mater., vol. 3, pp. 853–856, 2004.

[94] J. P. Wright, J. P. Attfield, and P. G. Radaelli, "Long range charge ordering in magnetite below the verwey transition," Phys. Rev. Lett., vol. 87, p. 266 401, 2001.

[95] N. A. Hill, "Density functional studies of multiferroic magnetoelectrics," Annu. Rev. Mater. Res., vol. 32, pp. 1–37, 2002.

[96] R. E. Cohen and H. Krakauer, "Electronic structure studies of the differences in ferroelectric behavior of $BaTiO_3$ and $PbTiO_3$," Ferroelectrics, vol. 136, pp. 65–83, 1992.

[97] N. A. Hill, "Why are there so few magnetic ferroelectrics?" J. Phys. Chem. B, vol. 104, pp. 6694–6709, 2000.

[98] V. V. Gagulin et al., "New seignette-magnets with hexagonal barium titanate structure," phys. stat. sol. (a), vol. 48, pp. 183–189, 1978.

[99] Y. Akishige, G. Oomi, T. Yamaoto, and E. Sawaguchi, "Dielectric properties of ferroelectric hexagonal $BaTiO_3$," J. Phys. Soc. Jpn., vol. 58, pp. 930–939, 1989.

[100] S. A. Ivanov, S.-G. Eriksson, J Erikssen, R. Tellgren, and H Rundlof, "Nuclear and magnetic structure of $Ba_3Fe_2WO_9$," Mater. Res. Bull., vol. 39, pp. 615–628, 2004.

[101] J. F. Scott, "Multiferroic memories," Nat. Mater., vol. 6, pp. 256–257, 2007.

[102] S. Dong, J.-M. Liu, S.-W. Cheong, and Z. Ren, "Multiferroic materials and magnetoelectric physics: Symmetry, entanglement, excitation, and topology," Adv. Phys., vol. 64, pp. 519–626, 2015.

[103] H. Katsura, N. Nagaosa, and A. V. Balatsky, "Spin current and magnetoelectric effect in noncollinear magnets," Phys. Rev. Lett., vol. 95, p. 057 205, 2005.

[104] I. A. Sergienko and E. Dagotto, "Role of the Dzyaloshinskii-Moriya interaction in multiferroic perovskites," Phys. Rev. B, vol. 73, p. 094 434, 2006.

[105] I. Dzyaloshinsky, "A thermodynamic theory of "weak" ferromagnetism of antiferromagnetics," J. Phys. Chem. Solids, vol. 4, pp. 241–255, 1958.

[106] T. Moriya, "Anisotropic superexchange interaction and weak ferromagnetism," Phys. Rev., vol. 120, pp. 91–98, 1960.

[107] L. Shekhtman, O. Entin-Wohlman, and A. Aharony, "Moriya's anisotropic superexchange interaction, frustration, and dzyaloshinsky's weak ferromagnetism," Phys. Rev. Lett., vol. 69, pp. 836–839, 1992.

[108] S.-W. Cheong and M. Mostovoy, "Multiferroics: A magnetic twist for ferro-electricity," Nat. Mater., vol. 6, pp. 13–20, 2007.

[109] N. Abe, K. Taniguchi, S. Ohtani, T. Takenobu, Y. Iwasa, and T. Arima, "Polarization reversal in multiferroic $TbMnO_3$ with a rotating magnetic field direction," Phys. Rev. Lett., vol. 99, p. 227 206, 2007.

[110] T Aoyama, K Yamauchi, A Iyama, S Picozzi, K Shimizu, and T Kimura, "Giant spin-driven ferroelectric polarization in $TbMnO_3$ under high pressure," Nat. Commun., vol. 5, p. 4927, 2014.

[111] N. Aliouane et al., "Flop of electric polarization driven by the flop of the mn spin cycloid in multiferroic $TbMnO_3$," Phys. Rev. Lett., vol. 102, p. 207 205, 2009.

[112] C. Jia, S. Onoda, N. Nagaosa, and J. H. Han, "Microscopic theory of spin-polarization coupling in multiferroic transition metal oxides," Phys. Rev. B, vol. 76, p. 144 424, 2007.

[113] T.-h. Arima, "Spin-driven ferroelectricity and magneto-electric effects in frustrated magnetic systems," J. Phys. Soc. Jpn., vol. 80, p. 052 001, 2011.

[114] H. J. Xiang, S.-H. Wei, M.-H. Whangbo, and J. L. F. Da Silva, "Spin-orbit coupling and ion displacements in multiferroic $TbMnO_3$," Phys. Rev. Lett., vol. 101, p. 037 209, 2008.

[115] A. Malashevich and D. Vanderbilt, "First principles study of improper ferro-electricity in $TbMnO_3$," Phys. Rev. Lett., vol. 101, p. 037 210, 2008.

[116] A. Malashevich and D. Vanderbilt, "First-principles theory of magnetically induced ferroelectricity in $TbMnO_3$," Eur. Phys. J. B, vol. 71, pp. 345–348, 2009.

[117] H. C. Walker et al., "Femtoscale magnetically induced lattice distortions in multiferroic $TbMnO_3$," Science, vol. 333, pp. 1273–1276, 2011.

[118] I. A. Sergienko, C. Şen, and E. Dagotto, "Ferroelectricity in the magnetic E-phase of orthorhombic perovskites," Phys. Rev. Lett., vol. 97, p. 227 204, 2006.

[119] S. Picozzi, K. Yamauchi, B. Sanyal, I. A. Sergienko, and E. Dagotto, "Dual nature of improper ferroelectricity in a magnetoelectric multiferroic," Phys. Rev. Lett., vol. 99, p. 227 201, 2007.

[120] H. W. Brinks, J. Rodríguez-Carvajal, H. Fjellvåg, A. Kjekshus, and B. C. Hauback, "Crystal and magnetic structure of orthorhombic $HoMnO_3$," Phys. Rev. B, vol. 63, p. 094 411, 2001.

[121] A. Munoz, M. T. Casáis, J. A. Alonso, M. J. Martínez-Lope, J. L. Martinez, and M. T. Fernandez-Diaz, "Complex magnetism and magnetic structures of

the metastable HoMnO$_3$ perovskite," <u>Inorg. Chem.</u>, vol. 40, pp. 1020–1028, 2001.

[122] J.-S. Zhou and J. B. Goodenough, "Intrinsic structural distortion in orthorhombic perovskite oxides," <u>Phys. Rev. B</u>, vol. 77, p. 132 104, 2008.

[123] Y. J. Choi, H. T. Yi, S. Lee, Q. Huang, V. Kiryukhin, and S.-W. Cheong, "Ferroelectricity in an ising chain magnet," <u>Phys. Rev. Lett.</u>, vol. 100, p. 047 601, 2008.

[124] M. Mochizuki, N. Furukawa, and N. Nagaosa, "Spin model of magnetostrictions in multiferroic Mn perovskites," <u>Phys. Rev. Lett.</u>, vol. 105, p. 037 205, 2010.

[125] M. Mochizuki, N. Furukawa, and N. Nagaosa, "Theory of spin-phonon coupling in multiferroic manganese perovskites RMnO$_3$," <u>Phys. Rev. B</u>, vol. 84, p. 144 409, 2011.

[126] T. Arima <u>et al.</u>, "Magnetic-field-induced transition in the lattice modulation of colossal magnetoelectric GdMnO$_3$ and TbMnO$_3$ compounds," <u>Phys. Rev. B</u>, vol. 72, p. 100 102, 2005.

[127] S. Z. Li <u>et al.</u>, "Modulated multiferroicity of Cr-doped orthorhombic polycrystalline YMnO$_3$," <u>J. Phys. D: Appl. Phys.</u>, vol. 45, p. 055 003, 2012.

[128] L. Lin, L. Li, Z. B. Yan, Y. M. Tao, S. Dong, and J.-M. Liu, "Ferroelectricity of polycrystalline GdMnO$_3$ and multifold magnetoelectric responses," <u>Appl. Phys. A</u>, vol. 112, pp. 947–954, 2013.

[129] N. Zhang, S. Dong, and J.-M. Liu, "Ferroelectricity generated by spin-orbit and spin-lattice couplings in multiferroic DyMnO$_3$," <u>Front. Phys.</u>, vol. 7, pp. 408–417, 2012.

[130] Y. Tokunaga, S. Iguchi, T. Arima, and Y. Tokura, "Magnetic-field-induced ferroelectric state in DyFeO$_3$," <u>Phys. Rev. Lett.</u>, vol. 101, p. 097 205, 2008.

[131] N. Lee, Y. J. Choi, M. Ramazanoglu, W. Ratcliff, V. Kiryukhin, and S.-W. Cheong, "Mechanism of exchange striction of ferroelectricity in multiferroic orthorhombic HoMnO$_3$ single crystals," <u>Phys. Rev. B</u>, vol. 84, p. 020 101, 2011.

[132] Y. W. Windsor <u>et al.</u>, "Multiple magnetic ordering phenomena in multiferroic o-HoMnO$_3$," <u>Phys. Rev. B</u>, vol. 102, p. 214 423, 2020.

[133] E. Morosan, D. Natelson, A. H. Nevidomskyy, and Q. Si, "Strongly correlated materials," <u>Adv. Mater.</u>, vol. 24, pp. 4896–4923, 2012.

[134]   P. P. Edwards, R. L. Johnston, C. N. R. Rao, D. P. Tunstall, and F. Hensel, "The metal-insulator transition: A perspective," <u>Philos. Trans. Royal Soc. A</u>, vol. 356, pp. 5–22, 1998.

[135]   M. Simón, M Balina, and A. Aligia, "Effective one-band hamiltonian for cuprate superconductor metal-insulator transition," <u>Physica C</u>, vol. 206, pp. 297–304, 1993.

[136]   Y. Nomura, M. Hirayama, T. Tadano, Y. Yoshimoto, K. Nakamura, and R. Arita, "Formation of a two-dimensional single-component correlated electron system and band engineering in the nickelate superconductor $NdNiO_2$," <u>Phys. Rev. B</u>, vol. 100, p. 205 138, 2019.

[137]   J. B. Goodenough, "Electronic structure of CMR manganites," <u>J. Appl. Phys.</u>, vol. 81, pp. 5330–5335, 1997.

[138]   N. F. Mott, "The basis of the electron theory of metals, with special reference to the transition metals," <u>Proc. Phys. Soc. A</u>, vol. 62, pp. 416–422, 1949.

[139]   N. F. Mott and R. Peierls, "Discussion of the paper by de boer and verwey," <u>Proc. Phys. Soc.</u>, vol. 49, pp. 72–73, 1937.

[140]   M. Imada, A. Fujimori, and Y. Tokura, "Metal-insulator transitions," <u>Rev. Mod. Phys.</u>, vol. 70, pp. 1039–1263, 1998.

[141]   H Eschrig, K Koepernik, and I Chaplygin, "Density functional application to strongly correlated electron systems," <u>J. Solid State Chem.</u>, vol. 176, pp. 482–495, 2003.

[142]   B. H. Brandow, "Electronic structure of mott insulators," <u>Adv. Phys.</u>, vol. 26, pp. 651–808, 1977.

[143]   J. Hubbard, "Electron correlations in narrow energy bands," <u>Philos. Trans. Royal Soc. A</u>, vol. 276, pp. 238–257, 1963.

[144]   G. Sordi, A. Amaricci, and M. J. Rozenberg, "Metal-insulator transitions in the periodic anderson model," <u>Phys. Rev. Lett.</u>, vol. 99, p. 196 403, 2007.

[145]   R. Pentcheva and W. E. Pickett, "Correlation-driven charge order at the interface between a Mott and a band insulator," <u>Phys. Rev. Lett.</u>, vol. 99, p. 016 802, 2007.

[146]   C. Escorihuela-Sayalero, O. Diéguez, and J. Íñiguez, "Strain engineering magnetic frustration in perovskite oxide thin films," <u>Phys. Rev. Lett.</u>, vol. 109, p. 247 202, 2012.

[147]   F. Liu et al., "Pressure-induced charge orders and their coupling to magnetism in hexagonal multiferroic $LuFe_2O_4$," <u>arXiv:2112.10036</u>, 2021.

[148] A. Kitaev, "Anyons in an exactly solved model and beyond," <u>Ann. Phys.</u>, vol. 321, pp. 2–111, 2006.

[149] G. Jackeli and G. Khaliullin, "Mott insulators in the strong spin-orbit coupling limit: From heisenberg to a quantum compass and kitaev models," <u>Phys. Rev. Lett.</u>, vol. 102, p. 017 205, 2009.

[150] Y. Tokura and N. Kanazawa, "Magnetic skyrmion materials," <u>Chem. Rev.</u>, vol. 121, pp. 2857–2897, 2020.

[151] L. Caretta <u>et al.</u>, "Interfacial dzyaloshinskii-moriya interaction arising from rare-earth orbital magnetism in insulating magnetic oxides," <u>Nat. Commun.</u>, vol. 11, p. 1090, 2020.

[152] A. Mook, J. Henk, and I. Mertig, "Edge states in topological magnon insulators," <u>Phys. Rev. B</u>, vol. 90, p. 024 412, 2014.

[153] Z. Cai <u>et al.</u>, "Topological magnon insulator spin excitations in the two-dimensional ferromagnet $CrBr_3$," <u>Phys. Rev. B</u>, vol. 104, p. L020402, 2021.

[154] M. Ma <u>et al.</u>, "Prominent role of spin-orbit coupling in FeSe revealed by inelastic neutron scattering," <u>Phys. Rev. X</u>, vol. 7, p. 021 025, 2017.

[155] J. Li <u>et al.</u>, "Spin-orbital-intertwined nematic state in FeSe," <u>Phys. Rev. X</u>, vol. 10, p. 011 034, 2020.

[156] W. Nolting and A. Ramakanth, <u>Quantum Theory of Magnetism</u>. Springer Science & Business Media, 2009.

[157] T. Takayama, J. Chaloupka, A. Smerald, G. Khaliullin, and H. Takagi, "Spin–orbit-entangled electronic phases in $4d$ and $5d$ transition-metal compounds," <u>J. Phys. Soc. Jpn.</u>, vol. 90, p. 062 001, 2021.

[158] J. M. D. Coey, <u>Magnetism and Magnetic Materials</u>. Cambridge university press, 2010.

[159] H. F. Li <u>et al.</u>, "Correlation between structural and magnetic properties of $La_{7/8}Sr_{1/8}Mn_{1-\gamma}O_{3+\delta}$ with controlled nonstoichiometry," <u>J. Phys.: Condens. Matter</u>, vol. 19, p. 016 003, 2006.

[160] J.-S. Zhou, "Structural distortions in rare-earth transition-metal oxide perovskites under high pressure," <u>Phys. Rev. B</u>, vol. 101, p. 224 104, 2020.

[161] M. I. Bradbury and D. J. Newman, "New superexchange model applied to Gd^{3+} pairs in $LaCl^{3+}$ and $EuCl^{3+}$," <u>J. Phys. Chem. Solids</u>, vol. 32, pp. 627–636, 1971.

[162] J. Ji et al., "Rare-earth chalcohalides: A family of van der Waals layered Kitaev spin liquid candidates," Chin. Phys. Lett., vol. 38, p. 047 502, 2021.

[163] H. A. Kramers, "L'interaction entre les atomes magnétogènes dans un cristal paramagnétique," Physica, vol. 1, pp. 182–192, 1934.

[164] R. M. White, Quantum Theory of Magnetism. Springer Science & Business Media, 2007.

[165] W. Geertsma and D. Khomskii, "Influence of side groups on 90° superexchange: A modification of the Goodenough-Kanamori-Anderson rules," Phys. Rev. B, vol. 54, pp. 3011–3014, 1996.

[166] M. A. Ruderman and C. Kittel, "Indirect exchange coupling of nuclear magnetic moments by conduction electrons," Phys. Rev., vol. 96, pp. 99–102, 1954.

[167] T. Kasuya, "A theory of metallic ferro-and antiferromagnetism on Zener's model," Prog. Theor. Phys., vol. 16, pp. 45–57, 1956.

[168] K. Yosida, "Magnetic properties of Cu-Mn alloys," Phys. Rev., vol. 106, pp. 893–898, 1957.

[169] S. S. P. Parkin and D. Mauri, "Spin engineering: Direct determination of the Ruderman-Kittel-Kasuya-Yosida far-field range function in ruthenium," Phys. Rev. B, vol. 44, pp. 7131–7134, 1991.

[170] H. Das, A. F. Rébola, and T. Saha-Dasgupta, "Exploring the possible origin of the spin reorientation transition in $NdCrO_3$," Phys. Rev. Mater., vol. 5, p. 124 416, 2021.

[171] J. K. Murthy and A Venimadhav, "$4f$-$3d$ exchange coupling induced exchange bias and field induced Hopkinson peak effects in Gd_2CoMnO_6," J. Alloys Compd., vol. 719, pp. 341–346, 2017.

[172] L. H. Yin et al., "Role of rare earth ions in the magnetic, magnetocaloric and magnetoelectric properties of $RCrO_3$ (R = Dy, Nd, Tb, Er) crystals," J. Mater. Chem. C, vol. 4, pp. 11 198–11 204, 2016.

[173] I. Fita, R. Puzniak, A. Wisniewski, and V. Markovich, "Spin switching and unusual exchange bias in the single-crystalline $GdCrO_3$ compensated ferrimagnet," Phys. Rev. B, vol. 100, p. 144 426, 2019.

[174] K. Luo and M. A. Hayward, "Complex cation order in anion-deficient $Ba_nYFe_{n-1}O_{2.5n}$ perovskite phases," Inorg. Chem., vol. 51, pp. 12 281–12 287, 2012.

[175] K. Luo, R. D. Johnson, T. T. Tran, P. S. Halasyamani, P. G. Radaelli, and M. A. Hayward, "$Ba_2YFeO_{5.5}$: A ferromagnetic pyroelectric phase prepared by topochemical oxidation.," Chem. Mater., vol. 25, pp. 1800–1808, 2013.

[176] A. K. Kundu, V. Hardy, V. Caignaert, and B. Raveau, "Interplay between $3d$-$3d$ and $3d$-$4f$ interactions at the origin of the magnetic ordering in the Ba_2LnFeO_5 oxides," J. Phys.: Condens. Matter, vol. 27, p. 486 001, 2015.

[177] A. K. Kundu, V. Caignaert, V. Hardy, and B. Raveau, "Superexchange interactions between Fe-$3d$ and Ln-$4f$ states: Long range antiferromagnetism in perovskite derivatives $Ba_3LnFe_2O_{7.5}$," J. Mater. Chem. C, vol. 5, pp. 7236–7242, 2017.

[178] E. Climent Pascual et al., "Zircon to scheelite phase transition induced by pressure and magnetism in $TbCrO_4$," Phys. Rev. B, vol. 81, p. 174 419, 2010.

[179] J. P. Joule, "On a new class of magnetic forces," Sturgeon's Annals of Electricity, vol. 8, p. 219, 1842.

[180] I. E. Dzialoshinskii, "The problem of piezomagnetism," Sov. Phys. JETP, vol. 6, pp. 621–622, 1958.

[181] N. B. Ekreem, A. G. Olabi, T. Prescott, A. Rafferty, and M. S. J. Hashmi, "An overview of magnetostriction, its use and methods to measure these properties," J. Mater. Process. Technol., vol. 191, pp. 96–101, 2007.

[182] A.-G. Olabi and A. Grunwald, "Design and application of magnetostrictive materials," Mater. Des., vol. 29, pp. 469–483, 2008.

[183] Y. C. Guo, Ferromagnetism (in Chinese). People's Education Press, Beijing, 1965.

[184] S. T. Jiang and W. Li, Condensed Matter Magnetic Physics (in Chinese). Science Press, Beijing, 2003.

[185] S. M. Bakharev, M. A. Borich, and S. P. Savchenko, "Caustic of magnetoelastic waves in elastically isotropic ferromagnets," J. Magn. and Magn. Mater., vol. 530, p. 167 862, 2021.

[186] A. Smith, "Who discovered the magnetocaloric effect?" Eur. Phys. J. H, vol. 38, pp. 507–517, 2013.

[187] E. Brück, "Developments in magnetocaloric refrigeration," J. Phys. D: Appl. Phys., vol. 38, R381, 2005.

[188] J. S. Amaral and V. S. Amaral, "On estimating the magnetocaloric effect from magnetization measurements," J. Magn. Magn. Mater., vol. 322, pp. 1552–1557, 2010.

[189] B. G. Shen, J. R. Sun, F. X. Hu, H. W. Zhang, and Z. H. Cheng, "Recent progress in exploring magnetocaloric materials," Adv. Mater., vol. 21, pp. 4545–4564, 2009.

[190] M. Balli, S. Jandl, P. Fournier, and A. Kedous-Lebouc, "Advanced materials for magnetic cooling: Fundamentals and practical aspects," Appl. Phys. Rev., vol. 4, p. 021 305, 2017.

[191] F. Casanova, X. Batlle, A. Labarta, J. Marcos, L. Mañosa, and A. Planes, "Entropy change and magnetocaloric effect in $Gd_5(Si_xGe_{1-x})_4$," Phys. Rev. B, vol. 66, p. 100 401, 2002.

[192] S. Wu et al., "Super-necking crystal growth and structural and magnetic properties of $SrTb_2O_4$ single crystals," ACS omega, vol. 5, pp. 16 584–16 594, 2020.

[193] J. Wen, "Interplay between magnetism and superconductivity in high-temperature superconductors $La_{2-x}Ba_xCuO_4$ and $Fe_{1+y}Te_{1-x}Se_x$: Crystal growth and neutron scattering studies," Ph.D. dissertation, Stony Brook University, 2010.

[194] H. Schäfer, "Preparative solid state chemistry: The present position," Angew. Chem. Int. Ed., vol. 10, pp. 43–50, 1971.

[195] J.-Q. Yan, Z. Huang, W. Wu, and A. F. May, "Vapor transport growth of $MnBi_2Te_4$ and related compounds," J. Alloy. Compd., vol. 906, p. 164 327, 2022.

[196] S. Rundqvist, L. Sillén, D Timm, K Motzfeldt, O Theander, and H Flood, "Phosphides of the B31 (MnP) structure type," Acta Chem. Scand., vol. 16, pp. 287–292, 1962.

[197] K. C. A. Smith and C. W. Oatley, "The scanning electron microscope and its fields of application," Br. J. Appl. Phys., vol. 6, p. 391, 1955.

[198] W. L. Bragg, "The specular reflection of X-rays," Nature, vol. 90, pp. 410–410, 1912.

[199] W. Friedrich, P. Knipping, and M. Laue, "Interferenzerscheinungen bei roentgenstrahlen," Ann. Phys., vol. 346, pp. 971–988, 1913.

[200] C. Suryanarayana and M. G. Norton, X-ray Diffraction: A Practical Approach. Springer Science & Business Media, 1998.

[201] H. Winick, Synchrotron Radiation Sources: A Primer. World Scientific, 1995.

[202] VEQTER, Bragg's law, `https://www.veqter.co.uk/residual-stress-measurement/x-ray-diffraction`.

[203] P. J. Brown, A. G. Fox, E. N. Maslen, M. A. O'keefe, and B. T. M. Willis, "Intensity of diffracted intensities," International Tables for Crystallography, 2006.

[204] J. Rodríguez-Carvajal, "Recent advances in magnetic structure determination by neutron powder diffraction," Physica B, vol. 192, pp. 55–69, 1993.

[205] T. A. Al-Dhahir, "Quantitative phase analysis for titanium dioxide from X-ray powder diffraction data using the Rietveld method," Diyala Journal For Pure Sciences, vol. 2, pp. 108–119, 2013.

[206] LibreTexts, X-ray diffraction, bragg's law and laue equation, https://eng.libretexts.org/@go/page/320.

[207] J. Chadwick, "Possible existence of a neutron," Nature, vol. 129, pp. 312–312, 1932.

[208] W. Reimers et al., Neutrons and synchrotron radiation in engineering materials science. John Wiley & Sons, 2008.

[209] A. Furrer, J. F. Mesot, and T. Strässle, Neutron Scattering in Condensed Matter Physics. World Scientific Publishing Company, 2009.

[210] C. Brown, High Resolution Powder Diffractometer - BT-1, https://www.nist.gov/ncnr/high-resolution-powder-diffractometer-bt-1.

[211] J. K. Stalick, E. Prince, A. Santoro, I. G. Schroder, and J. J. Rush, "Materials science applications of the new national institute of standards and technology powder diffractometer," MRS Online Proceedings Library (OPL), vol. 376, pp. 101–106, 1994.

[212] L. He et al., "First experimental results from the GPPD diffractometer at the CSNS," Neutron News, vol. 29, pp. 7–10, 2018.

[213] C.-M. Wu et al., "SIKA—the multiplexing cold-neutron triple-axis spectrometer at ANSTO," J. Inst., vol. 11, P10009, 2016.

[214] M. Arai et al., "Recent developments of instruments in a spallation neutron source at J-PARC and those prospects in the future," J. Phys. Soc. Jpn., vol. 82, SA024, 2013.

[215] M. Born and J. R. Oppenheimer, "Zur quantentheorie der molekeln," Ann. Phys., pp. 457–484, 1927.

[216] Y. Zhu, X. Ma, W. Lou, M. Wang, and C. Yang, "Symmetry-broken effects on electron momentum spectroscopy caused by adiabatic vibration," Chem. Phys. Lett., vol. 687, pp. 116–124, 2017.

[217] D. R. Hartree, "The wave mechanics of an atom with a non-coulomb central field. Part I. Theory and methods," Math. Proc. Cambridge Philos. Soc., vol. 24, pp. 89–110, 1928.

[218] J. C. Slater, "The theory of complex spectra," Phys. Rev., vol. 34, pp. 1293–1322, 1929.

[219] P. Lykos and G. W. Pratt, "Discussion on the hartree-fock approximation," Rev. Mod. Phys., vol. 35, pp. 496–501, 1963.

[220] C. D. Sherrill, An introduction to Hartree-Fock molecular orbital theory. Atlanta: School of Chemistry and Biochemistry Georgia Institute of Technology, 2000.

[221] L. H. Thomas, "The calculation of atomic fields," Math. Proc. Cambridge Philos. Soc., vol. 23, pp. 542–548, 1927.

[222] E. Fermi, "Un metodo statistico per la determinazione di alcune priorieta dell'atome," Rend. Accad. Naz. Lincei, vol. 6, p. 32, 1927.

[223] P. Hohenberg and W. Kohn, "Inhomogeneous electron gas," Phys. Rev., vol. 136, B864–B871, 1964.

[224] W. Kohn and L. J. Sham, "Self-consistent equations including exchange and correlation effects," Phys. Rev., vol. 140, A1133–A1138, 1965.

[225] D. S. Sholl and J. A. Steckel, Density functional theory: A practical introduction. John Wiley & Sons, 2011.

[226] J. P. Perdew and K. Schmidt, "Jacob's ladder of density functional approximations for the exchange-correlation energy," AIP Conf. Proc., vol. 577, pp. 1–20, 2001.

[227] J. P. Van der Ziel and L. G. Van Uitert, "Magnon-assisted optical emission in $YCrO_3$ and $LuCrO_3$," Phys. Rev., vol. 179, p. 343, 2 1969.

[228] A. L. Chernyshev and M. E. Zhitomirsky, "Spin waves in a triangular lattice antiferromagnet: Decays, spectrum renormalization, and singularities," Phys. Rev. B, vol. 79, p. 144 416, 14 2009.

[229] S. Jin, C. Luo, T. Datta, and D.-X. Yao, "Torque equilibrium spin wave theory study of anisotropy and Dzyaloshinskii-Moriya interaction effects on the indirect k-edge RIXS spectrum of a triangular lattice antiferromagnet," Phys. Rev. B, vol. 100, p. 054 410, 2019.

[230] D. X. Yao and E. W. Carlson, "Magnetic excitations of undoped iron oxypnictides," Front. Phys. China, vol. 5, p. 166, 2010.

[231] F. Keffer, "Moriya interaction and the problem of the spin arrangements in βMnS," Phys. Rev., vol. 126, pp. 896–900, 1962.

[232] T. Holstein and H. Primakoff, "Field dependence of the intrinsic domain magnetization of a ferromagnet," Phys. Rev., vol. 58, pp. 1098–1113, 1940.

[233] J. L. van Hemmen, "A note on the diagonalization of quadratic boson and fermion hamiltonians," Zeitschrift für Physik B Condensed Matter, vol. 38, pp. 271–277, 1980.

[234] N. Hur, S. Park, P. A. Sharma, J. S. Ahn, S. Guha, and S.-W. Cheong, "Electric polarization reversal and memory in a multiferroic material induced by magnetic fields," Nature, vol. 429, pp. 392–395, 2004.

[235] N. A. Spaldin and R. Ramesh, "Advances in magnetoelectric multiferroics," Nat. Mater., vol. 18, pp. 203–212, 2019.

[236] J.-M. Hu, L.-Q. Chen, and C.-W. Nan, "Multiferroic heterostructures integrating ferroelectric and magnetic materials," Adv. Mater., vol. 28, pp. 15–39, 2016.

[237] J. B. Goodenough, "Electronic and ionic transport properties and other physical aspects of perovskites," Rep. Prog. Phys., vol. 67, pp. 1915–1993, 2004.

[238] N. S. Fedorova et al., "Relationship between crystal structure and multiferroic orders in orthorhombic perovskite manganites," Phys. Rev. Mater., vol. 2, p. 104 414, 2018.

[239] N. Wagner, R. Seshadri, and J. M. Rondinelli, "Property control from polyhedral connectivity in ABO_3 oxides," Phys. Rev. B, vol. 100, p. 064 101, 2019.

[240] S. Mahana, U. Manju, P. Nandi, E. Welter, K. R. Priolkar, and D. Topwal, "Role of local structural distortion in driving ferroelectricity in $GdCrO_3$," Phys. Rev. B, vol. 97, p. 224 107, 2018.

[241] B. B. Van Aken, T. T. Palstra, A. Filippetti, and N. A. Spaldin, "The origin of ferroelectricity in magnetoelectric $YMnO_3$," Nat. Mater., vol. 3, pp. 164–167, 2004.

[242] D. G. Georgiev, K. A. Krezhov, and V. V. Nietz, "Weak antiferromagnetism in $YFeO_3$ and $HoFeO_3$," Solid State Commun., vol. 96, pp. 535–537, 1995.

[243] S. Petit, F. Moussa, M. Hennion, S. Pailhès, L. Pinsard-Gaudart, and A. Ivanov, "Spin phonon coupling in hexagonal multiferroic $YMnO_3$," Phys. Rev. Lett., vol. 99, p. 266 604, 2007.

[244] E. W. Lee, "Magnetostriction and magnetomechanical effects," Rep. Prog. Phys., vol. 18, pp. 184–229, 1955.

[245] J. P. Liu, F. R. de Boer, P. F. de Châtel, R. Coehoorn, and K. H. J. Buschow, "On the 4f-3d exchange interaction in intermetallic compounds," J. Magn. Magn. Mater., vol. 132, pp. 159–179, 1994.

[246] V. S. Bhadram, B. Rajeswaran, A. Sundaresan, and C. Narayana, "Spin-phonon coupling in multiferroic $RCrO_3$ (R-Y, Lu, Gd, Eu, Sm): A Raman study," Europhys. Lett., vol. 101, p. 17 008, 2013.

[247] S. Landron and M.-B. Lepetit, "Importance of t_{2g}-e_g hybridization in transition metal oxides," Phys. Rev. B, vol. 77, p. 125 106, 2008.

[248] H.-F. Li, Y. Zhu, S. Wu, and Z. Tang, "A method of centimeter-sized single crystal growth of chromate compounds and related storage device, China Invention Patent," pat. CN 110904497 B, 2019.

[249] B. Ouladdiaf, J. Archer, G. J. McIntyre, A. W. Hewat, D. Brau, and S. York, "Orientexpress: A new system for laue neutron diffraction," Physica B, vol. 385, pp. 1052–1054, 2006.

[250] J. P. Perdew, K. Burke, and M. Ernzerhof, "Generalized gradient approximation made simple," Phys. Rev. Lett., vol. 77, pp. 3865–3868, 1996.

[251] C. Franchini, R. Podloucky, J. Paier, M. Marsman, and G. Kresse, "Ground-state properties of multivalent manganese oxides: Density functional and hybrid density functional calculations," Phys. Rev. B, vol. 75, p. 195 128, 2007.

[252] A. B. Shick, A. I. Liechtenstein, and W. E. Pickett, "Implementation of the LDA+U method using the full-potential linearized augmented plane-wave basis," Phys. Rev. B, vol. 60, pp. 10 763–10 769, 1999.

[253] C. Franchini, R. Podloucky, J. Paier, M. Marsman, and G. Kresse, "Ground-state properties of multivalent manganese oxides: Density functional and hybrid density functional calculations," Phys. Rev. B, vol. 75, p. 195 128, 2007.

[254] G. Kresse and J. Furthmüller, "Efficiency of ab-initio total energy calculations for metals and semiconductors using a plane-wave basis set," Compt. Mater. Sci., vol. 6, pp. 15–50, 1996.

[255] G. Kresse and D. Joubert, "From ultrasoft pseudopotentials to the projector augmented-wave method," Phys. Rev. B, vol. 59, pp. 1758–1775, 1999.

[256] H. J. Monkhorst and J. D. Pack, "Special points for brillouin-zone integrations," Phys. Rev. B, vol. 13, pp. 5188–5192, 1976.

[257] S. L. Dudarev, G. A. Botton, S. Y. Savrasov, C. J. Humphreys, and A. P. Sutton, "Electron-energy-loss spectra and the structural stability of nickel oxide: An LSDA+U study," Phys. Rev. B, vol. 57, pp. 1505–1509, 1998.

[258] M. Cococcioni and S. de Gironcoli, "Linear response approach to the calculation of the effective interaction parameters in the LDA + U method," Phys. Rev. B, vol. 71, p. 035 105, 2005.

[259] C.-H. Wu, A. Park, and D. Joester, "Bioengineering single crystal growth," J. Am. Chem. Soc., vol. 133, pp. 1658–1661, 2011.

[260] Y. Qiao, L. Yang, J. Zhu, et al., "Crystal engineering of angular-shaped heteroarenes based on cyclopenta[b]thiopyran for controlling the charge carrier mobility," J. Am. Chem. Soc., vol. 143, pp. 11 088–11 101, 2021.

[261] K. Momma and F. Izumi, "VESTA: A three-dimensional visualization system for electronic and structural analysis," J. Appl. Cryst., vol. 41, pp. 653–658, 2008.

[262] M. Winter, The periodic table of the elements, `https://www.webelements.com/`.

[263] Q. Zhao et al., "Temperature-dependent structure and magnetization of $YCrO_3$ compound," Chin. Phys. B, vol. 31, p. 046 101, 2022.

[264] F. R. de Boer and K. H. J. Buschow, "Influence of the rare-earth transition-metal interaction on the room temperature magnetostriction," J. Alloy Compd., vol. 258, pp. 1–6, 1997.

[265] G. Bulai, L. Diamandescu, I. Dumitru, S. Gurlui, M. Feder, and O. Caltun, "Effect of rare earth substitution in cobalt ferrite bulk materials," J. Magn. Magn. Mater., vol. 390, pp. 123–131, 2015.

[266] M. Vagadia, S. Rayaprol, and A. K. Nigam, "Influence of mn-substitution on the magnetic and thermal properties of $TbCrO_3$," J. Alloys Compd., vol. 735, pp. 1031–1040, 2018.

[267] H.-F. Li, "Possible ground states and parallel magnetic-field-driven phase transitions of collinear antiferromagnets," npj Comput. Mater., vol. 2, p. 16 032, 2016.

[268] Y. Su, J. Zhang, Z. Feng, Z. Li, Y. Shen, and S. Cao, "Magnetic properties of rare earth $HoCrO_3$ chromites," J. Rare Earth, vol. 29, pp. 1060–1065, 2011.

[269] C. M. N. Kumar et al., "Hyperfine and crystal field interactions in multiferroic $HoCrO_3$," J. Phys.: Condens. Matter, vol. 28, p. 476 001, 2016.

[270] T. Chatterji, F. Demmel, N. Jalarvo, et al., "Quasielastic and low-energy inelastic neutron scattering study of $HoCrO_3$ by high resolution time-of-flight neutron spectroscopy," J. Phys.: Condens. Matter, vol. 29, p. 475 802, 2017.

[271] M Eibschütz, L Holmes, J. P. Maita, and L. G. Van Uitert, "Low temperature magnetic phase transition in ErCrO$_3$," Solid State Commun., vol. 8, pp. 1815–1817, 1970.

[272] Y. L. Su et al., "Novel magnetization induced by phase coexistence in multiferroic HoCrO$_3$ chromites," Ferroelectrics, vol. 410, p. 102, 2010.

[273] Y. Su et al., "The dependence of magnetic properties on temperature for rare earth ErCrO$_3$ chromites," Ceram. Int., vol. 38, S421–S424, 2012.

[274] J. Shi, S. Yin, M. S. Seehra, and M. Jain, "Enhancement in magnetocaloric properties of ErCrO$_3$ via A-site Gd substitution," J. Appl. Phys., vol. 123, p. 193 901, 2018.

[275] K. Yoshii, "Magnetization reversal in TmCrO$_3$," Mater. Res. Bull., vol. 47, pp. 3243–3248, 2012.

[276] T Tamaki, K Tsushima, and Y Yamaguchi, "Spin reorientation in TmCrO$_3$," Physica B+C, vol. 86, pp. 923–924, 1977.

[277] Y. Su et al., "Magnetization reversal and Yb^{3+}/Cr^{3+} spin ordering at low temperature for perovskite YbCrO$_3$ chromites," J. Appl. Phys., vol. 108, p. 013 905, 2010.

[278] L Wang, S. W. Wang, X Zhang, L. L. Zhang, R Yao, and G. H. Rao, "Reversals of magnetization and exchange-bias in perovskite chromite YbCrO$_3$," J. Alloys Compd., vol. 662, pp. 268–271, 2016.

[279] A. Durán, E. Morán, M. A. Alario-Franco, C. Ostos, et al., "Biferroic LuCrO$_3$: Structural characterization, magnetic and dielectric properties," Mater. Chem. Phys., vol. 143, pp. 1222–1227, 2014.

[280] X. Qian, L. Chen, S. Cao, and J. Zhang, "A study of the spin reorientation with t–e orbital hybridization in SmCrO$_3$," Solid State Commun., vol. 195, pp. 21–25, 2014.

[281] M. N. Siddique, M. Faizan, S. Riyajuddin, P. Tripathi, S. Ahmad, and K. Ghosh, "Intrinsic structural distortion assisted optical and magnetic properties of orthorhombic rare-earth perovskite La$_{1-x}$Eu$_x$CrO$_3$: Effect of t-e hybridization," J. Alloys Compd., vol. 850, p. 156 748, 2021.

[282] Y. Fujioka, J. Frantti, and R. M. Nieminen, "Electronic energy band structure of the double perovskite Ba$_2$MnWO$_6$," J. Phys. Chem. B, vol. 112, pp. 6742–6746, 2008.

[283] F. L. M. Bernal et al., "Jahn-teller active fluoroperovskites ACrF$_3$ (A=Na$^+$, K$^+$): Magnetic and thermo-optical properties," Phys. Rev. Mater., vol. 5, p. 064 420, 2021.

[284] K. D. Singh, R. Pandit, and R. Kumar, "Effect of rare earth ions on structural and optical properties of specific perovskite orthochromates; $RCrO_3$ (R= La, Nd, Eu, Gd, Dy, and Y)," Solid State Sci., vol. 85, pp. 70–75, 2018.

[285] M. Ardit, G. Cruciani, M. Dondi, M. Merlini, and P. Bouvier, "Elastic properties of perovskite $YCrO_3$ up to 60 GPa," Phys. Rev. B, vol. 82, p. 064 109, 2010.

[286] M. V. Kuznetsov and I. P. Parkin, "Convenient, rapid synthesis of rare earth orthochromites $LnCrO_3$ by self-propagating high-temperature synthesis," Polyhedron, vol. 17, pp. 4443–4450, 1998.

[287] K. Poplawski, J. Lichtenberger, F. J. Keil, K. Schnitzlein, and M. D. Amiridis, "Catalytic oxidation of 1, 2-dichlorobenzene over ABO_3-type perovskites," Catal. Today, vol. 62, pp. 329–336, 2000.

[288] K. Sardar, M. R. Lees, R. J. Kashtiban, J. Sloan, and R. I. Walton, "Direct hydrothermal synthesis and physical properties of rare-earth and yttrium orthochromite perovskites," Chem. Mater., vol. 23, pp. 48–56, 2011.

[289] J. Prado-Gonjal, R. Schmidt, J.-J. Romero, D. Ávila, U. Amador, and E. Morán, "Microwave-assisted synthesis, microstructure, and physical properties of rare-earth chromites," Inorg. Chem., vol. 52, pp. 313–320, 2013.

[290] W. J. Weber, C. W. Griffin, and J. L. Bates, "Electrical and thermal transport properties of the $Y_{1-x}M_xCrO_3$ system," J. Mater. Res., vol. 1, no. 5, pp. 675–684, 1986.

[291] G. F. Carini II, H. U. Anderson, D. M. Sparlin, and M. M. Nasrallah, "Electrical conductivity, Seebeck coefficient and defect chemistry of Ca-doped $YCrO_3$," Solid State Ionics, vol. 49, pp. 233–243, 1991.

[292] M. Kagawa, Y. Kato, and Y. Syono, "Ultrafine particles and thin films of $YCrO_3$ synthesized by the spray-ICP technique," J. Aeroso Sci., vol. 1001, S475–S476, 1997.

[293] J. H. Kim, H.-S. Shin, S.-H. Kim, J.-H. Moon, and B.-T. Lee, "Formation of $YCrO_3$ thin films using radio-frequency magnetron sputtering method for a wide range thermistor application," Jpn. J. Appl. Phys., vol. 42, p. 575, 2003.

[294] J. Seo, Y. Ahn, and J. Y. Son, "Multiferroic properties of $YCrO_3$ thin films on glass substrate," Ceram. Int., vol. 41, no. 9, pp. 12 471–12 474, 2015.

[295] V. Bedekar, R. Shukla, and A. K. Tyagi, "Nanocrystalline $YCrO_3$ with onion-like structure and unusual magnetic behaviour," Nanotechnology, vol. 18, p. 155 706, 2007.

[296] J. Bahadur, D. Sen, S. Mazumder, R. Shukla, and A. K. Tyagi, "Non-debye to debye transition of ac dielectric response in $YCrO_3$ nanoceramic under sintering: Effect of pore structure," J. Phys.: Condens. Matter, vol. 20, no. 34, p. 345 201, 2008.

[297] R. Sinha, S. Basu, and A. K. Meikap, "Effect of neodymium doping on electrical properties and relaxor ferroelectric behavior of $YCrO_3$ nanoparticles," Physica E, vol. 113, pp. 194–201, 2019.

[298] V. M. Jüdin and A. B. Sherman, "Weak ferromagnetism of $YCrO_3$," Solid State Commun., vol. 4, pp. 661–663, 1966.

[299] E. Bertaut et al., "Etude des propriétés magnétostatiques et des structures magnétiques des chromites des terres rares et d'yttrium," IEEE Trans. Magn., vol. 2, no. 3, p. 453, 3 1966.

[300] T. Morishita and K. Tsushima, "Susceptibility of the weak ferromagnets $ErCrO_3$ and $YCrO_3$ near the critical anomaly," Phys. Rev. B, vol. 24, p. 341, 1981.

[301] A Durán et al., "Magneto-thermal and dielectric properties of biferroic $YCrO_3$ prepared by combustion synthesis," J. Solid State Chem., vol. 183, p. 1863, 2010.

[302] L. Hao et al., "Layered B-site cation ordering: A key factor in ferrimagnetism of Y_2MnCrO_6," J. Alloys Compd., vol. 601, pp. 14–18, 2014.

[303] S. S. Ahmed, G. D. Ngantso, M. Boujnah, A. Benyoussef, and A. El Kenz, "Ab initio and Monte Carlo studies of phase transitions and magnetic properties of $YCrO_3$: Heisenberg model," Phys. Lett. A, vol. 383, pp. 121–126, 2019.

[304] J. P. Remeika, "Growth of single crystal rare earth orthoferrites and related compounds," J. Am. Chem. Soc., vol. 78, no. 17, pp. 4259–4260, 1956.

[305] W. H. Grodkiewicz and D. J. Nitti, "The flux growth of scandium oxide crystals," J. Am. Ceram. Soc., vol. 49, p. 576, 1966.

[306] N. D. Todorov et al., "Comparative raman study of isostructural $YCrO_3$ and $YMnO_3$: Effects of structural distortions and twinning," Phys. Rev. B, vol. 83, p. 224 303, 2011.

[307] S. Sugano, K. Aoyagi, and K. Tsushima, "Exciton absorption lines in anti-ferromagnetic rare-earth orthochromites–with particular reference to $YCrO_3$," J. Phys. Soc. Jpn., vol. 31, pp. 706–722, 1971.

[308] H.-F. Li et al., "Crystal and magnetic structure of single-crystal $La_{1-x}Sr_xMnO_3$ ($x \approx 1/8$)," Eur. Phys. J. B, vol. 74, pp. 457–461, 2010.

[309] H. Zheng et al., "Multiferroic BaTiO$_3$-CoFe$_2$O$_4$ nanostructures," Science, vol. 303, no. 5658, pp. 661–663, 2004.

[310] M. Lilienblum, T. Lottermoser, S. Manz, S. M. Selbach, A. Cano, and M. Fiebig, "Ferroelectricity in the multiferroic hexagonal manganites," Nat. Phys., vol. 11, pp. 1070–1073, 2015.

[311] G. A. Bain and J. F. Berry, "Diamagnetic corrections and pascal's constants," J. Chem. Educ., vol. 85, p. 532, 2008.

[312] B. B. Dash and S. Ravi, "Magnetization reversal and tunable exchange bias in GdCr$_{1-x}$Mn$_x$O$_3$ (x= 0-0.50)," J. Magn. Magn. Mater., vol. 429, pp. 281–286, 2017.

[313] H.-F. Li et al., "Magnetization, crystal structure and anisotropic thermal expansion of single-crystal SrEr$_2$O$_4$," RSC Adv., vol. 4, pp. 53 602–53 607, 2014.

[314] H.-F. Li et al., "Absence of magnetic ordering in the ground state of a SrTm$_2$O$_4$ single crystal," J. Mater. Chem. C, vol. 3, pp. 7658–7668, 2015.

[315] J. M. De Teresa et al., "Evidence for magnetic polarons in the magnetoresistive perovskites," Nature, vol. 386, pp. 256–259, 1997.

[316] J. Nogués et al., "Paramagnetic behavior and correlation between high- and low-temperature structural and magnetic transitions in La$_{1-x}$Sr$_x$MnO$_3$ ($x \sim$ 1/8) single-crystal perovskites," Phys. Rev. B, vol. 64, p. 024 434, 2001.

[317] K. H. J. Buschow, Handbook of magnetic materials. Elsevier, 2003.

[318] T. Katsufuji, S. Mori, M. Masaki, Y. Moritomo, N. Yamamoto, and H. Takagi, "Dielectric and magnetic anomalies and spin frustration in hexagonal RMnO$_3$ (R=Y, Yb, and Lu)," Phys. Rev. B, vol. 64, p. 104 419, 2001.

[319] A. P. Ramirez, "Strongly geometrically frustrated magnets," Annu. Rev. Mater. Sci., vol. 24, pp. 453–480, 1994.

[320] H. T. Diep, Frustrated Spin Systems. Singapore: World Scientific, 2004.

[321] M. P. Shores, E. A. Nytko, B. M. Bartlett, and D. G. Nocera, "A structurally perfect S = 1/2 kagomé antiferromagnet," J. Am. Chem. Soc., vol. 127, pp. 13 462–13 463, 2005.

[322] S. Blundell, Magnetism in Condensed Matter. New York: Oxford University Press, 2001.

[323] W. Tian, J. Li, H. Li, J. W. Lynn, J. L. Zarestky, and D. Vaknin, "Neutron scattering studies of LiCoPO$_4$ & LiMnPO$_4$," J. Phys.: Conf. Ser., vol. 251, p. 012 005, 2010.

[324] R. Toft-Petersen et al., "Magnetic phase diagram of magnetoelectric LiMnPO$_4$," Phys. Rev. B, vol. 85, p. 224 415, 2012.

[325] L. Vočadlo, K. S. Knight, G. D. Price, and I. G. Wood, "Thermal expansion and crystal structure of FeSi between 4 and 1173 k determined by time-of-flight neutron powder diffraction," Phys. Chem. Miner., vol. 29, pp. 132–139, 2002.

[326] D. C. Wallace, Thermodynamics of Crystals. New York: Dover, 1998.

[327] Y. Zhu et al., "Erratum: High-temperature magnetism and crystallography of a YCrO$_3$ single crystal [Phys. Rev. B 101, 014114 (2020)]," Phys. Rev. B, vol. 102, p. 019 901, 2020.

[328] A. S. Gibbs, K. S. Knight, and P. Lightfoot, "High-temperature phase transitions of hexagonal YMnO$_3$," Phys. Rev. B, vol. 83, p. 094 111, 2011.

[329] I.-K. Jeong, N. Hur, and T. Proffen, "High-temperature structural evolution of hexagonal multiferroic YMnO$_3$ and YbMnO$_3$," J. Appl. Cryst., vol. 40, pp. 730–734, 2007.

[330] C. J. Howard, B. J. Campbell, H. T. Stokes, M. A. Carpenter, and R. I. Thomson, "Crystal and magnetic structures of hexagonal YMnO$_3$," Acta Cryst., vol. B69, pp. 534–540, 2013.

[331] A. G. Christy, "Isosymmetric structural phase transitions: Phenomenology and examples," Acta Cryst., vol. B51, pp. 753–757, 1995.

[332] H. F. Li, Y. Su, J. Persson, et al., "Neutron-diffraction study of structural transition and magnetic order in orthorhombic and rhombohedral La$_{7/8}$Sr$_{1/8}$Mn$_{1-\gamma}$O$_{3+\delta}$," J. Phys.: Condens. Matter, vol. 19, p. 176 226, 2007.

[333] A. J. Millis, B. I. Shraiman, and R. Mueller, "Dynamic jahn-teller effect and colossal magnetoresistance in La$_{1-x}$Sr$_x$MnO$_3$," Phys. Rev. Lett., vol. 77, pp. 175–178, 1996.

[334] I. D. Brown and D. Altermatt, "Bond-valence parameters obtained from a systematic analysis of the inorganic crystal structure database," Acta Crystallogr. B, vol. 41, pp. 244–247, 1985.

[335] N. E Brese and M. O'keeffe, "Bond-valence parameters for solids," Acta Crystallogr. B, vol. 47, pp. 192–197, 1991.

[336] F. Mohri, "A new relation between bond valence and bond distance," Acta Crystallogr. B, vol. 56, pp. 626–638, 2000.

[337] J. Herrero-Martín, J. García, G. Subías, J. Blasco, and M. C. Sánchez, "Structural origin of dipole x-ray resonant scattering in the low-temperature phase of $Nd_{0.5}Sr_{0.5}MnO_3$," Phys. Rev. B, vol. 70, p. 024 408, 2004.

[338] C. J. Fennie and K. M. Rabe, "Ferroelectric transition in $YMnO_3$ from first principles," Phys. Rev. B, vol. 72, p. 100 103, 2005.

[339] N. N. Greenwood and A. Earnshaw, Chemistry of the Elements. Oxford: Elsevier Butterworth-Heinemann, 1997.

[340] W. L. Stephen, Theory of Neutron Scattering from Condensed Matter. Oxford: Clarendon Press, 1984.

[341] C. Kittel, Quantum Theory of Solids. New York: Wiley, 1987.

[342] A. Tari, The Specific Heat of Matter at Low Temperatures. London: Imperial College Press, 1987.

[343] M. F. Collins, Magnetic Critical Scattering. London: Oxford University Press, 1989.

[344] S. J. Payne, M. E. Hagen, and M. J. Harris, "A study of the magnetic critical scattering from $FeCO_3$ by time-of-flight neutron diffraction," J. Phys.: Condens. Matter, vol. 8, p. 91, 1996.

[345] Y. Xiao et al., "Neutron diffraction investigation of the crystal and magnetic structures in $KCrF_3$ perovskite," Phys. Rev. B, vol. 82, p. 094 437, 2010.

[346] H.-F. Li, J.-Q. Yan, J. W. Kim, R. W. McCallum, T. A. Lograsso, and D. Vaknin, "Anisotropic magnetoelastic coupling in single-crystalline CeFeAsO as seen via high-resolution x-ray diffraction," Phys. Rev. B, vol. 84, p. 220 501, 2011.

[347] H. Li et al., "Possible magnetic-polaron-switched positive and negative magnetoresistance in the GdSi single crystals," Sci. Rep., vol. 2, p. 750, 2012.

[348] A. Kotani, H. Nakajima, K. Harada, Y. Ishii, and S. Mori, "Field-temperature phase diagram of magnetic bubbles spanning charge/orbital ordered and metallic phases in $La_{1-x}Sr_xMnO_3$ ($x = 0.125$)," Phys. Rev. B, vol. 95, p. 144 403, 2017.

[349] S. E. Hahn et al., "Inelastic neutron scattering studies of $YFeO_3$," Phys. Rev. B, vol. 89, p. 014 420, 2014.

[350] J.-S. Zhou and J. B. Goodenough, "Unusual evolution of the magnetic interactions versus structural distortions in $RMnO_3$ perovskites," Phys. Rev. Lett., vol. 96, p. 247 202, 2006.

[351] Y. Xu, Z. Xiong, H.-Q. Wu, and D.-X. Yao, "Spin excitation spectra of the two-dimensional $S = 1/2$ heisenberg model with a checkerboard structure," Phys. Rev. B, vol. 99, p. 085 112, 2019.

[352] I. S. Jacobs, H. F. Burne, and L. M. Levinson, "Field-induced spin reorientation in $YFeO_3$ and $YCrO_3$," Journal of Applied Physics, vol. 42, pp. 1631–1632, 1971.

[353] G. V. S. Rao, C. N. R. Rao, and J. R. Ferraro, "Infrared and electronic spectra of rare earth perovskites: Ortho-chromites,-manganites and-ferrites," Appl. Spectrosc., vol. 24, pp. 436–445, 1970.

[354] B. M. Wanklyn, "The flux growth of single crystals of rare earth perovskites (orthoferrites, orthochromites and aluminates)," J. Cryst. Growth, vol. 5, pp. 323–328, 1969.

[355] K Yoshii, "Magnetic properties of perovskite $GdCrO_3$," J. Solid State Chem., vol. 159, pp. 204–208, 2001.

[356] S. Mahana et al., "Local inversion symmetry breaking and spin-phonon coupling in the perovskite $GdCrO_3$," Phys. Rev. B, vol. 96, p. 104 106, 2017.

[357] O. Sari and M. Balli, "From conventional to magnetic refrigerator technology," Int. J. Refrig., vol. 37, pp. 8–15, 2014.

[358] S. Yin and M. Jain, "Enhancement in magnetocaloric properties of holmium chromite by gadolinium substitution," J. Appl. Phys., vol. 120, p. 043 906, 2016.

[359] S. Mahana, U. Manju, and D. Topwal, "$GdCrO_3$: A potential candidate for low temperature magnetic refrigeration," J. Phys. D: Appl. Phys., vol. 51, p. 305 002, 2018.

[360] B. B. Dash and S Ravi, "Structural, magnetic and electrical properties of Fe substituted $GdCrO_3$," Solid State Sci., vol. 83, pp. 192–200, 2018.

[361] J. Jensen and A. R. Mackintosh, Rare Earth Magnetism: Structures and Excitations. Oxford: Clarendon Press, 1991.

[362] Q. Zhang et al., "Magnetic structures and interplay between rare-earth Ce and Fe magnetism in single-crystal CeFeAsO," Phys. Rev. B, vol. 88, p. 174 517, 2013.

[363] S. Kumar, I. Coondoo, M Vasundhara, V. S. Puli, and N. Panwar, "Observation of magnetization reversal and magnetocaloric effect in manganese modified $EuCrO_3$ orthochromites," Physica B, vol. 519, pp. 69–75, 2017.

[364] C. Domb and M. F. Sykes, "On the susceptibility of a ferromagnetic above the Curie point," Proc. R. Soc. London, Ser. A, vol. 240, pp. 214–228, 1957.

[365] C. Domb and M. F. Sykes, "Use of series expansions for the ising model susceptibility and excluded volume problem," J. Math. Phys., vol. 2, pp. 63–67, 1961.

[366] J. E. Noakes and A. Arrott, "Initial susceptibility of ferromagnetic iron and iron-vanadium alloys just above their Curie temperatures," J. Appl. Phys., vol. 35, pp. 931–932, 1964.

[367] J. S. Kouvel and M. E. Fisher, "Detailed magnetic behavior of nickel near its Curie point," Phys. Rev., vol. 136, A1626–A1632, 1964.

[368] T. Moriya, "Nuclear magnetic relaxation near the Curie temperature," Progr. Theor. Phys., vol. 28, pp. 371–400, 1962.

[369] Y. Ishikawa, Y. Endoh, and S. Ikeda, "Magnetic critical scattering from an itinerant antiferromagnet of $\gamma Fe_{0.5}Mn_{0.5}$ alloy I. Quasi elastic scattering," J. Phys. Soc. Jpn., vol. 35, pp. 1616–1626, 1973.

[370] A. Jaiswal et al., "Magnetic and dielectric properties and raman spectroscopy of $GdCrO_3$ nanoparticles," J. Appl. Phys., vol. 107, p. 013 912, 2010.

[371] M. Tripathi et al., "Role of local short-scale correlations in the mechanism of negative magnetization," Phys. Rev. B, vol. 99, p. 014 422, 2019.

[372] Y. Zhang et al., "In-plane antiferromagnetic moments and magnetic polaron in the axion topological insulator candidate $EuIn_2As_2$," Phys. Rev. B, vol. 101, p. 205 126, 2020.

[373] L. Fkhar, A. Mahmoud, F. Boschini, et al., "Structural, magnetic, and magnetocaloric properties in rare earth orthochromite (Sm, Nd, and La)CrO_3 for cooling product," J. Supercond. Nov. Magn., vol. 33, pp. 1023–1030, 2020.

[374] A. McDannald and M. Jain, "Magnetocaloric properties of rare-earth substituted $DyCrO_3$," J. Appl. Phys., vol. 118, p. 043 904, 2015.

[375] S. Yin, V. Sharma, A. McDannald, F. A. Reboredo, and M. Jain, "Magnetic and magnetocaloric properties of iron substituted holmium chromite and dysprosium chromite," RSC Adv., vol. 6, pp. 9475–9483, 2016.

[376] A. Rostamnejadi, M. Venkatesan, P. Kameli, H. Salamati, and J. M. D. Coey, "Magnetocaloric effect in $La_{0.67}Sr_{0.33}MnO_3$ manganite above room temperature," J. Magn. Magn. Mater., vol. 323, pp. 2214–2218, 2011.

[377] S. Mahana, U. Manju, and D. Topwal, "Giant magnetocaloric effect in $GdAlO_3$ and a comparative study with $GdMnO_3$," J. Phys. D: Appl. Phys., vol. 50, p. 035 002, 2017.

[378] A. Midya, N. Khan, D. Bhoi, and P. Mandal, "Giant magnetocaloric effect in magnetically frustrated EuHo$_2$O$_4$ and EuDy$_2$O$_4$ compounds," <u>Appl. Phys. Lett.</u>, vol. 101, p. 132 415, 2012.

Curriculum Vitae

Personal information

Family name: ZHU, Given name: Yinghao

Male

DOB: Feb. 1996

Nationality: Chinese

Email: yhzhu0229@gmail.com

Academic education & employment

2018.8-Present

<u>Ph.D. candidate</u> in Applied Physics and Materials Engineering

Supervisor: Prof. Haifeng Li

Institute of Applied Physics and Materials Engineering,

University of Macau, Macao SAR, China

2021.4-2021.6

<u>Visiting research student</u> in Physics

Supervisor: Prof. Ruiqin Zhang

Department of Physics,

City University of Hong Kong, Hong Kong SAR, China

2014.9-2018.6

<u>B. S.</u> in Physics

Supervisor: Prof. Xiaoguang Ma

School of Physics and Optoelectronic Engineering

Ludong University, Yantai, China

Publications   (*contribution equally)

[1] Structural evolution of single-crystal RECrO$_3$ (RE = Y,Eu–Lu) orthochromates
Yinghao Zhu, Pengfei Zhou, Kaitong Sun, Hai-Feng Li
Journal of Solid State Chemistry 313, 123298 (2022)

[2] Temperature-dependent structure of an intermetallic ErPd$_2$Si$_2$ single crystal: A combined synchrotron and in-house X-ray diffraction study
Kaitong Sun*, *Yinghao Zhu**, Si Wu*, Junchao Xia, Si Wu, Qian Zhao, Kaitong Sun, Pengfei Zhou, Chongde Cao, Hai-Feng Li
Powder Diffraction pp. 1-7 (2022)

[3] Crystal growth engineering and origin of the weak ferromagnetism in antiferromagnetic matrix of orthochromates from *t-e* orbital hybridization
Yinghao Zhu, Junchao Xia, Si Wu, Qian Zhao, Kaitong Sun, Pengfei Zhou, Yuewen Yang, Yanling Zhao, Hei Wun Kan, Yang Zhang, Ling Wang, Hui Wang, Jinghong Fang, Chaoyue Wang, Tong Wu, Yun Shi, Jianding Yu, Ruiqin Zhang, Hai-Feng Li
iScience 25, 104111 (2022)

[4] Temperature-dependent structure and magnetization of YCrO$_3$ compound
Qian Zhao*, *Yinghao Zhu**, Si Wu, Junchao Xia, Pengfei Zhou, Kaitong Sun, Hai-Feng Li
Chinese Physics B 31, 046101 (2022)

[5] Enhanced magnetocaloric effect and magnetic phase diagrams of single-crystal GdCrO$_3$
Yinghao Zhu, Pengfei Zhou, Tao Li, Junchao Xia, Si Wu, Ying Fu, Kaitong Sun, Qian Zhao, Zhen Li, Zikang Tang, Yinguo Xiao, Zhenqiang Chen, Hai-Feng Li
Physical Review B 102, 144425 (2020)

[6] Crystalline and magnetic structures, magnetization, heat capacity, and anisotropic magnetostriction effect in a yttrium-chromium oxide
Yinghao Zhu, Ying Fu, Bao Tu, Tao Li, Jun Miao, Qian Zhao, Si Wu, Junchao Xia, Pengfei Zhou, Ashfia Huq, Wolfgang Schmidt, Defang Ouyang, Zikang Tang, Zhubing He, Hai-Feng Li
Physical Review Materials 4, 094409 (2020)

[7] High-temperature magnetism and crystallography of a $YCrO_3$ single crystal
Yinghao Zhu, Si Wu, Bao Tu, Shangjian Jin, Ashfia Huq, Jörg Persson, Haoshi Gao, Defang Ouyang, Zhubing He, Dao-Xin Yao, Zikang Tang, Hai-Feng Li
Physical Review B 101, 014114 (2020)

[8] Super-necking crystal growth and structural and magnetic properties of $SrTb_2O_4$ single crystals
Si Wu*, *Yinghao Zhu**, Haoshi Gao*, Yinguo Xiao, Junchao Xia, Pengfei Zhou, Defang Ouyang, Zhen Li, Zhenqiang Chen, Zikang Tang, Hai-Feng Li
ACS Omega 5, 16584-16594 (2020)

[9] Symmetry-broken effects on electron momentum spectroscopy caused by adiabatic vibration
Yinghao Zhu, Xiaoguang Ma, Wenhua Lou, Meishan Wang, Chuanlu Yang
Chemical Physics Letters 687, 116-124 (2017)

[10] Enhancement of room-temperature magnetization in $GaFeO_3$-type single crystals by Al and Sc doping
Ling Wang, Tsukasa Katayama, Chaoyue Wang, Qin Li, Yun shi, Yuqiang Fang, Fuqiang Huang, *Yinghao Zhu*, Hai-Feng Li, Shintaro Yasui, Xintang Huang, and Jianding Yu
AIP Advances 12, 065015 (2022)

[11] Reducing systemic absorption and macrophages clearance of genistein by lipid-coated nanocrystals for pulmonary delivery
Yuan He, Chang Liu, Run Han, Yingmin Liang, Judith Choi Wo Mak, *Yinghao Zhu*, Haifeng Li, Ying Zheng
Chinese Chemical Letters accepted (2022)

[12] Single-crystal synthesis of ε-Fe_2O_3-type oxides exhibiting room-temperature ferrimagnetism and ferroelectric polarization
Yang Zhang, Hui Wang, Koki Tachiyama, Tsukasa Katayama, *Yinghao Zhu*, Si Wu, Hai-Feng Li, Jinghong Fang, Qin Li, Yun Shi, Ling Wang, Zhengqian Fu, Fangfang Xu, Jianding Yu, Shintaro Yasui, Mitsuru Itoh
Crystal Growth & Design 21, 4904-4908 (2021)

[13] Disorder-induced spin-liquid-like behavior in Kagome-lattice compounds
Zhen Ma, Zhao-Yang Dong, Si Wu, *Yinghao Zhu*, Song Bao, Zhengwei Cai, Wei

Wang, Yanyan Shangguan, Jinghui Wang, Kejing Ran, Dehong Yu, Guochu Deng, Richard A. Mole, Hai-Feng Li, ShunLi Yu, Jian-Xin Li, Jinsheng Wen
Physical Review B 102, 224415 (2020)

[14] Colossal Negative Magnetoresistance Effect in a $La_{1.37}Sr_{1.63}Mn_2O_7$ Single Crystal Grown by LaserDiode-Heated Floating-Zone Technique
Si Wu, *Yinghao Zhu*, Junchao Xia, Pengfei Zhou, Haiyong Ni, Hai-Feng Li
Crystals 10, 547 (2020)

[15] The investigation of excited-state intramolecular proton transfer mechanism of 2-Acetylindan-1, 3-Dion: the solvation effect
Mingshang Li, Weiyi Ren, Ziqi He, *Yinghao Zhu*
Journal of Cluster Science 28, 2111-2122 (2017)

[16] Gamma-ray spectra from low-energy positron annihilation process in molecules
Xiaoguang Ma, Meishan Wang, *Yinghao Zhu*, Yang Liu, Chuanlu Yang, Dehua Wang
Physical Review A 94, 052709 (2016)

[17] The gamma-ray spectra of 5-carbon alkane isomers in the positron annihilation process
Xiaoguang Ma, *Yinghao Zhu*, Yang Liu
Physical Letters A 380, 1848-1855 (2016)

[18] Positron-electron annihilation process in (2, 2)-difluoropropane molecule
Yang Liu, Xiaoguang Ma, *Yinghao Zhu*
Communications in Theoretical Physics 65, 531 (2016)

[19] The gamma-ray spectra of halocarbons in the positron annihilation process
Xiaoguang Ma, *Yinghao Zhu*, Yang Liu
Physical Letters A 379, 2306-2310 (2015)

Patents

[1] A method of centimeter-sized single crystal growth of chromate compounds and related storage device
Hai-Feng Li, *Yinghao Zhu*, Si Wu, Zikang Tang
China Invention Patent, CN 110904497 B

[2] A cover for X-ray diffraction sample holder, support stands and method of X-ray diffraction

Hai-Feng Li, *Yinghao Zhu*, Si Wu, Zikang Tang

China Invention Patent, 201911069156.4

[3] A sample holder for X-ray diffractometer, its application and X-ray diffractometer

Hai-Feng Li, Si Wu, *Yinghao Zhu*

China Invention patent, CN 110880856 B

[4] An autoclave for studying dendrite growth

Hai-feng Li, Pengfei Zhou, *Yinghao Zhu*, Junchao Xia, Si Wu, Haoshi Gao

China Utility Model Patent, CN 212483788 U

[5] In situ annealing equipment for single crystal growth

Hai-Feng Li, Si Wu, Junchao Xia, *Yinghao Zhu*, Pengfei Zhou, Zikang Tang

China Utility Model Patent, CN 212476954 U

[6] Swinging apparatus for single crystal growth & a system of swinging furnace for large-scale single crystal growth

Hai-Feng Li, Junchao Xia, Si Wu, *Yinghao Zhu*

China Utility Model Patent, CN 211872141 U

[7] A type of single crystal growth furnace

Hai-Feng Li, Junchao Xia, Si Wu, *Yinghao Zhu*, Pengfei Zhou

China Utility Model Patent, CN 211522370 U

[8] A gripping device for performance measurement of solid state electrolytes

Hai-Feng Li, Pengfei Zhou, Kaitong Sun, Qian Zhao, Junchao Xia, Si Wu, *Yinghao Zhu*

China Utility Model Patent, 202111421365.8

[9] A solid-state electrolyte of ceramic oxide and its preparation method

Hai-Feng Li, Kwun Nam Hui, Pengfei Zhou, Shunping Ji, Qian Zhao, Kaitong Sun, Junchao Xia, Si Wu, *Yinghao Zhu*

China Utility Model Patent, 202111421365.8